



HAL
open science

The electrochemistry and dealloying of Zn-Mg/Zn-Al pure phases and their significance for corrosion of Zn-Al-Mg alloys

Junsoo Han

► **To cite this version:**

Junsoo Han. The electrochemistry and dealloying of Zn-Mg/Zn-Al pure phases and their significance for corrosion of Zn-Al-Mg alloys. Material chemistry. Chimie ParisTech, 2018. English. NNT : . tel-02087202

HAL Id: tel-02087202

<https://theses.hal.science/tel-02087202>

Submitted on 1 Apr 2019

HAL is a multi-disciplinary open access archive for the deposit and dissemination of scientific research documents, whether they are published or not. The documents may come from teaching and research institutions in France or abroad, or from public or private research centers.

L'archive ouverte pluridisciplinaire **HAL**, est destinée au dépôt et à la diffusion de documents scientifiques de niveau recherche, publiés ou non, émanant des établissements d'enseignement et de recherche français ou étrangers, des laboratoires publics ou privés.

THÈSE DE DOCTORAT

de l'Université de recherche Paris Sciences et Lettres
PSL Research University

Préparée à
Institut de Recherche de Chimie de Paris (IRCP),
Interfaces, Electrochimie & Energie (I2E)

L'électrochimie et désalliage de Zn-Mg / Zn-Al phase pures et
l'importance pour la corrosion sur l'alliage de Zn-Al-Mg.

Ecole doctorale n° 388

Chimie physique et chimie analytique de Paris Centre

Spécialité Chimie physique

Soutenue par **Junsoo HAN**
le 29 août 2018

Dirigée par
Professeur **Kevin OGLE**



COMPOSITION DU JURY :

M. TERRY N Herman
Vrije Universiteit Brussel (VUB), Belgique, Rapporteur

Mme. SIMOES Alda
Instituto Superior Técnico (IST), Portugal, Rapporteur

M. THIERRY Dominique
Institut de la corrosion, France, Examineur

Mme. GRIMAUD Laurence
Ecole Normale Supérieure (ENS), France, Examineur

M. OGLE Kevin
Ecole Nationale Supérieure de Chimie de Paris,
(ENSCP), France, Directeur de thèse

Thèse de doctorat de
L'Université de recherche Paris Sciences & Lettres
PSL Research University

Institut de Recherche de Chimie de Paris (IRCP)

Interfaces, Electrochimie & Energie (I2E)

**The electrochemistry and dealloying of Zn-Mg/Zn-Al pure phases
and their significance for corrosion of Zn-Al-Mg alloys.**

Présentée par

Junsoo HAN

Pour obtenir le grade de

DOCTEUR DE L'UNIVERSITE DE RECHERCHE PARIS SCIENCE & LETTRES

Spécialité Chimie physique

Soutenue le 29 août 2018

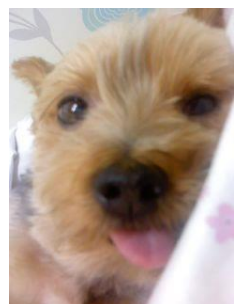
Devant le jury compose de:

Herman TERRYN	Professeur à Vrije Universiteit Brussel, Bruxelles, Belgique	Rapporteur
Alda SIMOES	Professeur à Instituto Superior Técnico, Lisbonne, Portugal	Rapporteur
Dominique THIERRY	Directeur de l'institut de la corrosion, Brest, France	Examineur
Laurence GRIMAUD	Directeur de l'ENS-département de Chimie, Paris, France	Examineur
Kevin OGLE	Professeur à Chimie ParisTech, Paris, France	Directeur de thèse

«Notre « moi » est fait de la superposition de nos états successifs. Mais cette superposition n'est pas immuable comme la stratification d'une montagne. Perpétuellement des soulèvements font affleurer à la surface des couches anciennes.»

A la recherche du temps perdu (1918),

Marcel Proust



Acknowledgement

I still remember the first day I arrived to the laboratory in France with totally different atmosphere from where I've lived. At that day, the most unforgettable feeling was a thrill to be re-starting an academic career, which still motivates me. Beyond all, I would like to appreciate to all people who gave me this opportunity, directly or indirectly. I wish to acknowledge everyone who shared a moment during these three years.

First of all, I would like to express my gratitude to all jury members of my PhD work to show their interest and evaluate it. It was a great pleasure to discuss with Prof. Herman Terryn during the Gordon research conference in summer 2018. It helped me hugely to think further about detailed mechanism of the system that I have worked. Prof. Alda Simoes, her kind advice before the PhD defense will not be forgettable for me. I cannot find the words to say thank to Dr. Dominique Thierry. I feel very lucky to work with him for the Microcorr project. Dr. Larence Grimaud, kindly accepted role of the president of the jury for the PhD defense. Her pertinent comments on the presentation will be a guideline for my future work.

I greatly appreciate to Prof. Kevin Ogle, my PhD advisor, for navigating this journey with me during three years. He is a nice and cool captain, giving brilliant ideas and inspirations to his crews. I undoubtedly enjoyed the time spending with him on discussion about the results, ongoing projects, publications, and developing new systems. He has been an excellent example of a scientist and a professor for me who I would like to be alike in the future.

I would like to appreciate to all the European Microcorr project partners. Dr. Christian Allély, *ArcelorMittal*, France always gave me useful advices for the project and also for my future. Dr. Bekir Salgin, *Tata steel*, the Nethelands, has been a role model of how a 'hard worker' drives a project in a successful way. *Swansea University* always has been a wonderful companion during my Ph.D. Prof. Neil McMurray, his keen insight and amazing presentation skill always inspires me. Whenever I met Prof. Geraint Williams in a conference, he kindly gave me advices on my presentation which was always incredibly helpful. Although I could not meet him directly, Prof. James Sullivan was always open to have a discussion by skype. I cannot forget the time I've worked with Dr. Nathan Cooze, always active and easy to communicate. Still I'm working with Mr. Callum Gallagher, brilliant graduate student giving me full of energy. I'm sure your Ph.D. will go very well! During two weeks of collaboration in *Max-Planck-Institut*, Düsseldorf in summer 2017, Prof. Michael Rohwerder, group leader of the corrosion department, gently greeted me and helped me enormously. Thanks to his arrangement, I could do the experiments for the project and could see how the research goes in other laboratories. I should mention that I could not do anything without helps from Mr. Matthias Uebel and Dr. Nicole Fink who actually worked with me on SKP and ICP-MS. I spent a lot of time discussing with Dr. Philippe Verpoort, *OCAS*, Belgium and Dr. Gerald Luckeneder, *Voestalpine*, Austria, during the Microcorr meeting which always gives me fresh ideas. I am truly grateful to Dr. Jan Stouilil of *University of Chemistry and Technology in Prague*, Czech Republic for supplying pure phases. Without him, I could have not accomplished my PhD work. I clearly recall the first day of the Microcorr meeting in 2015, with Dr. Tomas Prosek who explained me about the project. Also, many thanks to Dr. Nathalie LeBozec, *Institut de la Corrosion*, France for coordinating the project. I will not forget other members' help which I might not mention here.

I could not have achieved anything without team I2E members of Chimie ParisTech. I would like to appreciate to Prof. Michel Cassir who initially invited me to the team during my master internship. Dr. Armelle Ringuedé, I cannot forget the moment that we discussed about the literatures, culture, foods (most important!), language and history of France. Without her

help, I would not manage to speak and write French like now. Her kindness, patience and willing to have a discussion with a foreign student from Far East will not be forgotten.

Je vous remercie Valérie, Virginie d'avoir été patientes de parler avec moi en français (surtout au début !). Comme je t'ai souvent dit, je suis très fier de comprendre tes blagues, Marie-Hélène. Abdelilah, Peng, Jeffrey et Xuejie, 'team ICP', je vous remercie de m'avoir aidé pendant la rédaction. Je suis un gros fan de ton humour, Oumaïma. C'était toujours utile de discuter avec toi. Cyril et Perrine, je ne pourrai pas oublier les moments qu'on a partagés ensemble (surtout le temps difficile !). J'espère fortement qu'on va voyager tous ensemble en Asie et goûter des plats piquants ! Haitam, Ersan, Mélisande et Thomas, ça me manquera de 'réfléchir' à « qu'est-ce qu'on mange » chaque midi... ça me fait plaisir de déjeuner au jardin du Luxembourg en plein soleil avec vous ! Ma première présentation en français n'aurait pas été possible sans Aurélie. C'était un grand plaisir de discuter sur l'histoire et culture française avec elle. André, c'était tellement drôle de te voir à Saint-Pétersbourg. Merci de me laisser un bon souvenir avec Suyeon. Je tiens à remercier toute l'équipe, Diego, Alina, Dmitri, Oleg, Vladimir, Sanna, Mariem, Simone, Moussa, Anand, Nathaly, Dung, Bob, Marjorie, Elisabeth, Polina, et aussi les ancien(ne)s postdocs/thésards/stagiaires, Dorra, Débora, François, Karima, Nour, Arturo, Slava, Amandine(s), Barbara, Manel, Mathiew, Moussa, Caroline.

Mes remerciements vont aussi aux gens qui me dépannent au quotidien. Je remercie particulièrement Dr. Grégory Lefèvre pour discuter sur la simulation thermodynamique. Dr. Fan Sun toujours me donnait un coup de main sur le MEB. Et aussi je remercie tout le monde de l'équipe métallurgie pour leur gentillesse de discuter sur mes échantillons. Je remercie Dr. Odile Majérus pour me former au Raman et Dr. Pascal Loiseau pour les mesures DRX. Je remercie également Prof. Alexa Courty, Dr. Jolanta Swiatowska, Marion, Elise, Pascal, Louis, Dimitri, Sandrine, Rémi, Pauline, Mohamed, Anne-Ilham, Isabelle, Hervé, Paul, Shoshan, Jintao, Ali, Francine, Matinou, Didier, Nelly, Agnès, M. Bremier et M. Laurin (chez Horiba Jobin Yvon).

Youngju and Jin, thank you for all your help and your Korean foods (!). Chatting with you guys was relaxing to me. Bon-min et Constance, merci pour vous les deux de passer pas mal de temps avec moi. J'ai pu apprendre énormément chose grâce à vous.

I firstly apologize to my parents and sister who supported me from a distance because I could not go to South Korea during four years. Their unconditional support always made me move to the next step. I could not have a chance to do a PhD without their sacrifice.

At last, I would write another 300 pages (without figures!) of thesis to express my gratitude to Suyeon LEE, my wife, who always makes me laugh and happy. Honestly, even I was not sure how it will work when I firstly suggested her to go to France and do a PhD with me. Thank you for believing in me and coming here with me so far. I promise you that our next journey will be way more interesting with a lot of fun! Of course, it may be somewhat difficult, however I believe you will never regret as you'll not feel like being a zebra in a vast plain without lions ☺.

Junsoo HAN

November 2018, Paris

Table of content

Acknowledgement	5
List of acronyms and symbols	10
Résumé de la thèse	13

Introduction

I: Introduction	25
1.1. Origin and objectives of this Ph.D. study.....	26
1.2. The particularities of this Ph.D. study.....	28
1.3. Summary of the Ph.D. thesis	29
1.4. List of publications and conferences.....	36
II: State of the art	39
2.1. Introduction of Zn-based alloy coatings.....	40
2.2. Corrosion mechanisms of Zn-Al-Mg.....	41
2.2.1. Effect of chemical composition.....	41
2.2.2. Effect of microstructure	42
2.2.3. Effect of corrosion products	43
2.2.4. Summary of the corrosion mechanism of Zn-Al-Mg	47
2.3. Pure phase chemistry and dealloying of binary alloys.....	48
2.4. Conclusion and perspectives of dealloying on the corrosion mechanisms of Zn-Al-Mg ..	52
III: Atomic emission spectroelectrochemistry (AESEC)	53
3.1. Introduction of the spectroscopy	54
3.2. AESEC technique: methodology and instrumentation.....	56
3.2.1. Nature of atomic spectra	56
3.2.2. Instrumentation.....	57
Plasma torch	57
Nebulizer and cyclonic chamber.....	60
Electrochemical flow cell.....	60
Wavelength dispersive devices.....	62
3.2.3. Data analysis	63
Calibration of the ICP-AES signals	63
Residence time distribution	65
3.3. Signal noise and perturbation	68
3.4. Sample preparation	69
3.5. Electrochemical experiments.....	70
3.5.1. Potentiodynamic polarization.....	70
3.5.2. Chronoamperometry	70
3.5.3. Chronoamperometric step experiment	70
3.5.4. Alternative current AESEC	71
3.6. <i>Ex-situ</i> surface characterization techniques.....	71
3.6.1. Scanning electron microscopy-energy dispersive X-ray spectroscopy.....	71
3.6.2. Raman spectroscopy	72
3.6.3. X-ray diffraction.....	73

IV: Dealloying of MgZn₂ intermetallic in slightly alkaline chloride electrolyte and its significance in corrosion resistance	75
4.1. Introduction	77
4.2. Experimental	80
4.3. Results.....	82
4.3.1. Open circuit dissolution	82
4.3.2. Polarization curves of Mg and Zn	85
4.3.3. Polarization curve of MgZn ₂	88
4.3.4. MgZn ₂ chronoamperometric experiments	89
Cathodic dissolution at E _{ap} = -1.40 V.....	90
Anodic dissolution domain.....	91
Oxide formation domain	92
Evans diagram analysis	93
4.4. Discussions	95
4.5. Conclusions	98
V: Cathodic dealloying of α-phase Al-Zn in slightly alkaline chloride electrolyte and its consequence for corrosion resistance	99
5.1. Introduction	101
5.2. Experimental	103
5.3. Results.....	105
5.3.1. The dissolution of pure Al.....	105
5.3.2. The potential dependence of Al _{5,2} Zn dissolution: Overview.....	107
5.3.3. Anodic reactivity of Al _{5,2} Zn.....	110
5.3.4. Cathodic reactivity of Al _{5,2} Zn	111
5.3.5. The effect of O ₂ on cathodic dealloying	116
5.4. Discussions	119
5.5. Conclusions	123
VI: The anodic and cathodic dissolution of α-phase of Zn-68Al in alkaline media	125
6.1. Introduction	127
6.2. Experimental	128
6.3. Results.....	131
6.3.1. Spontaneous dissolution.....	131
6.3.2. The electrochemistry of pure Al.....	133
6.3.3. The electrochemistry of pure Zn	135
6.3.4. The electrochemistry of Al _{5,2} Zn	138
6.3.5. Chronoamperometric experiments of Al _{5,2} Zn	142
6.3.6. The effect of O ₂ on the LSV of Al _{5,2} Zn	147
6.4. Discussions	149
6.5. Conclusions	151
VII: Temperature dependence of the passivation and dissolution of Al, Zn and α-phase Zn-68Al	153
7.1. Introduction	155
7.2. Experimental	157
7.3. Results.....	158
7.3.1. Spontaneous dissolution as a function of temperature.....	158
7.3.2. AESEC polarization curves as a function of temperature.....	161
Pure Al	162

Pure Zn	163
Al _{5.2} Zn	167
7.4. Kinetic analysis and discussions.....	169
7.4.1. Al dissolution	170
7.4.2. Zn dissolution.....	171
7.5. Conclusions	174
VIII: Electrochemical database of Zn-Al-Mg system from neutral to alkaline media ..	177
8.1. Introduction	178
8.2. Experimental	178
8.3. Results.....	180
8.3.1. AESEC-LSV at pH=10.1	180
8.3.2. AESEC-LSV at pH=8.4.....	186
8.3.3. AESEC-LSV at pH=12.80	191
8.4. Data analysis with composition.....	197
8.4.1. Spontaneous dissolution analysis as a function of pH.....	197
8.4.2. Kinetic analysis	201
8.4.3. The effect of pH on Al dissolution mechanism	202
8.5. Conclusions	203
IX: Characterization of the artificially formed corrosion product by Raman spectroscopy	205
9.1. Introduction	206
9.2. Experimental	206
9.3. Results.....	207
9.3.1. Comparison between titration experiments and thermodynamic simulations ..	207
9.3.2. Characterization of artificially formed precipitations in solution.....	212
Individual Zn ²⁺ , Al ³⁺ and Mg ²⁺	212
Zn ²⁺ + Mg ²⁺	213
Al ³⁺ + Mg ²⁺	213
Zn ²⁺ + Al ³⁺ + Mg ²⁺	214
9.3.3. Comparison with the electrochemically formed corrosion products	215
9.4. Discussions and conclusions	216
Conclusions	
X: Summary and perspectives	219
Appendix	
Appendix 1: Alternative current AESEC (AC-AESEC) technique	226
Appendix 2: Comparison between ICP-MS and ICP-AES	241
Appendix 3: Bi-electrode analysis to understand interaction between elements	245
Appendix 4: Comparison of surface preparation methods for Zn-5Al commercial alloy coating	253
References.....	267

List of acronyms

AESEC	atomic emission spectroelectrochemistry
ICP-AES	inductively coupled plasma atomic emission spectroscopy
ICP-MS	inductively coupled plasma mass spectroscopy
HER	hydrogen evolution reaction
CA	chronoamperometry
SEM	scanning electron microscopy
SEM-EDS	scanning electron microscopy-energy dispersive spectroscopy
SE	secondary electron
BSE	backscattered electron
FEG	field emission gun
DPSS	diode pumped solid state
XRD	X-ray diffraction
AC-AESEC	alternative-current AESEC
STM	scanning tunneling microscopy
LIBS	laser-induced breakdown spectroscopy mapping
RDE	rotating disk electrode
SKP	scanning Kelvin probe
EQCM	electrochemical quartz crystal microbalance
QCM	quartz crystal microbalance
SEC	spectroelectrochemistry
UV-vis	ultraviolet-visible spectroscopy
IR	infrared spectroscopy
ICP	inductively coupled plasma
RF	radio frequency
RE	reference electrode
CE	counter electrode
WE	working electrode
Poly	polychromator
Mono	monochromator
PMT	photo-multiplier
RH	relative humidity
LSV	linear sweep voltammetry
Anodic LSV	LSV from E_{oc} to positive potential
Cathodic LSV	LSV from E_{oc} to negative potential
AESEC-LSV	atomic emission spectroelectrochemistry linear sweep voltammetry
EIS	electrochemical impedance spectroscopy
HDG	hot-dip galvanized steel or hot-dip galvanization
PVD	physical vapor deposition
SVET	scanning vibrating electrode technique
NSS	neutral salt spray test
XPS	X-ray photoelectron spectroscopy
AES	Auger electron spectroscopy
LDHs	layered double hydroxides
BZS	basic zinc salts
IRRAS	infrared reflection-absorption spectroscopy
PL	photoluminescence
LIBS	laser-induced breakdown spectroscopy mapping

NAZ	normal analytical zone
IRZ	initial radiation zone
IR	induction region
PHZ	pre-heating zone
AAS	atomic absorption spectroscopy
HZ	hydrocarbonate

List of the symbols

I_{λ}°	background intensity signal	N_B	mole fraction of more noble metal in binary alloys
I_M	elemental intensity signal	h	Planck constant
A	reaction surface	ν	frequency of the radiation
$C_{M(sat)}$	saturation concentration of a certain element	c	speed of light
C_M	elemental concentration	f	flow rate of the electrolyte in the flow cell
κ_{λ}	sensitivity factor for a given wavelength	E	electrical potential
M_M	molar mass of an element	E_{oc}	open circuit potential
z	oxidation state of an element	E_c^{Zn}	onset potential of Zn dissolution
ν_M	elemental dissolution rate	$E_c^{Zn/Zn-OH}$	onset potential of cathodic Zn dissolution
j_e	electrical current density	E_c	onset potential of bulk dissolution
j_e^*	convoluted electrical current density	$E_{j=0}$	potential where $j=0$
j_a	anodic current density	E°	standard reduction potential
j_c	cathodic current density	E_p^{Zn}	potential where passive Zn dissolution initiates from LSV
j_M	faradaic elemental current density	E_{AC}	potential perturbation with a fixed frequency
j_{Σ}	sum of elemental current densities	$Zn(0)$	Zn enriched layer
j_{ins}	current density of insoluble species	$E_a(M/Z)$	activation energy of M dissolution from Z
j_{Δ}	mass balance equation: $j_e^* - j_{\Sigma}$	$n^{OH^-}/n^{M^{z+}}$	ratio between moles of OH^- and cations
j_M^s	steady state elemental current density	$Q_{M(0)}$	surface enrichment of element, M
η	faradaic yield: j_{Σ} / j_e^*	Q_{ZnO}	total amount of Zn
$h(t)$	residence time distribution function	ν_e^* / ν_{Al}	stoichiometry of cathodic Al dissolution
F	Faraday constant	n_e	number of exchanged electrons
β	time constant defined for $h(t)$	$\sigma_{j_{Al}}$	perturbation signal of j_{Al}

Résumé

1. Origine et objectives de ces travaux de thèse

L'acier galvanisé

La première utilisation d'alliages de Zn aurait été une armure apparemment de Zn avant 1680 en Inde. En fait, il s'agissait d'un métal gris oxydé, obtenu par trempage à chaud d'un acier dans un bain de Zn fondu. En 1742, un chimiste français Melouin rapporte à l'Académie royale des sciences que l'immersion de l'acier dans un bassin de zinc fondu mène à la protection contre la corrosion. En 1780, un chimiste italien Luigi Galvani a observé le courant électrique en contractant une jambe de grenouille au contact du cuivre et du fer. Le mot «galvanisation» vient donc de Galvani, et est apparu en Europe au travers d'un brevet de 1836, par Sorel, chimiste français portant sur le procédé d'enduit d'acier. Le mot galvanisation indiquait initialement les propriétés intrinsèques qui pouvaient être obtenues par le revêtement lui-même plutôt que par le procédé. Il a été néanmoins assimilé aux chocs électriques, a également été appelé Faradism. À ce moment-là, le verbe «galvaniser» était défini comme provoquant une personne complaisante à bouger. L'année suivante, un brevet britannique a été accordé pour le même procédé par William Crawford. En 1850, plus de 10 000 tonnes de zinc ont été produites par an au Royaume-Uni pour la fabrication d'acier. C'était la période où le mot «galvaniser» était incorporé dans le langage des gens.

L'acier galvanisé a été utilisé dans diverses applications telles que la construction, l'automobile, l'ingénierie / fabrication, l'électroménager et d'autres domaines pour la protection de l'acier. En conséquence, la consommation de l'acier revêtu a été augmentée de 80 millions de tonnes en 2000 à 132 millions de tonnes en 2014 [1]. En 2014, 80 millions de tonnes (MnT) d'acier galvanisé, 25,24 MnT de GalfanTM / GalvalumeTM / galvanisé et 27,27 MnT d'Electro Galva ont été consommés dans le monde entier.

L'acier galvanisé a été étudié à l'échelle laboratoire pour améliorer sa résistance à la corrosion pendant plusieurs décennies. L'un des moyens les plus efficaces pour atteindre une meilleure efficacité face à la corrosion d'allier le Zn avec d'autres éléments. Les systèmes binaires d'alliage Zn de type Zn-Al, Zn-Cu, Zn-Fe et Zn-Pb ont été étudiés pour des applications

Résumé

spécifiques. En outre, des alliages ternaires et quaternaires obtenus en ajoutant des éléments tels que Mg, Ni, Ti et Cd ont également été développés. Pour prédire le comportement à la corrosion des revêtements en alliage à base de Zn, différents types de tests de corrosion tels que l'exposition atmosphérique, des tests de corrosion accélérée dans des conditions spécifiques, la caractérisation de surface et des expériences électrochimiques ont été réalisés.

Objectif de la thèse

Le comportement électrochimique des revêtements d'alliage Zn-Al et Zn-Al-Mg est compliqué en raison des multiples phases qui peuvent interagir entre elles provoquant alors un couplage galvanique entre ces phases. Dans les revêtements d'alliage hétérogènes, la phase métallique plus noble peut faciliter la corrosion des phases moins nobles. À cette fin, cette thèse de doctorat vise à étudier la cinétique de dissolution élémentaire des phases individuelles et des métaux purs des revêtements d'alliage. Trois solutions de pH différentes ont été choisies parce que les comportements chimique et électrochimique des composants peuvent varier avec le pH. Les données électrochimiques de chaque phase ont été utilisées pour prédire le comportement à la corrosion des revêtements d'alliage multi-phasés.

Les particularités de cette thèse

Dans le cadre de cette thèse, la spectroélectrochimie d'émission atomique (AESEC) a été mise en œuvre. C'est une technique idéale pour mettre en évidence la dissolution sélective du système multiéléments. Cette technique nous permet de mesurer non seulement la réponse élémentaire de la réaction chimique, mais aussi les réponses électriques dans le système.

Nous avons étudié le comportement électrochimique de la phase pure Al-Zn / Mg-Zn constituée des revêtements d'alliage Zn-Al / Zn-Al-Mg. Dans un premier temps, nous avons analysé le délestage des phases intermétalliques $MgZn_2$ (**Chapitre IV**) et Al-Zn (phase η de Zn et phase α de Al, **Chapitres V, VI et VII**). L'effet inhibiteur de la dissolution de Zn sur Al, trouvé dans tout le système Zn-Al dans ce projet, a été discuté à partir de la réponse électrochimique de chaque élément et aussi du rôle des produits de corrosion. Le rôle de la couche enrichie en oxyde métallique de Zn, $(Zn(0))$ a été étudié via un système différent. En outre, les alliages

commerciaux de Zn-Al et Zn-Al-Mg ont été examinés et comparés avec les résultats des métaux purs et des phases.

Une autre particularité de ce travail a été le développement d'une étape méthodologique de la technique AESEC. L'origine de certains pics de dissolution élémentaires observés au cours de l'expérience de polarisation AESEC a été vérifiée par des expériences de «chronoampérométrie». Ces mesures ont été effectuées à l'origine par Wagner et al. [2] mais ils ne pouvaient enregistrer que le courant transitoire total plutôt que la dissolution élémentaire. En outre, ils ont étudié seulement une petite plage de potentiels proches du potentiel de corrosion. Dans ce travail, nous avons confirmé et quantifié pour la première fois la formation d'une couche enrichie en l'élément le plus noble suite à la dissolution sélective des éléments les moins nobles.

La cinétique de dissolution élémentaire a été révélée par son énergie d'activation découplant l'oxydation des métaux, la formation des espèces insolubles et l'évolution de l'hydrogène. Autour du potentiel du circuit ouvert, la dissolution de Zn était limitée par la formation de $Zn(OH)_2$. A plus haute température, la quantité de ZnO non dissous augmentait en formant un film passif. Pour la phase Al-Zn, la vitesse de dissolution d'Al et Zn était contrôlée par un mécanisme de transfert de charge à travers le film de ZnO.

Une base de données de courbes de polarisation élémentaire pour 10 échantillons (métaux Zn / Al / Mg, Zn-0.7Al, Zn-22Al, Zn-68Al, phases pures $MgZn_2$, Zn-Al-Mg et deux alliages commerciaux Zn-Al) a été établie en fonction du pH et en présence/absence d'oxygène (**Chapitre VIII**). La dissolution élémentaire de chaque élément a été comparée avec des revêtements d'alliage sous forme de phase pure et d'alliage multiphasé. Les données de potentiel obtenues peuvent être appliquées pour prédire la cinétique de dissolution en tenant compte du couplage galvanique entre les phases.

Les produits de corrosion formés pendant les mesures électrochimiques ont été comparés aux espèces précipitées, formées dans la solution pendant l'expérience de titrage. Ces résultats ont également été comparés avec la base de données thermodynamiques (**Chapitre IX**).

La technique AESEC a été utilisée pour interpréter non seulement la dissolution élémentaire

mais aussi la réponse électrochimique. Par exemple, nous avons tenté de quantifier la réaction d'évolution de H_2 (HER) par la technique AESEC en utilisant des signaux de vitesse de dissolution d'Al perturbés. La relation linéaire entre la vitesse de dissolution de l'Al à l'état stationnaire et le signal d'écart-type a été observée dans tous les alliages contenant de l'Al, les phases pures et le métal dans toutes les conditions d'électrolyte étudiées dans ce travail. La bi-électrode Zn-Al a été construite et testée électrochimiquement pour comprendre l'interaction entre deux éléments indépendamment de l'effet de la microstructure. Une technique de courant alternatif AESEC (AC-AESEC) a été développée pour surveiller les caractéristiques spécifiques de la dissolution élémentaire.

Composition de cette thèse

1) Introductoire

Le **Chapitre I** présente un bref historique de l'acier galvanisé et l'origine de cette étude doctorale. Le **Chapitre II** est une revue des mécanismes de résistance à la corrosion engendrés par les revêtements d'alliage à base de Zn, en se concentrant sur trois parties ; composition chimique, microstructure et produits de corrosion. Par ailleurs, afin d'élucider le mécanisme de corrosion du système Zn-Al-Mg, ce chapitre également vérifie le désalliage des phases binaires. L'approche la plus importante de cette étude est l'analyse du comportement à la corrosion des éléments purs et des phases pures, composant du système d'alliage Zn-Al-Mg.

Le **Chapitre III** présente les méthodes expérimentales utilisées dans cette thèse, principalement la technique de spectroélectrochimie à émission atomique (AESEC) et d'autres techniques *ex-situ* pour analyser l'évolution de la surface au cours des réactions électrochimiques.

2) Résultats

Une description schématique de la dissolution élémentaire d'un système d'alliage Zn-Al-Mg est présentée **Fig. 1.1**. Les réactions anodiques dans des conditions spontanées ou potentielles induites sont mesurées par la technique AESEC. Le mécanisme de désalliage de $MgZn_2$ et la phase α d'Al sont discutés au **Chapitre IV ~ VII**. Les courbes de polarisation de dissolution élémentaire de chaque spécimen sont présentées au **Chapitre VIII**. Les produits de corrosion sont mesurés par balance de masse / charge et aussi caractérisés après les expériences électrochimiques. Ces produits ont été comparés à la précipitation dans la solution et aux simulations thermodynamiques (**Chapitre IX**).

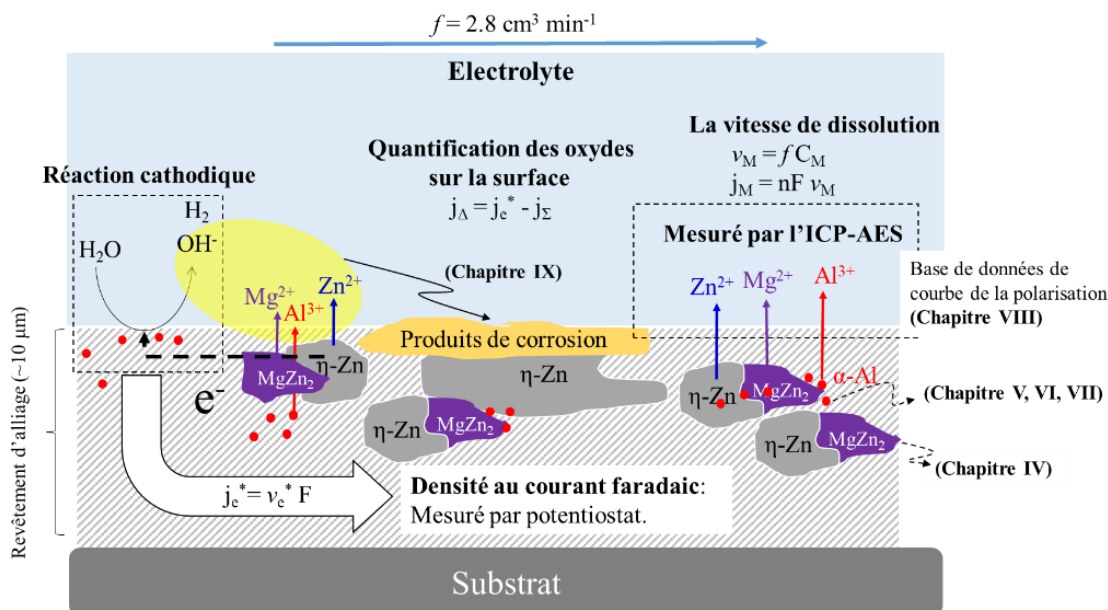


Fig. 1.1. Schéma illustrant la dissolution élémentaire du système Zn-Al-Mg et son analyse avec la technique AESEC.

Dans le **Chapitre IV**, le désalliage de la phase intermétallique MgZn_2 , un composant des revêtements d'alliage Zn-Mg/Zn-Al-Mg, a été étudié dans un milieu légèrement alcalin pour la première fois. La résistance à la corrosion améliorée de la phase MgZn_2 a été attribuée à la couche enrichie en Zn et appauvrie en Mg ($\text{Zn}(0)$) formée par la dissolution sélective de Mg au cours de la polarisation cathodique. Cette couche a également restreint la dissolution de Mg dans le domaine de potentiel cathodique. Au-dessus d'un potentiel critique, E_c , la dissolution était faradique et congruente. Le désalliage de MgZn_2 en fonction du potentiel a été suggéré comme représenté **Fig. 1.2**.

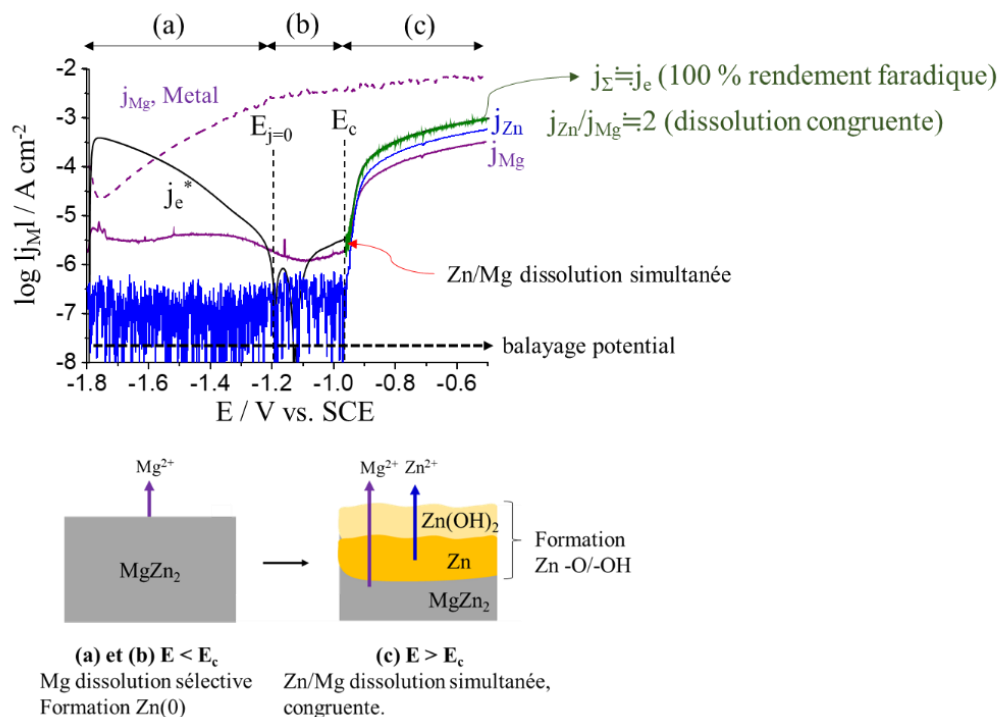


Fig. 1.2. Désalliage du $MgZn_2$ phase intermétallique en fonction du potentiel à $pH=10,1$, $NaCl$ 30 mM, électrolyte désaéré.

Au **Chapitre V**, le «*désalliage cathodique*» d'Al dans la phase $Al_{5,2}Zn$ (phase Zn-Al riche en Al) a été étudié en fonction du potentiel à $pH=10,1$. Il a été mis en évidence que la dissolution sélective de Al / Zn dans le potentiel cathodique conduisait à la formation d'une couche métallique de Zn, Zn (0). Dans le domaine de potentiel cathodique, cette couche ne présentait aucun effet inhibiteur sur la dissolution d'Al. Cependant, pour $E > E_c$, la dissolution d'Al était restreinte lorsque la dissolution de Zn était activée, comme montrée dans la **Fig. 1.3**. La formation de la couche de Zn (0) dans le domaine de potentiel cathodique a été vérifiée par chronoampérométrie (CA) ; 1000 s à un potentiel cathodique constant, suivi d'un pulse de potentiel anodique constant, forçait la couche de Zn (0) à se dissoudre. La stœchiométrie de la dissolution d'Al dans le domaine du potentiel cathodique pour le métal Al et la phase $Al_{5,2}Zn$ a montré une valeur similaire, indiquant le même mécanisme de dissolution.

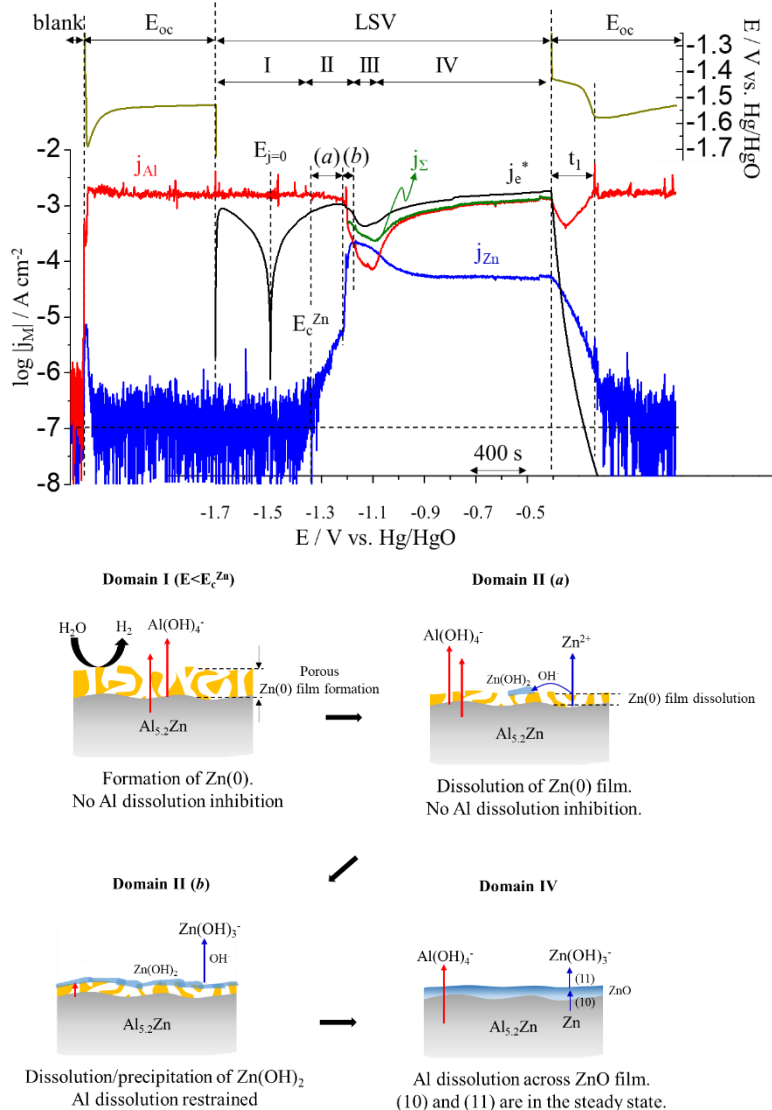


Fig. 1.4. Diagramme schématique de la dissolution de la phase Al_{5,2}Zn en fonction du potentiel dans NaOH 0,1 M, pH=12,80, électrolyte désaéré

Le **Chapitre VII** approfondit de l'étude à pH élevé, en étudiant la réactivité de dissolution anodique des métaux Al, Zn et de la phase α Zn-68Al (Al_{5,2}Zn) en fonction de la température. La dissolution de l'hydroxyde d'Al a été révélée comme une étape déterminant de la vitesse, mise en évidence par la vitesse de dissolution d'Al indépendante du potentiel pour le métal Al et la phase Al_{5,2}Zn. Zn et Al purs ont montré une dissolution élémentaire dépendant de la température sans variation significative du potentiel de circuit ouvert (E_{oc}). Pour la condition de dissolution spontanée, Al est sélectivement dissous en formant une couche enrichie en Zn (0). Les courbes de polarisation de Zn pourraient être décomposées en réactions élémentaires permettant d'analyser des paramètres cinétiques tels que l'énergie d'activation et la pente de

Tafel. Dans la courbe de potentiel anodique de la phase $Al_{5,2}Zn$, la dissolution d'Al et Zn a été déterminée par un mécanisme de transfert de charge par rapport au film de ZnO.

Le **Chapitre VIII** présente une base de données d'expériences électrochimiques du système Zn-Al-Mg à trois pH. Ce chapitre dévoile l'intérêt de comparer les métaux purs, les phases pures et chaque revêtement d'alliage à différents pH ainsi que la présence / absence de l'oxygène dans la solution. La série du couplage galvanique, obtenue par la base de données électrochimiques, pourrait être utilisée pour prédire le comportement corrosif du revêtement multiphasé. La **Fig. 1.5** montre un exemple de variation du potentiel de circuit ouvert (E_{oc}) en fonction du pH et de la composition élémentaire (% Zn).

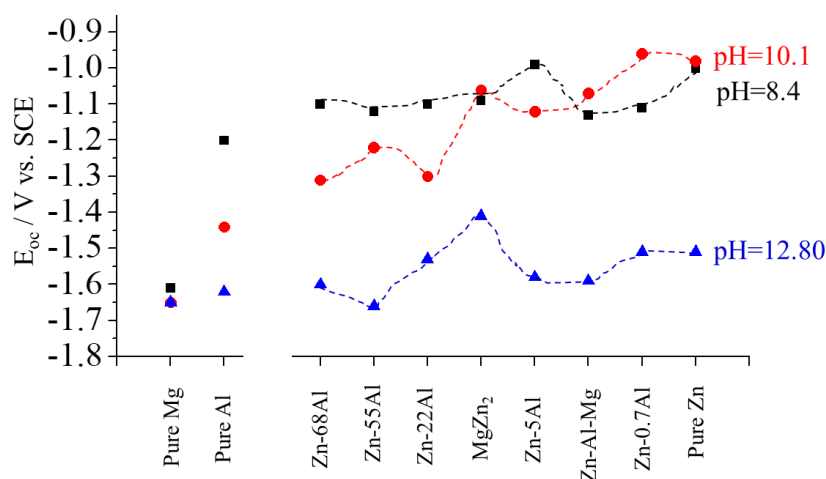


Fig. 1.5. La comparaison du potentiel de circuit ouvert (E_{oc}) en fonction du % Zn à trois pH différents, dans les électrolytes désaérés.

L'objectif du **Chapitre IX** est de comparer les expériences de corrosion en laboratoire, la corrosion sur le terrain et la base de données thermodynamiques décrit **Fig. 1.6**. Les espèces précipitées calculées pour le Zn-Al-Mg ont été comparées à des précipitations dans une solution obtenues pendant la titration. Les produits solides précipités ont été extraits à chaque pH de titration, caractérisés par spectroscopie Raman puis comparés à la prédiction thermodynamique. La formation de doubles hydroxydes de Mg-Al (LDHs) a été observée et a également été préférée par calcul thermodynamique plutôt que par précipitation de $Mg(OH)_2$.

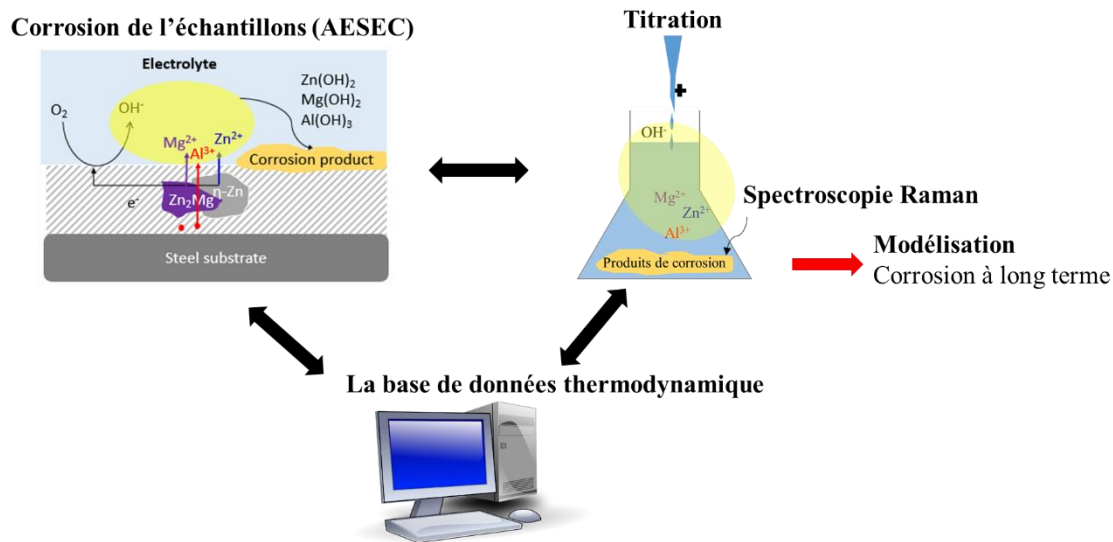


Fig. 1.6. Description schématique de la comparaison et de la corrélation entre les expériences.

3) Conclusions et perspectives

Le **Chapitre X** donne les conclusions et les perspectives des travaux. La base de données électrochimique établie dans ce travail pourrait être appliquée pour prédire le comportement à la corrosion des revêtements d'alliage multi-phase. Le mécanisme spécifique de désalliage de chaque phase révélé dans ce travail peut être utilisé comme une pierre angulaire pour anticiper l'interaction entre les phases.

La vitesse de dissolution élémentaire est corrélée à la formation / dissolution d'espèces précipitées et l'énergie d'activation de chaque étape donne de la lumière pour comprendre les mécanismes de dissolution individuels. Par exemple, l'évolution de l'hydrogène, la formation d'espèces insolubles et la dissolution élémentaire peuvent être distinguées par la technique AESEC. La comparaison entre les produits de corrosion formés pendant les mesures électrochimiques, les précipitations possibles calculées par la base de données thermodynamiques et des espèces solides formées dans la solution pendant la titration a été effectuée. Cette méthodologie nous permet de prédire quels produits de corrosion seront les plus stables pendant les conditions de corrosion réelles, par conséquent, utilisée pour modéliser la corrosion du système d'alliage de Zn.

Ce doctorat élargit les applications méthodologiques de la technique AESEC. La quantification d'évolution de l'hydrogène par la technique AESEC sera une information utile pour la corrosion induite par la fragilisation par l'hydrogène. Le prétraitement de surface du revêtement d'alliage à base de Zn peut être standardisé pour les expériences laboratoire. Il a été révélé que le stockage

Résumé

un échantillon dans un dessiccateur maintenant 50 % humidité relative, pourrait donner l'état de surface reproductible.

Chapter I: Introduction

“People are always shouting they want to create a better future. It is not true. The future is an apathetic void of no interest to anyone. The past is full of life, eager to irritate us, provoke and insult us, tempt us to destroy or repaint it. The only reason people want to be masters of the future is to change the past.”

The book of Laughter and Forgetting (1979),

Milan Kundera

1. Introduction

1.1. Origin and objectives of this Ph.D. study

Galvanized steel

The first use of Zn alloys is believed to have been as Zn plate armor before 1680 in India. This material was traced with a grey oxidized metal, probably made by dipping the steel into molten Zn. In 1742, French chemist Melouin reported to the Académie Royale des Sciences that immersing steel in a molten zinc pool led to enhanced corrosion protection. In 1780, Italian chemist Luigi Galvani observed electrical current by the twitching of a frog's leg in contact with copper and iron. The word 'galvanizing' was taken from Galvani and first appeared in a French patent (1836) for a process of coating steel by the French chemist Sorel. The year after, a British patent was granted for the similar process by William Crawford, and by the 1850's, more than 10,000 tons of zinc were produced a year in UK for steel fabrication.

The word "galvanized" initially indicated the intrinsic properties which could be obtained by the coating itself rather than the process itself. It was understood to describe the electric shocks, and was also referred to as Faradism. At these time, the verb 'galvanize' was defined as provoking a complacent person to move. This was the period that the word 'galvanizing' was embedded into the language of people.

Today, galvanized steel is used in various applications such as construction, automotive, engineering/fabrication, appliance and many other fields for the steel protection. Accordingly, the consumption of coated steel has been increased from 80 million tons in 2000 to 132 million tons in 2014 [1]. In 2014, 80 million tons (MnT) of galvanized steel, 25.24 MnT of GalfanTM/GalvalumeTM and 27.27 MnT of Electro Galva were consumed worldwide.

Galvanized steel has been investigated at the laboratory level to improve its corrosion resistance for many decades. One of the more efficient ways to achieve a better corrosion resistance can be made by alloying the Zn with other elements. The binary Zn alloy systems of Zn-Al, Zn-Cu, Zn-Fe and Zn-Pb have been investigated with their specific applications. Furthermore, ternary and quaternary alloys obtained by adding such elements as Mg, Ni, Ti and Cd have also been developed. To predict the corrosion behavior of the Zn based alloy coatings, different types of corrosion tests such as atmospheric exposure, accelerated corrosion tests

I. Introduction

under specific conditions, surface characterization and electrochemical experiments have been performed.

Research funding for coal and steel (RFCS) project

A European community of steel industry was initially proposed by French foreign minister Robert Schuman in 1950, as a way to avoid further conflicts between France and Germany. His stated intention for this community was: “La mise en commun des productions de charbon et d’acier (...) changera le destin de ces régions longtemps vouées à la fabrication des armes de guerre dont elles ont été les plus constantes victimes.” Which means “sharing carbon and steel production will change these regions which served for a long time to fabricate weapons during the war, has been consistently suffered.” [3]. After World War II, the European Coal and Steel Community (ECSC) was organized in 1951 by 6 European countries; Belgium, France, West Germany, Italy, the Netherlands and Luxembourg with the aim of coordinating the industrial production under a centralized authority. With this effort, it was created a common market for coal and steel among these members which eventually served to neutralize competition between European nations over natural resources. After the formation of European Union in 2002, the assets from ECSC was transferred to RFCS which has supported production processes like application, utilization and conversion of resources and environmental protection such as reducing CO₂ emission from coal and steel industry. This doctoral project is supported by an RFCS project which aims to establish the role of Zn-Al and Zn-Al-Mg alloy coating microstructure on the efficiency their corrosion protection.

Objectives of the Ph.D. project

Understanding the electrochemical behavior of the Zn-Al and Zn-Al-Mg alloy coatings is complicated due to multiple phases which may interact with each other causing galvanic coupling among the phases. In heterogeneous alloy coatings, the more noble metal phase may facilitate the corrosion of the less noble phases. To this end, this Ph.D. project aims to investigate the elemental dissolution kinetics of the individual phases and pure metals of the alloy coatings. Three different pH solutions were chosen because chemical and electrochemical

behavior of the components can vary with pH. The electrochemical data of each phase was used to predict the corrosion behavior of the multi-phase alloy coatings.

1.2. The particularities of this Ph.D. project

We have used atomic emission spectroelectrochemistry (AESEC), an ideal technique to monitor selective dissolution of the multi-element system. This technique allows us to measure not only elemental response from the chemical reactions but also the associated electrical responses.

We have investigated the electrochemical behavior of the Al-Zn/Mg-Zn pure phases consisting of the Zn-Al/Zn-Al-Mg alloy coatings. As the first part, we analyzed the dealloying of the $MgZn_2$ intermetallic (**Chapter IV**) and the Al-Zn phases (η -phase of Zn and α -phase of Al, **Chapter V, VI and VII**). The inhibitive effect of Zn dissolution on Al, found in all Zn-Al system in this project, was discussed based on both electrochemical response of each element and also the role of the corrosion products. The role of metallic Zn, Zn oxide ($Zn(O)$) enriched layer, was investigated for a different system. Furthermore, commercial alloys of Zn-Al and Zn-Al-Mg were examined and compared with the results of pure metals and phases.

Another particularity of this work was the development of a methodological milestone of the AESEC technique. The origin of certain elemental dissolution peaks observed during AESEC polarization experiment was verified by ‘chronoamperometric step’ experiments. These measurement were originally performed by Wagner et al. [2] but they could only see the total current transient rather than elemental dissolution. Also, they investigated only a small range of potential near the corrosion potential. In this work, we confirmed and quantified for the first time, the formation of a layer enriched in the more noble element following selective dissolution of the less noble elements.

The elemental dissolution kinetics was revealed by its activation energy decoupling metal oxidation, insoluble species formation and hydrogen evolution. Near open circuit potential, Zn dissolution was limited by $Zn(OH)_2$ formation. At higher temperature, the amount of undissolved ZnO increased forming passive film. For Al-Zn phase, Al and Zn dissolution rate was controlled by a charge transfer mechanism through the ZnO film.

I. Introduction

A database of elemental polarization curves for 10 specimens (Zn/Al/Mg metals, Zn-0.7Al, Zn-22Al, Zn-68Al, MgZn₂ pure phases, Zn-Al-Mg and two Zn-Al commercial alloys) was established as a function of pH and in the presence/absence of oxygen (**Chapter VIII**). Elemental dissolution of each element was compared with pure phase alloy and multi-phase alloy coatings. Potential data obtained from both spontaneous dissolution condition and electrochemical measurement may be applied to predict dissolution kinetics taking into account the galvanic coupling between phases.

Corrosion products formed during the electrochemical measurements were compared to the precipitated species formed in the solution during the titration experiment. These results were also compared with thermodynamic database.

The AESEC technique was used to interpret not only elemental dissolution but also diverse electrochemical responses. For example, H₂ evolution reaction (HER) was tried to be quantified by the AESEC technique using perturbed Al dissolution rate signals. The linear relationship between Al dissolution rate in the steady state and the standard deviation signal was observed in all Al containing alloys, pure phases and metal in all electrolyte conditions investigated in this work. The Zn-Al bi-electrode was constructed and electrochemically tested to understand interaction between two elements separating the effect of microstructure. Alternative current AESEC (AC-AESEC) technique was used to monitor specific characteristics of the elemental dissolution.

1.3. Summary of the Ph.D. thesis

This Ph.D. dissertation consists of 10 chapters including 3 introductory chapters giving a general idea of the work; 6 result chapters showing how the problems asked in the introductory chapters were solved; 1 concluding chapter which summaries the observations and suggests perspectives for the future applications.

1) Introductory:

Chapter I introduces a short history of galvanized steel and the origin of this Ph.D. study. **Chapter II** reviews the literatures about the mechanisms of corrosion resistance provided by Zn based alloy coatings focusing on three parts; chemical composition, microstructure and corrosion products. In order to elucidate the corrosion mechanism of the Zn-Al-Mg system, this

chapter also reviews the dealloying of binary phases. The most important approach of this study is analyzing the corrosion behavior of pure elements and pure phases, which are the base component of the Zn-Al-Mg alloy system.

Chapter III deals with the experimental methods used in this dissertation, primarily atomic emission spectroelectrochemistry (AESEC) technique and other *ex-situ* techniques to investigate surface evolution during electrochemical reactions. Experimental methodologies to answer specific questions asked in the introduction section are introduced in this chapter.

2) Experimental results:

A schematic description of the elemental dissolution of a Zn-Al-Mg alloy system is shown in **Fig. 1.1**. Anodic reactions in spontaneous or potential/current induced conditions are measured by means of AESEC technique. Dealloying mechanism of $MgZn_2$ and α -phase of Al are discussed in **Chapter IV~VII**. Elemental dissolution polarization curves of each specimen are presented in **Chapter VIII**. Corrosion products are measured by mass/charge balance and characterized after the electrochemical experiments. These species were compared with the precipitation in the solution and the thermodynamic simulations (**Chapter IX**).

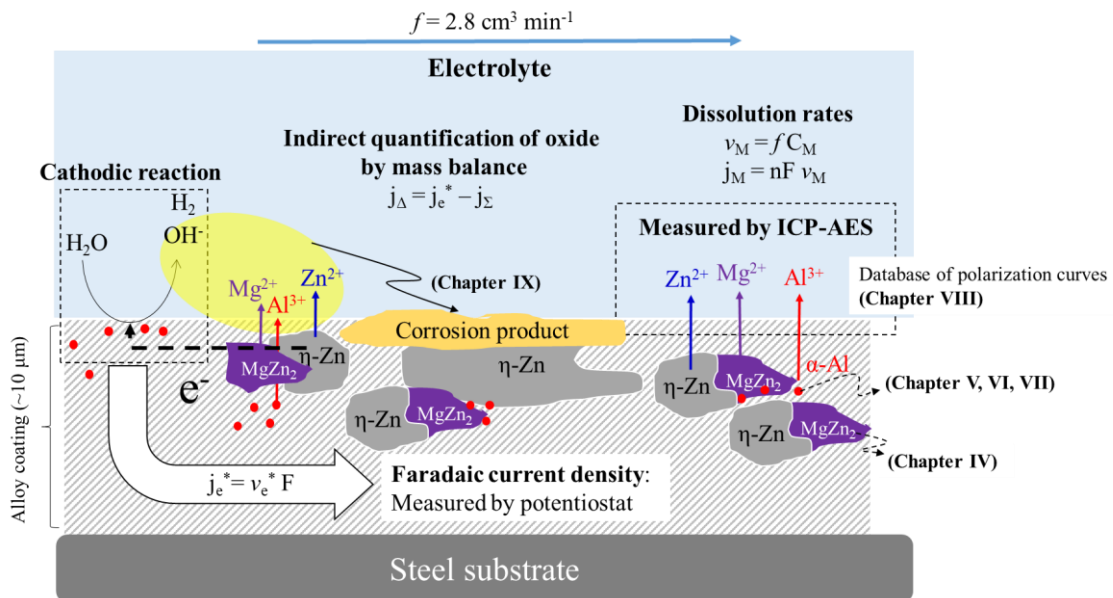


Fig. 1.1. Schematic description of the elemental dissolution of Zn-Al-Mg system and the AESEC technique measurement.

In **Chapter IV**, dealloying of $MgZn_2$ intermetallic phase, a component of Zn-Al-Mg alloy coatings, was investigated in a slightly alkaline media for the first time. The enhanced corrosion

resistance of MgZn_2 phase was attributed to the Mg-depleted Zn enriched ($\text{Zn}(0)$) layer formed due to the selective dissolution of Mg during cathodic potential polarization. This layer also restrained Mg dissolution in the cathodic potential domain. Above a critical potential, E_c , dissolution was faradaic and congruent. Dealloying of MgZn_2 as a function of potential was suggested as depicted in **Fig. 1.2**.

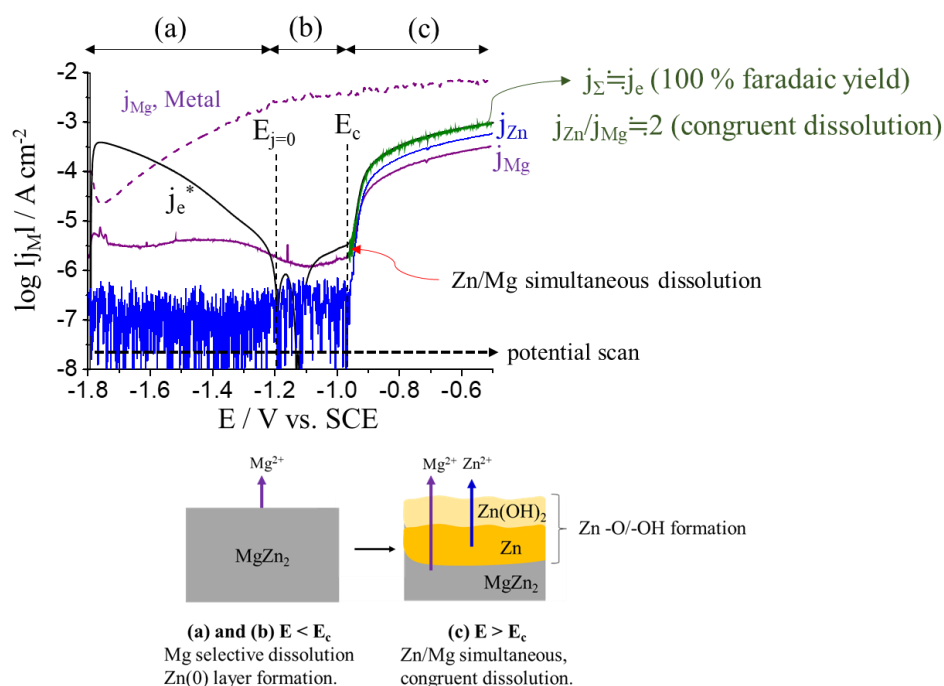


Fig. 1.2. Dealloying of MgZn_2 intermetallic phase as a function of potential at $\text{pH}=10.1$, 30 mM NaCl, Ar deaerated electrolyte.

In **Chapter V**, the ‘cathodic dealloying’ of Al in $\text{Al}_{5.2}\text{Zn}$ phase (Al-rich Zn-Al phase) was investigated as a function of potential at $\text{pH}=10.1$, 30 mM NaCl electrolyte. It was demonstrated that the selective dissolution of Al in the cathodic potential led to the formation of metallic Zn layer, $\text{Zn}(0)$, which shows its own onset potential (E_c^{Zn}) to dissolve. In the cathodic potential domain, this layer showed no inhibitive effect on Al dissolution. However, for $E > E_c^{\text{Zn}}$, Al dissolution was inhibited when Zn dissolution was activated, as described in **Fig. 1.3**. Formation of the $\text{Zn}(0)$ layer in the cathodic potential domain was verified by a chronoamperometric (CA) experiment, 1000 s at a constant cathodic potential pulse forming $\text{Zn}(0)$ layer, followed by a constant anodic potential pulse resulting in dissolution of the $\text{Zn}(0)$ layer. The stoichiometry of Al dissolution in the cathodic potential domain for Al metal and $\text{Al}_{5.2}\text{Zn}$ phase showed a similar value, indicating the same dissolution mechanism.

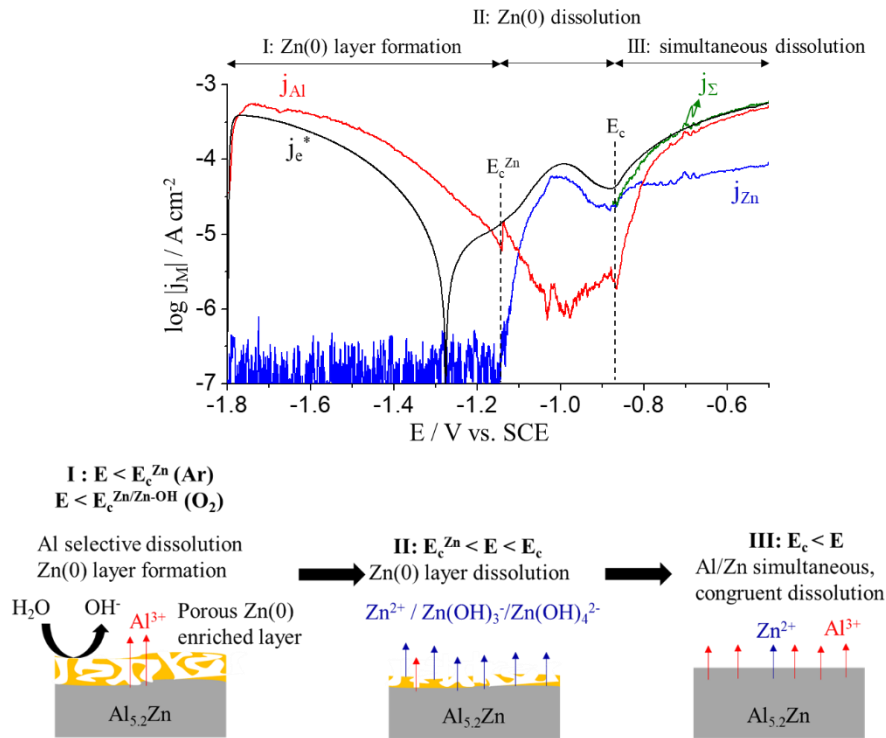


Fig. 1.3. Cathodic dealloying of $Al_{5.2}Zn$ phase as a function of potential at $pH=10.1$, 30 mM NaCl, Ar deaerated electrolyte.

In **Chapter VI**, the inhibitive effect of Zn on Al dissolution of $Al_{5.2}Zn$ phase was investigated at $pH=12.80$. A schematic image is shown **Fig. 1.4** describing elemental dissolution of Al-Zn in alkaline media. A clear inhibiting effect of active Zn dissolution on Al dissolution was observed when the Zn(0) dissolved in potentiodynamic experiments. Several mechanisms of Al dissolution kinetics were suggested: 1) Cathodic potential domain: Al dissolved directly coupled to H_2 evolution reaction (HER) by water reduction; 2) Passive domain: Al dissolved across an oxide/hydroxide layer. Following the electrochemical experiment, a passive ZnO layer formed during anodic polarization, dissolved during the spontaneous dissolution condition. Al dissolution was once again restrained during this period but rose slowly as the film dissolved. Detailed analysis was conducted by the CA to verify this inhibitive effect. The corrosion products formed at each potential domain were characterized by scanning electron microscopy (SEM) and Raman spectroscopy.

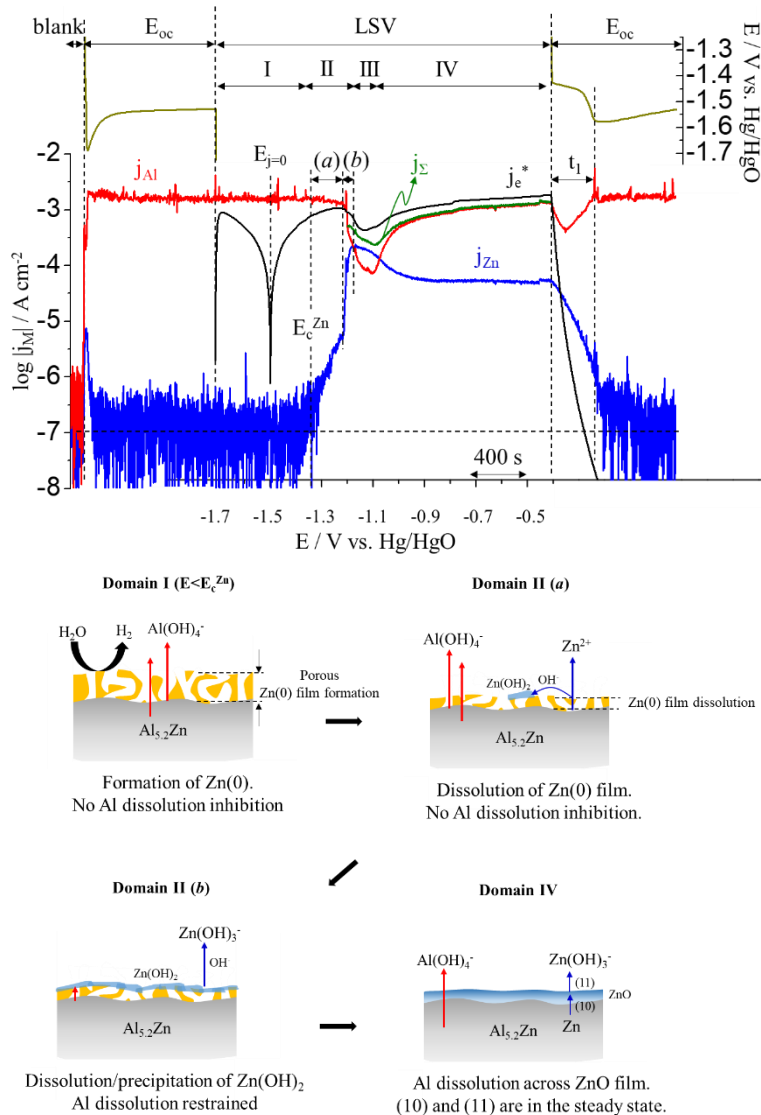


Fig. 1.4. Schematic diagram of dissolution of $Al_{5.2}Zn$ phase as a function of potential in 0.1 M NaOH, pH=12.80, Ar deaerated electrolyte.

Chapter VII enlarges scale of the study in alkaline pH, investigating anodic dissolution reactivity of Al, Zn metals and the α -phase Zn-68Al ($Al_{5.2}Zn$) depending on solution temperature. Al hydroxide dissolution was revealed as the rate determining step, evidenced by a potential independent Al dissolution rate for Al metal and the $Al_{5.2}Zn$ phase. Pure Zn and Al showed temperature dependent elemental dissolution without a significant variation of open circuit potential (E_{oc}). For the spontaneous dissolution condition, Al selectively dissolved to Zn forming a Zn(0) enriched layer. AESEC polarization curves of pure Zn could be decomposed into the elementary reactions which enable to analyze kinetic parameters, such as activation energy and Tafel slope. In the anodic polarization curve of the $Al_{5.2}Zn$ phase, Al and Zn dissolution were determined by a charge transfer mechanism across the ZnO film.

Chapter VIII presents a ‘database of electrochemical experiments’ of Zn-Al-Mg system at three pH values; neutral, slightly alkaline and alkaline. This chapter overviews the interest of comparing pure metals, pure phases and each alloy coatings at different pH and also the presence/absence of O_2 in the solution. Corrosion behavior of the multi-phase coating may be predicted by galvanic coupling between phases, based on this electrochemical database. **Fig. 1.5** shows an example of an open circuit potential (E_{oc}) variation depending on pH and elemental composition.

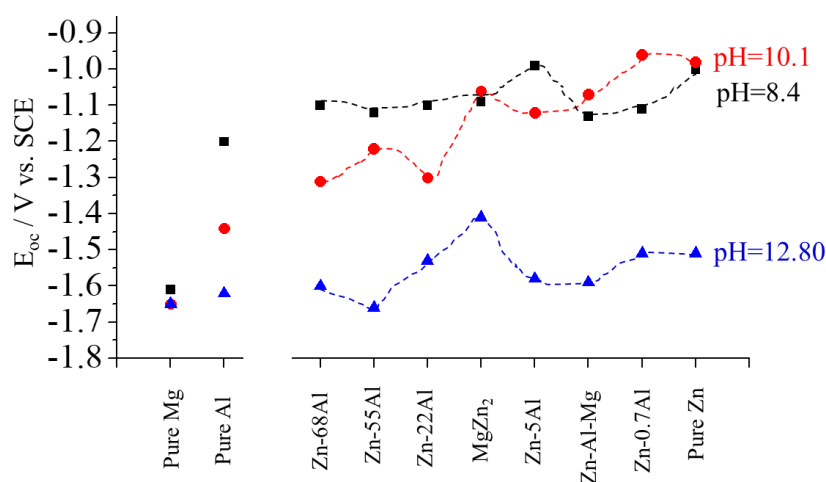


Fig. 1.5. The open circuit potential (E_{oc}) comparison between metals, phases and the alloys in increasing % mol Zn at three different pH, Ar deaerated electrolytes.

The objective of **Chapter IX** is to compare laboratory corrosion tests, field corrosion and the thermodynamic database as described in **Fig. 1.6**. Calculated precipitated species based on the thermodynamic database of Zn-Al-Mg system was compared with the corrosion products formed during the electrochemical tests. The precipitated solid products were extracted at each pH of the titration experiment, characterized by Raman spectroscopy then compared with the thermodynamic prediction. The Mg-Al layered double hydroxides (LDHs) formation was observed preferably to $Mg(OH)_2$ by thermodynamic simulation, precipitated species and corrosion products after the electrochemical tests of Zn-Al-Mg alloy.

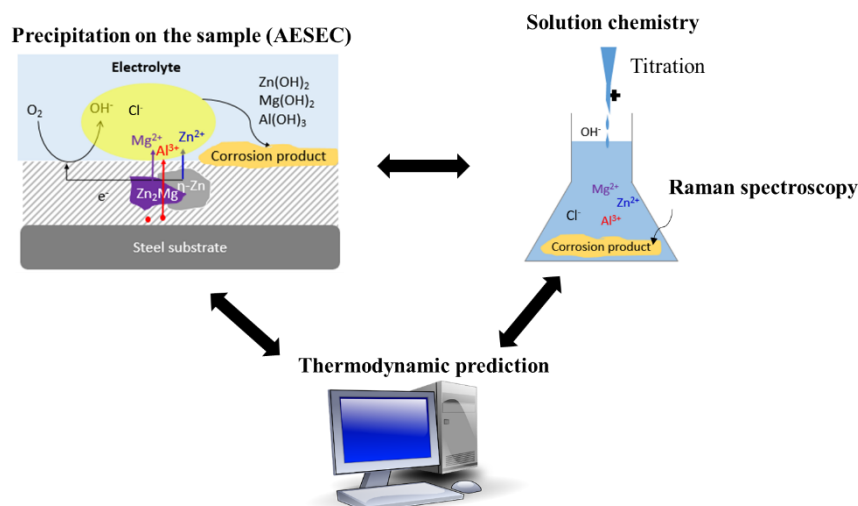


Fig. 1.6. Schematic description of the comparison and correlation between experiments.

3) Conclusions and perspectives:

Chapter X gives conclusions and perspectives of this Ph.D. thesis. Specific dealloying mechanism of each phase revealed in the present work may be used as a cornerstone to anticipate interaction between phases.

Elemental dissolution rates correlated to insoluble species formation/dissolution and activation energy of each step gives light to understand individual dissolution mechanisms. For example, hydrogen evolution reaction, insoluble species formation and elemental dissolution can be distinguished by AESEC technique.

The electrochemical database established in this work could be applied to predict the corrosion behavior of the multi-phase alloy coatings.

The corrosion products formed during the electrochemical measurements was compared with that of possible precipitations in the solution and thermodynamic simulation. This methodology allows us to predict which corrosion products will be the most stable species during the real corrosion condition, therefore, can be used to model corrosion of the whole alloy system.

This Ph.D. thesis enlarges methodological applications of AESEC technique. Hydrogen evolution reaction quantification by AESEC technique will be a useful information for hydrogen embrittlement induced corrosion. Surface pretreatment of the Zn based alloy coating can be standardized for the laboratory experiments as it was revealed that humidity chamber can give the reproducible surface condition.

1.4. List of publications and conferences

List of publications

- 1) J. Han and K. Ogle, “Editors’ choice: Dealloying of MgZn₂ intermetallic in slightly alkaline chloride electrolyte and its significance in corrosion resistance”, *J. Electrochem. Soc.* **164**(14) C952-C961 (2017).
- 2) J. Han and K. Ogle, “Cathodic dealloying of α -phase Al-Zn in slightly alkaline chloride electrolyte and its consequence for corrosion resistance”, *J. Electrochem. Soc.* **165**(7) C334-C342 (2018).
- 3) J. Han, D. Thierry, and K. Ogle, “Temperature dependence of the passivation and dissolution of Al, Zn and α -phase of Zn-68Al”, *Corrosion*, **75**(1) 68-78 (2019).
- 4) J. Han and K. Ogle, “The anodic and cathodic dissolution of α -phase Zn-68Al in alkaline media”, *Corrosion Science*, Submitted (July 2018).

Conferences

Oral presentations

- 1) 4th International Coal Coating symposium: **J. Han**, P. Volovitch, K. Ogle, “Selective dissolution and surface film formation of ZnMgAl alloys”, Paris, France, November 2016.
 - 2) Eurocorr 2017, 20th international corrosion congress: **J. Han**, K. Ogle, “The electrochemistry & corrosion of Zn-Al-Mg alloys: Dealloying of MgZn₂ phase in chloride containing alkaline media”, Prague, Czech Republic, September 2017.
- Journée de l’Ecole Doctorale (Ph.D. students’ day): **J. Han**, K. Ogle, “Quantifying the contribution of elemental components and individual phases”, Paris, France, June 2017.

Regular meeting for the Microcorr European research funding coal and coating (RFCS) project:

- i) **J. Han**, P. Volovitch “Phase stability as a function of pH: pure binary Zn-Al phases in alkaline solution”, Paris, France, April 2016.
- ii) **J. Han**, K. Ogle, “Selective dissolution and surface film formation of ZnMgAl alloys/AC-AESEC/surface characteristics”, Voestalpine, Linz, Austria, December 2016.

I. Introduction

iii) **J. Han**, G. Lefèvre, K. Ogle, “Quantifying the contribution of elemental components and individual phases”, ArcelorMittal, Maizières-lès-Metz, France, April 2017.

iv) **J. Han**, G. Lefèvre, K. Ogle, “Dealloying of Zn-Al pure phase in alkaline media / characterization of artificially formed corrosion product by Raman spectroscopy”, Paris, France, October 2017.

v) **J. Han**, G. Lefèvre, K. Ogle, “Phase stability and electrochemical database of the Zn-Al-Mg alloys, Ghent, Belgium, April 2018.

Participating

1) International society of electrochemistry (ISE) 68th annual meeting: K. Ogle, **J. Han**, “The electrochemistry & corrosion of Zn-Al-Mg alloys: Quantifying the contribution of elemental components and individual phases”, Providence, Rhode Island, USA, August 2017.

2) Aluminum Surface Science and Technology (ASST) 2018: K. Ogle, **J. Han**, “On the cathodic corrosion of Al and Al-Zn alloys”, Helsingor, Denmark, May 2018.

3) Eurocorr 2018, 21th international corrosion congress: K. Ogle, **J. Han**, “Dealloying of the Zn-Mg and Zn-Al pure phases and its consequence for the corrosion of Zn-Al-Mg system”, Krakow, Poland, September 2018.

Posters

1) L'école thématique CNRS sur les spectroscopies vibrationnelles: **J. Han**, P. Volovitch, K. Ogle, “Electrochemistry of homogenous binary alloys: effect of the surface film measured by AESEC and Raman spectroscopy“, Ile de Porquerolles, France, October 2016.

2) NACE Corrosion 2017: **J. Han**, K. Ogle, “The electrochemistry and corrosion of Zn-Al-Mg alloys: Quantifying the contribution of elemental components and individual phases”, New Orleans, USA, March 2017.

3) Gordon Research Conference 2018: **J. Han**, K. Ogle, “Dealloying of the Mg-Zn and Al-Zn phases and its consequence for the corrosion of Zn-Al-Mg system”, New Hampshire, USA, July 2018.

4) Journée de l'Ecole Doctorale (Ph.D. students' day): **J. Han**, P. Volovitch, K. Ogle, “Electrochemistry of homogeneous binary alloys: what relation with pure metals? Examples of Zn-Al alloys in alkaline media”, Paris, France, May 2016.

Chapter II. State of the art

«Toute existence connaît son jour de traumatisme primal, qui divise cette vie en un avant et un après et dont le souvenir même furtif suffit à figer dans une terreur irrationnelle, animale et inguérissable.»

Stupeur et tremblements (1999),

Amélie Nothomb

2. State of the art

2.1. Introduction of Zn-based alloy coatings

Zn based coating alloys have been used for corrosion protection of steel in a wide range of applications in atmospheric and industrial environments. The most important mechanism of corrosion resistance offered by Zn coatings is cathodic protection. Also, Zn can form an oxide/hydroxide barrier that slows down the overall corrosion of the system. Zn based alloy coatings are known as having multi-phase structure. The reactivity of each phase can vary as different elements become active or passive depending on the corrosion environment. Therefore, investigating electrochemical nature of each phase is essential for predicting corrosion behavior of Zn-based alloy coatings.

The most common Zn-coatings are based on the Zn-Al alloy family such as galvanized steel (0.1~0.2 wt.% Al), Zn-5wt.% Al (GalfanTM) and Zn-55wt.% Al-1.5wt.% Si (GalvalumeTM). Recently the Zn-Al-Mg and Zn-Mg family of coatings have been under development primarily aimed at the building and automotive applications. These coatings may be fabricated by either the conventional hot-dip galvanization (HDG) process or physical vapor deposition (PVD) technology. The interest of developing Zn-Al-Mg coating is its' significantly enhanced atmospheric corrosion properties as compared to conventional galvanized coatings.

The first commercial Zn-Al-Mg alloys coating went out into world in 1998, produced by the Japanese steelmakers, Nisshin Steel. They introduced a Zn-6Al-3Mg alloy, commercial name ZAMTM, which showed a superior corrosion resistance than conventional Zn-Al alloy coatings [4]. Following to them, in 2002, Zn-11Al-3Mg was released by another Japanese steelmaker, Nippon Steel Corporation, with the trade name SuperDymaTM. European steel makers continued to develop Zn-Al-Mg coating alloys by a conventional hot-dipping process. A commercial alloy coating named as MagiZincTM was introduced by Tata steel, launched in 2006. It showed at least four times higher corrosion resistance than the conventional galvanized steel evidenced by accelerated corrosion tests [5]. A similar composition of Zn-Al-Mg alloy coating having analogous microstructure to MagiZincTM was introduced by Voestalpine in 2007, with the commercial name CorrenderTM. From 2010, ArcelorMittal has produced a Zn-Al-Mg alloy (Zn-3.5Al-3Mg) named MagnelisTM [6].

2.2. Corrosion mechanism of Zn-Al-Mg

The corrosion mechanism of Zn-Al-Mg alloys may be explained by its chemical composition, microstructure and the nature of the corrosion products.

2.2.1. Effect of chemical composition

Table 2.1. gives a list of literatures about the effect of chemical composition on the corrosion of Zn-Al-Mg. Elvins et al. [7] added Mg from 0 to 0.05 wt.% to the 4.5 wt.% Al-Zn based alloy coating resulting in an increased volume fraction of the less corrosive Zn dendrites. It was observed that the microstructure modification finally led to an increase in cut edge corrosion monitored by scanning vibrating electrode technique (SVET) for 24 h exposure to 5% NaCl. Adding Mg to Zn-Al alloy resulted in an increased Zn loss, the number of active anodes, and the number of long lived anodes. Li et al. [8] added 0.5, 1.5 and 2.5 wt.% Mg to the commercial Zn-55Al alloy, then observed an enhanced compactness and stability of the corrosion products as compare to without Mg addition, after the neutral salt spray (NSS) test. This film was supposed to be less conductive, reducing the rate of electron transfer and hindering O₂ reduction. Prosek et al. [9] found that the enhanced corrosion protection can be obtained by adding a fourth element such as Si, Cr to the Zn-Al-Mg alloy coating. A quaternary Zn-Al-Mg-X alloy showed better corrosion resistance than Zn-Al-Mg by accelerated corrosion test and marine field exposure. Mehraban et al. [10] proposed adding the quaternary element as Ge to the Zn-Al-Mg system. A reduced Zn loss of the Ge added Zn-Al-Mg alloy was attributed to microstructural changes measured by SVET. They observed that the reactivity of the most active MgZn₂ phase of the coating was reduced by formation of Mg₂Ge crystal.

Table 2.1. Effect of chemical composition on the corrosion of Zn-Al-Mg.

References	Material	Category	Methods
Elvins et al. [7]	HDG+Mg	Composition, Microstructure	SVET, 24h exposure 5% NaCl
	Mg addition to alloy resulted in an increase of Zn dendritic phase. Microstructure change led to increase cut edge corrosion.		
Li et al. [11]	Zn-55Al+Mg	Composition, Microstructure, Corrosion product	NSS, aerated 5% NaCl
	Localized corrosion in Zn grain or Mg-rich regions was observed. Mg addition to alloy improved the stability of the corrosion products.		

Prosek et al. [9]	Zn-X, ZnAl-X, Zn-Mg-X, ZnAlMg-X	Composition, Microstructure	Cyclic accelerated test, marine field exposure
	Zn-Al-Mg-X showed better corrosion resistance than that of Zn-Al-Mg.		
Mehraban et al. [10]	Zn1.6Al1.6Mg+Ge	Composition, Microstructure	SVET
	Around 50% Zn weight loss for Ge added Zn-Al-Mg than that for Zn-Al-Mg. Most active MgZn ₂ phase was replaced by Mg ₂ Ge.		
Li et al. [8]	Zn0.2Al(1~3)Mg	Composition	Immersed in aerated 5% NaCl solution, electrochemical tests.
	Enhanced corrosion resistance was due to grain corrosion inhibition by Mg. Mg improved adherence of the corrosion product layer.		
Shimoda et al. [12]	Zn(6~8)Al+Mg	Composition	5% NaCl, mass loss
	%Al increase led to a better corrosion resistance. 3 wt. %Mg was the optimal composition.		

2.2.2. Effect of microstructure

The microstructure of the commercial Zn-Al-Mg alloy coatings manufactured by hot-dip galvanizing process was reported in elsewhere [11,13–18], having a hcp Zn rich phase, fcc Al phases and laves phase of MgZn₂ as shown in **Fig. 2.1** [6,19]. The phases present in the Zn-Al-Mg alloy are the η-phase of Zn dendrite, binary eutectic phase of Zn-MgZn₂ and ternary eutectic phase of Zn-Al-MgZn₂. In the right side of **Fig. 2.1**, a typical microstructure of Zn-5Al alloy coating (Galfan™) is shown with η-phase of Zn dendrite and lamella structure of β-phase of Al (Zn-rich Al phase) eutectic.

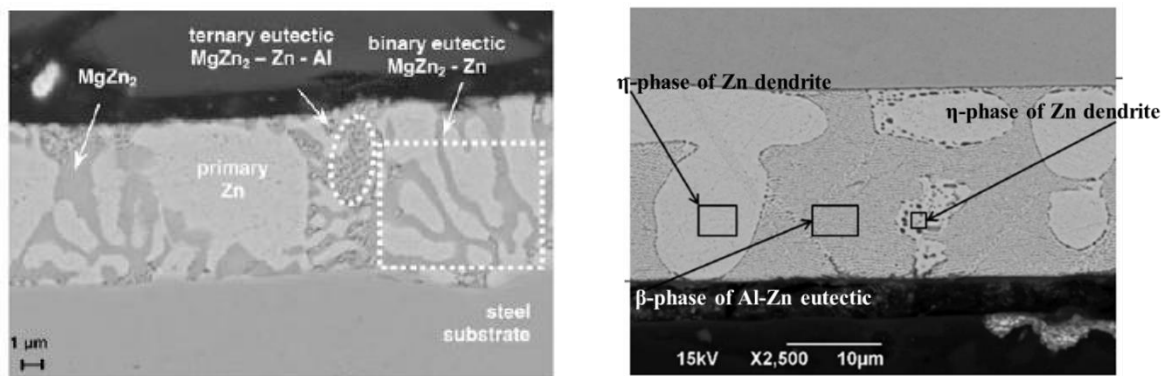


Fig. 2.1. Scanning electron microscopy (SEM) using backscattered electron (BSE) detector images of cross section of the pristine Zn-2Al-2Mg (left, [6]) and Zn-5Al alloy (right, [19]) coatings.

Table 2.2 summarizes the literatures about the effect of microstructure on the corrosion of Zn-Al-Mg. Corrosion mechanism related to preferential dissolution of a certain phase was

II. State of the art

also investigated. Prosek et al. [13] fabricated Zn-5Al and Zn-3Al-2Mg alloys having different microstructure and identical chemical composition by changing cooling rate when there were casted. They found that the finer microstructure showed a better corrosion resistance by mass loss which could be due to rapid blocking of cathodic sites. Sullivan et al. [20,21] introduced an *in-situ* time lapse technique to monitor microstructural wet corrosion mechanism of Zn-(1~2)Al-(1~2)Mg. In this way, the progression of the corrosion attack could be visualized directly for the multi-phase Zn-Al/Zn-Al-Mg alloys. It was observed that the initiation of the corrosion attack started at the binary and ternary eutectic regions where the dealloying of MgZn₂ phase occurred. Following the preferential dissolution of MgZn₂ phase, the corrosion attack moved on to the Zn-rich dendrite.

It was generally observed that the corrosion initiated from the most active phase in the alloy coating. The importance of investigating corrosion behaviors of individual phase thereby will be brought up by these studies.

Table 2.2. Effect of microstructure on the corrosion and suggested corrosion mechanisms of Zn-Al-Mg.

References	Material	Category	Methods
Sullivan et al. [21]	Zn(1~2)Al(1~2)Mg	Microstructure Mechanism	Time lapse microscopy
Sullivan et al. [20]	Zn3.7Al3Mg	Microstructure	Time lapse microscopy, SVET, 1% NaCl
	Initiative corrosion attack at MgZn ₂ phase followed by subsequent Zn-rich phase dissolution.		
Prosek et al. [13]	Zn5Al, Zn3Al2Mg	Microstructure Composition	Cyclic corrosion test, non-rinsing condition
	Finer microstructure showed better corrosion resistance by mass loss.		
Duchoslav et al. [18]	Zn2Al2Mg	Mechanism Microstructure	SST, XPS, AES
	Initial corrosion attack started at MgO surface layer. Preferential dissolution of binary and ternary phases.		

2.2.3. Effect of Corrosion products

The corrosion products formed on these alloys are widely recognized as having an inhibiting effect as diffusion barriers on the corrosion resistance of the Zn-Al/Zn-Mg/Zn-Al-Mg alloy coatings. The precise role of specific corrosion products however, remains largely

contested. Hosking et al. [22] investigated the corrosion products of Zn-Mg alloys formed during the corrosion test in a Cl⁻ containing acidic media. They observed O₂ reduction activity at the Zn cathodes was reduced by formation of Mg(OH)₂ which transformed to hydroxy carbonate species. According to these workers, the hydroxy carbonate species dissolved resulting in a lower surface pH, which in turn lead to the formation of insoluble simonkolleite (Zn₅Cl₂(OH)₈·H₂O) which protected the coating. Prosek et al. [23] found that weight loss of Zn-(1~16 wt.%) Mg alloys was lower than that of pure Zn after 28 days exposure to humid air. The enhanced corrosion resistance was attributed to the Mg-based corrosion products which enable stable passivity in Cl⁻ containing environment limiting O₂ reduction rate.

For the Zn-Al-Mg alloy coatings, readily available Mg²⁺ cations affect the surface pH and chemistry and facilitate the formation of protective Zn corrosion products to form specific spinel like oxides, precursors of Al-based layered double hydroxides (LDHs) [6,24–31]. Corrosion mechanisms of the Zn-Al-Mg, explained by the role of LDHs are summarized in **Table 2.3**.

Shuertz et al. [6] reported that the Zn-2Al-2Mg surface after spray salt test (SST) was converted into adherent Al-rich oxide layer protecting the steel substrate from corrosion reaction. Schürz et al. [26] investigated that Zn-Al carbonate hydroxide, Zn₆Al₂(CO₃)(OH)₁₆·4H₂O, formed on the Zn-2Al-2Mg surface gives the enhanced corrosion resistance. They characterized the sample surface after SST and observed Zn₅(OH)₅(CO₃)₂, ZnCO₃, Zn(OH)₂, Zn₅(OH)₈Cl·2H₂O and MgCO₃ rather than MgO or Mg(OH)₂.

Volovitch et al. [29,30] demonstrated that Mg²⁺ enhanced simonkolleite stability during wet-dry cycle test of Zn-(3~4)Al-(3~4)Mg alloy by removing carbonate. In their thermodynamic simulations, it was demonstrated that Mg²⁺ buffers the surface pH by forming Mg(OH)₂. It was also shown that the LDHs preferably formed to less protective corrosion products, by the cyclic corrosion test in NaCl and Na₂SO₄ media.

Duchoslav et al. [28] also demonstrated the formation of the LDHs on Zn-2Al-2Mg by XPS after a short exposure in salt spray test (SST). They concluded that the surface covered with LDHs stabilized the surface pH and might prohibit further increase in surface pH as previously observed for the Zn based coating alloys.

II. State of the art

Salgueiro Azevedo et al. [24] observed that the corrosion products of basic Zn salts (BZS) and LDHs could decrease the O₂ reduction rate of the Zn based alloy coatings. In the cathodic potential polarization of galvanized steel, they found that the transformation of BZS → ZnO which resulted in a reduced inhibiting effect. This transformation was attributed to the presence of Mg²⁺, however, it was not observed for the Zn-3.7Al-3Mg alloys.

Table 2.3. Effect of corrosion product, mainly layered double hydroxides (LDHs) on the corrosion of Zn-Al-Mg.

References	Material	Category	Methods
Duchoslav et al. [28]	Zn ₂ Al ₂ Mg	Corrosion product	SST
	Rapid formation of LDHs stabilized the surface pH, hindered further alkalization.		
Volovitch et al. [30]	Zn(3~4)Al(3~4)Mg	Corrosion product	Cyclic corrosion test (NaCl, Na ₂ SO ₄)
	Stabilization of simonkolleite due to preferential formation of MgCO ₃ . Mg ²⁺ enhanced simonkolleite stability during wet-dry cycle by removing carbonate and buffering pH, forming Mg(OH) ₂ . LDHs and simonkolleite showed a compact morphology, low electron density, hindering ion-transfer through the layer structure.		
Azevedo et al. [24]	Zn _{3.7} Al ₃ Mg	Corrosion product	Electrochemical test in NaCl, 'synthetic rain water' and Na ₂ SO ₄ . Accelerated corrosion SST.
	BZS and LDHs decreased O ₂ reduction rate. During cathodic polarization, BZS → ZnO losing barrier properties. Mg ²⁺ delayed BZS → ZnO transformation. Residual Al 'skeleton' made the corrosion product more compact.		
Schuerz et al. [6]	Zn ₂ Al ₂ Mg	Corrosion product	SST
	Sample surface was converted into an adherent Al-rich oxide layer.		
Schurz et al. [26]	Zn ₂ Al ₂ Mg	Corrosion product	SST
	Zn-Al LDHs was the main reason for the enhanced corrosion resistance. MgCO ₃ formed rather than MgO and Mg(OH) ₂ .		
Persson et al. [27]	Zn ₂ Al ₂ Mg	Corrosion product	NaCl induced atmosphere, IRRAS
	Initial corrosion caused the Mg/Al, Zn/Al LDHs formation by Zn-MgZn ₂ dissolution. No ZnO and simonkolleite formation were observed.		
Ueda et al. [31]	Zn _{1.1} Al ₃ Mg _{0.2} Si (pre-painted)	Corrosion product	Field exposure (9.5 years) in marine atmosphere
	Simonkolleite, NaZn ₄ (SO ₄)Cl(OH) ₆ •6H ₂ O, Zn-Al LDHs were found under the paint film. Mg-rich corrosion product was observed on the steel cut-edge.		
LeBozec et al. [32]	Zn ₂ Al ₂ Mg	Corrosion product	SST

II. State of the art

Simonkolleite and LDHs were mainly formed without CO ₂ . In ambient air, hydroxycarbonate and simonkolleite were dominant.
--

Some authors proposed that other corrosion products than LDHs enhanced corrosion resistance of Zn-Al-Mg. Also specific electrolyte composition was suggested without showing formation of LDHs. These are provided in **Table 2.4**.

Diler et al. [28] investigated the corrosion products of Zn metal and Zn-1.5Al-1.5Mg alloys after 6 months of field exposure in a marine environment. The enhanced corrosion resistance of the Zn-Al-Mg alloy was due to the presence of Mg²⁺ and Al³⁺ quenching the general activity of the coating after 7 days of exposure. MgCO₃ and MgSO₄ formation limited carbonate and sulphate ions which could react with stable simonkolleite. Strong enhancement of NaZn₄Cl(OH)₆SO₄·6H₂O formation was observed rather than LDHs which may result in an improved corrosion resistance by its insoluble and unfavorable to O₂ diffusion character.

Stouilil et al. [33] tested the electrochemical properties of corrosion products of the Zn-Al-Mg alloy by EIS, SKP and photoluminescence (PL) technique. They concluded that the low-energy band gap of corrosion products, ZnO, was related to their high conductivity and efficiency of the oxygen reduction reaction for HDG. In the alloy coating, the formation of ZnO was replaced by other more compact corrosion products which showed lower conductivity and better barrier properties.

Yao et al. [14] investigated the microstructure of the Zn-5Al-1.5Mg and the Zn-5Al-2Mg alloys. The better corrosion resistance attributed to formation of simonkolleite (Zn₅Cl₂(OH)₈·H₂O) in the outer surface which would inhibit the path of O₂ and H₂O transportation by a salt fog spray corrosion test.

Salgueiro Azevedo et al. [34,35] surveyed the role of electrolyte composition on the corrosion of Zn-3.7Al-3Mg introducing a ‘synthetic rain water’ containing NH₄⁺ and HCO₃⁻ for the corrosion test. This observation was attributed to the pH buffering effect of the NH₄⁺/HCO₃⁻ mixture at pH=8~10, which could delay the Al dissolution resulting in hindrance of LDHs formation.

Table 2.4. Effect of corrosion product, other than LDHs, on the corrosion of Zn-Al-Mg.

References	Material	Category	Methods
Diler et al. [36]	Zn1.5Al1.5Mg	Corrosion product	6 months exposure in marine area.
	Mg ²⁺ and Al ³⁺ induced quenching of corrosion activity. NaZn ₄ Cl(OH) ₆ SO ₄ •6H ₂ O formed rather than LDHs.		
Stoulil et al. [33]	Zn1.5Al1.5Mg, Zn11Al3Mg0.2Si	Electrochemical properties of corrosion products	NaCl deposition.
	The surface was covered with compact layers having low electric conductivity and better barrier properties.		
Yao et al. [14]	Zn5Al+(0~2)Mg	Microstructure Corrosion product	Salt fog spray chamber
	Flocculent type simonkolleite prolonged the micro-path and impeded the movement of O ₂ and H ₂ O, ultimately retarded the overall corrosion process.		
Azevedo et al. [34]	Zn3.7Al3Mg	Corrosion product Electrolyte composition	NH ₄ ⁺ , HCO ₃ ⁻ , field exposure, accelerated corrosion test
	NH ₄ ⁺ , HCO ₃ ⁻ may delay the formation of LDHs by buffering pH. No ZnO was detected. Role of Mg on corrosion mechanism was unclear.		
Azevedo et al. [35]	Zn3.7Al3Mg	Corrosion product Electrolyte composition	NH ₄ ⁺ , HCO ₃ ⁻ , Cl ⁻ media, AESEC
	No LDHs were formed in NH ₄ ⁺ , HCO ₃ ⁻ containing electrolyte. Mg(OH) ₂ was detected.		
Luckeneder et al. [37]	Zn2Al2Mg	Corrosion product	Delamination with evaluation after the VDA test, electrochemical test
	Zn-Al hydrotalcite formation was observed.		

2.2.4. Summary of the corrosion mechanism of Zn-Al-Mg

Corrosion mechanisms of Zn-Al-Mg stated above can affect one to the other in a real corrosion situation. The general consensus is that the enhanced corrosion resistance of the Zn-Al-Mg alloy coating is due to formation of the protective corrosion product layer. However, very few of them tried to explain a specific corrosion mechanism of Zn-Al/Zn-Mg/Zn-Al-Mg alloy system.

In every case, the formation of corrosion products depends upon the availability of the constituent elements which in turn depends upon the reactivity of the specific phases. Therefore, the performance and durability of these materials is intrinsically linked to the rates of

dissolution of the alloy components, Zn, Al and Mg. At the present time, little research has been carried out to determine how elemental dissolution rates vary between phases or to determine the electrochemical parameters of the pure phases which might permit the prediction of reactivity in a multiphase alloy. To this end, this Ph.D. project aims to fill this gap by identifying the mechanisms of elemental dissolution of pure metal, pure phases and the alloy coatings in different electrolyte conditions. The dealloying reactions are investigated as a function of potential and pH.

2.3. Pure phase chemistry and dealloying of binary alloys.

The multi-phase structure of the Zn based alloy complicates further the electrochemistry of Zn-Al/Zn-Mg/Zn-Al-Mg system. For example, galvanic coupling between phases in the same alloy should be altered because some elements can become active or passive depending on the history of the sample and the surrounding corrosion environment. Therefore, understanding individual dissolution behavior of each phase is necessary to predict the corrosion of multi-phase alloy system. In this sense, the dealloying of binary alloys has been studied by different authors. In the pioneering work of Pickering concerning the dissolution of binary alloys [38,39], different types of dealloying mechanisms were suggested depending on the critical potential (E_c) and elemental composition (N_B). It was concluded that the anodic polarization curves of the binary alloys showed distinctive behavior as compared to pure metals. Four different potential domains ((a) ~ (d)) were assigned which could be empirically identified based on the polarization curve. The dealloying types differ depending on the elemental dissolution of less noble metal (A) and more noble metal (B) as illustrated in **Fig. 2.2**.

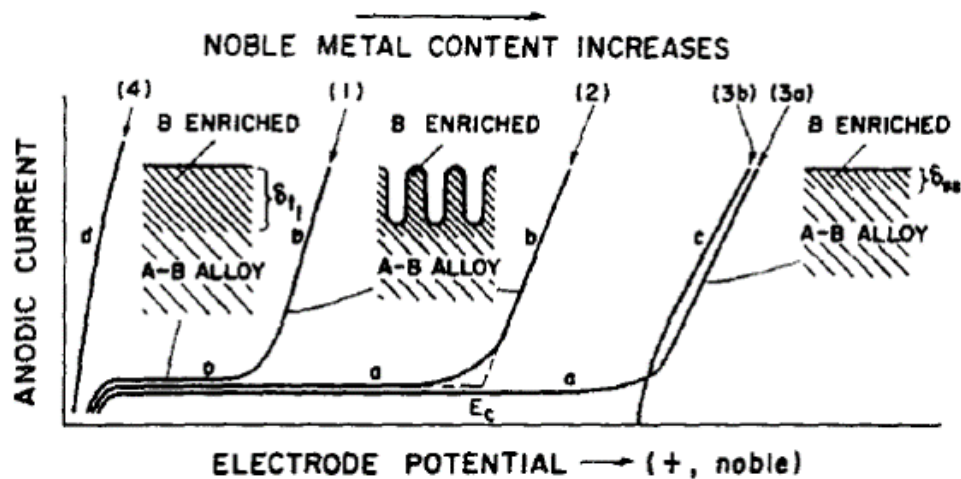


Fig. 2.2. Schematic illustration of the anodic polarization behavior of binary A-B alloys. Curves (1), (2) and (3a) are due to dissolution of A and curve (3b) to dissolution of B. The δ_{t_1} and δ_{ss} are the diffusion layer (dealloyed layer) thicknesses at time 1 (t_1) and steady state (ss), respectively, for the proposed transport mechanisms [39].

- (a) A potential dependent dissolution region where slightly positive over-potential than pure A metal.
- (b) A potential independent limiting current region where the electrical current was stable with potential sweep.
- (c) A potential dependent region where more noble metal B starts to dissolve.
- (d) A potential dependent region at which both A and B metal dissolve.

Pickering found that in a certain composition of A and B, the polarization path followed either (a)-(b) or (a)-(c) which was denoted as Type I and Type II dissolution respectively. For Type I dissolution in region (b), selective dissolution of A metal was predicted at lower potential than the critical potential of more noble metal B. In this region, the surface morphology would be extremely porous due to the selective leaching of A resulting in an enriched layer of B. When the potential increases above the critical potential of B, selective dissolution of B would occur with lower dissolution rate than that of A. Therefore, selective dissolution of B would dominate even in a relatively positive potential domain. Pickering concluded that Type I dissolution would be favored when the difference of standard reduction potential between less noble A and more noble B metals ($\Delta E^\circ = E_B^\circ - E_A^\circ$) increases, based on empirical data. Furthermore, the composition of more noble metal in mole fraction (N_B) also would have an effect on the transition from Type I to Type II dissolution. If content of the more noble B metal in binary alloy is low enough (as a rule of thumb, $N_B < 0.5 \Delta E^\circ$, [40]), Type I would be more favored.

Type I dissolution was reported for Cu rich Cu-Au alloy, Zn-rich brass, Fe rich Fe-Pt alloys [39].

For Type II dissolution in region (b), the selective dissolution of A would occur. Once the surface was enriched with B to a certain level, A and B would dissolve simultaneously in a congruent manner. This non-selective dissolution was reported for α -brass, Cu-20Zr [41]. Pickering predicted that Type II dissolution would be favored in all binary alloy systems having higher N_B than a critical value (N_B^*) with small ΔE° value. The lower ΔE° value would lead less amount of B needed to make the selective leaching of A, resulting in non-selective Type II dissolution. The empirical tendency for Type I and Type II dissolution depending on the N_B and ΔE° was suggested as shown in **Fig. 2.3**. Sieradzki et al. [42] presented that the composition of the binary alloys as the main factor which determines the threshold potential of the system by the Monte Carlo simulations.

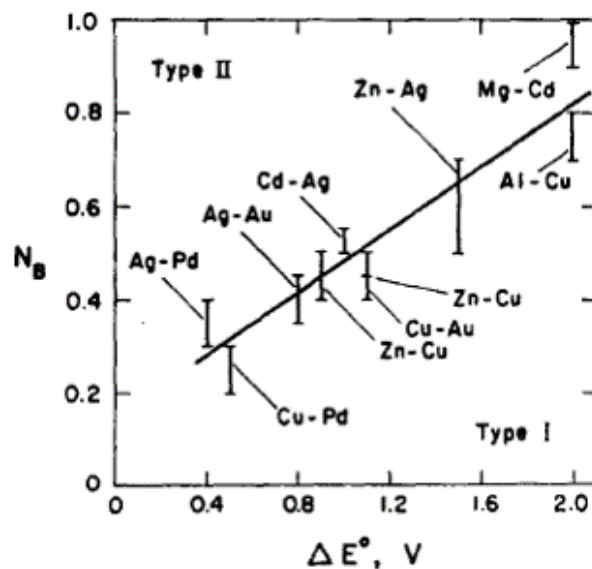


Fig. 2.3. Pickering's convention: binary alloys showing that the transition from Type I to Type II dissolution depending on N_B and ΔE° [39].

Dealloying mechanism of binary alloy has been electrochemically investigated mainly for the noble metals. Laurent et al. [43] tested anodic dissolution of Cu-Au and Ag-Pd alloys by potentiostatic polarization and Auger electron spectroscopy (AES). At the subcritical potential, the noble metal surface concentration increased due to selective dissolution of the less noble element. Wagner et al. [2] monitored enrichment of the noble metal on the surface of Ag-Au and Cu-Au binary alloys when a constant potential slightly lower than the corrosion

potential was applied. The noble element layer growth and the porous structure caused by bulk dealloying were monitored by *in-situ* scanning tunnel microscopy (STM).

However, this conventional model of dealloying has an evident limit in that it is based on experiments where relatively inactive elements were chosen as the binary alloy system. More complex surrounding the metallic dissolutions were not taken into account. For the less noble metal system in more complicated environments (such as high/low pH, presence of different anion/cation in the electrolyte, temperature variance), Pickering's convention cannot be directly applied. Sieradzki et al. [44] discussed the critical potential on dealloying process which could be changed by other experimental parameters such as the potential scan rate. Birbilis et al. [45] investigated the electrochemical behavior of the intermetallic using microcapillary electrochemical cell of intermetallic phases such as Al_3Fe , Al_2Cu , Al_3Zr_3 , Al_6Mn , Al_3Ti , $\text{Al}_{32}\text{Zn}_{49}$ and Mg_2Al_3 , which are commonly present in high-strength Al based alloys. The results showed that the electrochemical behavior of these intermetallic were more complicated than the conventional explanation. The alloys with the largest capability of sustaining cathodic current densities were not necessarily shown to be the most noble, similarly to the least noble were not necessarily those that could sustain the largest anodic current. They also revealed that the electrochemical properties of the intermetallic can markedly altered depending on pH [46].

Pareek et al. [47] observed the initial stages of electrochemical dealloying of the Cu_3Al by STM and AEM. They could visualize atomic level of the interlayer exchange between the topmost atomic layers by STM which is not in accordance with the discussion by Pickering and Wagner [38]. Temperature dependence of Al intermetallic phases was discussed by Cavanaugh et al. [48]. For the intermetallic of Mg_2Si , MgZn_2 , $\text{Al}_7\text{Cu}_2\text{Fe}$, Al_2Cu , Al_2CuMg and Al_3Fe , the electrochemical behavior was highly dependent on environmental temperature, affecting the localized corrosion. Geng et al. [49] found significant morphological modification at high homologous temperature for Li-Sn intermetallic system.

Dealloying of the intermetallic phases containing Mg, Zn and Cu were also studied. Ramgopal et al. [50] investigated the breakdown/corrosion potential of $\text{Mg}(\text{Zn}, \text{Cu}, \text{Al})_2$ intermetallic phases active to the matrix in the 7xxx series of Al alloys. It was concluded that the breakdown potential of MgZn_2 intermetallic was related to the dealloying of Zn. Also, they found that adding Cu to MgZn_2 phase resulted in increase of the breakdown potential while

adding Al up to 10 at.% showed no effect on the breakdown potential. The breakdown/corrosion potential could be altered by the presence of $\text{Mg}(\text{OH})_2$ film in highly alkaline solution and presence of O_2 incorporated into the thin films. For brass, dezincification kinetics were recently studied by atomic emission spectroelectrochemistry (AESEC) [51] technique and by laser-induced breakdown spectroscopy mapping (LIBS) [52].

2.4. Conclusion and perspectives of dealloying on the corrosion mechanism of Zn-Al-Mg

It was demonstrated that dealloying is an important factor to understand elemental dissolution in that it showed a clear tendency for some binary systems. However, prediction of dissolution type is limited only for relatively noble metals. For the heterogeneous alloy system, for example, the composition of noble metal (N_B) cannot predict the nature of dissolution type because in general, elements are non-evenly distributed on the surface, sometime in a form of a distinctive phase. Therefore, specimen of interest and electrolyte condition should be carefully chosen. Other electrochemical test than polarization experiment can be performed to separate experimental parameters. For instance, critical potential of some element can be altered depending on the preceding potential sweep by cathodic reaction which may result in increasing solution pH. To this end, chronoamperometric (CA) experiment was performed in this work to separate the effect of potential. The more noble element enrichment in the cathodic potential was elucidated by the CA experiment. Further, the enriched more noble element was quantified by the CA step experiment for the first time. Dealloying mechanism and different dissolution type studied in this chapter were taken into consideration to understand pure phases both by polarization and potentiostatic experiments.

Chapter III:

Atomic emission spectroelectrochemistry (AESEC) and other experimentations.

“Wir warden viel für die aesthetische Wissenschaft gewonnen haben, wenn wir nicht nur zur logischen Einsicht, sondern zur unmittelbaren Sicherheit der Anschauung gekommen sind, dass die Fortentwicklung der Kunst an die Duplicität des *Apollinischen* und des *Dionysischen* gebunden ist”

“We shall have gained much for the science of aesthetics when we have come to realize, not just through logical insight but also with the certainty of something directly apprehended, that the continuous evolution of art is bound up with the duality of the *Apolline* and the *Dionysiac*”

The Birth of Tragedy out of the Spirit of Music (1872),

Friedrich Wilhelm Nietzsche

3. Experimental

3.1. Introduction of the spectroscopy

Electrochemical methods are often used to characterize the corrosion and passivation mechanisms of the materials [27, 53–64]. Different technique has been used depending on the specific questions to answer. Conventional techniques such as rotating disk electrode (RDE), scanning Kelvin probe (SKP) and quartz crystal microbalance (QCM) have been widely used for electrochemical measurement of the specimen. By all manner of means, each technique has advantages and drawbacks depending on its applications. For example, RDE has been widely used because of its stable and reproducible system especially to measure polarization curve [53]. SKP technique has been developed to monitor the topography and potential distribution during the corrosion in a micrometer scale surface [54]. The electrochemical quartz crystal microbalance (EQCM) measures nano-gram changes in mass simultaneously with electrochemical measurement [26,55].

However, these electrochemical methods have a clear common limitation. For RDE, it is simple to measure the electron exchange of the system by an electrometer, however, it is hard to distinguish which chemical reaction caused that change. Therefore, electrochemistry coupled with more chemically specific spectroscopy, referenced as spectroelectrochemistry (SEC), could give a more complete analysis of complicated multiple electron transfer system [56]. A typical absorption spectroscopy such as ultraviolet (UV), the visible (VIS), the infrared (IR) or Raman spectroscopy have been used to combine with the electrochemical measurements [16,57–59]. From 80's, pioneering work of coupling IR to spectroelectroscopy technique has been extensively studied to investigate the redox species dissolved in solution [16]. Difficulty of applying IR spectroscopy to electrochemical solution process was the absorption of IR radiation by the solvent interfered to detect the vibrational mode of dissolved analytes. The electrochemical oxidation of iron in alkaline solution was monitored by RDE coupled with *in-situ* spectroelectrochemical techniques by Zhang et al. [60]. Keddani et al. [61] investigated the corrosion of Zn by impedance spectroscopy coupled with FTIR and *in-situ* Raman spectroscopy. *In-situ* Raman spectroelectrochemistry was used to monitor unequivocal determination of anatase phase in TiO₂ powder by Laskova et al. [62]. Sfez et al. [63] combined X-ray photoelectron spectroscopy with UV-vis-NIR spectroscopy to monitor electronic properties of the polyaniline (PAN) monolayers. A spectroelectrochemical cell was introduced coupling electrochemistry and fluorescence spectroscopy in order to test the reduction step of a soluble

III. AESEC technique and other experimentations

perylene derivative and its efficiency was compared with that of UV-Vis spectroelectrochemistry [64].

Atomic emission spectroelectrochemistry (AESEC) was introduced to measure both directly elemental dissolution mechanism by soluble species during their exposure to the electrolyte and indirectly insoluble species such as surface film formation [65]. This technique allows us to monitor the total electrical current caused by elemental dissolution coupled with a potentiostat. Therefore, it can be used to evaluate in real time elemental dissolution of the specimen in different environment such as various pH, electrolyte concentration and solution temperature. It is in particular suitable for kinetic measurements of dealloying. It has been proved to be a powerful technique in studying the selective leaching of Fe-Cr alloys in sulfuric and nitric acid [66], the enrichment of Cu on 304 stainless steel surface [65], the selective dissolution of Al from 2024 Al alloy at cathodic potential domain [67].

A brief history of atomic emission spectroscopy

In 1752, Thomas Melville gave a talk entitled “Observations on light and colours” to the Medical Society of Edinburgh [62]. He claimed that he had observed a yellow colored light emission from a flame by various salts that he had used. He reported that a yellow line was always present at the same place in the spectrum, eventually because of sodium included in his salts which he was not aware of at that time. Although Melville passed away one year after, in 1753 without proving further the origin of the flame color, he is considered as a father of atomic spectroscopy.

In 1776, Alessandro Volta, Italian physicist, chemist and inventor of the electrical battery, had discovered methane after reading a paper on “flammable air” written by Benjamin Franklin. He designed experiments to produce a static electric charge strong enough to create sparks and in this way was able to identify certain gases by the colors emitted from the spark.

Robert Bunsen and Gustav Kirchhoff contributed to the initial understanding of spectroscopy and are considered as pioneers of photochemistry. Bunsen and his laboratory assistant Peter Desaga developed the Bunsen burner by which the emission spectrum could be produced from a single gas flame. They highlighted that the dark lines in the absorption spectrum of the light correlated in wavelengths, with the wavelengths of the bright, sharp lines characteristics of the emission spectra of the same materials. In this way, they discovered Cs (in 1860) and Rb (in 1861) by the emission spectra of the heated elements.

In the latter half of the 19th century, tons of spectral data from the light emission was generated and the characteristic lines were precisely assigned to each element with its own wavelength. In 1885, J. J. Balmer showed that a simple mathematical formula could represent the wavelength of the visible spectral lines of hydrogen atom (Balmer series). Based on this, Niels Bohr proposed that the electron moves in circular orbits bound by the Coulomb attraction to the positively charged nucleus. Bohr explained that the light was emitted only in the case of a transition of an electron from a higher to a lower energy. The energy lost from the atom is carried away as the energy of a photon. This quantum theory of Bohr initiated a new paradigm of spectroscopy and atomic structure. In parallel with the development of the theory of the atomic structure, other important findings related to the spectroscopy were carried out, such as the splitting of atomic spectral lines in an applied magnetic field (Pieter Zeeman, 1896) and electric field splitting of the Balmer H₂ lines (W. Stark, 1913).

3.2. Atomic emission spectroelectrochemistry: methodology and instrumentation

3.2.1. Nature of atomic spectra

When a sufficiently high energy is supplied by the Ar plasma, an electron from an atom in the element becomes excited to a higher energy level. As this atom is in the less stable state, it will decay back to a stable ground state losing the excess energy by emitting a particle of electromagnetic radiation referenced as a photon. If the absorbed energy is high enough to completely dissociate an electron from an atom (ionization) the potential will be generated between an electron and an ion with net positive charge created by this excitation. Since this ionization potential is determined by each element, it can be used to identify different elements in an analyte. Ions also have their own ground and excited states and undergo absorption and emission of the energy like an atom as shown in **Fig. 3.1**.

The energy transition between the higher and lower energy state determines the wavelength of the emitted radiation by Planck's equation as:

$$E = h \nu \quad [3.1]$$

where E is the energy difference between two energy states, *h* is Planck constant and ν is the frequency of the radiation. Since the ν , speed of light (*c*) and wavelength (λ) are related by $\nu = c / \lambda$, the **Eq. 3.1** can be rewritten as:

$$E = h c / \lambda \quad [3.2]$$

III. AESEC technique and other experimentations

As every atom has a unique series of electronic energy levels, each element produces a unique atomic spectrum which may be considered as a “fingerprint” and used to identify the element and the emission intensity at a specific wavelength may be used to quantify the element.

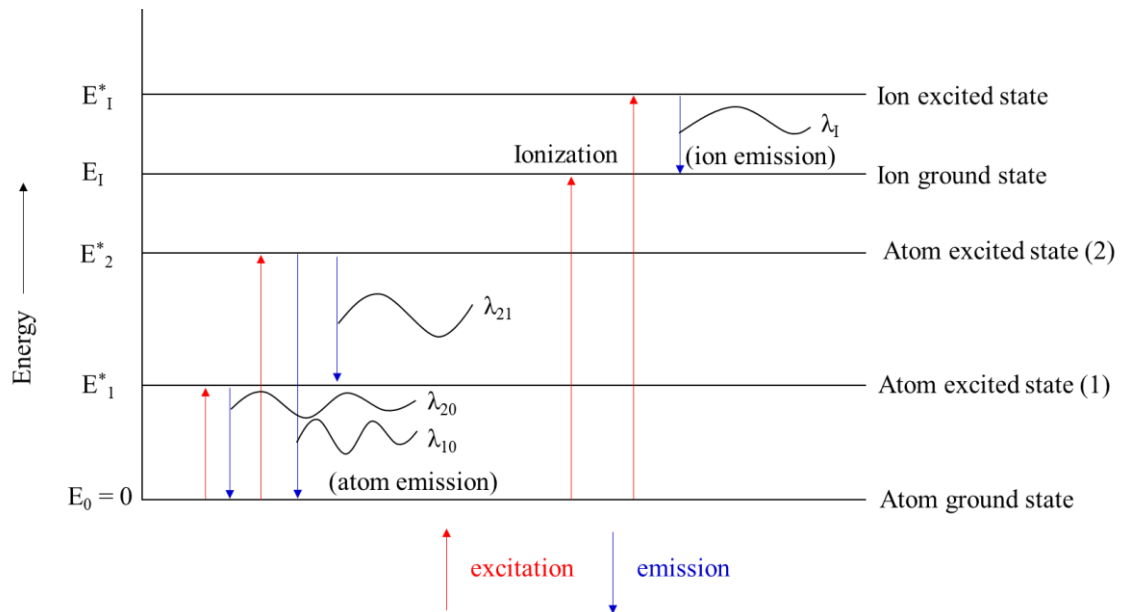


Fig. 3.1. Schematic description of energy transition in energy level diagram.

3.2.2. Instrumentation

Inductively coupled plasma–atomic emission spectrometer (ICP-AES) has been used in analytical chemistry not only to detect but also to quantify chemical elements, especially for multi-element system with a good sensitivity. The AESEC technique consists of an ICP-AES coupled with an electrochemical flow cell. The instrumentation can be divided into 3 parts: 1) An electrochemical flow cell, where a flat solid material (working electrode) is exposed to a flowing electrolyte; 2) A downstream ICP-AES spectrometer used to analyze the elemental dissolution from dissolved in the electrolyte from the material specimen; 3) A fast electronic system used to measure the emission intensities and electrochemical data as a function of time.

Plasma torch

The plasma sources are a radio frequency (RF) energy coupled to an Ar gas stream. The Ar gas is completely ionized by the RF energy to generate a high temperature plasma (5000~8000 K) which allows to ionize elements then emit electromagnetic radiation with its particular wavelength [68]. Excited atoms emit electromagnetic radiation ($h\nu$) when they relax to their ground energy state [69].

III. AESEC technique and other experimentations

The torch contains three concentric quartz tubes for Ar flow and aerosol injection as depicted in **Fig. 3.2**. A plasma is generated by the Ar flow into a quartz torch with applying a radio frequency (RF) power at 40.68 MHz. A magnetic field is induced through the load coil surrounding the top of the torch in which the intermediate part is positioned at the endpoint of the injector tube. The nebulizer flow carrying gas for solid aerosols from the concentric cyclonic chamber goes into the injector tube made of alumina. There is a narrow space between the two outer tubes in order to keep the high velocity of the Ar gas. At the plasma flow inlet, the Ar gas is introduced in a spiral tangentially around the chamber as it travels upward. This gas maintains the torch wall cool down during the procedure. Between the plasma flow and nebulizer flow, an auxiliary flow sends gas to keep the plasma away from the intermediate and the injector tubes. It enables the introduction of the analyte aerosol to the plasma easier and also helps to reduce salt formation on the tip of the injector tube when highly concentrated salt solutions are used [15]. Once the aerosol is vaporized and atomized, the plasma operates excitation and ionization. In order to make an atom or ion emit its own radiation, one of its electrons is needed to be excited to reach a higher energy level. In some elements, ionization is necessary as it may have its strongest emission lines emitted from the ICP by excited ions. These process take place in the initial radiation zone (IRZ) and the normal analytical zone (NAZ) marked in **Fig. 3.2**. The NAZ, 5000~8000 K, is where the analyte emission is measured.

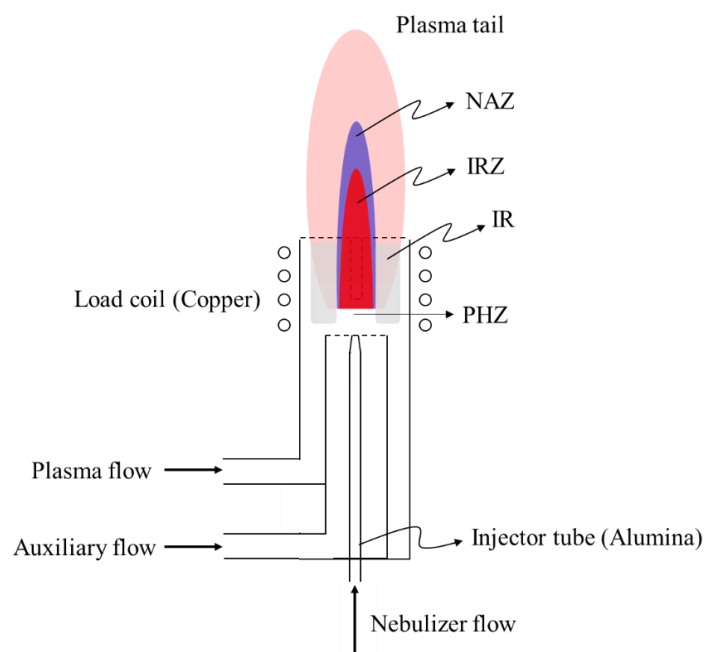


Fig. 3.2. Description of flow in the induced plasma torch. Each zone of the plasma is indicated; NAZ (normal analytical zone), IRZ (initial radiation zone), IR (induction region), PHZ (pre-heating zone).

It has been suggested that for the ICP, the electron-collisional excitation/de-excitation and ionization process are predominant for determining the atom and ion populations in the NAZ [70]. The process when a sample droplet is introduced into the ICP is described in **Fig. 3.3**. High gas temperature in the center of the ICP enables the improvement of excitation and ionization efficiencies and also reduces many chemical interferences may be found in the flames and furnaces. The aerosol can be surrounded by the high temperature plasma for a relatively long time (2 milliseconds) when it is introduced to the ICP resulting in lack of matrix interference in the ICP [71].

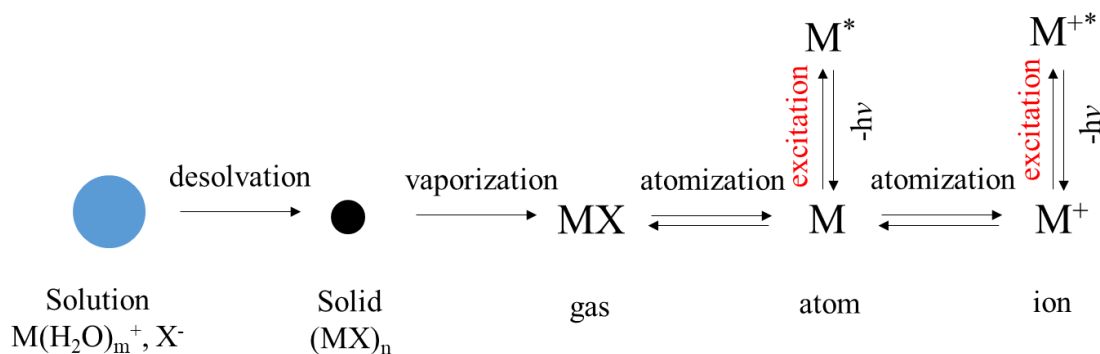


Fig. 3.3. Process after a sample droplet introduces to an ICP [15].

As the emission from the plasma is polychromatic, the radiation should be separated into individual wavelengths to identify the emission from each excited species. Also, the intensity should be measured without interference at other wavelengths. Extraction of information for ICP-AES is generally conducted by three spectral lines of the element. Relatively large number of emission lines is available for most of the element and avoid interference by selecting several different emission lines for one element. Quantitative information can be obtained using emission intensity vs. concentration curves. ICP calibration method will be discussed in the later section in this chapter. Standard solutions, prepared with known concentration of element, are introduced to ICP and measured the emission intensity including background signals. Calibration response in ICP is normally linear over a wide range of concentrations, valid over four to six orders of magnitude. However, it is limited at low concentrations by fluctuations of background emission from the plasma and scattered radiation. At high concentration, non-linear calibration curve is observed due to self-absorption in which the photons emitted in the center of the plasma can be absorbed by unexcited atoms may exist at much cooler plasma tail [65,72–74].

Nebulizer and cyclonic chamber

The electrolyte is fed continuously from the electrochemical cell by a peristaltic pump with Tygon™ capillaries. The flow rate of the electrolyte can be controlled by whether the thickness of the capillary or the speed of the peristaltic pump. In this Ph.D. thesis, a 2.8 mL min⁻¹ flow rate was chosen as previously stated. The electrolyte from the electrochemical flow cell is firstly introduced into the system containing a pneumatic nebulizer, a concentric glass nebulizer and a cyclonic spray chamber as described in **Fig. 3.4**. The high pressure Ar gas makes the electrolyte a fine aerosol form to spray it into the cyclonic spray chamber where the droplets having less than 10 μm diameter (approximately 5 % of total electrolyte) can be passed to the plasma torch by inertia effect. The residue of the electrolyte (approximately 95 %) is transferred to downstream by the peristaltic pump. An Ar humidifier is used to minimize the sample deposition on the torch injector and nebulizer tip. Also, it improves precision of the analysis especially for samples with a high dissolved solid content. When a Teflon nebulizer was used for a more concentrated solution, the Ar humidifier was not used because it can cause an accumulated salt around the tip of the nebulizer.

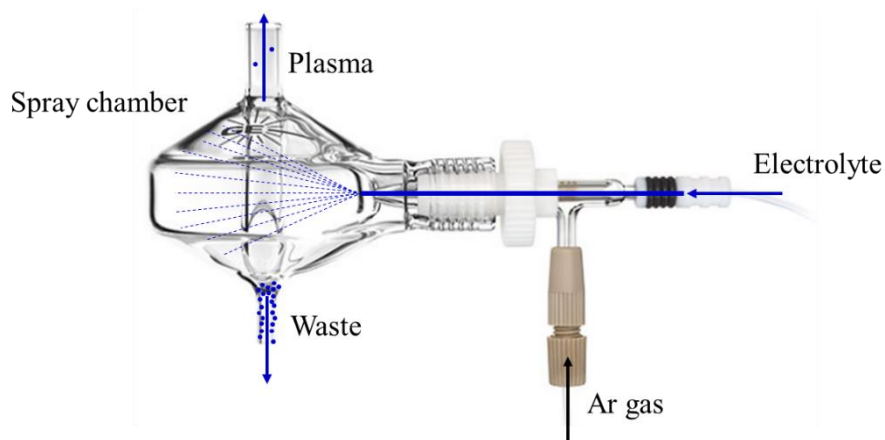


Fig. 3.4. A schematic image of the nebulizer and the spray chamber.

Electrochemical flow cell

The electrochemical flow cell of the AESEC technique is depicted in a schematic image in **Fig. 3.5**.

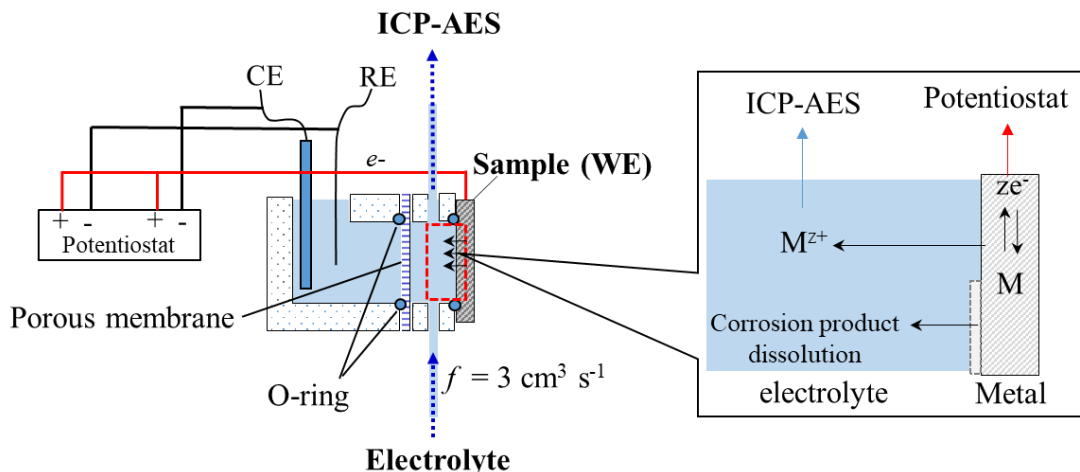


Fig. 3.5. A schematic image of the electrochemical flow cell.

The three-electrode electrochemical flow cell is divided into two compartments by a porous cellulose membrane: 1) reservoir of the electrolyte where the reference electrode (RE) and counter electrode (CE) are positioned, 2) the specimen (working electrode, WE) is in contact with a small volume ($\approx 0.2 \text{ cm}^3$) of constantly renewing electrolyte provided by a peristaltic pump. The porous membrane enables ionic current to pass between the two compartments where WE and CE are located, avoiding bulk mixing of the electrolytes between two compartments. The reaction area of the WE is defined by the contour of the o-ring which gives a constant reaction surface area. In this work, $A = 1.02 \pm 0.07 \text{ cm}^2$, measured by three different surface after the electrolyte exposure. An example of surface area calculation given in **Fig. 3.6.**

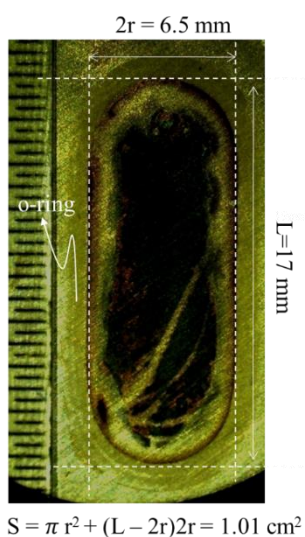


Fig. 3.6. Reaction surface calculation by optical microscope.

Soluble species formed at the material / solution interface will be carried downstream from the cell with a constant flow rate (in this work, $f \approx 2.8 \text{ mL min}^{-1}$) to an inductively coupled plasma

III. AESEC technique and other experimentations

of atomic emission spectrometer (ICP-AES). In this work, a Gamry Reference 600™ potentiostat/galvanostat was used for all electrochemical experiments. The ICP-AES electronics was specially adapted to measure the analog current and potential signals from the potentiostat in the same data file as the atomic emission intensities. In this way, electrochemical and spectroscopic data are measured on exactly the same time scale.

Wavelength dispersive devices

The differentiation of the emission radiation is carried out by a diffraction grating system. When the radiation strikes a grating, it is diffracted with a specific angle determined by the wavelength of the light and the line density of the grating. Therefore, multiple exit slits are needed to allow a specific wavelength to go through to the photo-detector blocking other wavelengths at the same time. In this work, the conventional Paschen-Runge (focal length of 0.5 m) mount of polychromator (Poly) consisting of an entrance slit, a concave grating and multiple exit slits was used to detect up to 30 preselected elements. A list of elements and its associated wavelengths can be used in the current system is given in **Table 3.1**. A schematic image of the light dispersive system is described in **Fig. 3.7**.

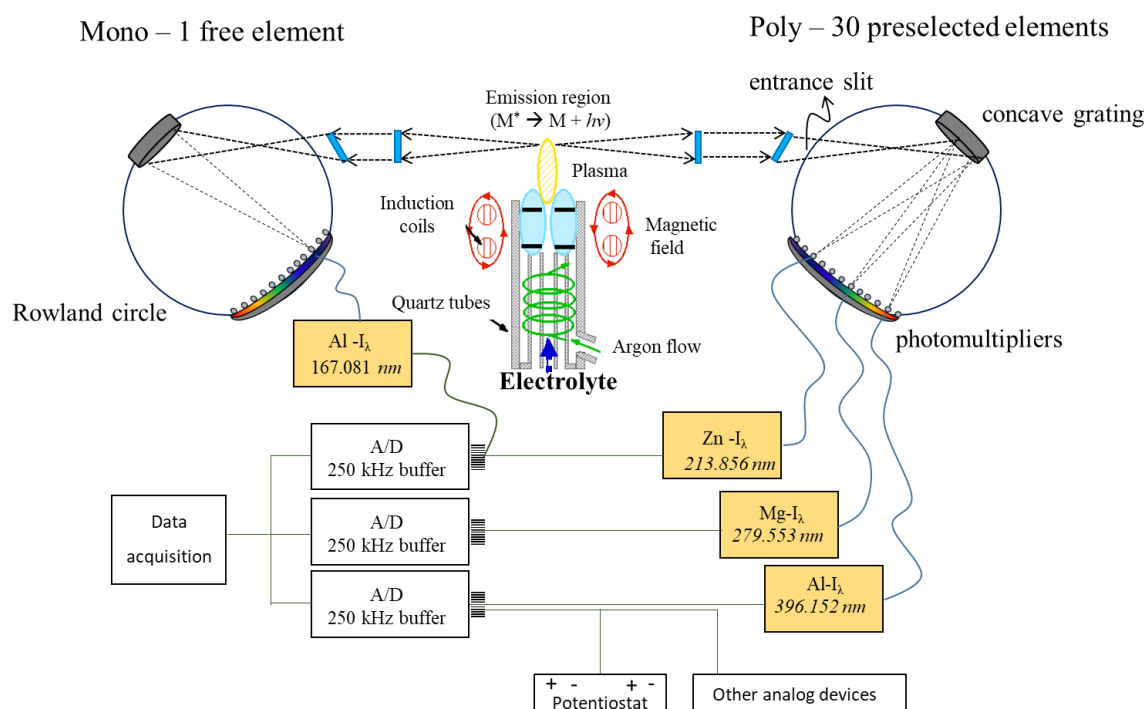


Fig. 3.7. Schema of inductively coupled plasma–atomic emission spectrometer (ICP-AES) [15].

III. AESEC technique and other experimentations

Table 3.1. Pre-selected elements (top) and its wavelength (bottom, /nm) on the polychromator.

Al 167.081	P 178.287	Sn 189.989	Mo 202.032	Sb 206.833	Zn 213.856	Pb 220.353	Co 231.604	Ni 233.527	Ba 233.527
Si 251.611	Mn 257.61	Fe 259.94	Cr 267.716	Mg 279.079	Mg 279.553	In 303.936	V 311.071	Nb 316.34	Cu 324.754
Ag 328.068	Zn 334.502	Ti 337.279	Zr 343.823	U 367.007	Y 371.029	Al 396.152	Ce 399.924	Sr 407.771	La 408.672

A Czerny–Turner monochromator (Mono) (focal length of 1.0 m) is used when a high spectral resolution is needed at a single wavelength and/or the element of interest is not included in the polychromator. For ICP-AES, emission lines in the UV/visible region, especially in the 190~450 nm is usually measured. Measuring emission lines under 190 nm is difficult in that it is easily absorbed by O₂ present in the surrounding environment. Therefore, a N₂ generator (Horiba Jobin Yvon SAS) was used to purge O₂ in the instrument. It produces high purity nitrogen gas (99.9995 %) from compressed air, after all, enables to detect sensitive Al (167.081 nm) signal.

3.2.3. Data analysis

Calibration of the ICP-AES signals

The analog signals received by the photo-multiplier (PMT) from mono and polychromator were digitized by three 16 bit A/D converters operating at a frequency of 250 kHz such that all signals were truly simultaneous. The digital data was monitored by the QuantumTM software (Horiba Jobin Yvon SAS) in real time. The intensity of the radiation emission signals from the elements can be quantified by a standard ICP-AES calibration method as described in **Fig. 3.8**. The 0.2, 0.42 and 0.58 ppm solutions of Al, Mg and Zn were prepared using standard solutions (SCP ScienceTM). Low concentration standard solutions were prepared to avoid contamination of the nebulizer and instrumental error. A clear linear relationship can be seen between the emission intensity and the solution concentration in all three elements.

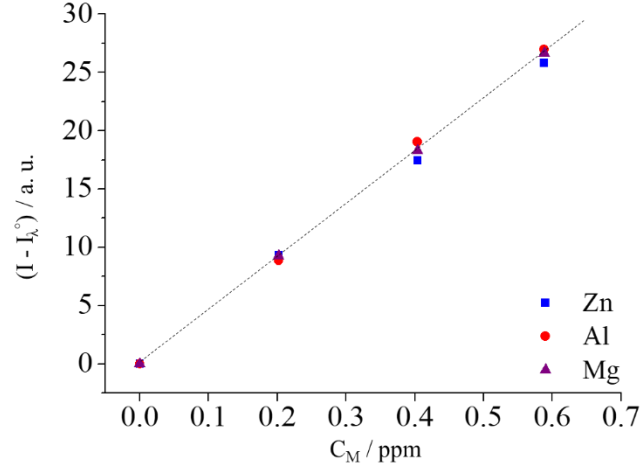


Fig. 3.8. Standard ICP calibration curve showing normalized emission intensities of Zn, Al and Mg at the characteristic wavelength of 213.86, 167.08 and 279.55 nm respectively.

The emission intensity of a specific element at its own wavelength is proportional to the concentration of the element in the plasma, which in turn is proportional to its concentration in the electrolyte which enters the plasma at a constant rate. The elemental concentration in the electrolyte, C_M ($/ \mu\text{g mL}^{-1}$), has relationship with the elemental intensity values (I_M) as:

$$C_M = (I_M - I_M^{\circ}) / \kappa_{\lambda} \quad [3.3]$$

where I_M° is the background intensity signal and κ_{λ} is the sensitivity factor for a given wavelength. From **Fig. 3.6**, κ_{λ} can be obtained experimentally with the slope of each line. The C_M value is in turn converted to elemental dissolution rate v_M ($/ \mu\text{g s}^{-1} \text{cm}^{-2}$) with the flow rate f ($/ \text{mL min}^{-1}$) and the exposed reaction area A ($/ \text{cm}^2$) as:

$$v_M = f C_M / A \quad [3.4]$$

By Faraday constant F (96485 C mol^{-1}), an equivalent elemental current density j_M ($/ \mu\text{A cm}^{-2}$) can be calculated based on v_M as:

$$j_M = zF v_M / M_M \quad [3.5]$$

where M_M (g mol^{-1}) is the molar mass of the element and z is the valence of the dissolving ions from the following reaction, $M \rightarrow M^{z+} + z e^{-}$.

The total current is given as the sum of anodic and cathodic partial currents, $i_e = i_a + i_c$. By definition, all current in this work is expressed as current density, therefore $j_e = j_a + j_c$. Both soluble (j_{Σ}) and insoluble (j_{ins}) component may contribute to the anodic current density, $j_a = j_{\Sigma}$

III. AESEC technique and other experimentations

+ j_{ins} . Only soluble components can be measured by the ICP-AES, however, in most circumstances we may assume that the unmeasurable insoluble component remains on the surface of the sample in the form of a corrosion product such as oxide film. The total current may be written as:

$$j_e = j_{\Sigma} + j_{\text{ins}} + j_c \quad [3.6]$$

It should be stressed the “insoluble” components (j_{ins}) means that at a given time, the formation of “slowly soluble” intermediates is more rapid than their dissolution leading to an oxide growth on the surface. In this manner, the term “insoluble” may not be appropriate to describe the nature of this non-faradaic feature. Therefore, we introduce here a new definition, j_{Δ} , to quantify the dissolution more precisely. By a mass balance equation, j_{Δ} can be determined as:

$$j_{\Delta} = j_e - j_{\Sigma} = j_{\text{ins}} + j_c \quad [3.7]$$

If $j_{\Delta} > 0$, the formation of unsolved species is predicted. If $j_{\Delta} < 0$, cathodic corrosion rate (j_c) can be calculated.

The faradaic yield of dissolution, η , may be determined by $\eta = j_{\Sigma} / j_e$. If $\eta \neq 1$ ($j_{\Delta} \neq 0$) it is often possible to calculate the rate of either cathodic reaction ($j_{\Delta} = j_c < 0$ for $\eta > 1$) or the formation of undissolved species ($j_{\Delta} = j_{\text{ins}} > 0$ for $\eta < 1$).

Residence time distribution

Under transient conditions, **Eq. 3.7** cannot be directly applied because of the temporal resolution difference between the electrochemical measurements and the spectrometric measurements. Electrochemical current transient, j_e , is essentially instantaneous (< 1 millisecond) on the time scale of the present experiments whereas elemental dissolution rate transients, j_M , are broadened by diffusion and mixing in the hydraulic system. To this end, a numerical simulation was proposed by Ogle to use a convolution method to put the same time resolution between two measurements thereby make them comparable [65]. This may be revised by calculating a numerical convolution of j_e and $h(t)$ such as:

$$j_e^*(t) = \int_0^t j_e(u) h(t-\tau) du \quad [3.8]$$

III. AESEC technique and other experimentations

where $h(t)$ is the residence time distribution function for the hydraulic system of the flow cell and τ is simply a variable of integration. Determining $h(t)$ and other time constants are described in the ‘residence time distribution’ section. Following this calculation, the electrochemical data will be on the same time resolution as the concentration data. More precisely, **Eq. 3.7** can be rewritten as:

$$j_{\Delta} = j_e^* - j_{\Sigma} \quad [3.9]$$

The time constant distribution, $h(t)$, was determined by the following experiment: A 99.9 % Cu electrode was exposed to deaerated 2 M HCl for 5 minutes at the open circuit potential, followed by a 1 s galvanostatic pulse at 1 mA and then returned to the open circuit potential. This released 1 mC of Cu(I) as CuCl_2^- into the electrolyte. A 1 mA by 1 s pulse was considered to be sufficiently short to be effectively “instantaneous” on the time scale of these experiments. The emission intensity (concentration) of Cu existing the flow cell was measured as a function of time. **Fig. 3.9** shows one example of the results. The pulsed anodic dissolution of Cu (I_{Cu}) rose to an asymmetric peak, which increased instantaneously to a maximum value then decreased to the background signal, I_{λ}° . The time, t° , between the galvanostatic pulse and the first point of Cu intensity which rose above the background, I° , is associated with the time necessary for the Cu ions to travel between the electrochemical cell and the nebulization system.

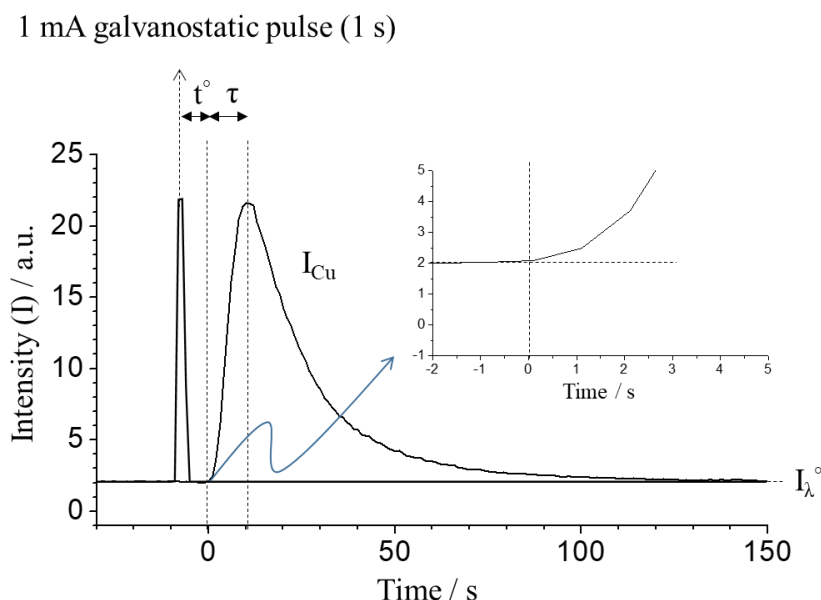


Fig. 3.9. Intensity-time response of Cu in 2 M HCl applying 1 mA galvanostatic pulse during 1 s. The intensity value is in arbitrary unit (a.u.). t° is determined as the time between the initial galvanostatic pulse and the first point at which the Cu signal increases over the background signal (I_{λ}°). τ is between $t=0$ and the time when the I_{Cu} reaches the maximum value.

III. AESEC technique and other experimentations

The residence time distribution, $h(t)$, was determined to be a log-normal distribution from both empirical [65] experiment and by numerical simulation [75] as:

$$h(t) = \frac{I_{\text{Cu}} - I_{\lambda}^{\circ}}{Q} = \sqrt{\frac{\beta}{\pi\tau^2}} e^{\frac{-1}{4\beta}} e^{-\beta \ln^2 \frac{t}{\tau}} \quad [3.10]$$

where Q is the integral of the transient in arbitrary units, β and τ are the time constants for the log-normal distribution and t is the experimental time. **Eq. 3.10** can be rewritten as:

$$I_{\text{Cu}} = Q \sqrt{\frac{\beta}{\pi\tau^2}} e^{\frac{-1}{4\beta}} e^{-\beta \ln^2 \left(\frac{t}{\tau}\right)} + I_{\lambda}^{\circ} \quad [3.11]$$

Four repeated experiments of log-normal distribution of Cu dissolution, I_{Cu} vs. $\log(t)$, in deaerated 2 M HCl solution, applying 1 mA galvanostatic pulse during 1 s shown in **Fig. 3.10**.

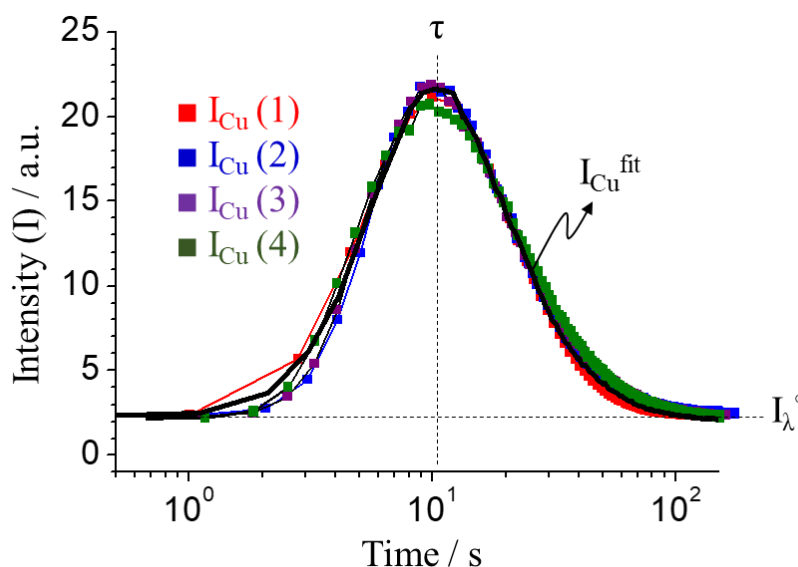


Fig. 3.10. Experimentally determined residence time distribution. Log-normal distribution of four repeated experiments Cu dissolution (I_{Cu} (1) ~ (4)) and numerical curve fitting by OriginTM software ($I_{\text{Cu}}^{\text{fit}}$) as a function of time in a $\log(t)$ axis.

Using the log-normal curve fitting function of OriginTM software (version 8.0), the time constants were determined as $\beta = 1.01 \pm 0.05$ and $\tau = 10.5 \pm 0.82$ for the repeated experiments.

In this work, all the measured j_e values were convoluted unless otherwise stated. It often gives information about residual film dissolution after electrochemical experiments by comparing decaying signal of j_e^* with that of j_M , described in **Chapter VI**.

3.3 Signal noise and perturbations

Eqs. 3.3 and **3.4** relate the dissolution rate of the element, M , to the emission intensity of the element at a specific wavelength. The emission intensity is proportional to the rate at which the element enters the plasma via the pump, nebulization and aspiration system (see section 3.2.2. for a detailed discussion). For a standard analysis, with an electrolyte of homogeneous concentration, the noise of the signal may be divided into two components. (1) An additive component, I° in **Eq. 3.3**, which is the background emission of the plasma and stray radiation at wavelength λ_M , and (2) a multiplicative factor, due to instantaneous variations in the nebulizer which affect the rate at which the electrolyte enters the plasma.

In some situations, however, the perturbations reflect the chemistry of the system [76]. Two of these situations are observed in this work: The detachment of particles from the sample which are carried to the plasma. The particles appear as a pulse of less than 0.01 s width and reflect the composition of the particles as concerns the constituent particles of Al alloys [67]. This phenomenon was observed here for Zn-Al alloys at high temperature in **Chapter VII**.

Another situation is when hydrogen evolution leads to the formation of bubbles that are carried into the plasma momentarily disturbing the nebulization system. This leads to a perturbed signal and in this work, will be used to identify situations where dissolution is driven by hydrogen evolution (perturbations present) or by cation migration across a passive film (no perturbations).

It is of interest to determine whether or not the amplitude of the perturbations may be used to estimate the intensity of the hydrogen evolution reaction (HER). Previously, HER quantification was conducted by the AESEC technique by coupling with video-visual camera recording method with excellent precision [77]. The **Fig. 3.11** gives the relationship between j_{Al} and $\sigma_{j_{Al}}$ of Al containing alloy, for the open circuit dissolution of pure Zn-Al phases and Al metal in pH=8.4, 10,1 and 12.80 electrolyte. It is assumed that Al dissolution is completely balanced by the HER.

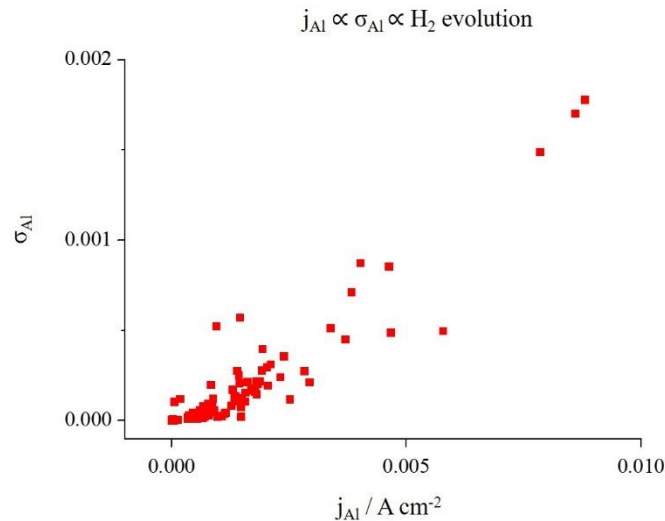


Fig. 3.11. Linear relationship between j_{Al} and $\sigma_{j_{Al}}$ of Al containing alloy, pure phase and Al metal in pH=8.4, 10,1 and 12.80 electrolyte.

These results demonstrate that hydrogen evolution leads to an enhanced perturbation of the emission intensity making it an excellent qualitative indication of the corrosion mechanism at hand. However, the high standard deviation would make quantitative measurement much less precise.

To go further with this methodology, the dynamics of bubble transfer to the plasma via the nebulization system needs to be investigated in more detail and the time resolution of the technique should perhaps be increased. It is possible to go up to extremely high data acquisition rates, > 1 kHz, and it is probably that the bubbles, like particles [67] give rise to very rapid transients.

3.4. Sample preparation

In this work, all samples were prepared in a same way in order to make sure a reproducible surface condition was obtained. All samples were degreased by ethanol in an ultrasonic bath for 10 minutes then dried by N_2 gas. After this procedure, pure phase intermetallic and nominally pure metal samples were ground by emery paper (Si-C) with P1200, P2400 and P4000 under ethanol during 10 minutes. The alloy coatings, on the other hand, were ground only with P4000 during 30 seconds since the commercial coatings are not necessarily uniform in depth. Samples were dried under flowing Ar gas, then stored in a humidity chamber of 50% relative humidity (RH) obtained from a water reservoir saturated with $Mg(NO_3)_2 \cdot H_2O$

during 20-24 hours [33]. The effect of different surface preparation methods is reported in **Appendix 4**.

3.5. Electrochemical experiments

3.5.1. Potentiodynamic polarization

A potentiodynamic polarization curve coupled with ICP-AES is a useful technique by measuring not only the electrical response from the potentiostat (E , i) but also elemental dissolution rates (j_M) monitored by ICP-AES. In this work, linear sweep voltammetry (LSV) was performed with a potential sweep from negative to positive potential, or from the open circuit potential (E_{oc}) to a negative (cathodic LSV) or positive potential (anodic LSV). The scan rate of this work is fixed at 0.50 mV s^{-1} unless otherwise stated.

3.5.2. Chronoamperometry

Applying a constant potential as a function of time is useful for isolating the effect of potential and time to the sample. In this sense, chronoamperometric (CA) experiments were conducted by choosing a potential of interest based on the polarization experiments. To avoid the complexity caused by dealloying and corrosion product formation during the open circuit exposure on the sample, a constant potential was applied after only a few seconds following the contact between the electrolyte and the specimen.

3.5.3. Chronoamperometric step experiment

An evident formation of more noble metal enrichment was revealed by AESEC chronoamperometric step experiment. Firstly, a constant cathodic potential was applied for a certain time to form a more noble metal layer due to a selective dissolution of the less noble metal. Thereafter, the potential was switched to an anodic potential to dissolve this layer where a clear noble metal dissolution was observed. Further, the more noble metal enriched layer showed a critical potential to dissolve.

3.5.4. Alternative-current atomic emission spectroelectrochemistry (AC-AESEC)

Coupling AESEC technique with electrochemical impedance spectroscopy (EIS) was proposed in reference [78]. The objective of this technique is to distinguish whether metal oxidation causes direct formation of dissolved ions or passes across an intermediate film. In this work, a low frequency (0.0046 Hz) potential perturbation was tested. A phase shift between Zn and Al dissolution rate was observed for all Zn-Al containing system except for the Al-rich Zn phase (Zn-68 wt.% Al, $Al_{5.2}Zn$ based on its molar composition). For the Zn-Al-Mg alloy coating, Al and Mg dissolution phase was varied depending on the potential. The preliminary results and discussions are presented in the **Appendix 1**.

3.6. *Ex-situ* surface characterization techniques

3.6.1. *Scanning electron microscopy – energy dispersive X-ray spectroscopy (SEM-EDS)*

The scanning electron microscopy (SEM) enables the characterization of surface morphology down to the nanometer scale. An electron beam is generated by an electron cathode and the electromagnetic lenses and sweep across the surface of a sample. A secondary electron (SE) and backscattered electron (BSE) detectors were used in this work. Secondary electrons are widely used in that they are most valuable for visualizing morphology and topography on samples and backscattered electrons are useful for illustrating contrasts of composition in multiphase samples.

Energy dispersive X-ray spectrometry (EDS) coupled with SEM was used to obtain a localized chemical analysis by attacking with a focused X-ray beam on the sample. It allows a qualitative analysis by identifying the lines in the spectrum and a quantitative analysis by measuring line intensities for each element in the sample. Spatial resolution of the SEM-EDS is determined by the penetration and spreading of the electron beam into the sample. Spatial resolution is a function of density of the sample as the electrons penetrate approximately a constant mass. X-ray intensities are obtained by counting photons, therefore, the sensitivity is limited by statistical error. The overall analytical accuracy is about $\pm 2\%$. The electrons give rise to a continuous X-ray spectrum (background signal) limiting the discernibility of small peaks. A typical detection limit which can be obtained by SEM-EDS is about 1000 ppm (by weight) [79].

III. AESEC technique and other experimentations

In this work, material surface before and after corrosion reaction was characterized by SEM using a Gemini 1530 microscope with field emission gun (FEG) source at 15 keV, 15 mm working distance. For EDS coupled with SEM, a Si(Li) detector and Quantax™ software (broker AXS) was used to evaluate the surface composition.

3.6.2. Raman spectroscopy

Raman spectroscopy has proven a useful technique to identify corrosion products [61,80,81] When monochromatic incident radiation from the laser beam strikes the sample surface, it interacts with the molecules of sample light is scattered in all directions. Most of the scattered light has the same frequency as the incident radiation which is called Rayleigh scattering. However, some of the scattered light will have a frequency shift from that of the incident light due to inelastic scattering. It is this inelastically scattered radiation that is used to construct Raman spectra. This radiation is referred to as Stokes or anti-Stokes lines corresponding to a frequency loss or a frequency gain. In contrast to atomic emission spectroscopy, Raman spectra of solid species occur usually as intensity peaks over a broad frequency range, referred to as a band. The polarizability caused by molecular vibration is needed to obtain a Raman spectrum. **Fig. 3.12** shows a schematic description of a Raman spectrum.

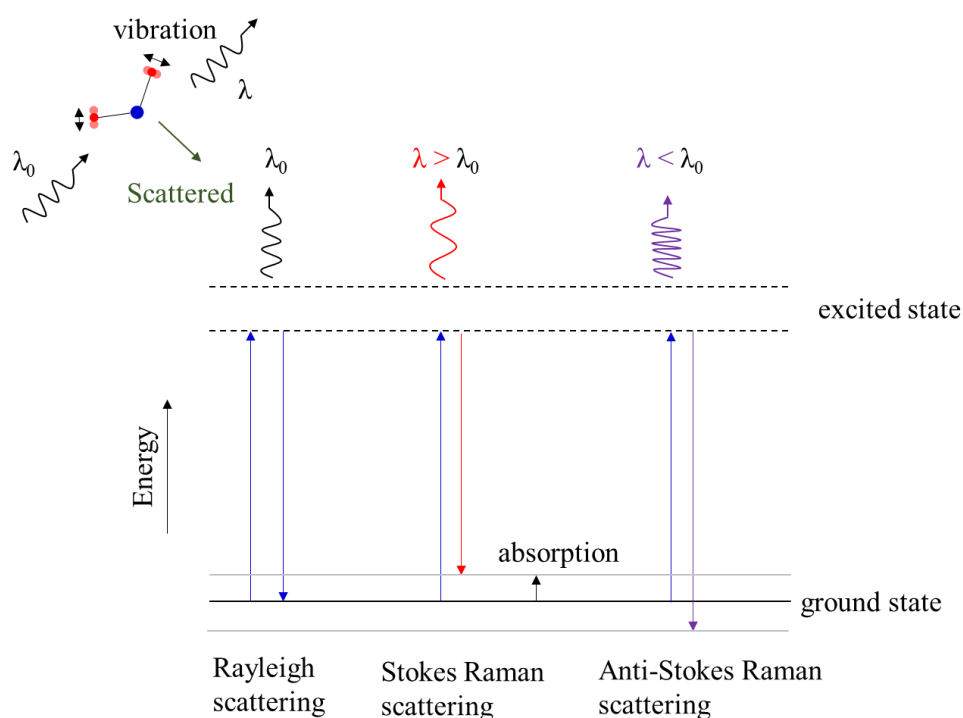


Fig. 3.12. Basic principle of Raman spectroscopy.

Raman spectrometry was performed using a Renishaw InviaTM confocal Raman microscope with excitation by a Co diode pumped solid state (DPSS) using a green laser (532 nm, 100 mW). The objectives with magnification factors of x5, x20, x50 and x100 were used. Spectral acquisition time was in the range of 1s to 10 s with more than 30 accumulations. The acquisition and evaluation of Raman spectra was performed by using WireTM software.

3.6.3. X-ray diffraction (XRD)

X-ray diffraction is a widely used rapid analytical technique mainly for identifying the phases of a crystalline material. The X-rays are generated by a cathode ray tube then filtered to supply a monochromatic radiation. A constructive interference only occurs when it satisfies Bragg's law ($n\lambda = 2d_{hkl} \sin \theta$) for parallel planes of atoms with a space d_{hkl} between the planes as shown in **Fig. 3.13**. The incident X-ray with an angle of θ collimates directly to the surface of the sample. Consequently, the beams are separately reflected by the atomic planes with a distance of d_{hkl} between diffracting planes of atoms. In the diffractometer, the X-ray wavelength is fixed, as a consequence, a series of atomic planes produce a diffraction peak only at a specific angle θ . By scanning with a range of 2θ , all possible directions of diffracted X-rays from the sample lattice should be obtained.

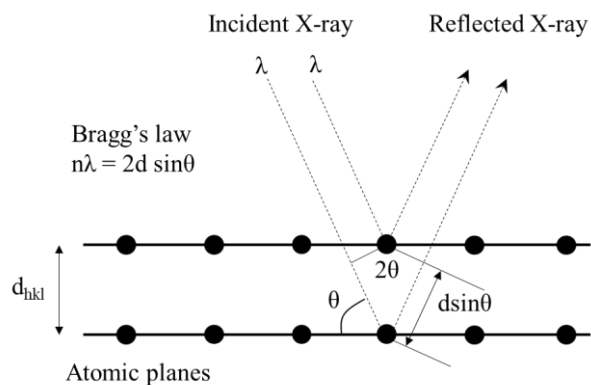


Fig. 3.13. Basic principle of X-ray diffraction with Bragg's law.

In this work, the XRD measurement was performed to identify phases in the alloy coatings and pure phase intermetallic and to characterize corrosion products after electrochemical experiments. A PANalytical X'Pert Pro diffractometer was used with Cu($K\alpha_1$) radiation ($\lambda=1.5418 \text{ \AA}$) directly on the specimen with the size of 20 mm x 20 mm. the angular resolution was 0.02° over the angular range of $5-80^\circ$ (2θ) with 0.5 seconds acquisition time. The identification of the data was performed by the HighScore PlusTM software package with JCPDS (ICDD) database files (version 2013).

Chapter IV:

Dealloying of MgZn₂ intermetallic in slightly alkaline chloride electrolyte and its significance in corrosion resistance.

«C'est le temps que tu as perdu pour ta rose qui rend ta rose importante.»

'It is the time you have wasted for your rose that makes your rose so important'

Le petit prince (1943),

Antoine de Saint-Exupéry

The content of this chapter repeats the article: “Editors’ choice: Junsoo Han and Kevin Ogle, Dealloying of MgZn₂ intermetallic in slightly alkaline chloride electrolyte and its significance in corrosion resistance, *Journal of The Electrochemical Society*, **164** (14) C952-C961 (2017)”, published in November 2017.

4. Dealloying of MgZn₂ intermetallic in slightly alkaline chloride electrolyte and its significance in corrosion resistance.

Abstract

The role of dealloying in the corrosion resistance of MgZn₂ has been investigated for the first time. The elemental dissolution kinetics of a synthetic, nominally pure MgZn₂ intermetallic compound was investigated and compared with pure Mg and Zn in 30 mM NaCl with pH=10.1. Atomic emission spectroelectrochemistry was used to monitor Zn and Mg dissolution as a function of time at open circuit, during linear scan polarization, and at various applied potentials. Zn and Mg displayed a mutual inhibitive effect at open circuit which was explained by the formation of Mg depleted Zn/Zn oxide film. Polarization experiments revealed a Type II dealloying mechanism in which Zn and Mg dissolve simultaneously and congruently above the critical potential, E_c , while preferential Mg dissolution dominates below E_c . Preferential Mg dissolution leads to the formation of a Mg-depleted metallic Zn layer which suppresses further Mg dissolution. In O₂ saturated electrolyte, O₂ reduction was the major cathodic reaction on Zn but was completely inhibited on Mg. The intense cathodic reduction of O₂ on Zn led to a cathodic dissolution of Zn, probably due to the increased interfacial pH.

Keywords: magnesium, zinc, pure phase alloy, dealloying

4.1. Introduction

The alloys of Zn, Mg and Al have shown a significantly improved atmospheric corrosion resistance as compared to conventional Zn coatings when used as coating materials for galvanized steel [6,9,14,26,29,32,82]. The enhanced corrosion performance has been investigated in terms of chemical composition, microstructure, and the nature of corrosion products in an effort to understand the origin of the improved corrosion resistance. Chemical composition is very important due to the very different and complementary chemical and electrochemical behavior of the three components as a function of pH. **Fig. 4.1** gives the calculated saturation concentrations of the three cations as a function of pH at T=25 °C with the dominant solid species of each cation shown above the graph. It is seen with the three elements together, at least one insoluble species dominates over a much wider pH range than would be the case for any component alone. At neutral pH, Al³⁺ is highly insoluble, forming primarily Al(OH)₃, rendering the Al surface passive. However, it becomes active in even mildly alkaline electrolytes. Zn²⁺ has similar behavior, forming Zn(OH)₂, but the saturation concentration vs. pH curve is shifted to higher pH with a minimum solubility around pH=10 and a relatively high solubility at neutral pH. Mg oxidation products are soluble as Mg²⁺ throughout the neutral range but the highly insoluble Mg(OH)₂ is formed for pH > 10. The presence of the three alloying components assures that at least one insoluble species will be dominant from neutral to alkaline pH. The nature of the corrosion products will depend upon the interfacial pH which may be altered with respect to the original electrolyte by hydroxide formation from the cathodic reaction, or H⁺ ions formed by hydrolysis of cations released in the anodic reaction.

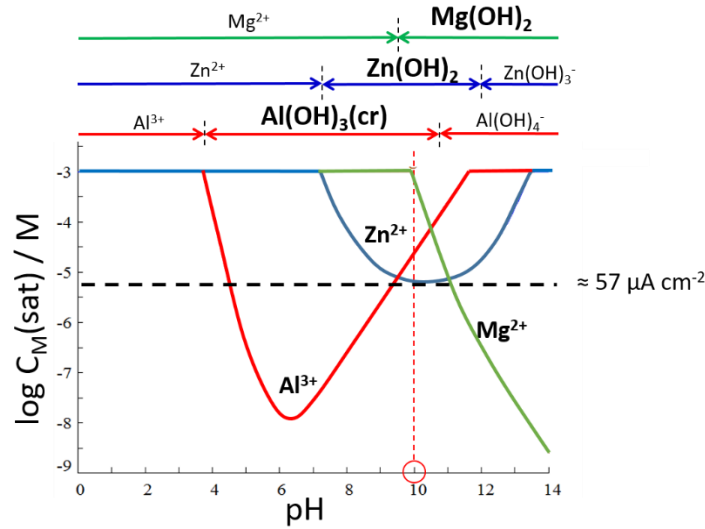


Fig. 4.1. $C_M(\text{sat})$ of Zn^{2+} , Al^{3+} and Mg^{2+} in pure water calculated by Hydra Medusa software (version 7.1) using the default database. The arrows above the curve indicate the predominant species in each pH range. The precipitated solid phase is indicated in bold. The metal ion complexes considered included the following soluble species: $\text{Al}(\text{OH})_2^+$, $\text{Al}(\text{OH})_3$, $\text{Al}(\text{OH})_4^-$, $\text{Al}_{13}\text{O}_4(\text{OH})_{24}^{7+}$, $\text{Al}_2(\text{OH})_2^{4+}$, $\text{Al}_3(\text{OH})_4^{5+}$, AlOH^{2+} , $\text{Mg}_4(\text{OH})_4^{4+}$, MgOH^+OH^- , $\text{Zn}(\text{OH})_2$, $\text{Zn}(\text{OH})_3^-$, $\text{Zn}(\text{OH})_4^{2-}$, $\text{Zn}_2(\text{OH})_6^{2-}$, $\text{Zn}_2\text{OH}^{3+}$, $\text{Zn}_4(\text{OH})_4^{4+}$, ZnOH^+ ; and insoluble species: $\text{Al}(\text{OH})_3(\text{am})$, $\text{Al}(\text{OH})_3(\text{cr})$, $\text{AlOOH}(\text{cr})$, $\text{Mg}(\text{OH})_2(\text{s})$, $\text{MgAl}_2\text{O}_4(\text{cr})$, $\text{MgO}(\text{cr})$, $\text{Zn}(\text{OH})_2(\text{s})$, $\text{ZnO}(\text{cr})$.

The role of corrosion product films as diffusion barriers or inhibitors has been emphasized by many authors [22,25,26,28,29,33,34]. The improved corrosion stability of the Zn-Mg alloy has been attributed to the formation of a compact simonkolleite ($\text{Zn}_5(\text{OH})_8\text{Cl}_2 \cdot \text{H}_2\text{O}$) layer, on the Zn-Mg coating serving as a barrier to oxygen diffusion [22,29]. Further, it has been suggested that the precipitation of alkali-resistant $\text{Mg}(\text{OH})_2$ is responsible for the reduced oxygen activity at the Zn cathode. Schürz et al. [26] measured surface corrosion products on Zn-Al-Mg coated steel after a salt spray test. They found that on the Zn-Al-Mg alloy coating, a stable protective film of $\text{Zn}_6\text{Al}_2(\text{CO}_3)(\text{OH})_{16} \cdot 4\text{H}_2\text{O}$ layer decreased further corrosion on the surface. Duchoslav et al. [28] surveyed the evolution of corrosion products on the surface of Zn-2 wt.% Al-2 wt.% Mg hot-dip galvanized alloy during short term exposure to standardized salt spray test. It was concluded that a rapid formation of layered double hydroxides (LDHs) stabilized the surface pH and hindered further surface alkalization as compared to the standard Zn coating during the initial corrosion attack. Salgueiro Azevedo et al. [34] analyzed the corrosion products formed on hot dip galvanized steel, Zn-0.2 wt.% Al alloy coating and Zn-3.7 wt.% Al-3.0 wt.% Mg alloy coating in 0.171 M NaCl solution and synthetic rain water. In their model, the presence of Mg^{2+} ions delayed the transformation of basic zinc salts (BZS) to

ZnO during the cathodic polarization. Otherwise, this transformation would have resulted in a loss of inhibiting effect.

The electrochemistry of the Zn-Al-Mg system is further complicated by the distribution of the elements into a complex, multi-phase structure. Galvanic coupling between phases should vary as different elements become active or passive depending on the environment and history of the sample. MgZn₂ is believed to be the most corrosive phase in Zn-Mg and Zn-Al-Mg alloy [8,11,13,21,50]. Sullivan et al. [21] visualized the preferential corrosion of MgZn₂ and Mg₂Zn₁₁ phases in Zn-Al-Mg alloy by time lapse optical microscopy. They found that the corrosion of Zn-(1-2) wt.% Mg-(1-2 wt.% Al) alloy coating initiated in the binary and ternary eutectic regions within the microstructure of the alloy with preferential dealloying of MgZn₂.

Prosek et al. [9,13,23] investigated the effect of microstructure on the corrosion of Zn-Al and Zn-Al-Mg alloys, focusing on the protective mechanism of Mg in Zn alloy during atmospheric exposure with NaCl contamination. They tested a series of compositions from 1 to 32 wt. % Mg in Zn alloy coating including various phases such as η -Zn, Mg₂Zn₁₁ and MgZn₂. They found that a superior corrosion stability of 4-8 wt.% Mg specimens containing the Mg₂Zn₁₁ and MgZn₂ phases by forming protective Mg-based film. Also, they demonstrated that the positive effect of Mg disappeared with increasing content of Mg in the alloy caused by a corrosion potential shift to the cathodic direction which enables the water reduction. More recently, they produced a series of Zn-Al and Zn-Al-Mg alloys with different microstructure by changing the cooling rate. The finer microstructure showed better corrosion stability probably due to the rapid blocking of the cathodic sites by precipitation of protective corrosion products and a more uniform pH/potential distribution [13].

The open circuit potential and breakdown/corrosion potential of the MgZn₂ intermetallic phase in a neutral/alkaline chloride containing electrolyte was investigated by Ramgopal et al. [50]. It was concluded that the MgZn₂ intermetallic phase was very active in neutral 0.5 M NaCl electrolyte (open circuit potential, $E_{oc} = -1400$ mV vs. SCE) and the breakdown potential of -1140 mV vs. SCE was associated with Zn dealloying. They also investigated the effect of adding Cu (0, 4, 8, 18 and 27 atom %) and Al (0, 4 and 10 atom %) to simulate the composition of precipitates commonly found in Al alloys.

B. Li et al. [8] concluded that adding 2 wt.% Mg to the Zn-Al-Mg coating can effectively inhibit the grain boundary corrosion during immersion tests in 5 wt.% NaCl solution. S. Li et al. [11] added 0.5, 1.5 and 2.5 wt.% Mg in the GalvalumeTM (Zn-55 wt.% Al-1.6 wt.% Si) to

IV. Dealloying of MgZn₂ phase

see the change of the microstructure and its effect on the corrosion behavior. They concluded that Mg improved the compactness of the corrosion products and enhanced the corrosion resistance of the Zn-rich inter-dendritic area of GalvalumeTM coating by forming MgZn₂ phase. The MgZn₂ phase contributed to delay the occurrence of localized corrosion in Al-Zn-Si-3Mg alloy by the weight loss test conducted by Liu et al. [83].

The major unresolved question is how to interpret the interaction of the three alloying elements? Is the effect of composition “simply” an effect of different elements interacting with one another via their unique chemistry and the nature of the corrosion products formed, or does the microstructure itself play a dominant role? In this work, our aim is to understand the dealloying mechanism of the binary MgZn₂ intermetallic, the most reactive phase in the Zn-Mg-Al system. Slightly alkaline chloride containing solution (30 mM NaCl, pH=10.1) was chosen because it has been demonstrated that the interfacial region usually becomes slightly alkaline during the corrosion of galvanized steel in a non-buffered electrolyte [84,85].

4.2. Experimental

Materials

The materials used in this work consisted of reference metals and nominally pure synthetic MgZn₂ intermetallic phase. Zn (99.998 %) and Mg (99.9 %) were obtained from *Goodfellow*. Nominally pure MgZn₂ (Zn-16 wt.% Mg) intermetallic phase was produced and characterized by the *Department of Metals and Corrosion Engineering, University of Chemistry and Technology in Prague*. The MgZn₂ intermetallic phase was produced by heating a mixture of pure metals in furnace with Ar protective atmosphere to prevent oxidation of Mg. The mixture composition before heating had to be optimized based on chemical composition of the castings due to Mg vaporization. Liquid alloy was also filtered through a frit and cast into a 50 mm diameter metal mold. MgZn₂ intermetallic phase was ground in a ball-mill, then fraction 25-45 μm powder was sintered by spark plasma sintering (SPS) method at 550 °C. X-ray diffraction (XRD) and electron backscatter diffraction (EBSD) indicated a single MgZn₂ intermetallic phase.

Prior to atomic emission spectroelectrochemistry (AESEC) experiments, the specimens were degreased by ethanol in the ultrasonic bath for 10 minutes and dried by N₂ gas. The sample surface was ground with emery paper (Si-C; P1200, P2400 and P4000) under ethanol and dried

IV. Dealloying of MgZn₂ phase

by flowing N₂. After the drying process, the sample was stored for 20-24 hours in a humidity chamber with 50 % relative humidity obtained from a water reservoir saturated with Mg(NO₃)₂·H₂O. All the experiments presented in this work were repeated at least three times and showed good reproducibility.

All electrolytes were prepared from analytical grade materials and deionized water of 18.2 MΩ cm obtained via a MilliporeTM system. A low concentration chloride solution, 30 mM NaCl, was prepared to minimize the effect of chloride-containing corrosion products. The final pH was adjusted to 10.1 by NaOH. The electrolyte was not buffered to avoid complications due to the anion of the buffer and to more accurately represent field conditions. The electrolyte was either deaerated by bubbling Ar for 20–30 minutes prior to the experiment and maintained by flowing Ar above the electrolyte during the experiment, or saturated with O₂ using the same procedure with pure O₂ (Air Liquide, SA, 100% O₂ compressed gas). The objective of deaeration is to reduce the cathodic current so as to better correlate the elemental dissolution rates with anodic current. The pH=10.1 was chosen as an intermediate pH where all three elements showed some solubility. Such pH values may easily be reached during the corrosion of galvanized steel for example on the cut edge where the cathodic and anodic reactions are in close proximity [7,84–86].

The AESEC technique

The specimen of interest serves as the working electrode in a small volume three electrode electrochemical flow cell. Elements released from the working electrode are transported to an Ultima 2CTM Horiba Jobin-Yvon inductively coupled plasma atomic emission spectrometer (ICP-AES) equipped with a Paschen-Runge polychromator (focal length 0.5 m) using an array of thirty photomultipliers for the simultaneous analysis of different elements and a monochromator (focal length 1 m) to measure a single element with higher spectral resolution. In this work, the time resolved concentration of Zn and Mg were determined from the emission intensity of the plasma monitored at 213.86 and 279.55 nm wavelength respectively, using standard ICP-AES calibration techniques.

A Gamry Reference 600TM potentiostat was used to control and measure the electrochemical potential and current. Conventional polarization experiments were performed to characterize the dissolution rate vs. applied potential characteristic curve using a linear potential sweep of 0.5 mV s⁻¹ scan rate from cathodic (-1.80 V vs. SCE) to anodic potential (-0.50 V vs. SCE).

4.3. Results

4.3.1. Open circuit dissolution

The improved corrosion resistance of MgZn₂ as compared to pure Zn and Mg may be observed in the spontaneous reactivity of the metals. This is demonstrated by the AESEC dissolution profiles (**Figs. 4.2~4.4**) where the elemental dissolution rates expressed as current densities (j_{Zn} and j_{Mg}) and the open circuit potential (E_{oc}) are given as a function of time during the exposure of the specimens to the electrolyte. The exposure began at $t = 0$, indicated by the vertical dashed line in **Figs. 4.2~4.4**. For $t < 0$, the cell was dry and the electrolyte bypassed the cell and was fed directly into the ICP-AES to measure the background emission signal, I_{λ}° , in **Eq. 3.3**. Not shown is a third period in which the background was measured again to verify that no change had occurred during the experiment due to plasma instability.

The dissolution profiles of nominally pure Mg (99.9 %) and Zn (99.998 %) show very different reactivities. Mg dissolution (**Fig. 4.2**) began immediately on contact with the electrolyte and j_{Mg} passed through a maximum ultimately obtaining a steady state dissolution rate of about $92 \mu\text{A cm}^{-2}$. Saturating the electrolyte with O₂ had no significant effect on the dissolution rate indicating that the primary cathodic reaction was water reduction. The open circuit potential was -1.65 V and shifted by about +20 mV in the presence of O₂.

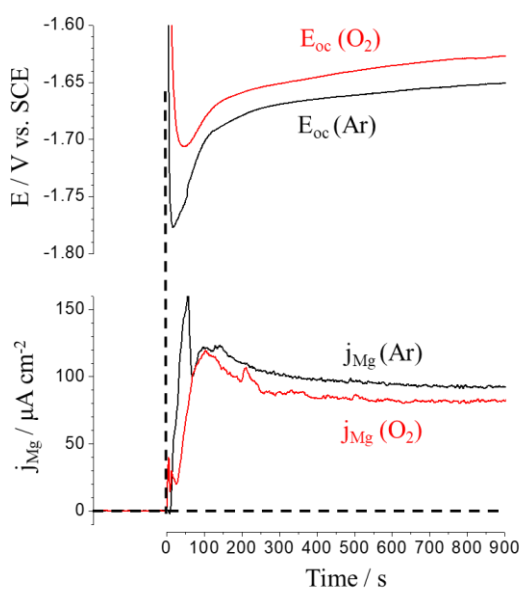


Fig. 4.2. Spontaneous elemental current densities and open circuit potentials of Mg metal exposed to a 30 mM NaCl, pH=10.1 electrolyte with Ar deaeration and O₂ saturation at T=25 °C.

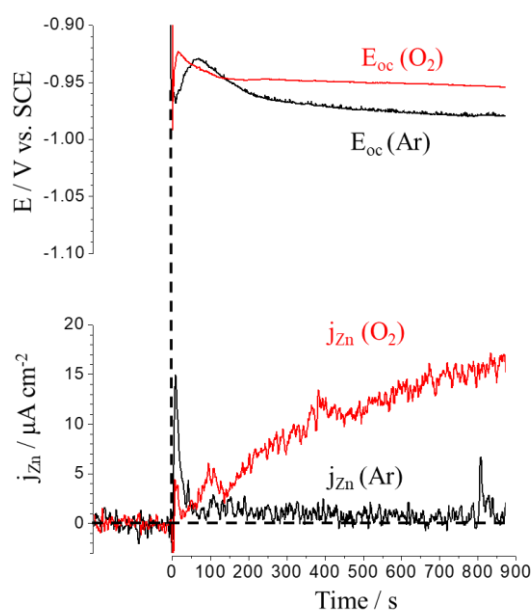


Fig. 4.3. Spontaneous elemental current densities and open circuit potentials of Zn metal exposed to a 30 mM NaCl, pH=10.1 electrolyte with Ar deaeration and O₂ saturation at T=25°C.

The dissolution of Zn metal (**Fig. 4.2**), by contrast, demonstrated a very low dissolution rate in the absence of O₂, around 0.7 μA cm⁻². In O₂ purged electrolyte, j_{Zn} rose slowly approximately 17 μA cm⁻² after 900 s, although a steady state had not been obtained and j_{Zn} was still rising at the end of the experiment. It is evident that O₂ reduction is the major cathodic reaction in Zn dissolution. From **Fig. 4.1**, the calculated saturation concentration of Zn²⁺ at pH=10.1 is 6.3 x 10⁻⁶ M equivalent to approximately 57 μA cm⁻² by **Eq. 3.4**, higher than the measured value. The open circuit potential was -0.98 V in the absence of O₂, and shifted about +30 mV under saturation O₂.

The dissolution profile of MgZn₂ shows a radically different behavior as presented in **Fig. 4.4**. A sharp dissolution peak of Mg was observed at early times reaching 42 μA cm⁻². However, j_{Mg} dropped off quickly to obtain a steady state of about 2.2 μA cm⁻². Zn dissolution was hardly detectable above the detection limit in O₂ saturated electrolyte. However a very slight Zn dissolution rate, corresponding to about 0.1 μA cm⁻² equivalent current, was detectable under Ar. O₂ saturation had essentially no effect on the dissolution rate again suggesting that water reduction was the major cathodic reaction for the intermetallic. The Mg dissolution peak correlates with a dip in the open circuit potential indicating that the peak was due to the dissolution of the metal rather than pre-existing oxides. Integration of the peak yields approximately 34 nmol Mg cm⁻² which would correspond to 9 nm of Mg(OH)₂ assuming a

IV. Dealloying of MgZn₂ phase

uniform distribution with the normal density of 2.34 g cm⁻³, which is probably thick for an oxide film formed under the conditions of the constant humidity exposure used here.

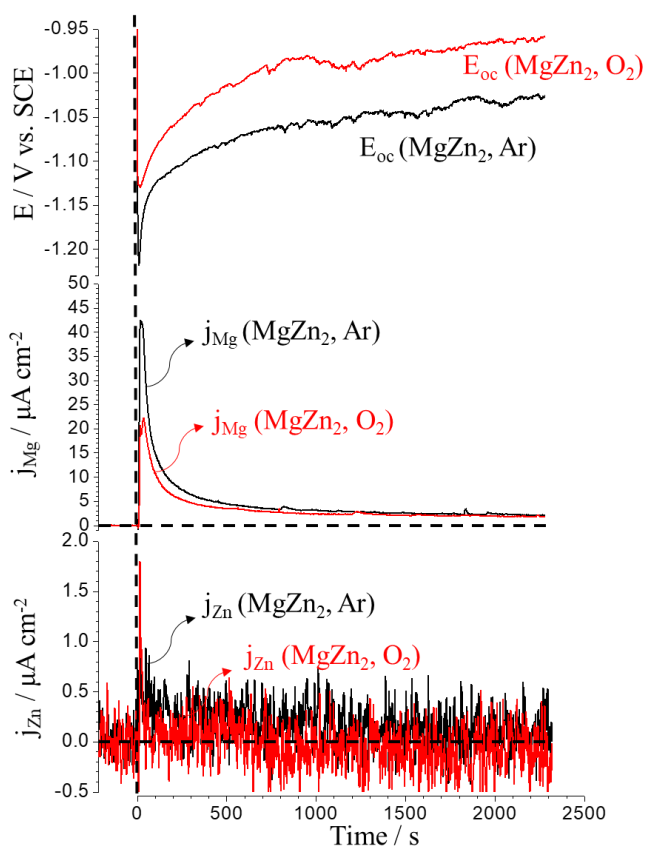


Fig. 4.4. Spontaneous elemental current densities and open circuit potential of MgZn₂ intermetallic exposed to a 30 mM NaCl, pH=10.1 electrolyte with Ar deaeration and O₂ saturation at T=25°C.

The results presented here are consistent with the following mechanism. The presence of Mg in the MgZn₂ intermetallic pulls the potential of the system to below the dissolution potential of Zn so that there is a significant preferential dissolution of Mg at early times. This leaves behind a Zn-rich surface layer consisting of metallic Zn which grows progressively with time. This is indicated by the increase of the open circuit potential which approaches but does not reach the potential of pure Zn. The dealloyed layer inhibits Mg dissolution explaining the rapid decrease of j_{Mg} with time. However, Mg remains sufficiently in contact with the electrolyte to obtain a steady state Mg dissolution rate and maintain the open circuit potential below the potential of Zn dissolution. In this way, both the Zn and the Mg dissolution rates are below those obtained for pure Zn and Mg metals. In **Table 4.1**, the average spontaneous elemental dissolution rates (j_M^s) and E_{oc} of Zn, Mg metals and MgZn₂ intermetallic are summarized.

IV. Dealloying of MgZn₂ phase

Table 4.1. Comparison between the average spontaneous dissolution rates, j_{M}^s , and open circuit potential (E_{oc}) of Zn, Mg metal and MgZn₂ intermetallic phase at spontaneous corrosion condition at pH=10.1, 30 mM NaCl with Ar deaeration and O₂ saturation at T=25°C.

$\mu\text{A cm}^{-2}$	j_{Zn}^s		j_{Mg}^s		E_{oc} / V	
	Ar	O ₂	Ar	O ₂	Ar	O ₂
Zn metal	0.7 ± 0.6	16.9 ± 0.8	-	-	-0.98	-0.95
Mg metal	-	-	92.5 ± 0.5	82 ± 1	-1.65	-1.63
MgZn ₂	0	0	2.2 ± 0.1	1.70 ± 0.04	-1.06	-0.98

4.3.2. Polarization curves of Mg and Zn

The corrosion potential is an easily accessible parameter which reflects the electrochemical activity at the metal / solution interface. In order to correctly interpret the corrosion potential, however, it is necessary to know how the Zn and Mg dissolution rates vary with potential. The AESEC linear sweep voltammetry (AESEC-LSV) curves of Mg metal in 30 mM NaCl, pH=10.1 electrolyte with either an Ar deaerated or an O₂ saturated are shown in **Figs. 4.5A and 4.5B** respectively. Mg dissolution occurred across the entire potential domain, rising by two orders of magnitude between $E = -1.70 \text{ V}$ and -0.50 V . Note that the initial decrease observed at the beginning of the potential sweep was due to Mg that dissolved during the open circuit exposure. Above $E = -1.40 \text{ V}$ the increase in j_{Mg} with E was exponential. The good agreement between j_{Mg} and j_e^* (at $E = -0.60 \text{ V}$, $\eta = j_{\text{Mg}}/j_e^* = 1.14$ and 1.02 under Ar deaeration and O₂ saturation respectively) demonstrates that Mg dissolution was faradaic with $n=2$ and that oxide formation was negligible. The slight deviation observed under Ar deaeration at $E = -0.60 \text{ V}$ ($\eta=1.14$) could be due to an anodically enhanced cathodic reaction (NDE, or negative difference effect) [77,87–91]. The relatively sluggish increase of j_{Mg} with potential suggests that Mg dissolution occurred across an oxide/hydroxide film in this electrolyte. As j_e^* and j_{Mg} in both electrolyte conditions show almost identical polarization behavior, the effect of O₂ on Mg metal dissolution may be considered negligible.

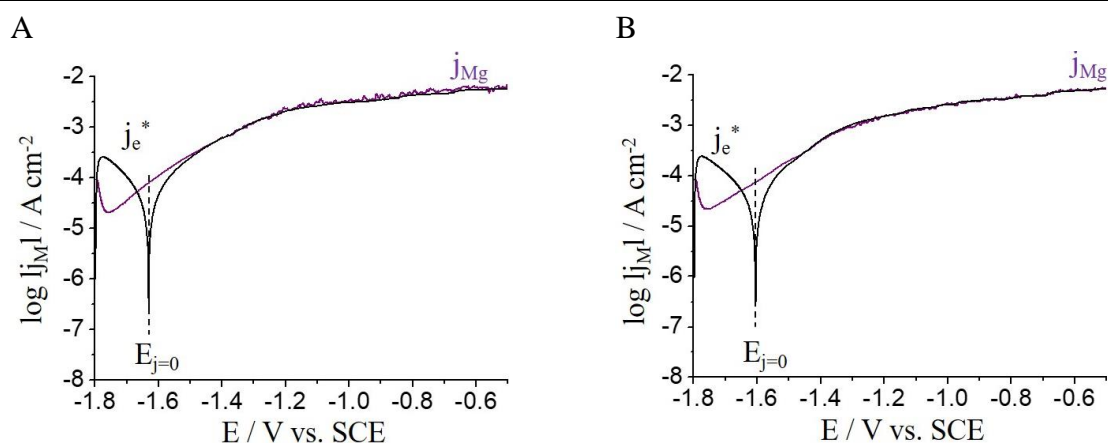


Fig. 4.5. Elemental AESEC polarization curves of Mg metal exposed to **A:** Ar deaerated and **B:** O₂ saturated electrolytes at pH=10.1, 30 mM NaCl at T=25°C.

The AESEC polarization curves of Zn metal in 30 mM NaCl, pH=10.1 electrolyte are shown under Ar deaeration and O₂ saturation (**Figs. 4.6A** and **4.6B**, respectively). The onset potential of Zn dissolution, E_c^{Zn} , occurred around -1.10 V. However j_e^* became positive at a lower potential of -1.21 V, the zero current potential, $E_{j=0}$. For $-1.21 \text{ V} < E < -1.10 \text{ V}$, an anodic peak is clearly visible in j_e^* which shows no corresponding elemental dissolution peak in j_{Zn} . Therefore, this peak must correspond to the formation of a slowly dissolving Zn oxide or hydroxide film. Further, $j_e^* > j_{Zn}$ throughout much of the anodic domain although they approach each other being approximately equal ($\eta = 0.97$ at -0.60 V) at the end of the sweep. The effective Tafel slope of Zn dissolution determined from j_{Zn} was 71 mV decade⁻¹, larger than other measurements conducted in more alkaline media (pH > 12) by the AESEC technique (41-48 mV decade⁻¹) [92–94].

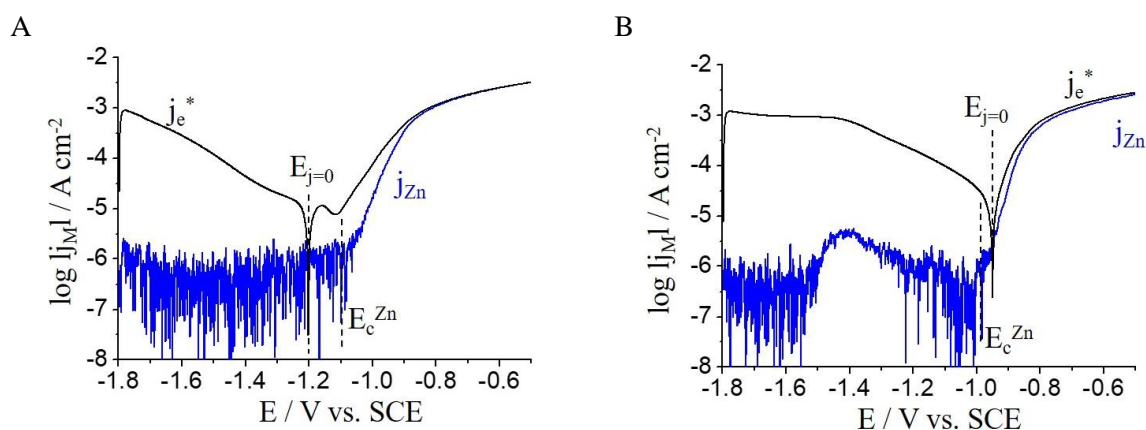
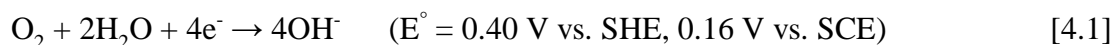


Fig. 4.6. AESEC-LSV of Zn metal exposed to **A:** Ar deaerated and **B:** O₂ saturated electrolytes at pH=10.1, 30 mM NaCl solution at T=25 °C.

Saturating the electrolyte with O₂ (**Fig. 4.6B**) dramatically increased the cathodic reaction, completely masking the oxide formation peak observed with Ar deaeration at -1.14 V (**Fig. 4.6A**). Nevertheless, $j_e^* > j_{Zn}$ throughout the potential sweep, with $\eta=0.88$ at the end of the experiment indicating that oxide formation is favored and apparently more extensive than under anaerobic conditions. The Tafel slope of Zn dissolution in O₂ saturated electrolyte was 45 mV decade⁻¹, similar to that obtained in more alkaline solution (pH > 12), suggesting that the interfacial pH in O₂ saturated electrolyte could increase to near 12 due to the O₂ reduction during the cathodic polarization.

For both Zn and Mg metals, the anodic dissolution was nearly faradaic taking into account that the oxidation states of Zn and Mg are 2. This is an important result in that it confirms the accuracy of the method. Therefore, when $\eta < 1$ we can assume that the difference is due to the formation of slowly dissolving oxide products.

The AESEC technique may detect anodic reactions that occur during the cathodic polarization, even if completely masked by a large cathodic current [66]. This is the case for the Zn dissolution peak observed in j_{Zn} at -1.40 V in **Fig. 4.6B**. This peak becomes visible in the polarization curve in the presence of O₂ despite a cathodic current that is nearly two orders of magnitude more intense. This ‘‘cathodic dissolution’’ of Zn may be due to the increase of the interfacial pH due to O₂ reduction via **Reaction 4.1**. The formation of the Zn(OH)₄²⁻ complex will shift the potential to more negative values [95].



To verify the stability of the dissolution reaction at -1.40 V, chronoamperometric (CA) experiments were conducted. The dissolution profiles associated with a potential step directly to -1.40 V in Ar deaerated and O₂ saturated electrolytes are shown in **Fig. 4.7**. In O₂ saturated electrolyte, the dissolution rate of Zn increased to $3.7 \pm 0.7 \mu\text{A cm}^{-2}$ while j_e^* was $-680 \mu\text{A cm}^{-2}$. By comparison, with an Ar deaerated electrolyte, j_e^* was $-3.5 \mu\text{A cm}^{-2}$, a factor of 200 less, and no Zn dissolution was detected. These results confirm that the cathodic dissolution of Zn is linked to excess hydroxide ions caused by the O₂ reduction.

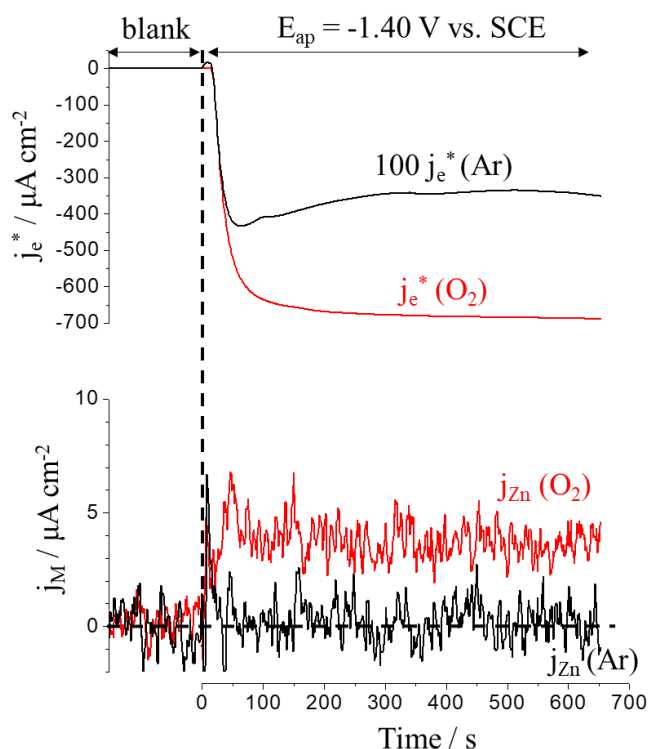


Fig. 4.7. AESEC-CA of Zn metal exposed to a pH=10.1, 30 mM NaCl electrolyte at 25°C, at $E_{ap} = -1.40$ V.

4.3.3. Polarization curves of MgZn₂

Fig. 4.8A gives the elemental polarization curve for MgZn₂ with Ar deaeration. Mg and Zn dissolution both increased sharply and simultaneously at $E = -0.96$ V. For Zn, the elemental polarization curve was very similar to that obtained for the pure metal, however E_c was shifted anodically by about +0.14 V. Also, the onset was much sharper, showing a Tafel slope of 20 mV decade⁻¹ as compared with 71 mV decade⁻¹ for pure Zn. The elemental polarization curve for Mg dissolution was, however, radically altered with respect to pure Mg. For $E < E_c = -0.96$ V, Mg dissolution from MgZn₂ was two orders of magnitude lower than for pure Mg. With Ar deaeration, Mg dissolution rate was nearly constant with potential ($j_{Mg} = 4.1 \mu\text{A cm}^{-2}$), until the potential of Zn oxide formation ($E = -1.21$ V) was obtained, at which point it dropped by half an order of magnitude ($j_{Mg} = 1.2 \mu\text{A cm}^{-2}$ at -1.14 V).

The simplest interpretation of these results is that below E_c for simultaneous Zn and Mg dissolution, Mg dissolution is inhibited by a residual film of Mg-depleted Zn metal/Zn oxide as proposed in the previous section. The inhibitive effect is enhanced in the potential range where oxide formation occurs. A very slight increase in the Zn dissolution rate was also observed in this potential range although it remained below $1 \mu\text{A cm}^{-2}$. Once the Zn dissolution potential is reached, however, fresh MgZn₂ would be exposed. The results of **Fig. 4.8** show that, above E_c ,

IV. Dealloying of MgZn₂ phase

Zn and Mg dissolution were instantaneous with approximately a 90 % faradaic yield with $\eta = 0.88$ and 0.93 at $E = -0.60$ V in Ar deaerated and O₂ saturated electrolytes respectively. In this potential domain, nearly congruent dissolution was observed as the elemental dissolution ratio between Zn and Mg ($j_{\text{Zn}}/j_{\text{Mg}}$) is 1.8 and 1.9 with Ar deaeration and O₂ saturation respectively, close to its bulk composition, Zn/Mg=2.

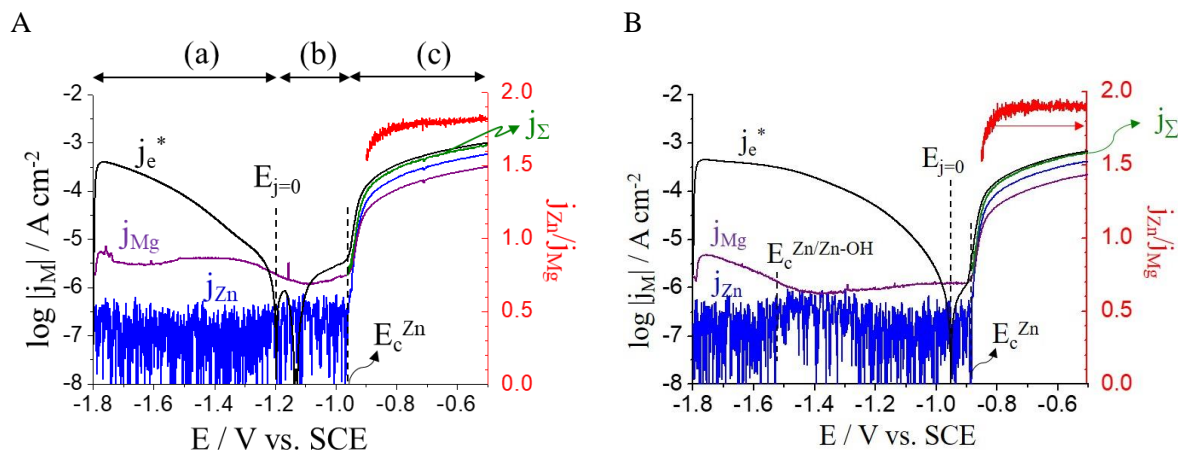


Fig. 4.8. AESEC-LSV of MgZn₂ intermetallic in **A:** Ar deaerated and **B:** O₂ saturated electrolytes at pH=10.1, 30 mM NaCl solution at T=25°C. The elemental current density ratio ($j_{\text{Zn}}/j_{\text{Mg}}$) is shown in the second y-axis in the anodic polarization domain. Three potential domains are indicated as (a), (b) and (c) for dealloying model in **Fig. 4.15**.

The effect of O₂ saturation, shown in **Fig. 4.8B**, was similar to that observed for pure Zn. Prior to the Zn/Mg onset potential ($E_c^{\text{Zn}} = -0.88$ V), the Zn oxide formation peaks were masked by the intense cathodic current. The anodic shoulder however appears just below E_c^{Zn} of Zn/Mg. The latter is shifted anodically by +0.08 V as compared to Zn metal ($E_c^{\text{Zn}} = -0.96$ V). As before, Zn and Mg dissolved simultaneously with a very low Tafel slope giving the same value as for the Ar deaerated electrolyte (20 mV decade⁻¹). The cathodic Zn dissolution peak, identified at $E = -1.40$ V was also clearly observed. Mg dissolution dropped off rapidly obtaining 1.1 $\mu\text{A cm}^{-2}$ at -1.5 V and remained at this level until the rapid onset potential is obtained.

4.3.4. MgZn₂ chronoamperometric (CA) experiments

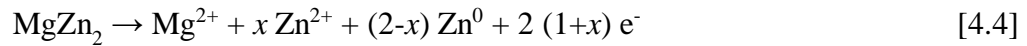
The elemental polarization curves of **Fig. 4.8** demonstrate that different dissolution mechanisms of the MgZn₂ dominate in different potential domains. These domains include a) cathodic domain, -1.80 V < E < $E_{j=0}$; b) oxide formation domain, $E_{j=0}$ < E < E_c^{Zn} ; c) anodic domain, E_c^{Zn} < E < -0.50 V. Chronoamperometric (CA) experiments were conducted at three

IV. Dealloying of MgZn₂ phase

constant potentials, $E_{ap} = -1.40$ V, -1.14 V and -0.80 V corresponding to the three domains, as shown in **Figs. 4.9~4.11**. The potential step was applied within seconds of electrolyte contact so as to avoid dealloying or corrosion product formation at the open circuit potential.

Cathodic dissolution at $E_{ap} = -1.40$ V

The kinetics of dissolution in the cathodic domain were measured as elemental dissolution profiles following a potential step from open circuit to -1.40 V, in Ar deaerated (**Fig. 4.9A**) and O₂ saturated electrolyte (**Fig. 4.9B**). In the absence of O₂, j_{Zn} was below the detection limit while j_{Mg} was initially intense but dropped off in a sigmoidal fashion with time. The electrical current (j_e^*) also decreased in intensity during this period. As previously mentioned, the apparent inhibition of Mg dissolution observed for the MgZn₂ intermetallic may be attributed to the existence of a Mg depleted layer of metallic Zn and/or Zn oxide/hydroxide. Given the negative potential, it is reasonable to assume that Zn oxide makes a negligible contribution. The thickness of a hypothetical Mg depleted layer, δ_{Zn} , may be estimated by a mass balance from the total amount of Zn, Q_{Zn} . The overall dissolution reaction is given by **Eq. 4.4**:



where x is dissolved Zn in moles. Assuming that the resulting film is pure Zn metal, Zn(0), uniformly distributed on the surface, a mass balance yields:

$$Q_{Zn} = \int_0^t (2v_{Mg} - v_{Zn}) dt \quad [4.5]$$

$$\delta_{Zn} = (M_{Zn}/\rho_{Zn}) Q_{Zn} \quad [4.6]$$

where M_{Zn} and ρ_{Zn} are the atomic mass and bulk density of Zn respectively. Based on this calculation, the δ_{Zn} is estimated to be approximately 17 nm at the end of the experiment as presented in **Fig. 4.9A**. Of course, the assumptions of a uniform distribution and a pure Zn layer are probably not correct, however this gives us an order of magnitude approximation of the thickness.

When the electrolyte is saturated with O₂, the situation was more complex. The cathodic current increased in intensity by a factor of three at short times and continued to increase with

IV. Dealloying of MgZn₂ phase

time obtaining $-220 \mu\text{A cm}^{-2}$ at the end of the experiment. Zn showed a significantly enhanced dissolution rate (again associated with the increased interfacial pH) and Mg dissolution was a factor of two or three less intense. This could be due to either the decreased solubility of Mg oxides/hydroxides with increased pH or a thicker and/or more compact Zn oxide and Zn metallic film on the surface. At the end of the experiment, $j_{\text{Zn}}/j_{\text{Mg}}=0.64$ which indicates a significant preferential dissolution of Mg as compared to the expected value is $j_{\text{Zn}}/j_{\text{Mg}}=2$. The estimated Zn(0) enriched layer thickness (δ_{Zn}) determined from the results of **Fig. 4.9B** is 5.5 nm, significantly smaller than the 17 nm from **Fig. 4.9A**. This calculation assumes that all Mg is soluble.

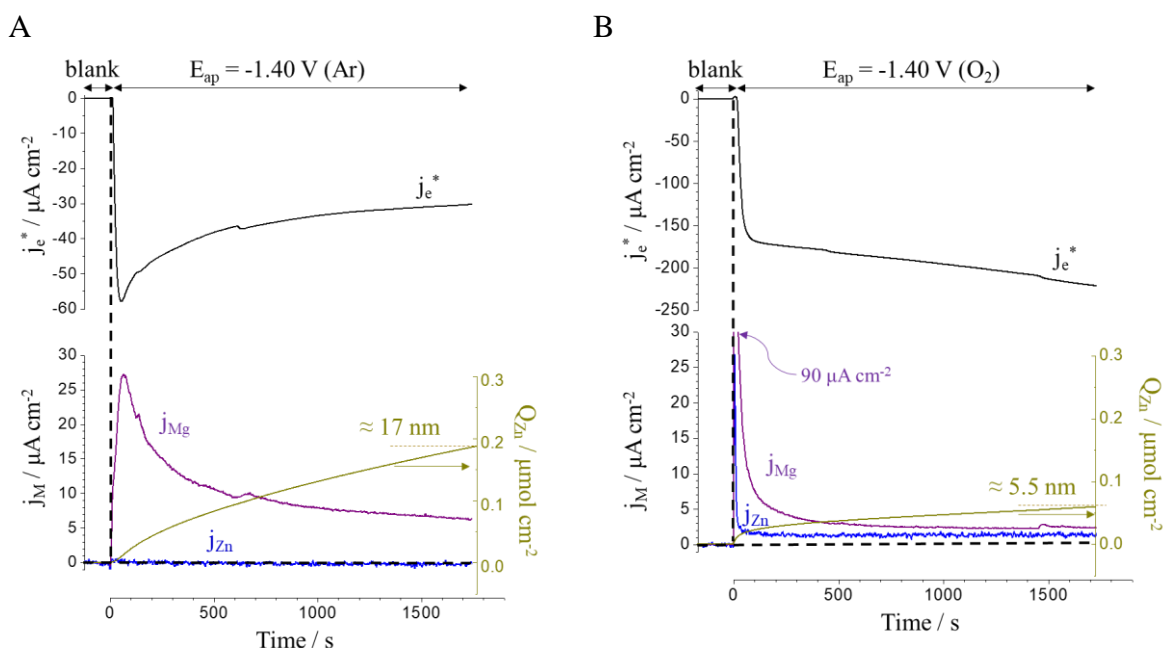


Fig. 4.9. AESEC-CA of MgZn₂ intermetallic at $E_{\text{ap}} = -1.40 \text{ V}$ in 30 mM NaCl, pH=10.1 in **A:** Ar deaerated, **B:** O₂ saturated electrolytes.

Anodic dissolution domain

Dissolution profiles during polarization into the anodic potential domain ($E_{\text{ap}} = -0.80 \text{ V}$) are shown in **Fig. 4.10** with Ar deaeration. Faradaic dissolution was apparent as the average $\eta = 0.97 \pm 0.02$, very close to 1. Nearly congruent dissolution was also observed as $j_{\text{Zn}}/j_{\text{Mg}} = 1.92 \pm 0.03$. The slight deviation of j_e^* and j_{Zn} may be interpreted as the formation of ZnO although the quantification of the ZnO must be taken with caution. This is given here as an order of magnitude approximation. From **Eq. 4.4**, the slowly soluble species under anodic polarization can be estimated by integration of the total quantity of electricity, Q_e :

$$Q_e(t) = \int_0^t (j_e^* - j_\Sigma) dt \quad [4.7]$$

In the anodic domain, it is reasonable to assume that any residual Zn will be in the form of Zn(II) oxide or hydroxide, the total amount of which, Q_{ZnO} , may be estimated as

$$Q_{ZnO} = Q_e/2 \quad [4.8]$$

presented as a function of time on the second y-axis in **Fig. 4.10**. Q_{Zn} is 0.09 $\mu\text{mol cm}^{-2}$ at the end of the experiment, equivalent to 6.8 nm of δ_{Zn} from **Eq. 4.8**. Again, there is only a small difference between j_e^* and j_Σ as compared to the absolute values (< 5 %) and the error in this estimation may be quite large.

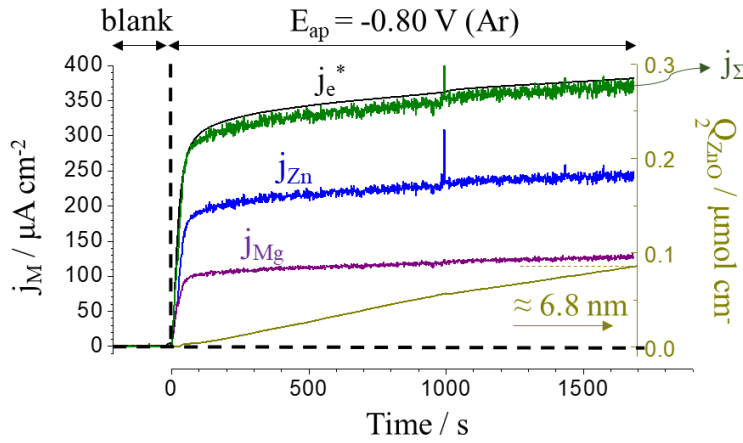


Fig. 4.10. AESEC-CA of MgZn₂ intermetallic at $E_{ap} = -0.80$ V vs. SCE in 30 mM NaCl, pH=10.1 in Ar deaerated electrolyte.

Oxide formation domain

A very curious result was obtained during the polarization into the oxide formation domain, $E = -1.14$ V. This potential is just positive of $E_{j=0}$ but below E_c^{Zn} (**Fig. 4.11**) and corresponds to the formation of oxide as indicated in the polarization curves of pure Zn and MgZn₂. The current density, j_e^* , initially showed a sharp anodic peak and then dropped off rapidly becoming increasingly cathodic with time. The anodic peak maximum coincided with a sharp peak of Mg dissolution. However, Mg dissolution rose to about 30 $\mu\text{A cm}^{-2}$ while the anodic current only rose to about 1.6 $\mu\text{A cm}^{-2}$. Again, this result supports the hypothesis that Mg dissolution is initially very rapid but is progressively inhibited by the presence of a Mg-depleted layer at the surface of the sample. This Mg-depleted layer forms during the first 200 seconds and, as it inhibits the anodic dissolution of Mg, the overall net reaction becomes increasingly cathodic. Although the net dissolution rates of Mg and Zn were very low, the

IV. Dealloying of MgZn₂ phase

preferential dissolution of Mg was indicated with $j_{Zn}/j_{Mg} = 0.26$. The estimated $\delta_{Zn} = 4.6$ nm by **Eq. 4.6**. It is difficult to estimate the quantity of ZnO since the cathodic reaction makes a non-negligible contribution to j_e^* .

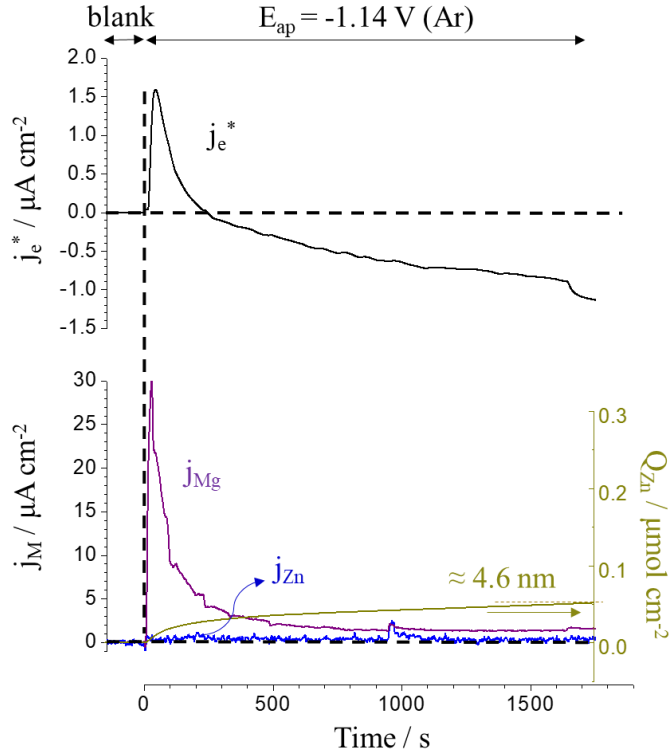


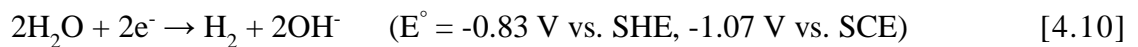
Fig. 4.11. AESEC-CA of MgZn₂ intermetallic at $E_{ap} = -1.14$ V in 30 mM NaCl, pH=10.1 in Ar deaerated electrolyte.

Evans Diagram Analysis

As an aid to future experimentation and modeling, it is of interest to present the potential dependence of the cathodic and oxide formation reactions. It is possible to extract the cathodic current from the AESEC polarization curves. In the absence of oxide formation, the cathodic current may be calculated as;

$$j_c = j_\Delta = j_e^* - j_\Sigma \quad [4.9]$$

from **Eq. 3.7**. This is shown in **Fig. 4.12** for the three systems investigated here, for the potential range between -1.80 V and -0.95 V. These results clearly show that O₂ did not contribute to the cathodic reaction on Mg but made a major contribution to the cathodic reactions on Zn. A diffusion limited oxygen reduction plateau near $E = -1.50$ V was observed for Zn metal in O₂ purged electrolyte as **Reaction 4.1**. For $E < -1.50$ V, water reduction is expected as:



IV. Dealloying of MgZn₂ phase

These results are in contrast to previous work for Zn metal and Zn-Al alloy coatings in alkaline borate buffer solution that was reported by Dafydd et al. [53] in which a two-electron mechanism for O₂ reduction to peroxide was elucidated:



From the experiments reported here, O₂ reduction on the intermetallic MgZn₂ shows a kinetic behavior similar to pure Zn metal although the cathodic reactions are attenuated by a factor of approximately 2 probably due to the presence of Mg.

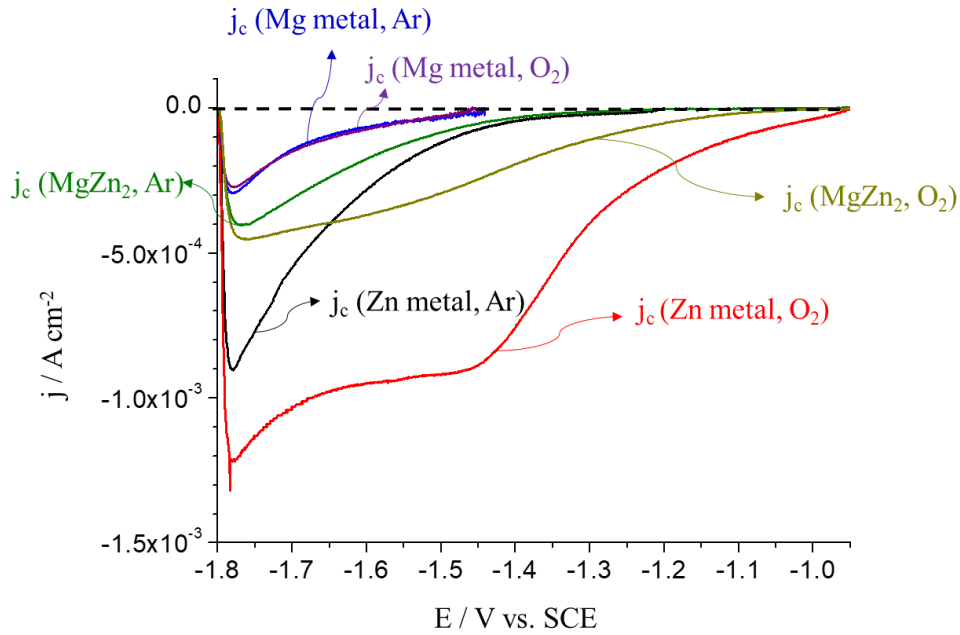


Fig. 4.12. Estimated cathodic current ($j_c = j_e^* - j_\Sigma$) of Zn, Mg metals and MgZn₂ intermetallic in the cathodic potential domain (from -1.80 V to -0.95 V) at pH=10.1, 30 mM NaCl in Ar deaerated and O₂ saturated electrolytes.

With saturation of O₂, oxide formation may be masked by the intense O₂ reduction current. However, in the absence of O₂, the cathodic current probably contributes little to j_e^* during the anodic domain. Therefore, it is possible to calculate the partial current due to oxide formation, $j_\Delta = j_{\text{ox}}$ (Eq. 3.7) in the oxide formation and simultaneous dissolution domain, from -1.20 V to -0.50 V. These are presented for pure Zn and MgZn₂ (Ar deaeration) in Fig. 4.13. j_Δ for Mg metal was near zero in the anodic polarization and is not shown. j_Δ for pure Zn showed a peak at E = -1.16 V. After this potential, j_Δ of Zn metal decreased then increased to a maximum value at -0.92 V then continuously decreased to zero as potential increases. For the MgZn₂ intermetallic, j_Δ was almost zero when E < -0.97 V following which it increased linearly with

IV. Dealloying of MgZn₂ phase

potential until the potential sweep reached to $E = -0.92$ V where it obtained a plateau. The results were consistent with the potentiostatic polarization in the anodic domain, where slight oxide formation was observed for the MgZn₂ intermetallic.

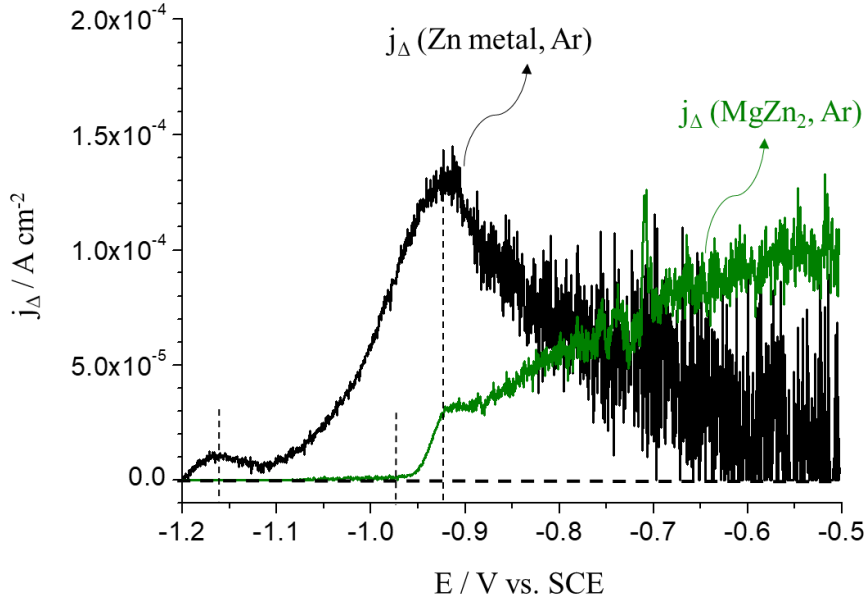


Fig. 4.13. Estimated oxide formation current ($j_{\Delta} = j_{\text{ox}} = j_e^* - j_{\Sigma}$) of Zn metal and MgZn₂ intermetallic in the anodic potential domain (-1.20 V $< E < -0.50$ V) at pH=10.1, 30 mM NaCl in Ar deaerated electrolyte.

4.4. Discussion

The results presented here demonstrate that the dealloying of MgZn₂ plays an important role in the corrosion resistance of this intermetallic compound. To our knowledge, the significance of dealloying in these materials has never before been suggested. The enhanced stability of the MgZn₂ intermetallic in 30 mM NaCl, pH=10.1 electrolyte, may be attributed to the formation of a Mg-depleted metallic Zn(0) film. The formation of this layer is due to the preferential dissolution of Mg below the onset potential of Zn/Mg dissolution, E_c^{Zn} . The Zn(0) layer grows progressively with time, considerably lowering the Mg dissolution rate.

This hypothesis is consistent with the differences observed between the elemental polarization curves between pure Mg and the MgZn₂. For Mg metal, j_{Mg} shows a steady increase with increasing E throughout the entire potential sweep with an essentially faradaic dissolution ($j_{\text{Mg}}/j_e^* \approx 1$). For the MgZn₂ intermetallic, however, j_{Mg} is notably suppressed below E_c . Above E_c , nearly congruent dissolution of Mg and Zn is observed consistent with the hypothesis that

IV. Dealloying of MgZn₂ phase

the dissolution of Mg is limited by the removal of the Zn(0) film, at which point Zn dissolution occurs, exposing fresh Mg.

The enhanced stability of the MgZn₂ is indicated by the anodic shift of E_c^{Zn} as compared to pure Zn. For both Ar deaerated and O₂ saturated electrolytes, the onset potential of Mg and Zn dissolution of MgZn₂ intermetallic occur simultaneously and at a potential that is shifted in the anodic direction ($E_c = -0.96$ V and -0.88 V with Ar deaeration and O₂ saturation respectively) as compared to pure Zn metal ($E_c^{Zn} = -1.10$ V and -0.96 V with Ar deaeration and O₂ saturation respectively). It probably reflects the fact that MgZn₂ is an intermetallic compound and the bonding energy between Mg and Zn stabilizes the material as compared to pure Zn. The covalent, ionic and metallic bonding characteristics of the MgZn₂ phase have been discussed by several authors [96,97].

Much of the pioneering work on the dealloying of binary alloys has focused on alloys of noble elements and the Zn-Cu system. The importance of elemental composition on the critical potential, E_c , for the dealloying of binary alloys has been suggested by different authors [38–40,47,98,99]. In the pioneering work of Pickering [39], two mechanisms of dealloying were distinguished which gave rise to characteristic features in the polarization curves. For both mechanisms, enrichment of the more noble element occurs at potentials below the critical potential, E_c a rapid onset of dissolution occurs. Consider a binary alloy of A-B where A is the least noble and B the most noble element. In this potential domain, $E < E_c$, the enriched surface film of B suppresses the dissolution of A. The Type I mechanism involves $E_c < E^\circ(B)$, and is characterized by the preferential dissolution of A, even for $E > E_c$. When $E > E^\circ(B)$, the dissolution of B will occur although with a much lower dissolution rate than that of A.

Type II dissolution is characterized by congruent dissolution for $E > E_c$ with $E_c > E^\circ(B)$. The formation of a film of the more noble metal (B) will suppress the dissolution of A until E_c is obtained. Once B dissolution occurs, A and B are exposed to the electrolyte and congruently dissolve. Clearly, from the polarization curves presented in **Fig. 4.8**, MgZn₂ exhibits Type II behavior in the electrolyte investigated here.

The different potential domains of MgZn₂ dealloying are presented in **Fig. 4.14**. The MgZn₂ shows nearly the same $E_{j=0}$ as Zn metal ($E = -1.21$ V). Interestingly the MgZn₂ shows a more positive onset potential of Zn/Mg dissolution ($E_c = -0.96$ V) than Zn metal ($E_c^{Zn} = -1.10$ V) consistent with other Type II dissolution alloys. The Mg-depleted layer formed during the Mg

IV. Dealloying of MgZn₂ phase

preferential dissolution and Zn oxide formation domains block Mg dissolution below E_c . For $E > E_c$, Zn and Mg dissolve congruently with j_{Zn}/j_{Mg} approximately equal to 2.

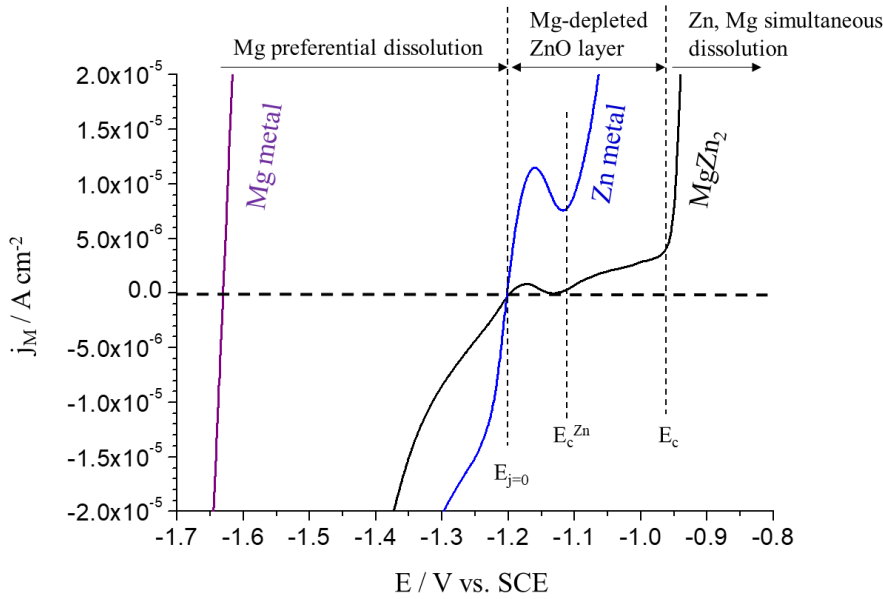


Fig. 4.14. Total current density j_e^* for pure Zn, Mg and MgZn₂ intermetallic in pH=10.1, 30 mM NaCl in Ar deaerated electrolyte.

Based on this dealloying mechanism, a dissolution model of MgZn₂ intermetallic in the three potential domains from **Fig. 4.8A** is suggested as shown in **Fig. 4.15**; (a) Mg preferential dissolution, (b) Zn(0) surface layer formation and Mg-depleted layer growth, (c) Type II non-preferential congruent Zn and Mg dissolution.

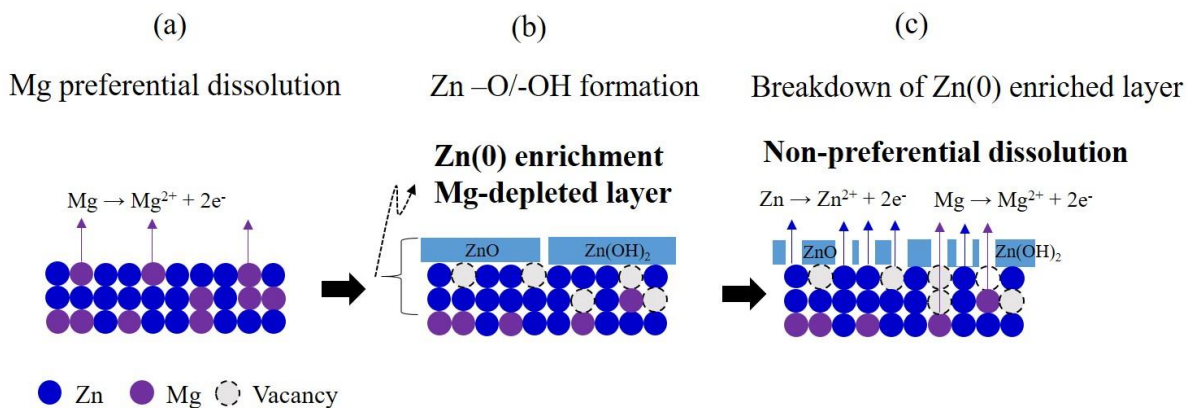


Fig. 4.15. Dealloying model of MgZn₂ intermetallic in pH=10.1, 30 mM NaCl in Ar deaerated electrolyte as a function of potential. (a): Mg preferential dissolution, (b): Mg-depleted Zn(0) enriched layer formation, (c): non-preferential congruent Zn and Mg dissolution.

4. 5. Conclusions

1) The MgZn₂ intermetallic at open circuit potential, showed significantly reduced elemental dissolution rates for both Zn and Mg as compared with either pure Zn or Mg metal. This enhanced corrosion resistance was attributed to the preferential dissolution of Mg forming a residual Mg-depleted Zn/Zn oxide (Zn(O) enriched) layer which suppressed Mg dissolution. The presence of Mg maintained the potential below the critical potential for Zn dissolution ($E < E_c^{Zn}$) thereby suppressing Zn dissolution as well.

2) O₂ reduction was the major cathodic reaction for pure Zn, while it was completely inhibited on Mg metal and partially inhibited on the MgZn₂ intermetallic. In an O₂ saturated electrolyte, cathodic dissolution of Zn was observed for both pure Zn and the MgZn₂ intermetallic. This was attributed to the increase in the interfacial pH in the presence of O₂ resulting in the formation of Zn(OH)₄²⁻ which enhances Zn dissolution.

3) The dealloying mechanism of the MgZn₂ intermetallic depends on the potential. Three domains were identified in the polarization curve of MgZn₂: (a) a cathodic domain where Mg preferential dissolution dominates forming a metallic Zn(O) enriched layer, (b) an intermediate domain where Mg preferential dissolution is coupled with Zn oxide formation, and (c) the anodic dissolution ($E > E_c$) with nearly congruent dissolution of Zn and Mg.

4) The formation of either oxide and the Mg-depleted Zn(O) enriched layer could be quantified by as a function of time during potentiostatic experiments by mass balance. Under the conditions of these experiments, the estimated film thicknesses were on the order of several nanometers. The variation of the cathodic reaction and the oxide formation rates were determined by mass balance and presented as a function of potential to eventually serve as Evans diagrams given partial currents of the elementary phenomena of dissolution and passivation.

Chapter V: Cathodic dealloying of α -phase Al-Zn in slightly alkaline chloride electrolyte and its consequence for corrosion resistance.

«Savoir où l'on veut aller, c'est très bien ; mais il faut encore montrer qu'on y va.»

L'argent (1891),

Emile Zola

This chapter repeats the article: “Junsoo Han and Kevin Ogle, Cathodic dealloying of α -phase Al-Zn in slightly alkaline chloride electrolyte and its consequence for corrosion resistance, *Journal of The Electrochemical Society*, **165**(7) C334-C342 (2018)”, published in May 2018.

5. Cathodic dealloying of α -phase Al-Zn in slightly alkaline chloride electrolyte and its consequence for corrosion resistance

Abstract

Cathodic dealloying of Al-Zn phases may be a significant, albeit poorly understood, phenomenon occurring during field corrosion of Zn-Al and Zn-Al-Mg coatings. The reactivity of α -phase Al-Zn (Zn-68 wt.% Al, $\text{Al}_{5,2}\text{Zn}$) has been investigated as a function of potential in pH=10.1, 30 mM NaCl. The dealloying of Al during cathodic polarization (cathodic dealloying) led to the formation of a Zn(0) enriched surface layer. The dealloyed layer did not affect the rate of cathodic Al dissolution or the open circuit corrosion rate. The dissolution of Zn from the Zn(0) enriched layer showed an onset potential below the critical potential (E_c) where Al and Zn simultaneously dissolve. The cathodic dissolution of Zn was observed in O_2 saturated electrolyte which correlated with an order of magnitude decrease in the Al dissolution rate.

Keywords: zinc, aluminum, pure phase, dealloying

5.1. Introduction

Alloys of Zn, Al and Mg are frequently used as coatings for galvanized steel due to their enhanced corrosion resistance in a wide variety of conditions. This enhanced resistance has been confirmed in atmospheric field exposures, accelerated atmospheric corrosion tests, and in immersion in chloride containing electrolytes [6,7,30,32–36,100–103,9,104–106,11,13,18,21,26–28]. The role of microstructure on the corrosion resistance was highlighted by Prosek et al. [13]. They produced Zn-Al and Zn-Al-Mg alloys with identical chemical composition but differing microstructure by changing the cooling rate when they were casted. They concluded that the finer microstructure of Zn-5wt.% Al alloy showed better corrosion resistance under atmospheric exposure conditions. The origin of this effect and the interactions between the different phases however has yet to be revealed. Indeed, the commercial Zn-Al and Zn-Al-Mg alloy coatings present a complex multi-phase structure. For example, Zn-5 wt.% Al alloy (GalfanTM, denoted as Zn-5Al) has a eutectic structure consisting of a dendritic η -phase of Zn interspersed within the lamella of Zn rich Al phase (β -phase of Al) [17,93,107,108]. The Zn-55 wt.% Al-1.6 wt.% Si, (GalvalumeTM, denoted as Zn-55Al) is composed of a dendritic α -phase of Al, and a Zn rich inter-dendritic phase [109–113]. The Zn-Al-Mg alloys have a dendritic η -phase of Zn, a Zn-MgZn₂ binary eutectic, and a Zn-Al-MgZn₂ ternary eutectic phase [21,26,30,33–35,102–104].

In order to understand and predict the corrosion of complex Zn-Al and Zn-Al-Mg alloys, it is important to characterize the electrochemical stability of the individual phases. The MgZn₂ intermetallic phase and the α -phase of Al represent the extremes of the phases present in the coating alloys in terms of Mg content and Al content respectively. In previous work, the dealloying mechanism of MgZn₂ intermetallic phase was investigated in slightly alkaline chloride containing electrolyte [114]. It was concluded that a Mg-depleted Zn metallic/oxide layer inhibits the dissolution of Mg and Zn resulting in improved corrosion resistance. This work extends the previous work to a consideration of a pure Al-Zn α -phase system. The α -phase of Al (0~32 wt.% Zn) is representative of the high Al content phases of the Zn-Al and Zn-Al-Mg system. The α -phase of Al is present in the ternary eutectic phase of Zn-Al-Mg where it may be in intimate contact with the η -phase of Zn and the MgZn₂ phase [20,115]. The ternary eutectic has been shown to be the most reactive phase, preferentially corroding leaving the Zn rich phase unattacked [20,21,34]. Other phases such as the β -phase of Al may dissociate to form the η -phase of Zn and the α -phase of Al at room temperature [116,117].

A particularity of Al and Al alloys is their tendency to undergo dissolution in the presence of cathodic currents, commonly referred to as cathodic dissolution [55,118–123]. This is usually thought of as a two-step process, involving the dissolution of the oxide film by reaction with hydroxide generated by the cathodic reaction and the subsequent oxidation of the exposed Al metal. The net reaction, with either water or O₂ as the oxidizing agent, may be written as:



Reactions 5.1 and 5.2 predict a 1:1 stoichiometry of electrons to dissolved Al ions (v_e/v_{Al}) during cathodic polarization. In fact, a value of $v_e/v_{\text{Al}} = 1.83 \pm 0.35$ was obtained where the excess electrons were attributed to the diffusion of hydroxide away from the interface in the electrochemical flow cell [122]. The stoichiometry was obtained for Al metal, Al₂Cu pure phase and various Al alloys (2000 and 6000 series) [120–122]. Cathodic Al dissolution has also been observed during the polarization of Zn-5Al and Zn-(3~4) wt.% Al-(3~4) wt.% Mg [35].

During corrosion, the α -phase of Al may be polarized cathodically when coupled to a less noble phase such as MgZn₂. Therefore, it is reasonable to think that cathodic Al dissolution (cathodic dealloying) may be important under field conditions. This could play an important role in corrosion resistance: the Zn-Al-Mg and Zn-Al alloy coatings are known to form Zn-Al layered double hydroxides (LDHs) which have been associated with improved corrosion resistance [6,26]. Cathodic Al dissolution may serve as a reservoir of Al³⁺ release into solution even when the Al rich alloy is the cathode in a galvanic couple.

In this work, the anodic and cathodic polarization of the α -phase of Al is investigated with an emphasis on cathodic dealloying. To this end, atomic emission spectroelectrochemistry (AESEC) is used to measure the dissolution rates of Al and Zn simultaneously with the electrical current. This permits a direct measurement of cathodic Al dissolution which cannot be obtained by consideration of the conventional polarization curve since the anodic dissolution of Al is masked by the intense cathodic current. The effect on corrosion of the dealloyed metallic Zn enriched (Zn(0)) layer formed during cathodic dealloying is investigated. Other phenomena brought to light in this work are the cathodic dissolution of Zn and the passivation

of the Al film in the presence of O₂. The pH=10.1 was chosen because, during corrosion, the interfacial pH of the Zn-Al-Mg alloy becomes alkaline due to the cathodic reaction [21,28,85].

5.2. Experimental

Materials

Al metal (99.99%) from *Goodfellow* and a α -phase of Al (Zn-68 wt.% Al) were used in this work. The latter was produced and characterized by the *Department of Metals and Corrosion Engineering, University of Chemistry and Technology, Prague*. The chemical composition of α -phase of Al was chosen as 68 wt.% Al because it showed a single α -phase with only a trace of η -phase of Zn. In this work, this phase will be denoted as Al_{5,2}Zn based on its molar composition. Al_{5,2}Zn was produced from pure metals, heated in a ceramic crucible in a muffle furnace, filtered through a frit and cast into a 50 mm diameter metal mold. Al_{5,2}Zn was treated by water quenching after 24 hours in a 400 °C muffle furnace. The chemical composition of the Al_{5,2}Zn was 67.6 wt.% Al and 32.4 wt.% Zn obtained by atomic absorption spectroscopy (AAS). The sample and electrolytes were prepared as in the previous chapters. 30 mM NaCl, pH=10.1 electrolyte was prepared from analytical grade reagent and deionized water (18 M Ω cm) obtained via a MiliporeTM system either deaerated by Ar or saturated by O₂. All the experiments presented herein showed reproducible results from the measurements repeated at least three times.

The AESEC technique

AESEC was used for analyzing the elemental dissolution kinetics of the specimens. The specimen of interest was brought into contact with a flowing electrolyte in a small volume ($\approx 0.2 \text{ cm}^3$) three-electrode electrochemical flow cell. A saturated calomel electrode, SCE and a Pt foil were used as reference and counter electrodes, respectively. In this work, the time resolved concentration of Zn was determined from the emission intensity of the plasma monitored at 213.86 nm wavelength on the polychromator and Al at 167.08 nm on the monochromator using standard inductively coupled plasma atomic emission spectrometry (ICP-AES) calibration techniques.

V. Cathodic dealloying of Al and Al-Zn phase

A Gamry Reference 600TM potentiostat was used to control and measure the electrochemical potential (E) and current density (j_e^*). A number of different electrochemical experiments were performed including measurements of the spontaneous dissolution at the open circuit potential (dissolution profile), linear sweep voltammetry (LSV) using a scan rate of 0.5 mV s⁻¹, and constant potential (E_{ap}) chronoamperometry (CA). Specific experimental descriptions will be given in the text.

Surface characterization

The material surface before and after electrochemical experiments was characterized by scanning electron microscopy (SEM) using a Zeiss Leo 1530TM microscope with field emission gun (FEG) source at 15 keV, 15 mm working distance. Raman spectroscopy was performed to identify oxide species on the sample surface using a Renishaw InviaTM confocal Raman microscope with excitation by a Co diode pumped solid state (DPSS) using a green laser (532 nm). The acquisition and evaluation of Raman spectra were conducted by using WireTM software.

Data analysis

The basic principle of AESEC is to simultaneously measure the elemental dissolution rates, v_M (M=Al and Zn in this work), the electrochemical current density, j_e and the potential, E. The dissolution rates may be expressed as equivalent elemental current densities, j_M ($= zFv_M$ where F is the Faraday constant and z is the oxidation state of each element) to facilitate comparison with j_e . For the determination of the cathodic dealloying stoichiometry, it is convenient to present the cathodic current as a rate of electron transfer, $v_e^* = -j_e^*/nF$, for $j_e^* < 0$.

During dealloying or selective leaching, the least noble element (Al) will dissolve leaving behind a surface layer enriched in the more noble element (Zn). The elemental dissolution rates may be used to construct a mass balance so that the surface excess of an element, $Q_{M(0)}$, may be determined. This permits a real time, indirect analysis of the growth of a surface enriched (dealloying) layer during the selective dissolution of one or more elements.

A mass/charge balance may be constructed by comparing j_e^* with the sum of the dissolution rates, j_z . The faradaic yield of dissolution, η , may be determined as the ratio of $\eta =$

j_{Σ} / j_e^* . For $\eta \neq 1$, it is often possible to calculate the rate of either the cathodic reaction, j_c ($\eta > 1$), or the formation of undissolved corrosion products, j_{ox} for ($\eta < 1$). Note that the comparison of transients in j_M and j_e requires the convolution of the latter with the residence time distribution in the flow cell. The convoluted form of j_e is designated as j_e^* .

5.3. Results

5.3.1. The dissolution of pure Al

The spontaneous reaction of Al metal with the electrolyte was investigated in the experiments of **Fig. 5.1**. Shown are the Al dissolution rate expressed as the equivalent current density, j_{Al} , and the open circuit potential, E_{oc} , as a function of time, t , during the exposure to deaerated (Ar purged) and O_2 saturated electrolyte. The steady state Al dissolution rates (j_{Al}^s) in Ar deaerated and O_2 saturated electrolytes were nearly identical with $j_{Al}^s = 21 \mu A cm^{-2}$ despite a +150 mV shift of E_{oc} in O_2 saturated electrolyte.

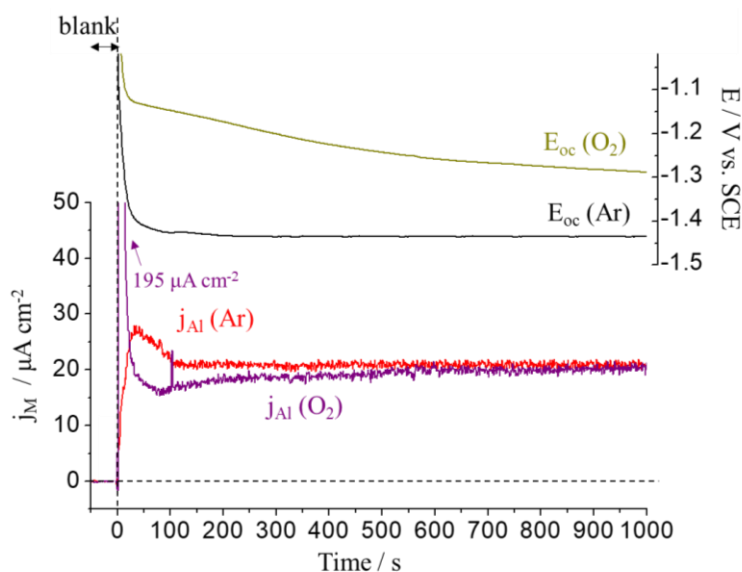


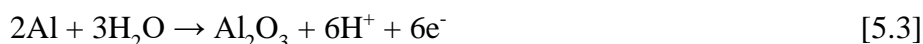
Fig. 5.1. Spontaneous elemental current densities (j_M) and open circuit potential (E_{oc}) as a function of time for nominally pure Al exposed to a 30 mM NaCl, pH=10.1 electrolyte with Ar deaeration and O_2 saturation at $T=25^\circ C$.

All potential values presented in this work are referenced to a SCE electrode.

The cathodic dissolution of Al is clearly visible in the AESEC linear sweep voltammetry (AESEC-LSV) of **Fig. 5.2**, as evidenced by the significant Al dissolution occurring during the cathodic branch of the curve. Cathodic dissolution of Al was observed for both the Ar deaerated and the O_2 saturated electrolyte although the cathodic current was significantly more intense for the latter situation. The anodic domain of **Fig. 5.2** is typical of pure Al metal showing a passive domain for $E > E_{j=0}$ with a passive current of approximately $j_e^* = 10 \mu A cm^{-2}$, essentially independent of the presence of O_2 . In the transpassive domain for $E > -0.6 V$, passive film

breakdown was observed as indicated by the sudden increased in j_e^* associated with an increased in the j_{Al} . The transpassive breakdown was somewhat more intense in the presence of O_2 .

It is obvious from **Fig. 5.2** that a conventional Tafel extrapolation of j_e^* to $E_{j=0}$ does not in any way predict the corrosion rate for this system as j_{Al} is significantly higher than j_e^* throughout the potential sweep in cathodic branch. The dashed lines in **Fig. 5.2** represent a mixed potential analysis of the Al dissolution rate. The vertical lines designate the $E_{j=0}$ and the horizontal lines indicate j_{Al} observed at $E_{j=0}$. It is seen that both $E_{j=0}$ and j_{Al} values are in excellent agreement with the E_{oc} and j_{Al}^s values observed in the dissolution profiles (**Fig. 5.1**). The interesting point is that O_2 saturation markedly increased the cathodic intensity (**Fig. 5.2**), however the potential change exactly compensated this increase such that the open circuit j_{Al} value was apparently independent of O_2 saturation. This is reasonable if we consider that the anodic reaction may be due to a passivation reaction such as;



and is, by and large, independent of potential. In this interpretation, O_2 saturation would shift the cathodic branch of the Evans diagram, corresponding to **Eqs. 5.1** or **5.2**, to higher potentials but would have little effect on the anodic reaction.

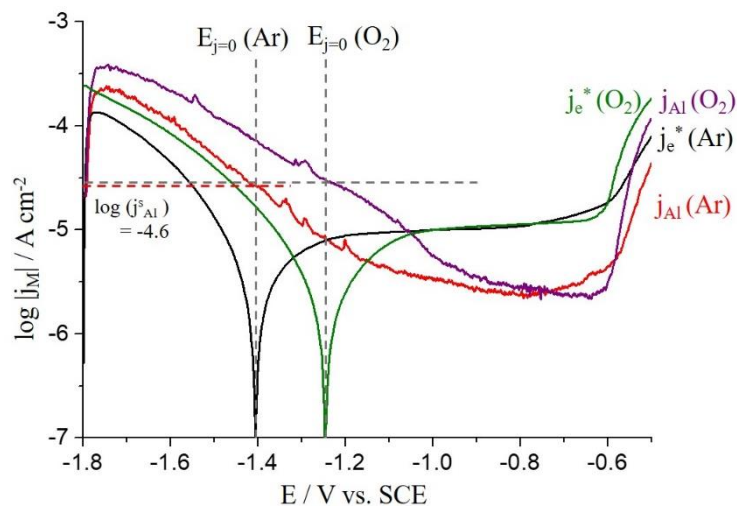


Fig. 5.2. Elemental AESEC- LSV curves of Al metal in 30 mM NaCl, pH=10.1, electrolyte with Ar deaeration and O_2 saturation at $T=25$ °C. The potential was swept from -1.80 V to -0.50 V with 0.5 mV s^{-1} scan rate following an open circuit exposure for approximately 15 minutes.

5.3.2. The potential dependence of $Al_{5,2}Zn$ dissolution: Overview

Spontaneous j_M of $Al_{5,2}Zn$ in Ar deaerated and O_2 saturated electrolytes are shown in **Fig. 5.3**. A steady state Al dissolution rate was measured at $j_{Al}^s = 36.3 \pm 2.3 \mu A cm^{-2}$ (Ar deaeration) and $27.3 \pm 0.4 \mu A cm^{-2}$ (O_2 saturation) respectively. The error bar represents the standard deviation of five different measurements. The steady state E_{oc} in Ar deaerated electrolyte ($E_{oc} = -1.31 V$) was 200 mV lower than that in O_2 saturated electrolyte ($E_{oc} = -1.11 V$). In both cases, j_{Zn} was below the detection limit. The positive shift of the potential with respect to pure Al (**Fig. 5.1**) may be attributed to the presence of Zn. In both cases, the O_2 saturation caused a further anodic shift in the potential by 150 to 200 mV and, in this case, a diminution of the Al dissolution rate.

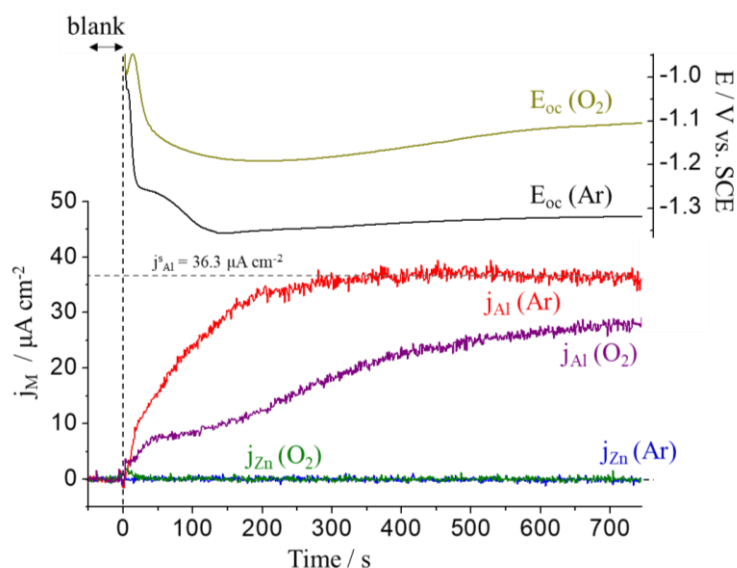


Fig. 5.3. Spontaneous elemental current densities and open circuit potential for $Al_{5,2}Zn$ phase in 30 mM NaCl, pH=10.1, electrolyte with Ar deaeration and O_2 saturation at $T=25 \text{ }^\circ\text{C}$.

The AESEC linear sweep voltammetry (AESEC-LSV) curve of $Al_{5,2}Zn$ in an Ar deaerated electrolyte (**Fig. 5.4**) may be divided into three potential domains based on the rate of Zn dissolution:

- I. $E < E_c^{Zn}$, selective Al dissolution.
- II. $E_c^{Zn} < E < E_c$, Zn(0) dissolution.
- III. $E > E_c$, congruent dissolution.

where E_c^{Zn} is the onset potential for Zn dissolution and E_c is the onset potential of spontaneous Al/Zn dissolution. The cathodic dissolution of Al was evident during the cathodic branch (domain I) as was observed for pure Al in **Fig. 5.2**. Throughout the cathodic branch, j_{Zn}

remained below the detection limit. By mass balance, it follows that a Zn(0) enriched layer was building up on the surface via a “**cathodic dealloying**” mechanism.

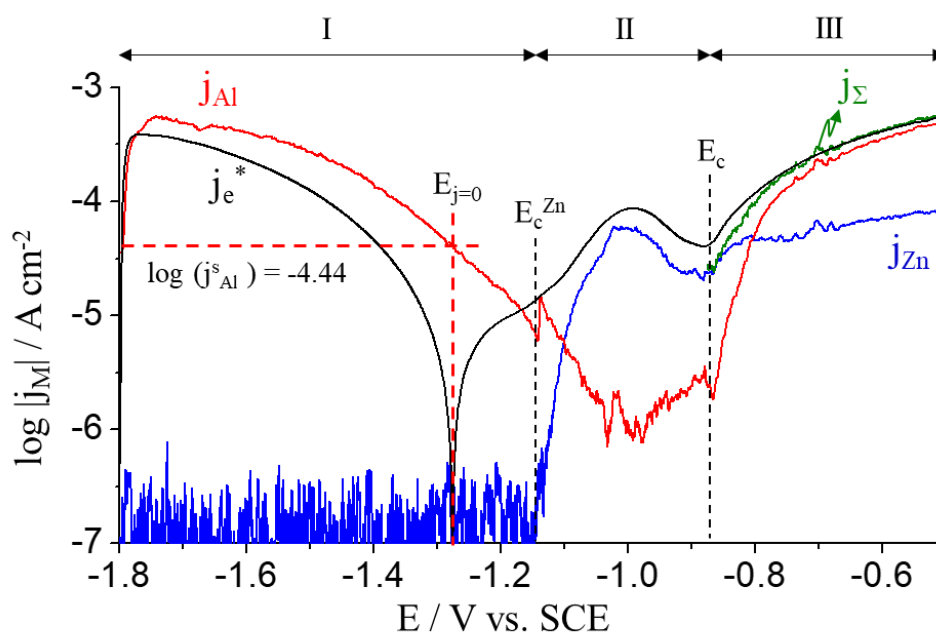


Fig. 5.4. Elemental AESEC-LSV curve of $\text{Al}_{5.2}\text{Zn}$ phase in 30 mM NaCl, pH=10.1, electrolyte with Ar deaeration at $T=25\text{ }^\circ\text{C}$.

Zn dissolution became active in domain II. The peak maximum at $E = -1.05\text{ V}$ was due to the dissolution of Zn(0) built up on the surface during the cathodic Al dissolution phase as will be demonstrated later. In the same potential range, j_{Al} reached its lowest level corresponding approximately to the passive dissolution rate of pure Al metal (**Fig. 5.2**). In domain III, simultaneous dissolution of Al and Zn occurred at $E_c = -0.88\text{ V}$ approaching congruent dissolution ($j_{\text{Al}}/j_{\text{Zn}} = 5.8 \pm 0.1$ and still increasing at the end of the polarization, as compared to a bulk value $j_{\text{Al}}/j_{\text{Zn}} = 7.8$) and close to a 100% faradaic yield ($\eta = j_{\Sigma}/j_e^* = 1.09 \pm 0.12$ with $j_{\Sigma} = j_{\text{Al}} + j_{\text{Zn}}$).

The AESEC polarization curve of $\text{Al}_{5.2}\text{Zn}$ (**Fig. 5.4**) can be used to predict the spontaneous, open circuit dissolution rate and potential (**Fig. 5.3**). From **Fig. 5.4**, $E_{j=0} = -1.28\text{ V}$ as compared to $E_{\text{oc}} = -1.31\text{ V}$ in **Fig. 5.3**. Further, $j_{\text{Al}} = 37\text{ }\mu\text{A cm}^{-2}$ at $E_{j=0}$ in **Fig. 5.4** reasonably identical to j_{Al}^s in **Fig. 5.3**.

The stoichiometric relationship between cathodic current and Al dissolution ($v_e^*/v_{\text{Al}} = -3j_e^*/j_{\text{Al}}$) for $-1.80\text{ V} < E < -1.40\text{ V}$, are indicated in **Fig. 5.5** for both Al metal and the $\text{Al}_{5.2}\text{Zn}$

V. Cathodic dealloying of Al and Al-Zn phase

phase in Ar deaerated and O₂ saturated electrolytes. For Al_{5.2}Zn phase in O₂ saturated electrolyte, the v_e^*/v_{Al} value is shown at $E < -1.46$ V. The average v_e^*/v_{Al} values are summarized in **Table 5.1**. The values are similar to what was measured for pure Al, the Al₂Cu pure phase, and various Al alloys in previous work [122] and are consistent with **Eqs. 5.1 or 5.2**. The values are higher than the theoretical $v_e^*/v_{Al}=1$ due to the diffusion of OH⁻ away from the surface. A kinetic model taking into account mass transport has been presented [122]. For Al metal, the value of v_e^*/v_{Al} was identical within experimental error for the Ar deaerated and the O₂ saturated electrolytes (**Table 5.1**), despite the significantly more intense cathodic current in the latter, demonstrating that it is indeed the cathodic current that drives Al dissolution.

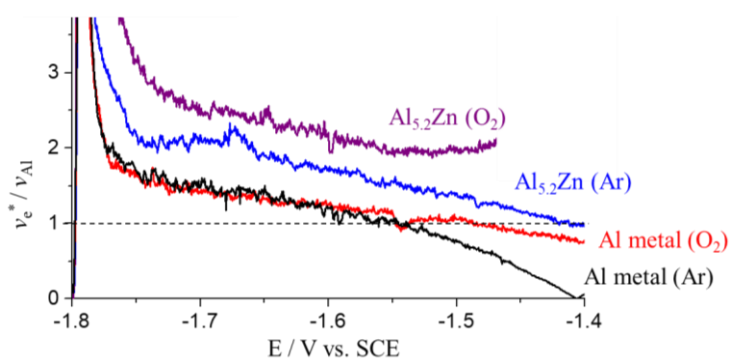


Fig. 5.5. Cathodic dissolution analysis by v_e^*/v_{Al} of Al metal and Al_{5.2}Zn in 30 mM NaCl, pH=10.1, electrolyte with Ar deaeration and O₂ saturation at T=25 °C in domain I (-1.80 V < E < -1.40 V).

For Al_{5.2}Zn, the v_e^*/v_{Al} values were slightly higher than those of pure Al probably due to the presence of metallic Zn making Al less available at the surface. Further, for the Al_{5.2}Zn phase, the v_e^*/v_{Al} value in O₂ saturated solution was slightly higher (2.3) than that in Ar deaerated electrolyte (1.6). Note that the initially high v_e^*/v_{Al} was due to the high current associated with the imposition of the starting potential for the sweep and was not taken into account.

Table 5.1. The average v_e^*/v_{Al} value of Al metal and Al_{5.2}Zn α -phase for -1.80 V < E < -1.40 V in Ar deaerated and O₂ saturated electrolytes. The error bar represents the standard deviation of one measurement.

v_e^*/v_{Al}	Al _{5.2} Zn		Al metal	
	Ar	O ₂	Ar	O ₂
	1.6 ± 0.4	2.3 ± 0.3	1.3 ± 0.3	1.2 ± 0.2

5.3.3. Anodic reactivity of $Al_{5.2}Zn$

To minimize the effect of residual metallic Zn, individual anodic and cathodic polarization curves were obtained beginning at the open circuit potential near -1.1 V, denoted as anodic and cathodic LSV respectively. The anodic AESEC polarization curve in Ar deaerated solution is shown in **Fig. 5.6**. Note that the sample was exposed at the open circuit for 10 s prior to the potential sweep, sufficient time for the flow cell to fill with electrolyte but short enough to minimize the build-up of residual metallic Zn. Following a short rise period, a stable $j_e^* \approx j_{Al}$ of approximately $5 \mu A cm^{-2}$ was obtained, essentially independent of the potential sweep. This is consistent with passive behavior as observed for pure Al metal in this potential range in **Fig. 5.2**. Throughout this potential range, j_{Zn} was below the detection limit indicative of Al selective dissolution. At $E = -0.88 V$, Al and Zn dissolved simultaneously showing a slight Zn dissolution peak at $E = -0.85 V$. Note that the onset of Zn dissolution was shifted by +260 mV in the positive direction with respect to **Fig. 5.4**.

The anodic LSV is less perturbed by residual metallic Zn formed by the cathodic dealloying mechanism. Therefore, $E = -0.88 V$ may be considered as approaching the critical, onset potential (E_c) for simultaneous Al and Zn dissolution. Chronoamperometric experiments (CA) for $E > E_c$ confirmed the faradaic yield and the congruent dissolution (not shown here).

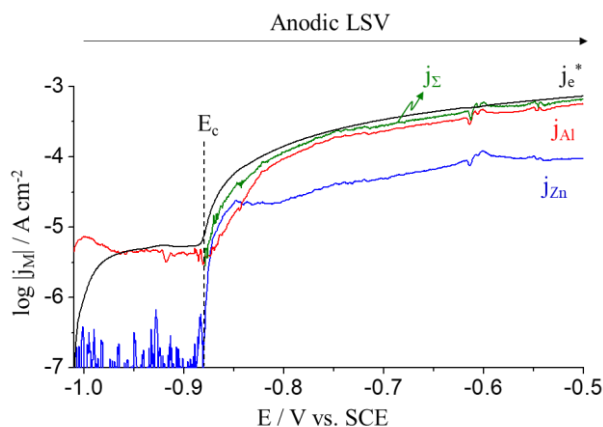


Fig. 5.6. Elemental AESEC anodic polarization curve (anodic LSV) of $Al_{5.2}Zn$ in 30 mM NaCl, pH=10.1, electrolyte with Ar deaeration at $T=25 \text{ }^\circ\text{C}$. The potential was swept from E_{oc} to -0.50 V with 0.5 mV s^{-1} scan rate following an open circuit exposure for 10 s.

5.3.4. Cathodic reactivity of $Al_{5.2}Zn$

The cathodic LSV of $Al_{5.2}Zn$ starting at E_{oc} in Ar deaerated electrolyte is presented in **Fig. 5.7** showing a similar result to the LSV in **Fig. 5.4**. For $E < -1.34$ V, j_e^* and j_{Al} increased simultaneously indicating that once again, j_{Al} was coupled to the cathodic reaction. Cathodic dealloying occurred as no Zn dissolution was observed during the potential sweep. Interestingly, for -1.34 V $< E < E_{oc}$, the total current was anodic showing a maximum j_e^* of $5.4 \mu A cm^{-2}$, with j_{Al} at approximately the same value. This is consistent with the potential transient of **Fig. 5.3** where E_{oc} was initially positive and dropped to approximately -1.31 V at steady state.

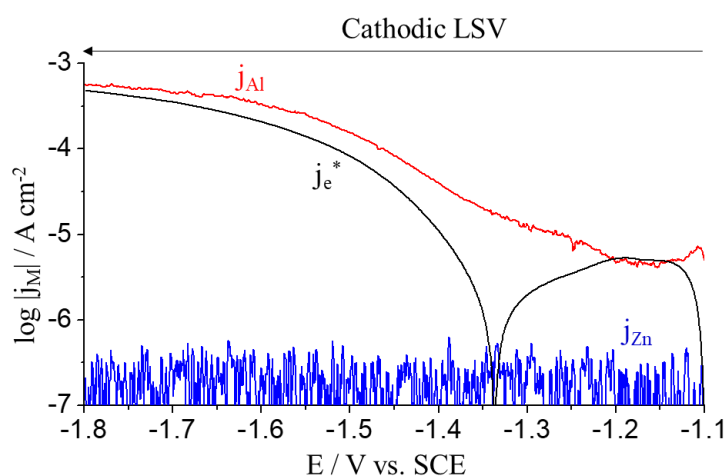


Fig. 5.7. Elemental AESEC cathodic polarization curve (cathodic LSV) of $Al_{5.2}Zn$ pure phase in 30 mM NaCl, pH=10.1, electrolyte with Ar deaeration at $T=25$ °C. The potential was swept from E_{oc} to -1.80 V with 0.5 mV s^{-1} scan rate following an open circuit exposure for 10 s.

Further insight into the cathodic dealloying reaction may be gained by measuring the response of the system (chronoamperometry, CA) to a series of applied potentials, E_{ap} . Two types of experiment were performed;

(1) E_{ap} was applied for 1000 s, and then the relaxation of the system to open circuit was recorded. This permits a verification of the cathodic dissolution mechanism free from the effect of sweep rate or surface conditioning and observation of the effect of the Zn(0) enriched dealloyed layer on the j_{Al}^s .

(2) E_{ap} was applied for 1000 s and then the potential was stepped to a more positive value to dissolve the Zn from the Zn(0) enriched dealloyed layer.

Fig. 5.8 shows the CA experiments at various applied potentials as indicated. In all cases, j_{Zn} (not shown) was below the detection limit, demonstrating a mechanism of cathodic dealloying. The average values of j_{Al} and j_e^* at the steady state are summarized in **Table 5.2**. The v_e^*/v_{Al} values measured during a constant cathodic potential pulse were 1.86 ± 0.06 at $E_{\text{ap}} = -1.60$ V and 1.00 ± 0.04 at $E_{\text{ap}} = -1.40$ V in rather good agreement with those measured from the polarization experiment of **Fig. 5.5** summarized in **Table 5.2**.

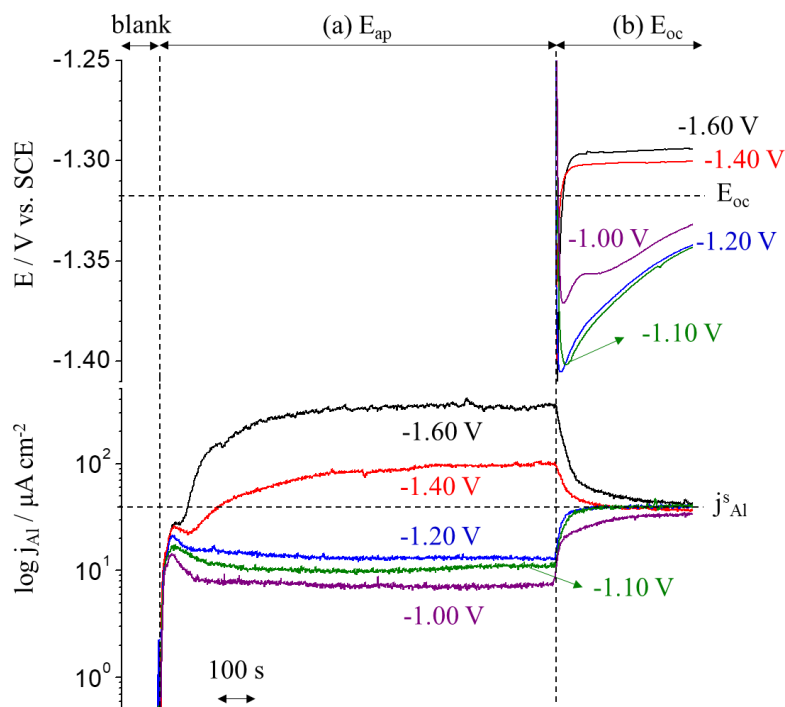


Fig. 5.8. AESEC chronoamperometric (AESEC-CA) experiment of $\text{Al}_{5.2}\text{Zn}$ at cathodic potentials of $E_{\text{ap}} = -1.60$ V, -1.40 V and anodic potentials of $E_{\text{ap}} = -1.20$ V, -1.10 V and -1.00 V, at $\text{pH}=10.1$, 30 mM NaCl electrolyte at $T=25$ °C. Shown are (a) j_{Al} transient during the CA experiments; (b) the spontaneous E_{oc} and j_{Al} trends after the CA experiments. To facilitate the comparison, j_{Al} values are displayed in log-scale. j_{Zn} is not displayed.

For all applied potentials, after release of E_{ap} , j_{Al} returned to j_{Al}^{s} decaying with the time constant of the flow cell and E returned to E_{oc} . This result demonstrates unambiguously that the $\text{Zn}(0)$ enriched dealloyed layer had no significant effect on the selective dissolution of Al. Further, the dissolution transients give no indication that either Zn oxide or Al oxide was present on the alloy surface following E_{ap} .

V. Cathodic dealloying of Al and Al-Zn phase

Table 5.2. The average j_{Al} and j_e^* of chronoamperometric (CA) experiment at $E_{\text{ap}} = -1.60$ V, -1.40 V, -1.20 V, -1.10 V and -1.00 V from **Fig. 5.8**. The error bar represents the standard deviation in the steady state of one measurement.

	$E_{\text{ap}} = -1.60$ V	$E_{\text{ap}} = -1.40$ V	$E_{\text{ap}} = -1.20$ V	$E_{\text{ap}} = -1.10$ V	$E_{\text{ap}} = -1.00$ V
$j_{\text{Al}}/\mu\text{A cm}^{-2}$	340 ± 14	104 ± 3	13.1 ± 0.3	10.5 ± 0.5	7.2 ± 0.2
$j_e^*/\mu\text{A cm}^{-2}$	-213 ± 3	-35.3 ± 0.1	12.6 ± 0.2	14.20 ± 0.02	11.50 ± 0.01
v_e^*/v_{Al}	1.86 ± 0.06	1.00 ± 0.04	-	-	-

To corroborate the formation of the Zn(0) enriched layer during the cathodic potential domain, a Zn(0) enriched layer was formed at a constant cathodic potential ($E_{\text{ap}} = -1.60$ V) during 1000 s. Then the potential was instantly switched to an anodic value at which the Zn(0), formed by cathodic dealloying would dissolve, but below the critical potential of Zn dissolution from the bulk alloy ($E_c = -0.88$ V from **Figs. 5.4** and **5.6**). **Fig. 5.9A** gives an example of the j_{Zn} transients during an anodic step ($E_{\text{ap}} = -1.00$ V) either with or without a preceding 1000 s at $E_{\text{ap}} = -1.60$ V. Without the cathodic potential step, j_{Zn} was always below the detection limit, as in **Fig. 5.8** demonstrating that Zn in the $\text{Al}_{5.2}\text{Zn}$ matrix did not dissolve at these potentials. Following the cathodic potential step, however, a large peak of Zn dissolution was observed, clearly linked to the enrichment of Zn(0) during cathodic dealloying.

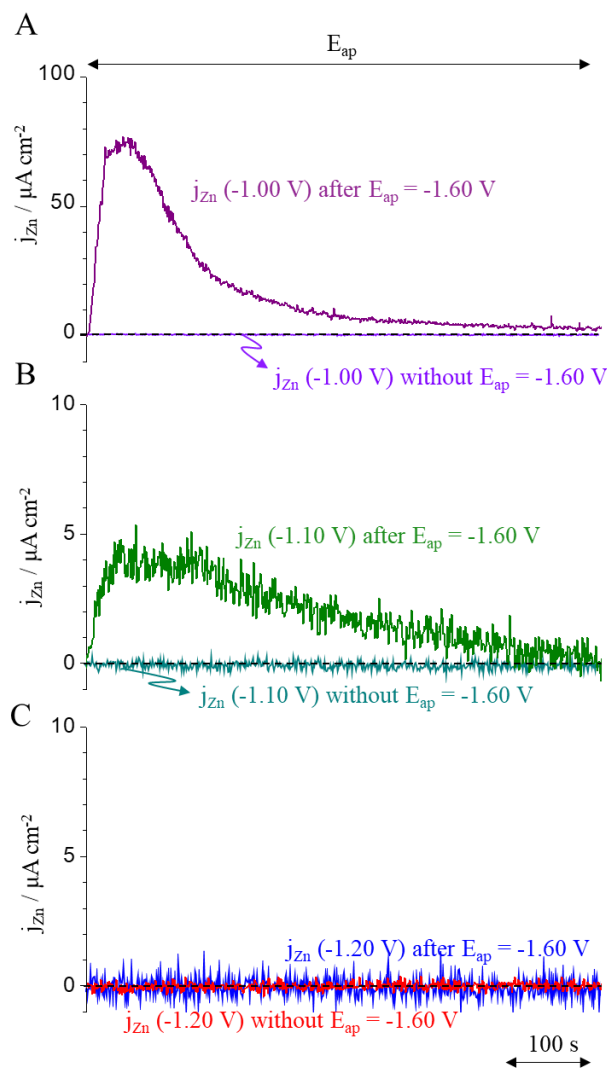


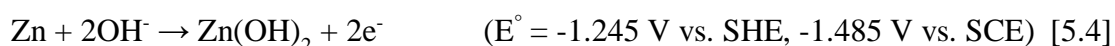
Fig. 5.9. Zn dissolution (j_{Zn}) with and without a preceding potential pulse during 1000 s at $E_{\text{ap}} = -1.60$ V to **A**: -1.00 V, **B**: -1.10 V and **C**: -1.20 V in 30 mM NaCl, pH=10.1, electrolyte with Ar deaeration at $T=25$ °C.

This attribution is also consistent with a mass balance: integration of j_{Al} during the cathodic dealloying step yields $420 \text{ nmol Al cm}^{-2}$, as compared with $63 \text{ nmol Zn cm}^{-2}$ obtained from the j_{Zn} transient during the anodic step. This yields a stoichiometry of Al/Zn=6.7, somewhat higher than the bulk composition of Al/Zn=5.2. The incomplete dissolution of the excess Zn(0) in the dealloyed layer is not surprising as the quantity of Zn dissolved depends strongly on potential. At $E_{\text{ap}} = -1.10$ V (**Fig. 5.9B**), the rate of Zn(0) dissolution was decreased by a factor of 5 (integration of peak gives $6.4 \text{ nmol Zn cm}^{-2}$), and at $E_{\text{ap}} = -1.20$ V (**Fig. 5.9C**) no Zn dissolution was observed.

SEM images following each potential pulse are shown in **Fig. 5.10**. At $E_{\text{ap}} = -1.60$ V, a rough surface was observed caused by highly selective dissolution of Al. Lighter spots are observed after $E_{\text{ap}} = -1.60$ V probably due to undissolved $\text{Al}(\text{OH})_3$. At $E_{\text{ap}} = -1.40$ V, Zn

V. Cathodic dealloying of Al and Al-Zn phase

oxide/hydroxide species could be seen at a grain boundary. These were identified as ZnO by Raman spectroscopy with characteristic Raman frequency of 345, 442 and 563 cm^{-1} [80,124]. The nature of the crystals was investigated at higher resolution in the middle right of **Fig. 5.10**. Grain boundary corrosion of Zn-Al alloys was observed by Devillers et al. [125] by polarization experiments and SEM characterization in $\text{pH}=9\sim 11$ electrolytes. They concluded that the cathodic reaction occurred at the tip of the corroding grain boundary was due to hydrogen evolution causing a local pH increase within the grain boundaries. For $\text{Al}_{5.2}\text{Zn}$ at $E_{\text{ap}} = -1.40$ V, locally increased concentration of OH^- in the grain boundaries could lead $\text{ZnO}/\text{Zn}(\text{OH})_2$ precipitation as:



At the more positive potentials, $E_{\text{ap}} = -1.20$ V, -1.10 V (not shown) and -1.00 V, the surface was not remarkably altered as compared to the surface after the humidity chamber. This may be attributed to less pronounced selective Al dissolution at these potentials.

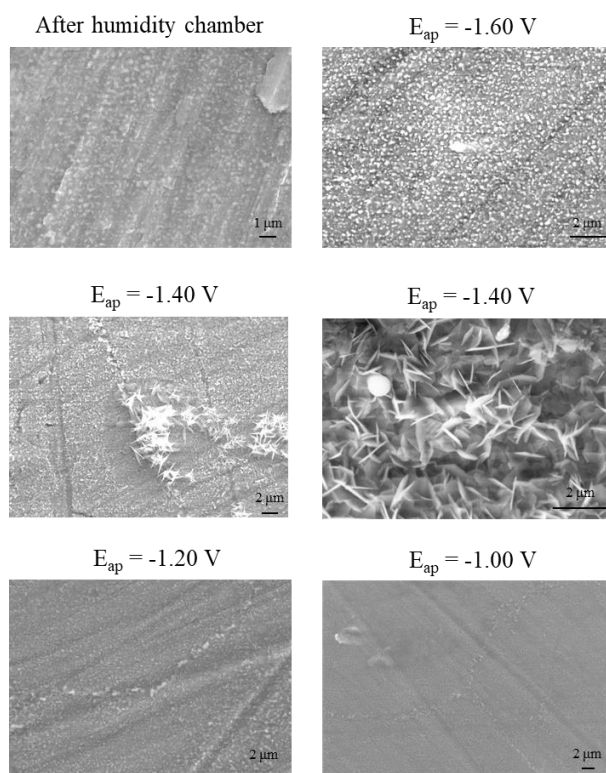
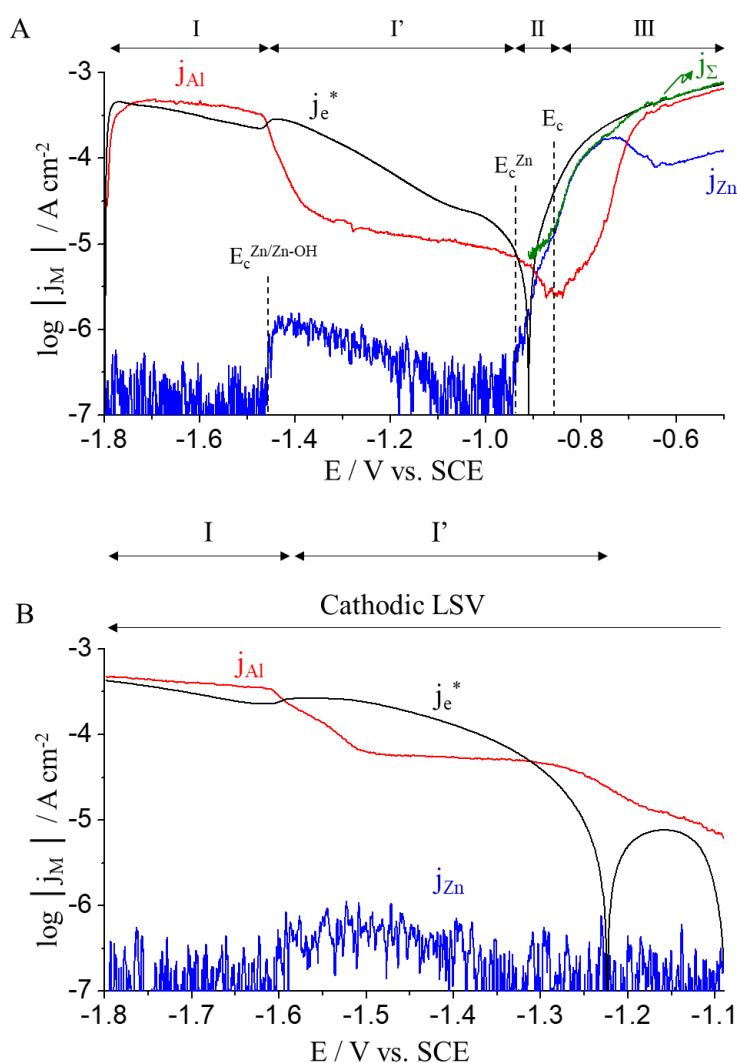


Fig. 5.10. SEM images of $\text{Al}_{5.2}\text{Zn}$ α -phase 1000 seconds after the CA experiments at $E_{\text{ap}} = -1.60$ V, -1.40 V, -1.20 V and -1.00 V in 30 mM NaCl, $\text{pH}=10.1$, electrolyte with Ar deaeration at $T=25$ °C, from **Fig. 5.8**. For $E_{\text{ap}} = -1.40$ V, a higher resolution image is present in the middle right showing crystal corrosion products. An equal mix of secondary electron and back-scattered electron detection was used.

5.3.5. The effect of O_2 on cathodic dealloying

The presence of O_2 in the electrolyte increases the cathodic reaction rate and may affect the anodic reactions in various ways. The AESEC-LSV for $Al_{5.2}Zn$ phase in O_2 saturated 30 mM NaCl, pH=10.1, is shown in **Fig. 5.11A**. The individual cathodic and anodic AESEC-LSV curves are shown in **Figs. 5.11B** and **5.11C** respectively. Cathodic Al dealloying was observed for $E < -1.46$ V (**Fig. 5.11A**) as previously described with a stoichiometric ratio slightly higher than observed in the Ar deaerated electrolyte (**Fig. 5.5** and **Table 5.1**). These results were qualitatively and quantitatively similar to the case of the deaerated electrolyte.



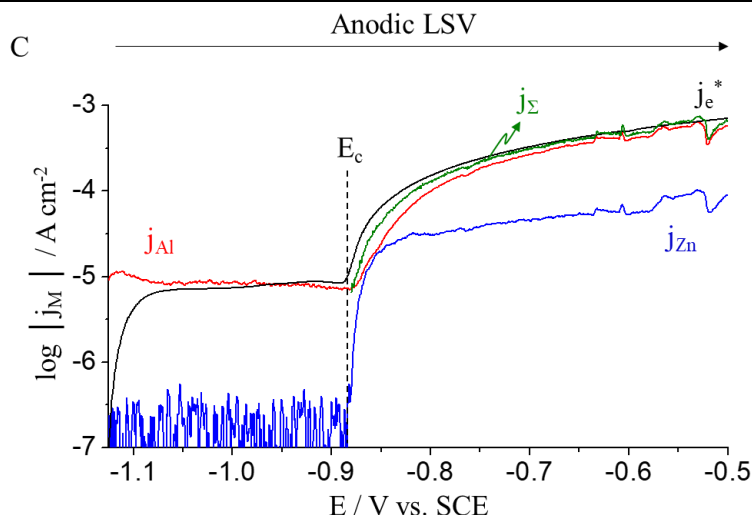


Fig. 5.11. Elemental AESEC-LSV curves of $\text{Al}_{5.2}\text{Zn}$ phase in O_2 saturated, 30 mM NaCl, pH=10.1, electrolyte at $T=25^\circ\text{C}$. Shown are **A**: cathodic to anodic LSV, **B**: cathodic LSV, **C**: anodic LSV with 0.5 mV s^{-1} scan rate.

From **Fig. 5.11A**, the cathodic dissolution of Zn was observed over a 200 mV range ($-1.46\text{ V} < E < -1.20\text{ V}$) and correlated with a substantial drop in j_{Al} by approximately a factor of 30. There was also a strong enhancement of the cathodic reaction in this potential range. The cathodic dissolution and its inhibitive effect on Al dissolution was confirmed by the cathodic LSV (**Fig. 5.11B**) and the CA at $E_{\text{ap}} = -1.40\text{ V}$ (**Fig. 5.12**). The $E_{\text{c}}^{\text{Zn/Zn-OH}}$ is the onset potential of cathodic Zn dissolution. Note that for the cathodic LSV starting at E_{oc} (**Fig. 5.11B**) the potential range of Zn dissolution was shifted to more negative potential ($-1.60\text{ V} < E < -1.40\text{ V}$) as compared to that in **Fig. 5.11A**, no doubt due to the slower increase in interfacial pH associated with the cathodic potential sweep. The anodic LSV with O_2 saturation, shown in **Fig. 5.11C**, demonstrates that O_2 has no discernable effect on anodic dissolution of $\text{Al}_{5.2}\text{Zn}$ with $E_{\text{c}} = -0.88\text{ V}$ for both electrolytes. For the CA experiment at $E_{\text{ap}} = -1.40\text{ V}$ (**Fig. 5.12**), the cathodic current (j_{c}^*) with O_2 saturation was 6 times more intense than with the Ar deaeration.

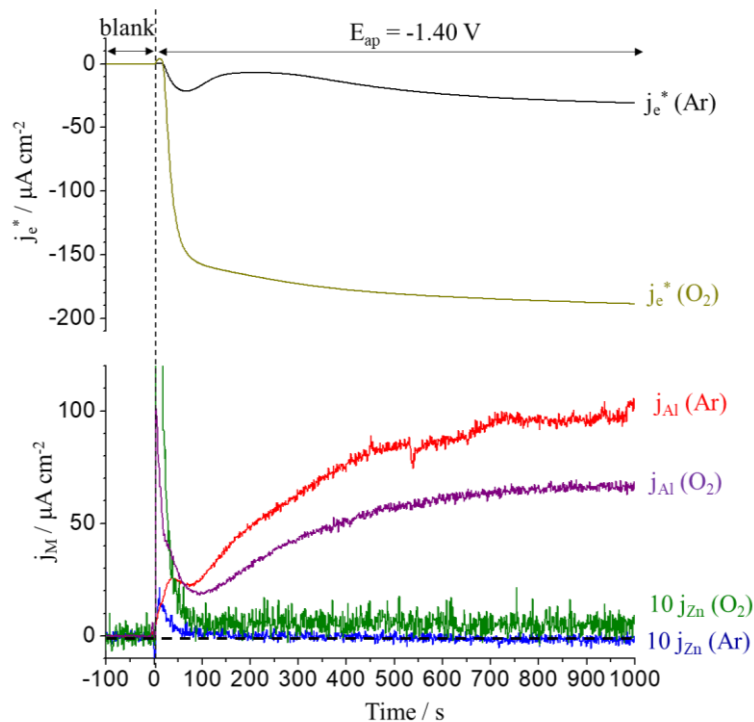
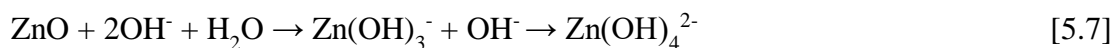


Fig. 5.12. AESEC-CA experiments of $\text{Al}_{5.2}\text{Zn}$ at $E_{\text{ap}} = -1.40$ V between Ar deaerated and O_2 saturated, 30 mM NaCl, pH=10.1, electrolyte at $T=25$ °C.

Insight into the mechanism of cathodic Zn dissolution may be gained from the SEM micrographs (**Fig. 5.13**) of the surface obtained after the CA experiment at $E_{\text{ap}} = -1.40$ V. With Ar deaeration (**Fig. 5.13A**), crystals of ZnO were clearly observed at what appears to be grain boundaries as in **Fig. 5.10**. In the O_2 saturated condition (**Fig. 5.13B**), however, these crystals were not observed. These results support the hypothesis that Zn oxidation occurs at $E = -1.40$ V especially around the grain boundaries. The cathodic dissolution of Zn occurs in the presence of saturation O_2 , because the ZnO formed will dissolve directly by complexation with OH^- generated by O_2 reduction. The overall reaction would be as follows;



where the hydroxide generated by the cathodic reaction drives **Eq. 5.7**.

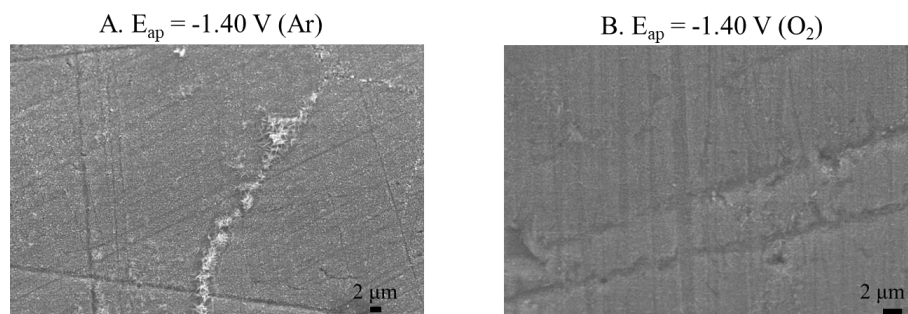


Fig. 5.13. SEM images after $E_{ap} = -1.40$ V in **A:** Ar deaerated and **B:** O_2 saturated electrolytes from **Fig. 5.12**.

5.4. Discussion

As stated in the introduction, the α -phase $Al_{5.2}Zn$, investigated here, and the $MgZn_2$ investigated previously [114], are representative of the extremes of Al and Mg content in the Zn-Al-Mg coating. Both phases were demonstrated to undergo dealloying reactions when polarized to cathodic potentials. In both cases, this results in the formation of a Zn(0) enriched layer. For $MgZn_2$, the Zn(0) enriched layer significantly reduced Mg dissolution [114]. However, the cathodic dealloying of α -phase $Al_{5.2}Zn$ was not restrained by this layer despite the fact that the quantity of Zn(0) in the enriched layer was approximately 9 times thicker for $Al_{5.2}Zn$ than for $MgZn_2$ intermetallic. (A mass balance in Ar deaerated solution from **Fig. 5.12**, predicts 155 nm of Zn(0) as compared to 17 nm from a similar experiment in [114], assuming a uniformly distributed, homogenous metallic Zn(0) layer.)

The consequence of this is that the $MgZn_2$ phase undergoes a type of passivity at open circuit as the Zn(0) layer forms and progressively hinders further dissolution. Further, the presence of Mg maintains the potential below E_c^{Zn} , preventing the dissolution of the Zn(0) film. The α -phase $Al_{5.2}Zn$ however remains active during cathodic polarization due to the high Al dissolution rate. In practice, this would suggest that the high %Al phase remains anodic to the high %Mg phase despite the fact that Mg is the less noble element in the Zn-Al-Mg coating. This may be understood if it is considered that the dealloyed Zn(0) layer is no doubt porous, and the cathodic reaction within the confined porosity would intensify the pH increase. The precipitation of $Mg(OH)_2$ in the porosity would most likely block the contact between the electrolyte and the underlying $MgZn_2$ phase. No similar effect would be predicted for the α -

phase Al-Zn pure phase, as the solubility of Al(III) oxides and hydroxides increases with pH due to the formation of $\text{Al}(\text{OH})_4^-$.

A schematic dealloying model of α -phase $\text{Al}_{5.2}\text{Zn}$ is proposed in **Fig. 5.14**. The cathodic dealloying of Al occurs in potential domain I forming a Zn(0) enriched layer. In the O_2 saturated electrolyte, Al dissolution is inhibited in domain I'. In domain II, $E_c^{\text{Zn}} < E < E_c$, Zn in the Zn(0) rich film dissolves independently of the Zn in the matrix. Finally, in domain III, $E > E_c$, both Al and Zn dissolve simultaneously.

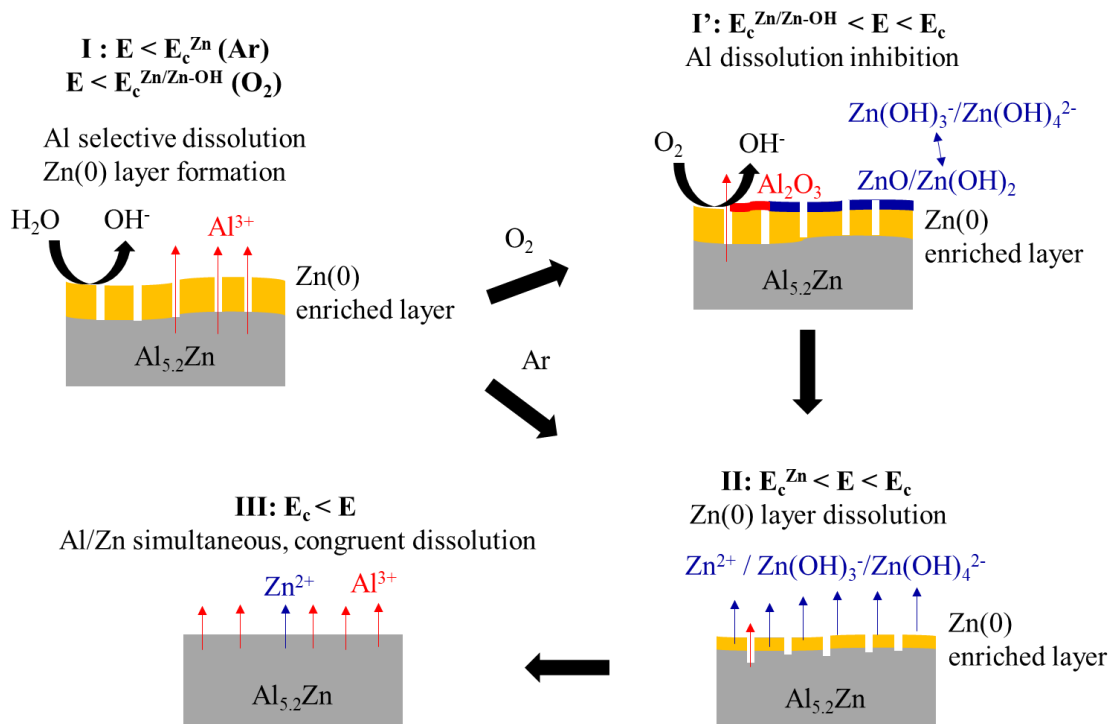


Fig. 5.14. Dealloying model of the dissolution of $\text{Al}_{5.2}\text{Zn}$ α -phase in the different potential domains (Ar deaerated and O_2 saturated, 30 mM NaCl, pH=10.1, electrolyte at $T=25^\circ\text{C}$). I: Zn(0) layer formation caused by selective Al dissolution, I' (O_2 saturation): Al dissolution inhibition and cathodic Zn dealloying coupled with O_2 reduction, II: dissolution of Zn(0) layer for $E > E_c^{\text{Zn}}$ and III: simultaneous, congruent dissolution of Al and Zn for $E > E_c$.

Pickering et al. [39] classified dealloying reactions as based on whether or not dissolution was selective at the critical potential. For Type I dealloying, the critical potential corresponds only to the onset of dissolution of the least noble element. For Type II dealloying, both elements dissolve congruently at the critical potential. The polarization curve of MgZn_2 intermetallic [114] showed a clear Type II behavior, as does the anodic LSV (**Fig. 5.6**) of $\text{Al}_{5.2}\text{Zn}$, in that j_{Al} increased simultaneously with j_{Zn} . However, the onset of cathodic dealloying of Al precludes application of the Pickering classification in that Al dissolution increases in the

cathodic direction and Zn dissolution in the anodic direction. For example, in the potential domain II of the cathodic to anodic LSV (**Fig. 5.4**), the enriched Zn(0) (more noble) is dissolved selectively with respect to Al (least noble). In the domain III, however, dissolution is congruent.

The nature of the cathodic reaction in the presence of saturated O₂ is not well understood. Saturated O₂ showed no effect on the cathodic current below the onset of cathodic Zn dissolution ($E < E_c^{Zn/Zn-OH}$, domain I) irrespective of the sweep direction (**Figs. 5.11A** and **5.11B**), suggesting that only water reduction occurred in this potential domain. This is surprising in that O₂ reduction was clearly observed on pure Al (**Fig. 5.2**) and pure Zn [114]. In the potential domain I' (**Figs. 5.11A** and **5.11B**), the cathodic reaction increased markedly. Simultaneously, j_{Al} decreased by an order of magnitude while j_{Zn} rose above the background level indicating cathodic Zn dissolution. The enhanced cathodic reaction suggests that O₂ reduction begins at this potential. The increase in j_{Zn} was described as due to the oxidation of the Zn followed by its dissolution as hydroxide complexes (Zn(OH)₃⁻ and Zn(OH)₄²⁻). The decrease in j_{Al} is more difficult to explain. It is possible that the higher redox potential associated with saturation O₂ might favor a more compact passive film less susceptible to reaction with hydroxide. In any case, the low dissolution rate of Zn and the absence of Zn based corrosion products would argue against an inhibitive mechanism induced by Zn corrosion products on Al dissolution. Dafydd et al. [53] observed that Zn metal, Zn-0.1Al and Zn-4.3Al showed clear 4e⁻ (n=4) pathway O₂ reduction reaction at pH=9.6 whereas for Zn-55Al, an apparent n=2.8 was determined. They attributed the low n value to O₂ reduction occurring only on the Zn rich zones of the Zn-55Al alloy. Cathodic Al dissolution of the α-phase of Al-Zn in the Zn-55Al could also contribute to an apparently low n value since the real cathodic current would be more intense than the measured cathodic current.

As an aid in predicting the coupling between the different phases in the technical coatings, a galvanic series was constructed for the alloys and metals investigated in this study. **Table 5.3** summarizes the potential values obtained for Al, Zn, and Mg metals, Zn-5Al, Zn-55Al commercial alloy coatings, the MgZn₂ intermetallic, and the α-phase Al₅Zn in Ar deaerated and O₂ saturation electrolyte. For Zn, Mg metals and the MgZn₂ intermetallic, these values were obtained from data from Ref. [114]. For the commercial alloys of Zn-5Al and Zn-55Al, the potential values were obtained in the same experimental condition. Based on the E_{oc}

V. Cathodic dealloying of Al and Al-Zn phase

data, the α -phase $Al_{5.2}Zn$ is cathodic to pure Al and anodic to both Zn-Al alloy coatings, pure Zn and $MgZn_2$. The more noble potential of the $MgZn_2$ is due to the formation of the Zn(0) film by selective dissolution of Mg.

Table 5.3. Comparison of potential values for Al, Zn, Mg metals, Zn-5Al, Zn-55Al commercial alloy coatings, $Al_{5.2}Zn$ and $MgZn_2$ pure phases.

$/V_{SCE}$	Al metal		$Al_{5.2}Zn$		Zn-55Al		Zn-5Al		Zn metal [114]		Mg metal [114]		$MgZn_2$ [114]	
	Ar	O ₂	Ar	O ₂	Ar	O ₂	Ar	O ₂	Ar	O ₂	Ar	O ₂	Ar	O ₂
E_{oc}	-1.44	-1.29	-1.31	-1.11	-1.22	-1.10	-1.12	-0.93	-0.98	-0.95	-1.65	-1.63	-1.06	-0.98
$E_{j=0}$	-1.41	-1.25	-1.28	-0.91	-1.30	-0.90	-1.31	-0.91	-1.21	-0.96	-1.64	-1.62	-1.21	-0.96
E_c^{Zn}	-	-	-1.14	-0.94	-1.10	-0.91	-1.12	-0.93	-1.10	-0.96	-	-	-0.96	-0.88
E_c	-	-	-0.88	-0.88	-	-	-	-	-	-	-	-		
$E_c^{Zn/Zn-OH}$	-	-	-	-1.46	-	-1.51	-	-1.61	-	-1.54	-	-	-	-1.57

The E_c^{Zn} values are nearly identical for $Al_{5.2}Zn$, Zn-55Al and Zn-5Al, which may indicate that the onset potential of Zn(0) enriched layer dissolution is determined independently of Al content. The $E_{j=0}$ values of $Al_{5.2}Zn$ in both Ar pure and O₂ saturation were nearly identical to those of Zn-55Al and Zn-5Al coatings. This suggests that the electrochemical behavior of the alloys is determined by the $Al_{5.2}Zn$ phase contained in these alloys. On the other hand, the spontaneous dissolution of Zn-5Al is controlled by the Zn of the Zn rich phase. Preferential dissolution of the ternary eutectic phase of Zn-Al-Mg alloys can be attributed to the more negative E_{oc} of $Al_{5.2}Zn$ as compared to that of the other phases present in the alloy coating.

This hypothesis is consistent with field exposure data of the coating alloys. Higher reactivity of the α -phase of Al-Zn was evidenced by the less noble potential observed by Ramus Moreira et al. [110] during atmospheric corrosion tests of the Zn-55Al alloy coating in six different exposure sites. The result showed that the Zn rich inter-dendritic phase of Zn-55Al was composed of one other Zn rich phase and the other Al rich phase (α -phase of Al-Zn). A preferential corrosion of Al rich phase in the inter-dendritic region was observed by SEM and X-ray energy dispersive spectroscopy (SEM-EDS) after five years of atmospheric exposure demonstrating that the significance of α -phase of Al-Zn phase for the corrosion of the Zn-Al alloys.

5.5. Conclusion

- 1) The α -phase $\text{Al}_{5.2}\text{Zn}$, and pure Al undergo a mechanism of cathodic dealloying due to the selective dissolution of Al during the application of a cathodic current. The stoichiometry of the reaction (v_e^*/v_{Al}) was between 1 and 2 consistent with **Eqs. 5.1** and **5.2**.
- 2) Cathodic dealloying led to the formation of a Zn(0) enriched layer. This layer did not inhibit further Al dissolution. This is very different from the previously studied MgZn_2 , in which the dealloyed film of Zn(0) did yield an inhibitive effect on Mg dissolution.
- 3) The Zn(0) layer dissolved at a potential, E_c^{Zn} , below the critical, onset potential, E_c of Zn in the $\text{Al}_{5.2}\text{Zn}$ matrix.
- 4) Al and Zn in the α -phase $\text{Al}_{5.2}\text{Zn}$ dissolved simultaneously for $E > E_c = -0.88$ V with almost 100% faradaic yield. The E_c was not affected by the precedent potential sweep or O_2 saturation in the electrolyte.
- 5) The cathodic dissolution of Zn was observed in O_2 saturated electrolyte for $E > E_c^{\text{Zn/Zn-OH}}$. This was attributed to the enhanced cathodic reaction due to the increased O_2 concentration resulting in the dissolution of ZnO/Zn(OH)_2 by complexation with OH^- .
- 6) The cathodic dissolution of Zn correlated with a simultaneous cathodic current increase and an order of magnitude decrease in the Al dissolution rate. The latter probably reflects a passivation of the Al due to reaction with O_2 .
- 7) The α -phase Al-Zn present in Zn-Al and Zn-Al-Mg alloy coatings maybe polarized anodically or cathodically depending on conditions. Cathodic Al dissolution observed in this work can be important to predict corrosion behavior of these alloys because the Al rich phase may supply Al^{3+} into solution contributing the formation of the corrosion resistant Zn-Al LDHs.

Chapter VI:

The anodic and cathodic dissolution of α -phase Zn-68Al in alkaline media

“인간과 짐승을 구별하는 것은 인륜을 가진 데만 있는 것이 아니라 기술을 소유하고 그걸 발전시켜 나가는 데 있다.”

다산 정약용

“What can differentiate between human beings and animals is not only having a morality but also having a technique and improving it.”

Yakyoung Jung (1762~1836)

Scholar of the realist school of Confucianism in the Joseon dynasty

This chapter repeats the article: Junsoo Han and Kevin Ogle, “The anodic and cathodic dissolution of α -phase of Zn-68Al phase in alkaline media” *Corrosion Science*, submitted in July 2018.

6. The anodic and cathodic dissolution of α -phase Zn-68Al in alkaline media

Abstract

The mechanisms of Zn and Al of a pure α -phase Al-Zn in a moderately alkaline electrolyte have been characterized using atomic emission spectroelectrochemistry to decouple the elementary dissolution rates. It was found that the selective dissolution of Al leads to the formation of a metallic Zn(0) surface layer. In the metallic form, this layer did not seem to affect the dissolution rate of Al. However, the oxidation of this layer led to a significant decrease in the Al dissolution rate, referred to as the negative correlation effect (NCE). These mechanisms were identified and characterized via linear sweep voltammetry and potentiostatic experiments.

Keywords: aluminum, zinc, selective dissolution, corrosion product

6.1. Introduction

Al-Zn alloys are commonly used in galvanized steel, and Zn-rich Al phases occur as constituent particles in the high strength 7000 series Al alloys [126–131]. Therefore, the reactivity of these phases with an alkaline electrolyte is of considerable interest for a number of applications. Most significant for this work is that high pH values may be reached during the corrosion of galvanized steel under atmospheric conditions, especially on the cut edge where the cathodic reaction may occur in close proximity to anodic reaction area [84,85,111,132], or when the galvanized steel is coupled to more noble materials such as bare steel in confined zones [133]. Galvanized steel may also be exposed to an alkaline environment when used as a reinforcement [134] or as a sacrificial anode [135] for concrete. Finally, alkaline cleaning is ubiquitous for galvanized steel and common for Al alloys such as the 7000 series which contains a high Zn content. In addition to removing oil, the alkaline treatment can alter the surface chemistry of the galvanized steel by dissolving pre-existing Al oxide layer and replacing it with Zn-O/-OH species [136–138].

The dissolution mechanisms of Zn [92,95,139,140] and Al [118,141,142] alone in alkaline media have been widely investigated. Bockris et al. [95] proposed multi-step Zn dissolution reactions in alkaline solution by the rotating-disk electrodes (RDE) measurement where the charge transfer reaction forming zincate ions was considered as the rate-determining step (rds) identified from the Tafel parameters. Mokaddem et al. [92] observed three types of Zn -O/-OH species formation depending on the potential during the polarization experiment coupled with atomic emission spectroelectrochemistry (AESEC) resulted in different dissolution mechanisms at each potential domain. For Al, Pyun et al. [118] investigated corrosion of pure Al in 0.01 M, 0.1 M and 1 M NaOH solutions by RDE and a.c. impedance spectroscopy. It was proposed that the Al dissolution mechanism in alkaline solution in the presence of the native oxide film can be explained as consecutive oxide film formation and dissolution, and simultaneous water reduction.

By contrast, very little information is available concerning the electrochemistry of Zn-Al alloys in alkaline solution. This may be due in part to the difficulty of interpreting the electrochemical experiments because of the difficulty in decoupling the contributions of Zn and Al. This decoupling requires measurement of the elemental dissolution rates. A particularity of the Zn-Al system and the focus of this paper is the profound interaction of Zn dissolution on Al dissolution that we refer to as the negative correlation effect (NCE). It was previously observed for Zn-5 wt.% Al, that the onset of Zn dissolution led to a simultaneous decrease in the Al

dissolution rate [93]. The origin of the phenomenon was not elucidated but it might be assumed that Zn corrosion products either block Al active sites or buffer the interfacial pH to lower values, making Al^{3+} corrosion products less soluble. However, in the previous work, interpretation was difficult because of the multiphase nature of this alloy, being essentially segregated into a nearly pure Al phase and a Zn-rich phase.

In the present study, the individual elemental dissolution mechanisms and also the interaction between Zn and Al using an Al-Zn pure phase in moderately alkaline solution were investigated for the first time. A pure phase alloy, Zn-68 wt.% Al (α -phase of Al) was used as representatives of high Al content of Zn-Al and Zn-Al-Mg alloy coating. The formation of a Zn(0) enriched surface layer by the selective dissolution of Al is clearly demonstrated by both potentiodynamic and potentiostatic experiments. The Zn(0) enriched surface layer has different electrochemical properties from the Zn-Al alloy as indicated by a cathodic shift in the onset potential for Zn dissolution. The effect of this layer on Al dissolution is presented for the first time.

6.2. Experimental

Materials

99.998 % Zn and 99.99 % Al metal obtained from *Goodfellow* were used as reference metal. Nominally pure η -phase of Zn (Zn-0.7 wt.% Al, denoted as Zn-0.7Al) and α -phase of Al (Zn-68 wt.% Al, denoted as $\text{Al}_{5.2}\text{Zn}$ based on its molar composition) were used in the present study. The Zn-Al pure phases were produced and characterized by the *Department of Metals and Corrosion Engineering, University of Chemistry and Technology, Prague*. Chemical composition of pure phases was chosen based on the Zn-Al phase diagram, obtaining a single phase after annealing and water quenching. A single η -phase of Zn (Zn-0.7Al) and α -phase of Al ($\text{Al}_{5.2}\text{Zn}$) with only a trace of η -phase of Zn were identified by X-ray diffraction (XRD).

In the present work, all the electrolytes were prepared from analytical grade materials with deionized water obtained by a MilliporeTM system (18 M Ω cm). The pH=12.80, 0.1 M NaOH electrolyte was prepared either deaerated by Ar or saturated by O₂ (Air Liquide, SA, 100% O₂ compressed gas) bubbling Ar or O₂ for 30 minutes prior to the experiments and maintaining the gas flow during the experiments. Deaeration with Ar was to minimize the effect of cathodic current then have a better correlation between elemental dissolution rate and anodic current

density. Saturation with O₂ was to see the effect of O₂ on the elemental dissolution without mixing with other gas present in the air such as CO₂.

A Gamry Reference 600TM potentiostat was used to measure and control the electrochemical potential (E) and current density (j_e). AESEC linear sweep voltammetry (AESEC-LSV) was performed following to 1000~2000 s of spontaneous dissolution measurement, starting from -1.72 V to -0.42 V with 0.5 mV s⁻¹ scan rate. Anodic-going and cathodic-going LSV (anodic and cathodic LSV, respectively) were also conducted starting potential scan from the open circuit potential (E_{oc}) to -0.42 V and -1.72 V, respectively. The objective of anodic and cathodic LSV is to reduce the effect of surface modification maybe caused by the previous potential sweep. In order to separate the effect of potential and time, chronoamperometry (CA) were conducted by choosing constant potentials (E_{ap}) based on the AESEC-LSV experiment.

The AESEC technique

The working electrode is in contact with an electrochemical flow cell chamber (≈ 0.2 cm³) where a reference electrode and counter electrode (Pt foil) are located, separated by a porous membrane. All potential values presented in this work are referenced to an Hg/HgO in 0.1 M NaOH (-165 mV vs. SHE) electrode. Dissolved elements from the working electrode are brought to an Ultima 2C Horiba Jobin-Yvon inductively coupled plasma atomic emission spectrometer (ICP-AES) equipped with a Paschen-Runge polychromator (focal distance 0.5 m) with an array of thirty photomultipliers for the simultaneous measurement of different elements and a N₂ purged Czerny-Turner monochromator (focal distance 1.0 m) to obtain a higher spectral resolution of a single element. In this work, the time resolved concentration of Zn and Al were determined from the emission intensity of the plasma monitored at 213.86 nm and 167.08 nm respectively by using standard ICP-AES calibration technique.

Data analysis

Elemental concentration (C_M, M=Al and Zn in this work) measured by AESEC technique can be used to calculate elemental dissolution rate (v_M) then simultaneously can be

VI. Interaction between Zn and Al dissolution in alkaline media

compared with the electrochemical current density (j_e^*). An equivalent elemental current density j_M can be calculated by Faraday constant F as;

$$j_M = zF v_M \quad [6.1]$$

where z is the valence of the dissolving ions. The ICP-AES detects only the soluble components of the reaction. Oxide and other insoluble corrosion products may form on the surface. These species may, under certain circumstances, be quantified by a mass-charge balance. The total electrical current is the sum of the anodic and cathodic partial currents, $j_e^* = j_a + j_c$. The anodic partial current may be decomposed into a soluble component, j_Σ , (where j_Σ is the sum of dissolution currents, $= j_{Zn} + j_{Al}$) and an insoluble component, j_{ins} indicating the formation rate of the unmeasurable insoluble species which remain on the surface of the sample in the form of a corrosion product such as oxide film.

$$j_e^* = j_\Sigma + j_{ins} + j_c \quad [6.2]$$

By a mass balance equation, j_Δ is introduced referring to the different between electrical current and the sum of the dissolution currents:

$$j_\Delta = j_e^* - j_\Sigma \quad [6.3]$$

If $j_\Delta > 0$, undissolved species formation may be predicted. If $j_\Delta < 0$, cathodic current, j_c , can be calculated assuming no insoluble species formation. Note that j_e^* is the convoluted value of j_e taking into consideration of the residence time distribution in the flow cell which enables comparison with j_M . The faradaic yield of elemental dissolution may be determined as $\eta = j_\Sigma / j_e^*$ when $j_\Delta = 0$ from **Eq. 6.3**.

Surface characteristics

The material surface before and after electrochemical experiments was characterized by scanning electron microscopy (SEM) using a Zeiss Leo 1530TM microscope with field emission gun (FEG) source at 15 keV, 15 mm working distance. A Renishaw InviaTM confocal Raman microscope was used to identify oxide species on the sample surface after each electrochemical tests with excitation by a Co diode pumped solid state (DPSS) using a green laser (532 nm). WireTM software was used for the acquisition and evaluation of Raman spectra.

6.3. Results

6.3.1. Spontaneous dissolution

The spontaneous elemental dissolution of nominally pure Zn and Al metal as a function of time was determined by AESEC. Typical “dissolution profiles” are shown in **Figs. 6.1 and 6.2** displaying the spontaneous Zn and Al dissolution rates (j_{Zn} and j_{Al}) and open circuit potential (E_{oc}) as a function of time for pH=12.80, 0.1 M NaOH electrolyte in both Ar deaerated and O₂ saturated electrolytes. The specimen was brought into contact with the electrolyte at t=0.

The Zn dissolution rate (j_{Zn}) increased markedly by the addition of O₂ as shown in **Fig. 6.1**. For pure Zn, O₂ saturation led to a 2.5x increase in j_{Zn} and a 580 mV increase in E_{oc} . This result demonstrates that O₂ is the major oxidizing agent for the dissolution of Zn.

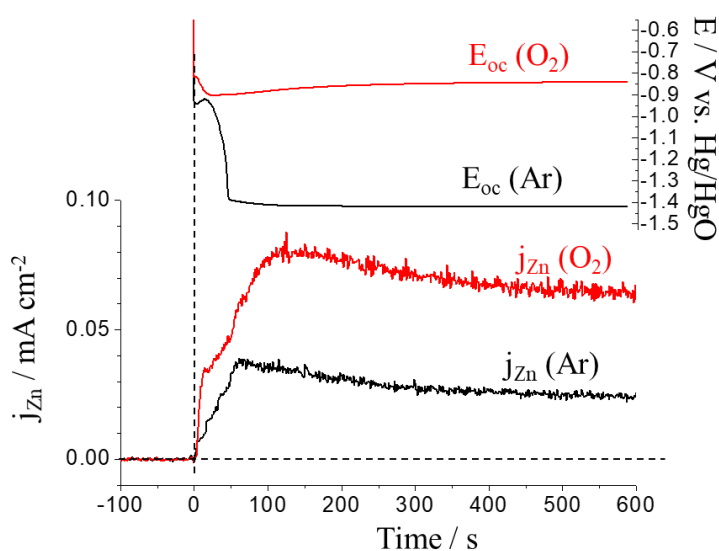


Fig. 6.1. Spontaneous elemental dissolution rate (j_{Zn}) and E_{oc} for pure Zn exposed to a 0.1 M NaOH, pH=12.80 electrolyte with Ar deaeration and O₂ saturation at T=20 °C.

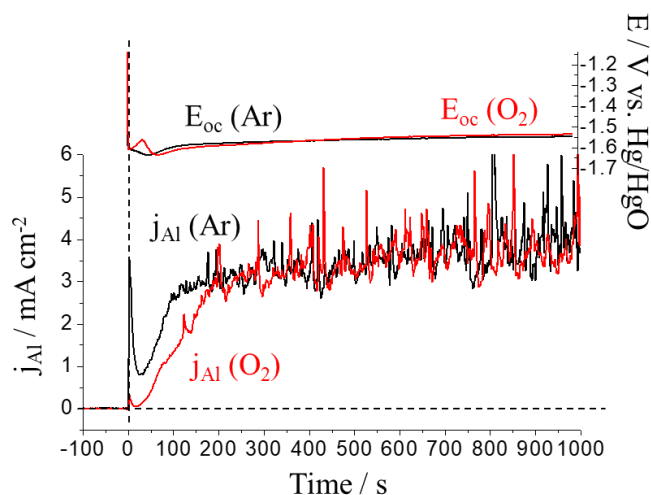


Fig. 6.2. Spontaneous elemental dissolution rate (j_{Al}) and E_{oc} for pure Al exposed to a 0.1 M NaOH, pH=12.80 electrolyte with Ar deaeration and O₂ saturation at T=20 °C.

VI. Interaction between Zn and Al dissolution in alkaline media

For Al metal (**Fig. 6.2**), however, j_{Al} and E_{oc} were not measurably affected by the presence of O_2 . This may be understood by the fact that the Al dissolution was approximately 100x more rapid than Zn dissolution in the deaerated electrolyte. Therefore, the contribution of O_2 reduction, if it existed, would not have been detectable. In this sense, it can be concluded that water reduction was the major cathodic reaction on Al at pH=12.80.

A similar trend is observed for the spontaneous dissolution of Zn-Al pure phases are shown in **Fig. 6.3**. For Zn-0.7Al (**Fig. 6.3A**), j_{Zn} was increased in O_2 saturation electrolyte with respect to Ar deaeration, while j_{Al} was not affected by O_2 saturation (**Figs. 6.1** and **6.2**). For $\text{Al}_{5.2}\text{Zn}$ (**Fig. 6.3B**), j_{Al} values in both electrolytes were reasonably identical to each other while no Zn dissolution was observed. This indicates that a significant selective Al dissolution occurred regardless of absence/presence of O_2 . The $E_{\text{oc}}(\text{Ar}) = -1.53$ V and $E_{\text{oc}}(\text{O}_2) = -1.51$ V of $\text{Al}_{5.2}\text{Zn}$ were close to the E_{oc} of pure Al demonstrating that Al dissolution was dominant during spontaneous dissolution for $\text{Al}_{5.2}\text{Zn}$ phase.

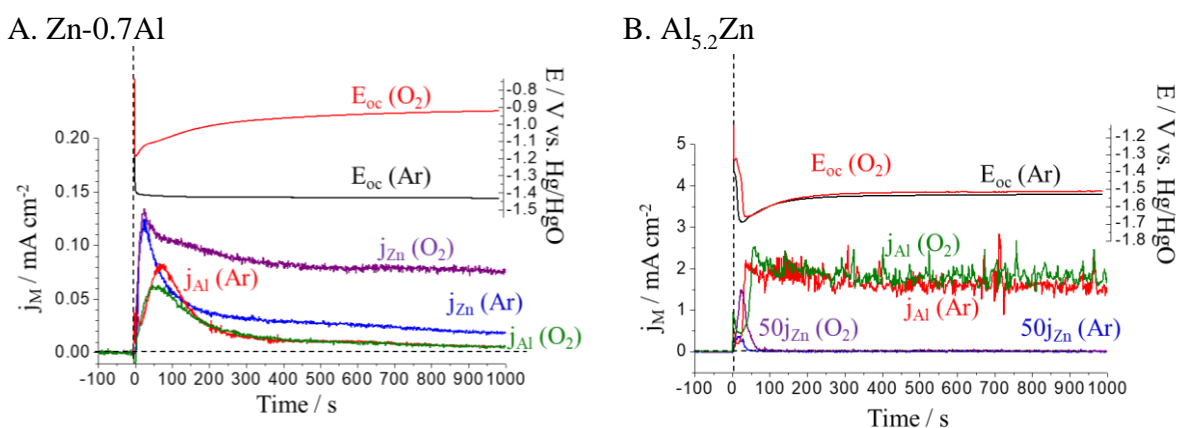


Fig. 6.3. Spontaneous elemental dissolution rate (j_M) and E_{oc} for **A:** Zn-0.7Al, **B:** $\text{Al}_{5.2}\text{Zn}$, exposed to a 0.1 M NaOH, pH=12.80 electrolyte with Ar deaeration and O_2 saturation at $T=20$ °C.

The steady state elemental dissolution rates and E_{oc} for all specimens investigated in this work are summarized in **Table 6.1**. The elemental dissolution behavior and reactivity with O_2 of Zn-0.7Al and $\text{Al}_{5.2}\text{Zn}$ phases were similar to pure Zn and Al, respectively. For the Zn-0.7Al phase, the average steady state Al dissolution rate (j_{Al}^{s}) was very low with Ar deaeration (7 ± 1 $\mu\text{A cm}^{-2}$) and insensitive to O_2 . The average steady state Zn dissolution rate (j_{Zn}^{s}) was nearly equivalent to pure Zn and increased by a factor of 3.9x with O_2 saturation. The $\text{Al}_{5.2}\text{Zn}$ phase

VI. Interaction between Zn and Al dissolution in alkaline media

showed an extremely low Zn dissolution rate: undetectable in Ar deaerated electrolyte, approximately $0.4 \pm 0.2 \mu\text{A cm}^{-2}$ in O_2 saturated electrolyte. The j_{Al}^{s} was lowered by a factor of 2 as compared to pure Al and again, was independent of O_2 saturation within experimental error.

Table 6.1. The average steady state values (j_{M}^{s}) and open circuit potential (E_{oc}) in spontaneous dissolution for pure Zn, Al, Zn-0.7Al and $\text{Al}_{5.2}\text{Zn}$ in 0.1 M NaOH, pH=12.80, Ar deaerated and O_2 saturated electrolytes at $T=20^\circ\text{C}$.

	$j_{\text{Zn}}^{\text{s}} / \mu\text{A cm}^{-2}$		$j_{\text{Al}}^{\text{s}} / \text{mA cm}^{-2}$		$E_{\text{oc}} / \text{V vs. Hg/HgO}$	
	Ar	O_2	Ar	O_2	Ar	O_2
Pure Zn	25 ± 1	64 ± 2	-	-	-1.42	-0.84
Pure Al	-	-	4.0 ± 0.9	3.7 ± 0.5	-1.55	-1.53
Zn0.7Al	20 ± 2	77 ± 2	0.007 ± 0.001	0.006 ± 0.001	-1.43	-0.92
$\text{Al}_{5.2}\text{Zn}$	-	0.4 ± 0.2	1.6 ± 0.2	1.8 ± 0.1	-1.53	-1.51

6.3.2. The electrochemistry of pure Al

Before considering the complex electrochemistry of the Zn-Al system, it is important to overview the chemistry of the alloy components alone as a point of reference. As will be shown, the AESEC technique permits measurement of the elemental dissolution rates even when the electrical current is cathodic, revealing a significant complexity to the electrochemistry of the individual elements these materials which is not apparent in the conventional polarization curves. AESEC linear sweep voltammetry (AESEC-LSV) experiments, starting from -1.72 V to -0.42 V with 0.5 mV s^{-1} scan rate, were performed for pure Al (**Fig. 6.4**) and pure Zn (**Fig. 6.5**).

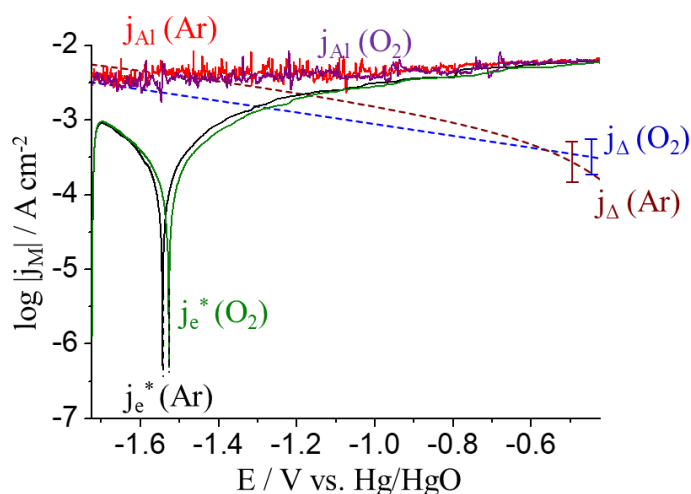


Fig. 6.4. Elemental AESEC-LSV curves of pure Al in 0.1 M NaOH, pH=12.80 electrolyte with Ar deaeration and O_2 saturation at $T=20^\circ\text{C}$.

VI. Interaction between Zn and Al dissolution in alkaline media

The AESEC linear sweep voltammetry (AESEC-LSV) of pure Al in Ar deaerated and O₂ saturated electrolytes are shown in **Fig. 6.4**. This curve presents the total current density (j_e^*) and the elemental dissolution rates expressed as a current densities (j_M) as a function of potential. A very large Al dissolution rate was observed ($j_{Al} \approx 3 \text{ mA cm}^{-2}$) throughout the potential sweep, nearly independent of potential for $E < -0.9 \text{ V}$, slightly increasing for $E > -0.9 \text{ V}$. The potential independent Al dissolution in the cathodic potential domain was observed in a Zn-5Al alloy in the same electrolyte condition [93]. Saturating the electrolyte with O₂, had no measurable effect on either j_{Al} or j_e^* which implies that the major cathodic reaction is hydrogen evolution from the reduction of water. The cathodic reaction rate may be determined directly from mass balance as $j_c = j_{\Delta} = j_e^* - j_{Al}$ (**Eq. 6.3**). j_{Δ} is also shown in **Fig. 6.4**. In fact, j_{Δ} showed nearly identical trend in both deaerated and O₂ saturated, within experimental error again demonstrating that the effect of O₂ is undetectable under the conditions of these experiments.

The fact that Al dissolution is independent of potential at pH=12.80 indicates that the dissolution rate is controlled by the steady state formation and dissolution of the passive film, most likely Al(OH)₃. The net reactions may be written as



At pH=12.80, hydroxide is provided by the electrolyte and is therefore potential independent. At lower pH, the OH⁻ is provided by the cathodic reaction leading to a dissolution rate that is proportional to the cathodic current, referred to as cathodic dissolution of Al [143].

The mass balance provides a rigorous measure of the true cathodic reaction rate through the experiment, however the intensity of the cathodic reaction may also be seen in the perturbations of the j_{Al} signal apparent in **Figs. 6.1, 6.3B** and **6.4**. These perturbations are due to the formation H₂ bubbles which, when carried into the plasma, momentarily disturb the nebulization system. These perturbations, quantitatively estimated by the standard deviation of the signal, $\sigma_{j_{Al}}$, may be used to identify situations where dissolution is driven by the hydrogen evolution reaction (perturbed signals present) or by cation migration across a passive film (no perturbed signals). It can be seen in **Fig. 6.4** that $\sigma_{j_{Al}}$ decreased from with increasing potential. This correlates with the decrease in the cathodic current as determined from $j_c = j_{\Delta}$.

6.3.3. *The electrochemistry of pure Zn*

The AESEC-LSV of pure Zn in deaerated solution is given in **Fig. 6.5A**, showing j_e^* , j_{Zn} and j_Δ , as for pure Al. For ease of reference, $E_{j=0}$ is the potential where $j=0$ (zero-current potential), and E_c^{Zn} is the onset potential for Zn dissolution as indicated in the **Fig. 6.5A**. Four potential domains are indicated in **Fig. 6.5A** as labelled. (I) $E < E_c^{Zn}$: the cathodic domain where j_{Zn} was under the detection limit. (II) the Tafel domain where j_{Zn} rose above the detection limit and increased exponentially with potential. (III) the peak maximum domain where j_{Zn} maintained a maximum value during around 150 mV independent of potential sweep. In this domain, the j_e^* curve shows two anodic peaks, labelled a_1 and a_2 . These are most clearly visible under O_2 saturation (**Fig. 6.5B**). (IV) the passive domain where both j_{Zn} and j_e^* decreased to obtain a steady state independent of potential. In Ar deaerated electrolyte (**Fig. 6.5A**), a nearly 100 % faradaic dissolution ($\eta \approx 1$) was observed throughout the anodic potential sweep (from domain II to IV) indicating that anodic dissolution was the major reaction and oxide formation was undetectable. The $E_c^{Zn} = -1.47$ V shifted 50 mV below the $E_{j=0}$. In the domain II, j_{Zn} increased exponentially with current obtaining an effective Tafel slope of 36 mV decade⁻¹ determined from j_{Zn} over nearly 2 orders of magnitude. The overall form of the elemental Zn dissolution curve is consistent with previous work [92,93,144].

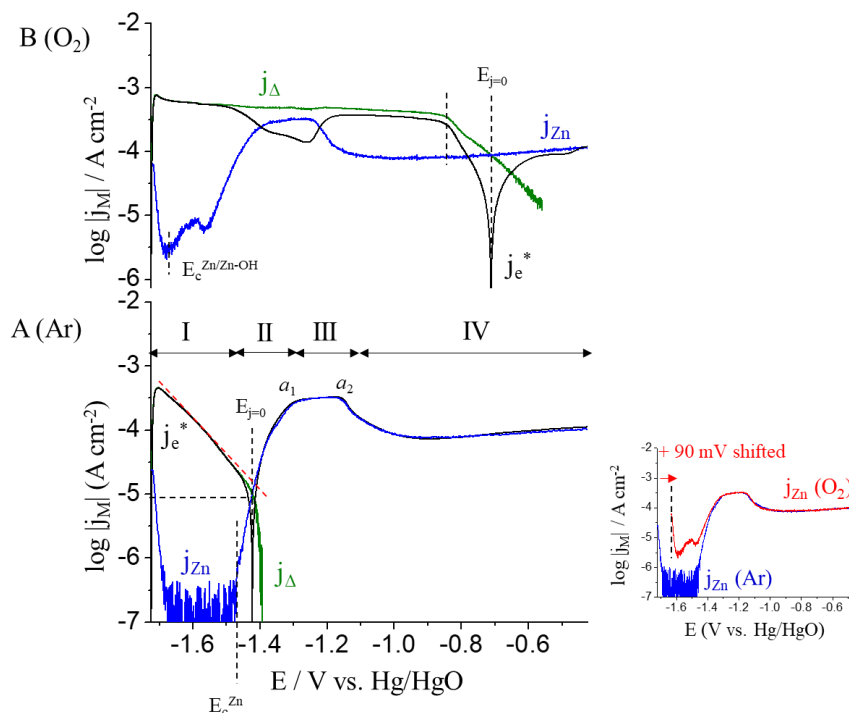


Fig. 6.5. Elemental AESEC-LSV of pure Zn in 0.1 M NaOH, pH=12.80 electrolyte with **A**: Ar deaeration, **B**: O₂ saturation at T=20 °C. On the right of **A**, a superimposed j_{Zn} vs. E for both electrolytes is given. For O₂ saturation, j_{Zn} was shifted to +90 mV to facilitate the comparison.

In the absence of O₂ (**Fig. 6.5B**), in domain I, the hydrogen evolution reaction (HER) was the major contributing factor to the cathodic current density. Zn oxidation and dissolution were negligible, therefore, $j_{\Delta} = j_c$ from **Eqs. 6.2** and **6.3**. The apparent cathodic Tafel slope determined from j_{Δ} was 154 mV decade⁻¹ is consistent with mechanisms involving adsorbed H intermediates (M-H) such as the Heyrovsky mechanism:



for which Tafel slopes of around 120 mV decade⁻¹ are commonly observed [53,145–150].

Unlike Al, the pure Zn showed a significant aptitude for O₂ reduction. In O₂ saturated electrolyte (**Fig. 6.5B**), the cathodic current was significantly increased ($j_{\Delta} = j_c \approx -400 \mu\text{A cm}^{-2}$) and occurred over a much wider potential range ($-1.72 \text{ V} \leq E < -0.71 \text{ V}$) as compared to that in Ar deaerated electrolyte (**Fig. 6.5A**, $-1.72 \text{ V} \leq E < -1.42 \text{ V}$). Zn dissolution was observed in the cathodic potential domain as indicated in the $\log |j_e^*|$ by an inverse peak which correlated perfectly with the j_{Zn} dissolution transient. The onset potential of Zn dissolution in the cathodic

VI. Interaction between Zn and Al dissolution in alkaline media

potential domain is denoted as $E_c^{Zn/Zn-OH}$ considering the formation of Zn-O/-OH species. j_Δ vs. E curve showed a nearly constant value from -1.72 V to -0.84 V, indicative of diffusion limited O_2 reduction.

As the cathodic reaction rate, indicated by j_Δ , decreased for $E > -0.84$ V, j_e^* approached j_{Zn} , and for $E > E_{j=0}$, the faradaic yield, η , approached 1 as in the deaerated case (**Fig. 6.5A**). The $E_{j=0}$ was shifted into the passive domain of Zn dissolution, consistent with the large positive potential shift of E_{oc} with O_2 saturation observed in **Fig. 6.1**. Zn dissolution for $E > E_c^{Zn-ZnOH}$ was not affected by the presence of O_2 in that the j_{Zn} vs. E characteristic curves superimposed perfectly with the exception of a 90 mV cathodic shift in the presence of O_2 (see inset in **Fig. 6.5**). The effective Tafel slopes determined from j_Δ , j_e^* (Ar) and j_{Zn} (Ar and O_2) are summarized in **Table 6.2**. Potential values obtained from the AESEC-LSV experiments are also provided in **Table 6.3**.

Table 6.2. Tafel slopes in the cathodic potential domain determined from j_Δ and j_e^* for pure Zn, Zn-0.7Al and $Al_{5.2}Zn$ from the AESEC-LSV. Tafel slopes in the anodic potential domain determined from j_{Zn} are also provided.

	Cathodic j_Δ /mV decade ⁻¹	Cathodic j_e^* /mV decade ⁻¹	j_{Zn} /mV decade ⁻¹	
	Ar	Ar	Ar	O_2
Pure Zn	160	162	36	76
Zn-0.7Al	184	184	35	109
$Al_{5.2}Zn$	207	212	85/10	42/23

Table 6.3. Potential values obtained from the AESEC-LSV for pure Zn, Al, and $Al_{5.2}Zn$ phases.

V vs. Hg/HgO	E_c^{Zn}		$E_{j=0}$	
	Ar	O_2	Ar	O_2
Pure Zn	-1.47	$E_c^{Zn/Zn-OH} = -1.56$	-1.42	-0.71
Pure Al	-	-	-1.54	-1.53
$Al_{5.2}Zn$	-1.37	-1.45	-1.51	-1.49

Individual cathodic and anodic going polarization experiments were conducted starting from E_{oc} to -1.72 V and to -0.42 V respectively, were performed in order to minimize the surface

VI. Interaction between Zn and Al dissolution in alkaline media

modification which may be caused by the preceding potential sweep, denoted as cathodic LSV and anodic LSV respectively. The cathodic LSV of pure Zn in Ar deaerated and O₂ saturated electrolytes are shown in **Figs. 6.6A** and **6.6B**. Both systems gave an E_{oc} around -0.9 V, in the passive domain (IV) of Zn dissolution in Fig. 4. This is consistent with the initial potentials of **Fig. 6.1** for both systems. In the domain IV, j_{Zn} = 56 ± 2 μA cm⁻² for Ar deaerated and j_{Zn} = 70 ± 4 μA cm⁻² for O₂ saturated electrolytes, both nearly independent of potential sweep. Interestingly, j_{Zn} > j_e^{*} (j_Δ < 0) throughout the cathodic LSV which may mean that the cathodic current was always present. The anodic LSV, not shown, showed almost 100 % faradaic dissolution under both Ar deaeration and O₂ saturation.

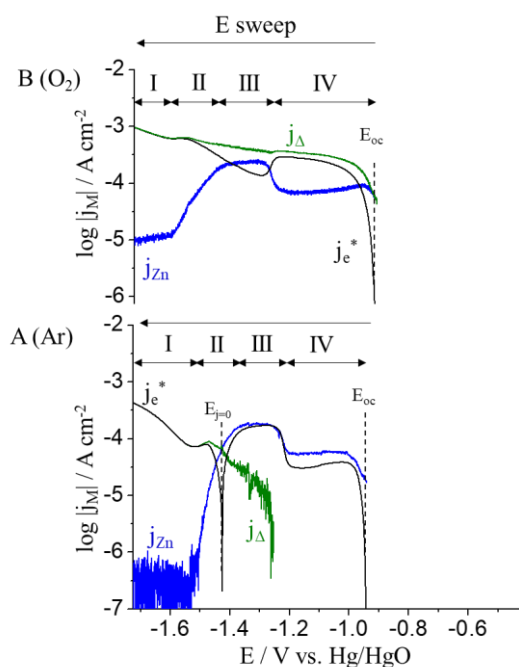


Fig. 6.6. Elemental AESEC cathodic polarization (cathodic LSV) curves of pure Zn in 0.1 M NaOH, pH=12.80 electrolyte with **A:** Ar deaeration and **B:** O₂ saturation at T=20 °C. The potential was swept from E_{oc} to -1.72 V with 0.5 mV s⁻¹ scan rate following an open circuit exposure for 10 s.

6.3.4. The electrochemistry of Al_{5,2}Zn

The AESEC-LSV for Al_{5,2}Zn in Ar deaerated electrolyte is depicted in **Fig. 6.7A**. The Zn partial current, j_{Zn} vs. E, showed a similar trend to that of pure Zn (**Fig. 6.5A**) and the different domains I – IV are indicated on the figure based on the j_{Zn} curve. For E < E_c^{Zn} = -1.32 V (domain I), no measurable j_{Zn} was observed whereas j_{Al} was remained at the same level as the spontaneous Al dissolution, j_{Al}^s (see **Fig. 6.7B**), and was independent of potential. This is indicative of the selective dissolution of Al, leading to the formation of a metallic Zn enriched surface layer Zn(0).

The negative correlation effect, described in the introduction, is evident in the potential domain II. In domain II (a), j_{Zn} started to increase above the detection limit while j_{Al} was at the same level as during the preceding potential sweep. In the potential domain II (b), j_{Zn} abruptly increased and this increase was correlated with an equally abrupt decrease in the j_{Al} . In the domain III, j_{Zn} reached at a maximum value while j_{Al} decreased to a minimum value. This negative correlation effect (NCE) was previously observed for the Zn-5Al alloy coating in a similar electrolyte [93]. It is also of interest to note that Zn dissolution seemingly occurred in two potential domains with effective Tafel slopes determined from j_{Zn} as (a) 85 mV decade⁻¹ and (b) 10 mV decade⁻¹.

The dissolution rate in the passive domain IV ($E > -1.1$ V) is most likely due to the migration of Al^{3+} across the Zn oxide film. The rate of obtained since the j_{Al} , j_{Zn} and j_e^* show only a modest variation with potential. The change in mechanism is indicated by the amplitude of the Al signal perturbations as well: a relatively large $\sigma_{j_{\text{Al}}}$ in domain I, indicative of H_2 evolution, while $\sigma_{j_{\text{Al}}}$ is significantly reduced in the passive domain IV.

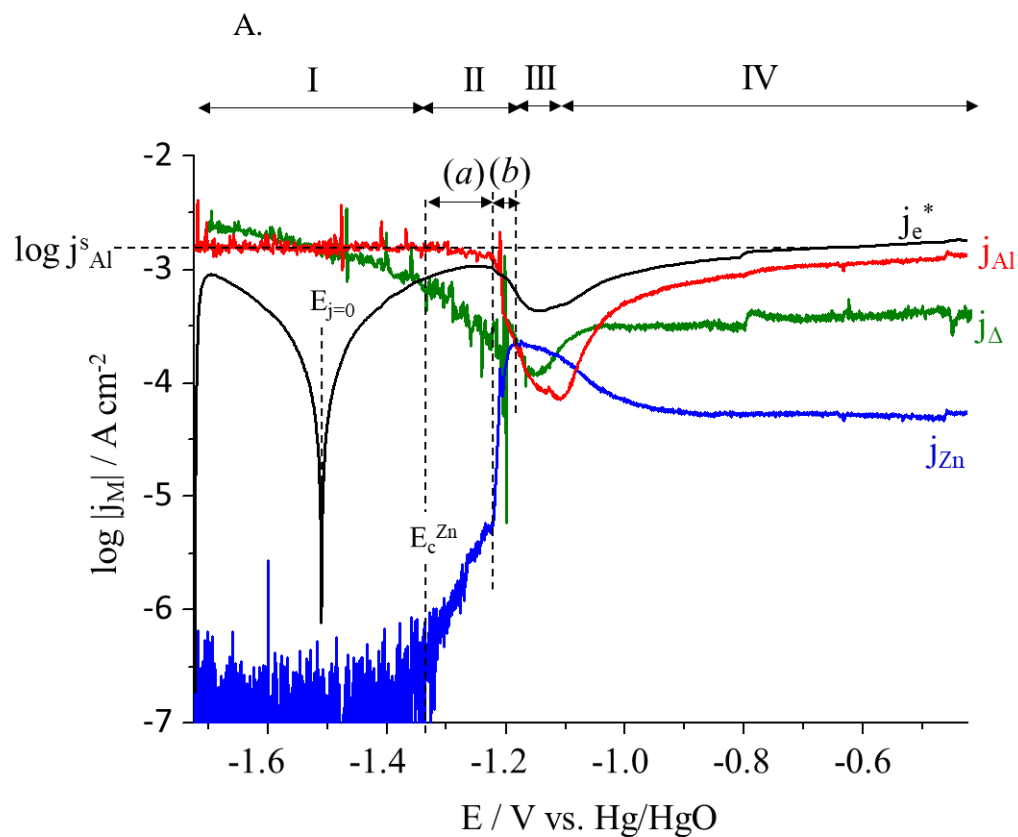
The nature of the oxide films formed during the LSV experiment may be investigated by considering the open circuit dissolution profiles before and after the LSV experiment shown in left hand side of **Fig. 6.7B**. Before the LSV, selective Al dissolution was observed during initial open circuit potential (E_{oc}) with $j_{\text{Al}}^{\text{s}} = 1.6 \pm 0.2$ mA cm⁻² with j_{Zn} below the detection limit, nearly identical to that measured during the domain I of the cathodic sweep.

However, after the LSV, right hand side of **Fig. 6.7B**, the E_{oc} period shows evidence for the dissolution of a Zn oxide film and its effect on the Al dissolution rate. Observed are two unique domains. At first, a potential plateau near -1.43 V during approximately 250 s bounded by an abrupt decrease to -1.58 V, marked as t_1 . This period is consistent with the dissolution of the oxides formed during the potential sweep and is confirmed by the transient dissolution of Zn (j_{Zn}) during the potential plateau. Following this period, the system attains a near steady state open circuit potential with E_{oc} rising slowly to -1.53 V, nearly identical to the potential of spontaneous dissolution prior to the LSV (left side of **Fig. 6.7B**).

The effect of the oxide film on the Al dissolution rate is also indicated by this result. When the potential is released, j_{Al} decreases by a factor of 5 and slowly increases as the Zn

VI. Interaction between Zn and Al dissolution in alkaline media

oxide film dissolves, ultimately achieving the initial open circuit dissolution rate, j_{Al}^{s} . Integration of the j_{Zn} peak in t_1 gives 32 nmol cm^{-2} Zn, corresponding to 3.7 nm of ZnO assuming a uniform distribution and the standard ZnO density (5.61 g cm^{-3}). The slow increase of j_{Al} during t_1 demonstrates that the ZnO film was a barrier to Al dissolution consistent with the conclusions concerning domain II (b) in **Fig. 6.7A**, showing a negative correlation effect (NCE).



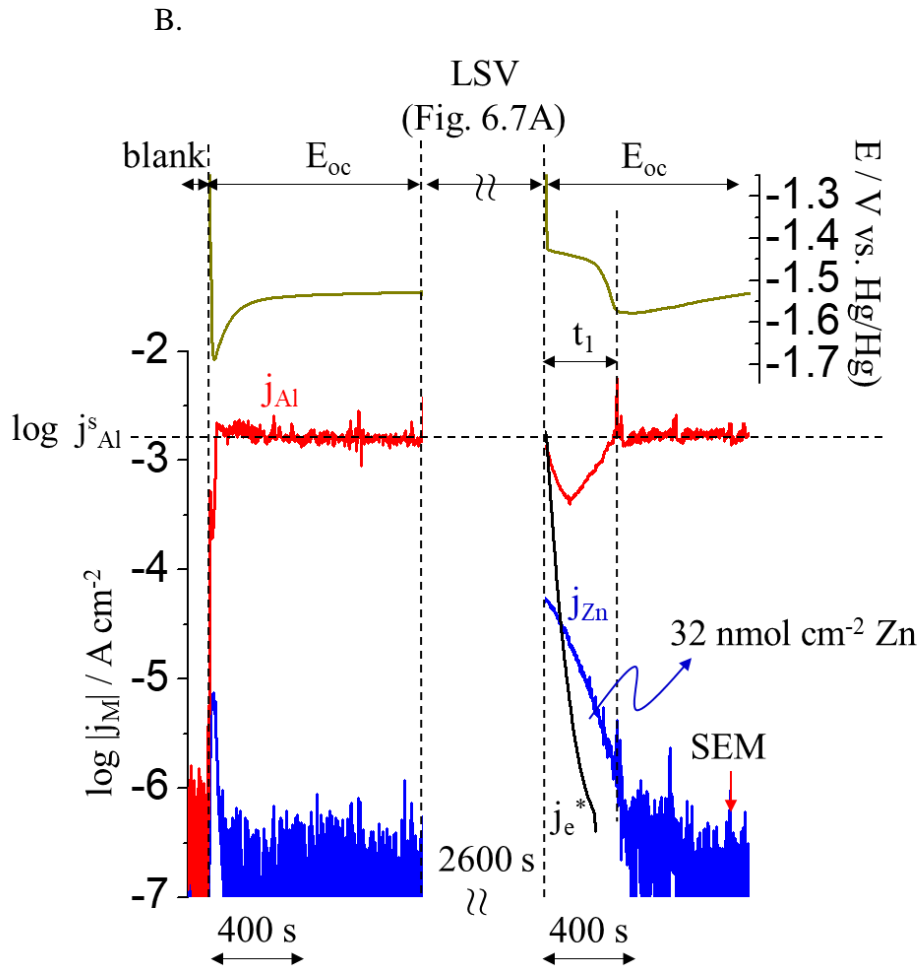


Fig. 6.7. A: Elemental AESEC-LSV of $\text{Al}_{5.2}\text{Zn}$ phase in 0.1 M NaOH, pH=12.80 electrolyte with Ar deaeration at $T=20^\circ\text{C}$. **B:** j_M and E_{oc} in spontaneous dissolution before and after the LSV.

Fig. 6.8 shows the SEM images taken after t_1 in **Fig 6.7B**, suggesting that the thin films were not completely dissolved at the second E_{oc} period. This thin film was characterized as ZnO and Zn_{1+x}O as it showed 430 cm^{-1} and 540 cm^{-1} Raman shift [124,151]. Individual cathodic and anodic polarization experiments, cathodic and anodic LSV, were performed. They showed, however, no distinctive difference with respect to the LSV from cathodic to anodic potential (**Fig. 6.7A**), and are not shown herein.

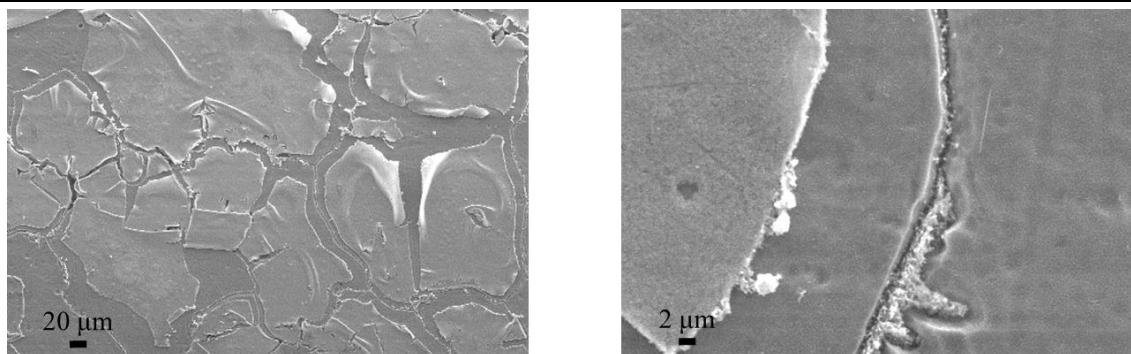


Fig. 6.8. SEM images taken in the second E_{oc} period in **Fig. 6.7B** (arrow). An equal mix of secondary electron and back-scattered electron detection was used.

6.3.5. Chronoamperometric experiments of $Al_{5.2}Zn$

Interpretation of LSV experiments is often difficult as the experiment involves a simultaneous variation of time and potential as recently discussed by Moshaweh and Burstein [152]. This is particularly true for systems exhibiting dealloying mechanisms as the nature of the surface changes radically as a function of time as selective dissolution leads to the build-up of the more noble element, in this case Zn. To apprehend these phenomena, we attempted to isolate the various mechanisms of dissolution which occur in the different potential domains of the LSV experiment by measuring the dissolution profiles at a constant applied potential and following j_e^* , j_{Al} and j_{Zn} as a function of time, referred to as chronoamperometry (CA). Average steady state values of j_M , j_e^* , j_{Al}/j_{Zn} , and η at each potential pulse are summarized in **Table 6.4**. For $E > E_c^{Zn}$ of the CA (domain II ~ IV), dissolution was both congruent and faradaic with $j_{Al}/j_{Zn} \approx 7.8$ (ratio of the bulk composition) and $\eta \approx 1$.

Fig. 6.9 gives typical CA results for polarizations into A: the selective Al potential domain at $E_{ap} = -1.60$ V and -1.40 V (domain I in **Fig. 6.7A**), B: the congruent Zn-Al dissolution domain at $E_{ap} = -1.25$ V (domain II (a) in **Fig. 6.7A**) and C: at $E_{ap} = -1.18$ V (domain II (b) in **Fig. 6.7A**). For $t < 0$, the electrolyte was not in contact with the specimen and the background signals were measured to define the emission zero. At $t=0$, indicated with a vertical dashed line in Fig. 8, the electrolyte was brought in contact with the sample and after approximately 10 s, a constant potential was applied to the sample.

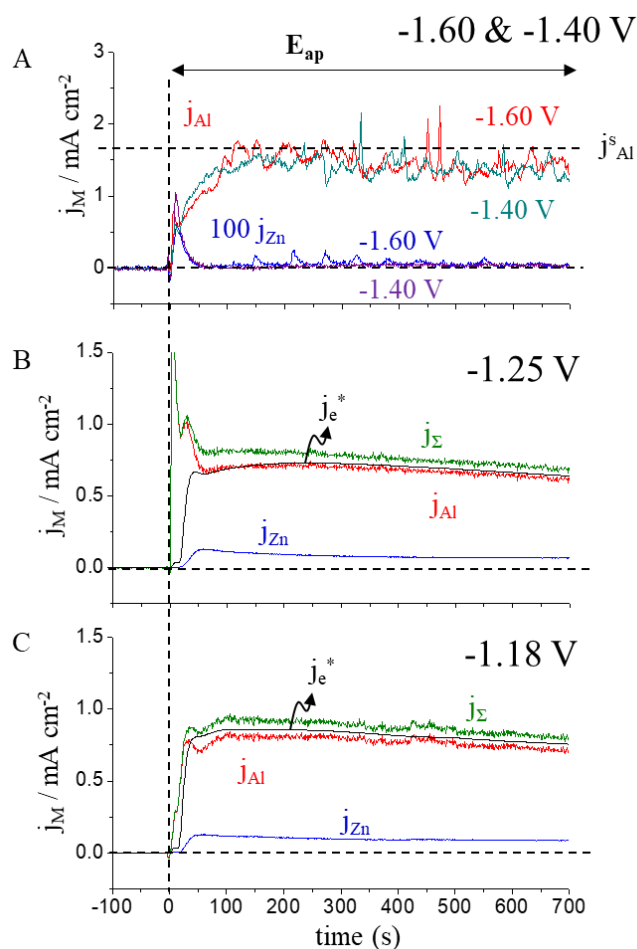


Fig. 6.9. AESEC-chronoamperometry (CA) of $\text{Al}_{5.2}\text{Zn}$ phase at **A**: the selective Al potential domain at $E_{\text{ap}} = -1.60$ V and -1.40 V, **B**: the congruent Zn-Al dissolution domain at $E_{\text{ap}} = -1.25$ V (domain *a*) and **C**: at $E_{\text{ap}} = -1.18$ V (domain *b*) in 0.1 M NaOH, pH=12.80, Ar deaerated electrolyte at $T=20$ °C. Potential domains are referenced from **Fig. 6.7A**.

Selective Al dissolution is clearly demonstrated in the CA experiments (**Fig. 6.9A**) for domain I, in good agreement with the LSV of **Fig. 6.7A** in that the j_{Al} . The potential independence of Al dissolution is likewise confirmed as the j_{Al} values at $E_{\text{ap}} = -1.60$ V and -1.40 V were essentially identical to each other and also nearly the same as the open circuit value, j_{Al}^{s} . Note that j_{Zn} was very low and has been multiplied by 100 on the axis of this experiment. A relatively high level of Al signal perturbation, $\sigma_{j_{\text{Al}}}$, was observed, indicative of H_2 evolution as previously noted. The total current was cathodic during this experiment and is not shown.

The negative correlation effect is observed at applied potentials above E_{c}^{Zn} , in potential domain II at -1.25 V and -1.18 V, **Figs. 6.9B** and **9C**. Displayed are j_e^* , j_{Zn} , j_{Al} , and j_{Σ} as a function of time. In agreement with the polarization curve of **Fig. 6.7**, j_{Zn} has increased by orders of magnitude, while j_{Al} has decreased by a factor of two. Otherwise dissolution is approximately faradaic with j_{Σ} slightly $> j_e^*$ consistent with a non-negligible cathodic reaction at these potentials.

VI. Interaction between Zn and Al dissolution in alkaline media

Of particular interest for this work is the CA profile at $E_{ap} = -1.32$ V given in **Fig. 6.10**. At this potential, a clear time dependent transition is observed at $t = t'$ between the selective Al dissolution mechanism ($t < t'$) and the congruent dissolution mechanism ($t > t'$). Until t' , selective Al dissolution was observed. However, as the excess Zn(0) built up on the surface, j_{Zn} increased. This correlated with a drop in j_{Al} demonstrating the onset of the negative correlation effect. The isolation of this mechanism at a constant potential again demonstrates the importance that this mechanism may have for any long term experiment.

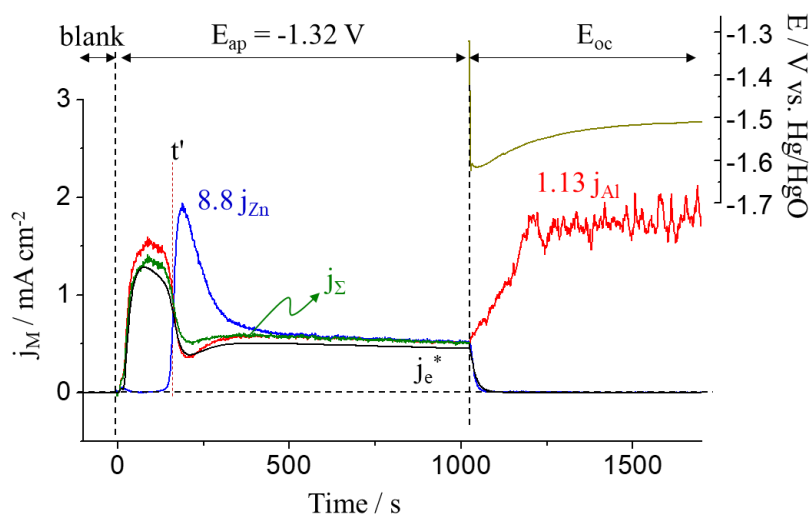


Fig. 6.10. AESEC-CA of $Al_{5.2}Zn$ phase at $E_{ap} = -1.32$ V and after the potential release in 0.1 M NaOH, pH=12.80, Ar deaerated electrolyte at $T=20^\circ C$. j_M values were normalized based on its molar composition.

Note that in **Fig. 6.10**, j_{Zn} and j_{Al} have been normalized by their bulk molar composition so that information on selective dissolution may be obtained at a glance. Towards the end of the CA experiment, Zn and Al dissolution were congruent as demonstrated by the fact that $8.8 j_{Zn} \approx 1.13 j_{Al} \approx j_\Sigma$ consistent with the stoichiometry of **Eq. 6.7** assuming Al(III) and Zn(II) oxidation:



The change in mechanism was once again revealed by consideration of the Al signal perturbations, $\sigma_{j_{Al}}$. Significant perturbations were observed only through the j_{Zn} maximum and the abrupt halt of the perturbations suggests a change of mechanism from direct Al dissolution with hydrogen evolution to the passive film mechanism involving migration across the passive Zn-O/-OH film as previously mentioned. Significantly, the perturbations returned when, at the

end of the CA experiment, the potential was released to open circuit (right hand side of **Fig. 6.10**.)

It is of interest to contrast the reactivity of $\text{Al}_{5.2}\text{Zn}$ at $E_{\text{ap}} = -1.32$ V (**Fig. 6.10**) with that obtained at a more extreme anodic potential, $E_{\text{ap}} = -0.60$ V (**Fig. 6.11**). In the latter case, Zn oxide formation is clearly indicated by mass balance ($j_{\Delta} > 0$). It is clearly seen that $1.13 j_{\text{Al}} = j_{\Sigma} \approx j_e^*$, demonstrating that essentially all Al dissolution contributed to electrical current without forming significant insoluble species. However, since $8.8 j_{\text{Zn}} < j_e^*$, it is evident that some Zn^{2+} was not detected, indicative of Zn oxide formation.

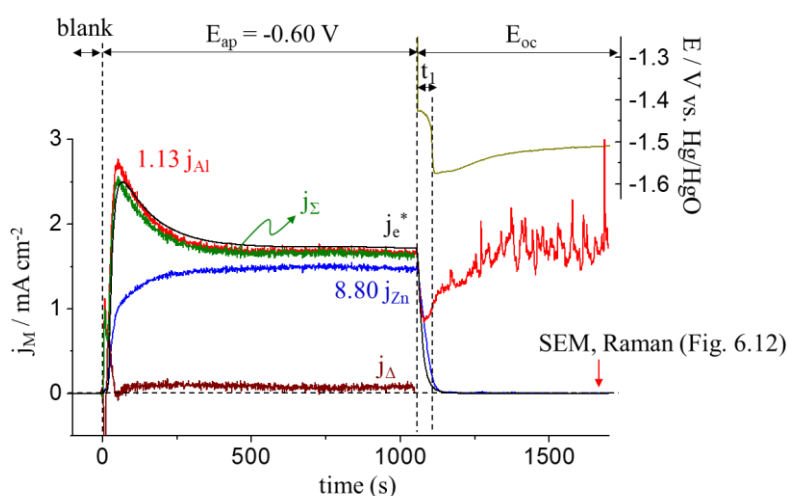


Fig. 6.11. AESEC-CA of $\text{Al}_{5.2}\text{Zn}$ phase at $E_{\text{ap}} = -0.60$ V and after the potential release in 0.1 M NaOH, pH=12.80, Ar deaerated electrolyte at $T=20^\circ\text{C}$. j_M values were normalized based on its molar composition.

The nature of this oxide was further revealed by direct observation of the spontaneous dissolution profile, following the CA experiment, on the right hand sides of **Figs. 6.10** and **11**. A potential plateau of oxide dissolution (t_1) was observed following $E_{\text{ap}} = -0.60$ V (**Fig. 6.11**). Significantly, this plateau was not observed at $E_{\text{ap}} = -1.32$ V (**Fig. 6.10**) similar in magnitude to that of **Fig. 6.7B**. Likewise, it was coupled to the dissolution of Zn.

VI. Interaction between Zn and Al dissolution in alkaline media

Table. 6.4. The average j_M , j_e^* , j_{Al}/j_{Zn} and η obtained at $E_{ap} = -1.60$ V, -1.40 V, -1.32 V, -1.25 V, -1.18 V and -0.60 V from the CA in **Figs. 6.9-6.11**.

	$E_{ap} = -1.60$ V (Fig. 6.9A)	$E_{ap} = -1.40$ V (Fig. 6.9A)	$E_{ap} = -1.32$ V (Fig. 6.10)
	Domain I	Domain I	Domain II (a)
$j_{Al} / \text{mAcm}^{-2}$	1.4 ± 0.1	1.4 ± 0.1	0.48 ± 0.02
$j_{Zn} / \text{mAcm}^{-2}$	0.0003 ± 0.0002	0.0003 ± 0.0002	0.063 ± 0.003
j_e^* / mAcm^{-2}	-0.51	0.68	0.48
j_{Al}/j_{Zn}	-	-	7.6
$\eta (j_{\Sigma} / j_e^*)$	-2.8	2.0	1.13
	$E_{ap} = -1.25$ V (Fig. 6.9B)	$E_{ap} = -1.18$ V (Fig. 6.9B)	$E_{ap} = -0.60$ V (Fig. 6.11)
	Domain II (a)	Domain II (b)	Domain IV
$j_{Al} / \text{mAcm}^{-2}$	0.58 ± 0.01	0.67 ± 0.02	1.47 ± 0.03
$j_{Zn} / \text{mAcm}^{-2}$	0.069 ± 0.001	0.086 ± 0.002	0.167 ± 0.002
j_e^* / mAcm^{-2}	0.61	0.72	1.65 ± 0.007
j_{Al}/j_{Zn}	8.4	7.7	8.8
$\eta (j_{\Sigma} / j_e^*)$	1.06	1.03	0.98

The sample surface was characterized by SEM (**Fig. 6.12A**) and Raman spectroscopy (**Fig. 6.12B**) at the end of the CA experiment (arrow in **Fig. 6.11**). From the SEM images displayed in **Fig. 6.12A**, the surface can be divided into darker (i) and porous lighter (ii) areas separated by grain boundaries. A higher magnification images (bottom) show that the highly porous lighter area was covered by a less porous thin darker layer which seems to be partly dissolved as indicated by arrows and a dashed line in the bottom right image. Raman spectra (**Fig. 6.12B**) shows that the darker thin layer (i) is composed of ZnO (430 cm^{-1}) and Zn_{1+x}O (540 cm^{-1}) [124,151] while the lighter area (ii) showed no Raman spectra. The porosity in the lighter area could be due to the selective Al dissolution in the E_{oc} period after t_1 .

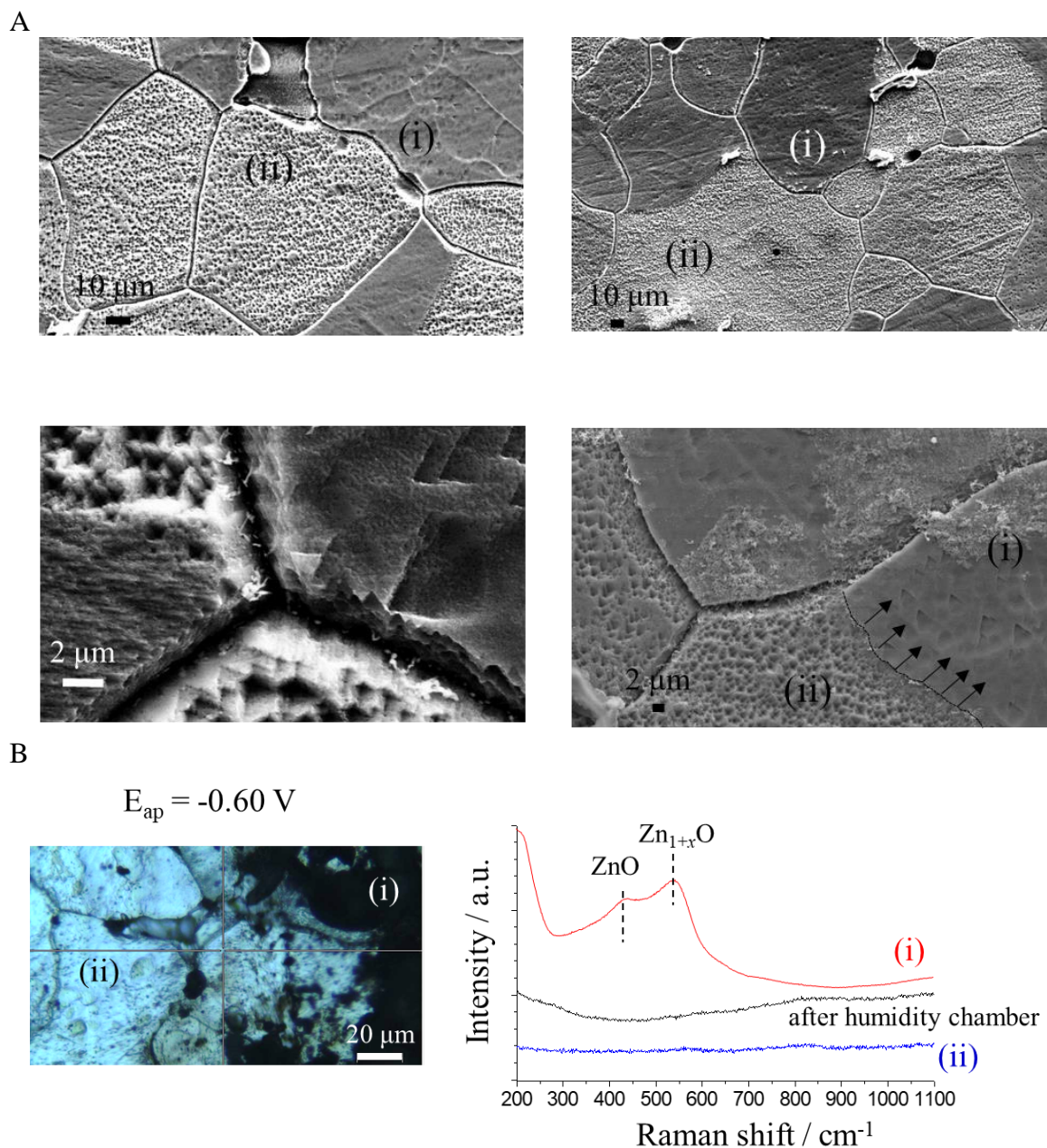


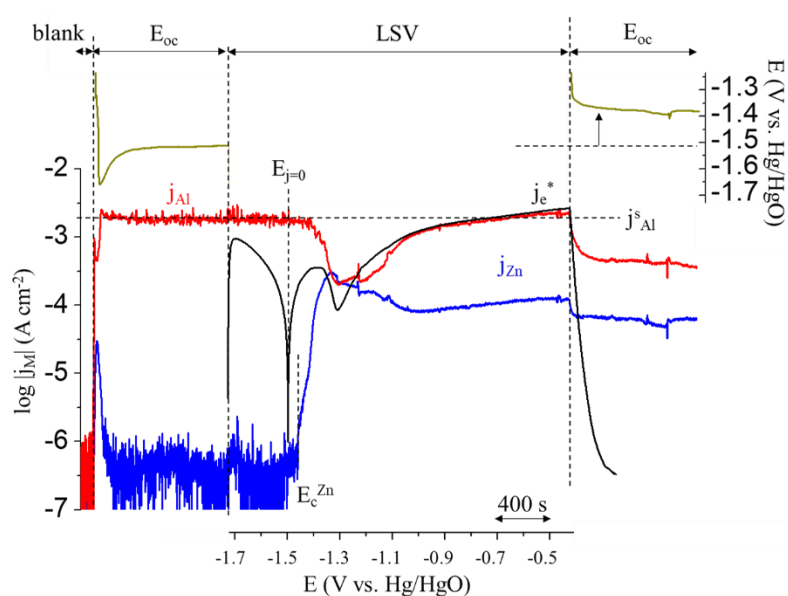
Fig. 6.12. **A:** SEM images, **B:** Raman spectra at a thin darker area (i) and porous lighter area (ii) of $Al_{5.2}Zn$ in the spontaneous dissolution after the CA at $E_{ap} = -0.60 \text{ V}$ at $\text{pH}=12.80$, Ar deaerated electrolyte at $T=20 \text{ }^\circ\text{C}$, arrowed in **Fig. 6.11**.

6.3.6. The effect of O_2 on the LSV of $Al_{5.2}Zn$

The formation of Zn oxide is markedly enhanced by saturating the electrolyte with O_2 . This is demonstrated by the AESEC-LSV and the anodic LSV of $Al_{5.2}Zn$ in O_2 saturated electrolyte are shown in **Fig. 6.13A** and **13B** respectively. Both curves include the time sequence before and after the LSV experiment.

The overall j_M vs. E was not greatly altered as compared to that in Ar deaerated electrolyte (**Fig. 6.7**). j_{Al} in the cathodic potential domain in **Fig. 6.13A** remained at the same level as j_{Al}^s in open circuit dissolution, as in the Ar deaerated electrolyte (**Fig. 6.7**). This again demonstrates that Al dissolution varies little with O_2 . Zn dissolution occurred at $E_c^{Zn} = -1.45$ V, only +40 mV than $E_{j=0}$, supporting the hypothesis that the ZnO formed during cathodic polarization, would dissolve directly forming $Zn(OH)_3^-/Zn(OH)_4^{2-}$ complex in a more negative potential range as compared to that in the absence of O_2 [114,143].

A



B

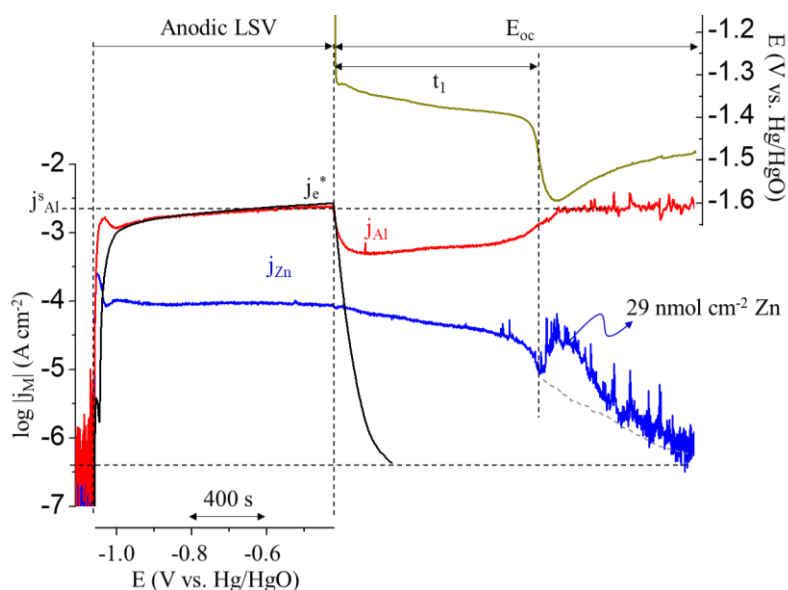


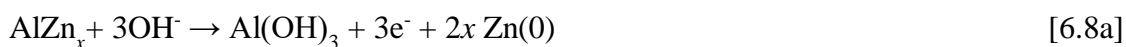
Fig. 6.13. A: Elemental AESEC-LSV including the spontaneous dissolution before/after the LSV and B: anodic anodic LSV including the spontaneous dissolution after the potential release for $Al_{5,2}Zn$ phase at pH=12.80, 0.1 M NaOH, O_2 saturated electrolyte at $T=20$ °C.

A more consequent ZnO film was formed with O₂ as evidenced by the +130 mV shift in E_{oc} = -1.38 V after the LSV with respect to the first E_{oc} = -1.51 V. In the second open circuit dissolution period, j_{Zn} increased by a factor of 180 while j_{Al} decreased a factor of 5 as compared to those in the first open circuit period again illustrating the negative correlation effect due to the presence of ZnO. The intensity of the σ_{j_{Al}} was markedly decreased with respect to that measured in the first E_{oc} period as well. This demonstrates that the ZnO film formed during the anodic sweep, dissolved slowly after the potential release, correlated to the Al dissolution across this ZnO film.

For the anodic LSV (**Fig. 6.13B**), j_M showed similar trends to the cathodic to anodic LSV (**Fig. 6.13A**). After the potential release, at t₁, j_{Zn} was slowly decreasing while j_{Al} was increasing without showing a significant perturbation signal. However, after t₁, j_{Al} increased to j_{Al}^s level with higher σ_{j_{Al}} whereas j_{Zn} decreased to the level of its detection limit showing a distinctive Zn dissolution peak. Again, this unambiguously demonstrates that the origin of the negative correlation is effect is due to the formation of Zn oxides, presumably ZnO, from the dealloyed Zn(0) rich surface layer. During t₁, E_{oc} decreased slowly in a range of -1.32 V < E_{oc} < -1.45 V. After t₁, the potential dropped to E = -1.6 V when the j_{Zn} peak was measured, indicating an evident Zn -O/-OH dissolution. The quantity of ZnO formed was measured from the integral of the Zn dissolution transient from the end of the applied potential to t₁, and was found to be 29 nmol cm⁻² corresponding to 3.4 nm.

6.4. Discussion

A schematic of the proposed mechanism for the cathodic and anodic dissolution of Zn-68 wt.% Al (α-phase of Al) is given in **Fig. 6.14**, describing the elemental dissolution of the phase in alkaline media as a function of potential. For the domain I (from **Fig. 6.7A**, E < E_c^{Zn}), selective Al dissolution leads to the formation of the Zn(0) enriched surface layer. The dissolution of Al occurs, coupled with water reduction forming H₂:



VI. Interaction between Zn and Al dissolution in alkaline media

The existence of the intermediate surface film, presumably $\text{Al}(\text{OH})_3$, limits the rate of the reaction between water and Al. However, the dissolution of the film is rapid on the time scale of these experiments due to the availability of OH^- . **Reaction 6.8b** is essentially independent of potential. The presence of the $\text{Zn}(0)$ enriched surface layer does not affect the Al dissolution rate so **Reactions 6.8** continue unhindered for ($E < E_c^{\text{Zn}}$).

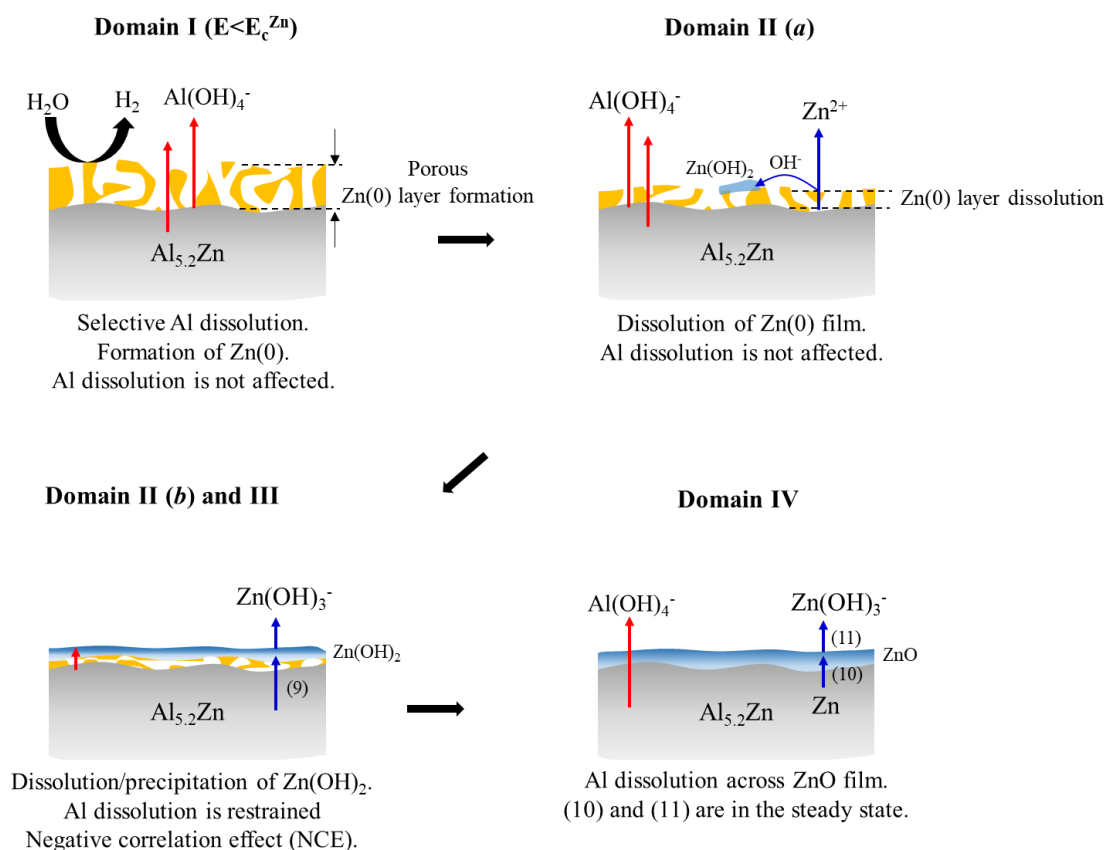


Fig. 6.14. Schematic model of dissolution of $\text{Al}_{5.2}\text{Zn}$ α -phase Al-Zn in alkaline media as a function of potential. Potential domains are determined in **Fig. 6.7A**.

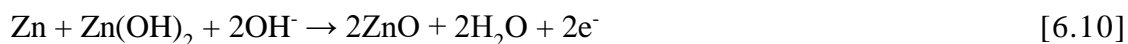
The behavior at $\text{pH}=12.80$ differs from that observed at lower pH (neutral to slightly alkaline) where potential dependent Al dissolution was observed in the cathodic potential domain for pure Al, Al alloys and Al-Zn pure phases [120,122,143] by the ASESEC technique. The elementary reactions are identical, however, at lower pH , the hydroxide in **Eq. 6.8a** and **6.8b** is only provided by the cathodic current, hence the dissolution rate is stoichiometrically proportional to the cathodic current, and the phenomena is referred to as cathodic dissolution of Al, or cathodic dealloying.

The $\text{Zn}(0)$ enriched surface layer starts to dissolve in the domain II (a), ($E > E_c^{\text{Zn}}$), but Al dissolution is not restrained. As Zn^{2+} increases in the solution, $\text{Zn}(\text{OH})_2$ can be formed on

the surface reacting with OH^- in the electrolyte. When the Zn(OH)_2 builds up with potential increase covering the surface as Reaction 9, Al dissolution is restrained by this layer in the domain II (b) and III.



either by the presence of Zn oxides on the surface. In the domain IV, ZnO formation passivates the surface via **Reaction 6.10** [153]. At the same time, this ZnO can be dissolved via **Reaction 6.11** as follows:



Given that j_{Zn} in the domain IV was independent of potential for pure Zn and the $\text{Al}_{5.2}\text{Zn}$ phase (**Figs. 6.5** and **7A**, respectively), it can be concluded that **Reaction 6.10** and **Reaction 6.11** are in the steady state. Al dissolution occurs across this ZnO film as evidenced by the absence of perturbations on the j_{Al} signal.

This mechanism resembles the classical ‘dissolution-precipitation’ model [154–156] which explains the passivation of Zn by the critical concentration of zincate ions in the vicinity of the electrode. However, in this case, the passivation may be driven by potential rather than local saturation, in accordance with previous observations [92,157–159]. The CA experiment directly polarized to the passive domain (**Fig. 6.11**) revealed that ZnO was formed during the potential pulse as evidenced by $j_{\Delta} > 0$ and congruent Al dissolution. The dissolution of this ZnO film was observed after the potential release, restraining Al dissolution (NCE).

6.5. Conclusion

1) Zn in $\text{Al}_{5.2}\text{Zn}$ dissolved in a similar manner to pure Zn in pH=12.80 Ar deaerated and O_2 saturated electrolytes. Al dissolved similar to pure Al for $E < E_c^{\text{Zn}}$, but was restrained during the Tafel (active) domain of Zn dissolution. For more positive potential (passive domain IV), Al dissolved by migration across a ZnO.

2) Potential independent Al dissolution for pure Al and $\text{Al}_{5.2}\text{Zn}$ was observed at pH=12.80. This result is different from the potential dependent Al dissolution in a lower pH media, indicating distinct elemental dissolution mechanisms at each pH. The AESEC-LSV of pure Al and $\text{Al}_{5.2}\text{Zn}$

VI. Interaction between Zn and Al dissolution in alkaline media

demonstrated that the formation and dissolution of Al(OH)_3 were in the steady state at $\text{pH}=12.80$.

3) The “negative correlation effect (NCE)” of Zn on Al dissolution was clearly due to the oxidation/dissolution of a Zn(0) enriched surface layer formed by a selective Al dissolution. It was evidenced by the potential domain II (b) in **Fig. 6.7A** and ZnO dissolution at t_1 in the spontaneous dissolution after the LSV (**Fig. 6.7B**).

4) The transition between selective Al and congruent Zn/Al dissolution was clearly demonstrated by the CA at $E_{\text{ap}} = -1.32 \text{ V}$ (**Fig. 6.10**). Al selectively dissolved during the first 150 s leading to formation of the Zn(0) enriched surface layer. When this layer dissolved, Al dissolution was restrained (NCE) then both elemental dissolution reached to a congruent dissolution condition. After releasing the potential pulse, Al dissolution rate returned to its spontaneous dissolution rate value with highly perturbed j_{Al} signal ($\sigma_{j_{\text{Al}}}$) indicative of the H_2 evolution (**Reaction 6.8**).

5) In the passive potential domain (**Fig 6.7A** and **Fig 6.11**), potential driven ZnO formation and its dissolution were in the steady state (**Reactions 6.10** and **6.11**). Al dissolution occurred across this layer, as evidenced by significantly decreased perturbation signal of j_{Al} ($\sigma_{j_{\text{Al}}}$) with respect to that for spontaneous dissolution condition.

6) The slowly soluble Zn-O/-OH species formed during the anodic polarization was characterized as a thin $\text{ZnO/Zn}_{1+x}\text{O}$ layer covered the surface.

Chapter VII:

Temperature dependence of the passivation and dissolution of Al, Zn, and α -phase of Zn-68Al

“The world is changed because you are made of ivory and gold. The curves of your lips rewrite history”

The Picture of Dorian Gray (1890),

Oscar Wilde

The content of this chapter repeats the article: Junsoo Han, Dominique Thierry, and Kevin Ogle, “Temperature dependence of the passivation and dissolution of Al, Zn, and α -phase Zn-68Al”, *Corrosion*, **75**(1) 68-78 (2019).

7. Temperature dependence of the passivation and dissolution of Al, Zn and α -phase Zn-68Al

Abstract

The reactivity of a pure α -phase of Al-Zn (Zn-68 wt.% Al, $\text{Al}_{5.2}\text{Zn}$), in deaerated 0.1 M NaOH solution (simulating industrial pretreatments) was investigated and compared with that of pure Al and Zn. The elementary phenomena of metal oxidation, dissolution, oxide formation, and hydrogen evolution were decoupled using atomic emission spectroelectrochemistry. At the open circuit potential, the $\text{Al}_{5.2}\text{Zn}$ phase reacted similarly as pure Al, undergoing selective Al dissolution to form a Zn(0) enriched layer. The Zn in the alloy shifted the potential to just below the onset of Zn dissolution. Elementary polarization curves showed that Zn dissolution was similar for the $\text{Al}_{5.2}\text{Zn}$ phase as for pure Zn. Near the open circuit potential, Zn dissolution was faradaic limited by the formation of surface $\text{Zn}(\text{OH})_2$. At higher temperature, significant amounts of ZnO formed resulting in passivation. For the $\text{Al}_{5.2}\text{Zn}$ phase, the rates of Al and Zn dissolution were determined by a charge transfer mechanism across the ZnO film. Kinetic parameters (activation energies and Tafel slopes) were measured for some of the elementary processes.

Keywords: aluminum alloy, aluminum, dealloying, zinc, corrosion rate, surface cleaning

7.1. Introduction

The cleaning process is an essential step for Al alloys and Zn-Al alloy coatings of galvanized steel prior to further surface treatment such as anodization or conversion coating and painting. The cleaning step usually involves an alkaline electrolyte, and is used primarily to remove residual oil applied before rolling, or for temporary corrosion protection. The process will also remove pre-existing surface oxides [137] and alter the surface chemistry of Zn based alloy coatings [136–138,160,161]. This is especially critical for the Zn-Al coatings as the spontaneously formed Al oxide film may act as a poison for subsequent conversion treatments. For Al alloys, the surface cleaning may enhance corrosion resistance [67,162,163] and is an essential step for further treatments such as conversion coating or anodization.

The reactivity of Zn and Zn-Al alloys in alkaline solution has been rather extensively investigated in recent years [92,93,143] at ambient temperature. Alkaline cleaning however, is carried out at elevated temperature, typically between 40 °C and 65 °C, and the reactivity of the materials in this temperature range is much less known. This behavior is all the more interesting given the fact that Zn solubility decreases with increasing temperature while Al does exactly the opposite making the temperature dependence difficult to predict. This effect is illustrated by **Fig. 7.1**, which gives the calculated saturation concentrations ($C_M(\text{sat})$) of Zn^{2+} and Al^{3+} as a function of pH at $T=20\text{ °C}$ and $T=50\text{ °C}$. The dominant precipitated species of each cation are indicated above the graph. It is important to point out that the solubility of $\text{Al}(\text{OH})_3$ increases while that of ZnO decreases with increasing temperature.

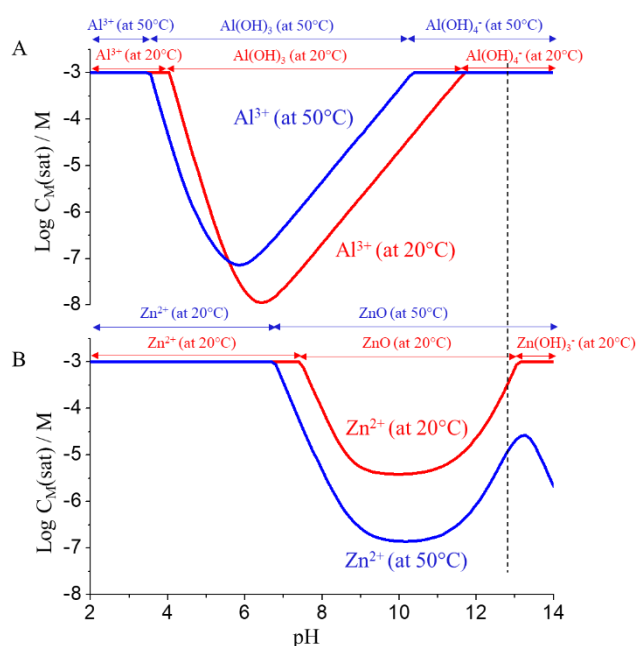


Fig. 7.1. $C_M(\text{sat})$ of **A:** Al^{3+} and **B:** Zn^{2+} in pure water calculated by Phreeplot™ software (version 1) using thermodynamic database at $T=20\text{ °C}$ and $T=50\text{ °C}$. The arrows above each curve indicate the predominant precipitated species as a function of pH.

The formation of solid Zn oxidation products is favored by higher temperature, indeed, the enhanced stability of Zn oxide may even result in the passivity of the material. This can lead to a change in the polarity of a Zn electrode, referenced as polarity reversal, when Zn is galvanically coupled to steel [164–168]. The ennoblement of the Zn with increasing solution temperature from 40 °C to 70 °C, has been attributed to the formation of a ZnO film having low conductivity [164,165]. Gilbert [167] also observed that the transition of Zn polarity, Zn became cathodic to steel, occurred at $T > 60$ °C resulting in the transformation from Zn(OH)_2 to ZnO. For the Zn-Al system, Devillers et al. observed a rapid increase of grain boundary corrosion rate with temperature for Zn-0.1 wt.% Al alloy [125]. It was attributed to increased Al reactivity with temperature present in the form of particles at grain boundary.

Metallic Al reacts spontaneously and rapidly with water in aqueous solution (standard potential for Al/Al(OH)_4^- is -2.328 V vs. NHE) and in practice, the rate is limited by the presence of an oxide film separating the metal from the electrolyte. The rate of Al dissolution is known to increase markedly with temperature [119,142,169]. This is primarily due to the destabilization of the passive film as the solubility of Al(OH)_3 increases with increasing temperature [142] as shown in **Fig. 7.1**. Enhanced diffusion of OH^- across the Al oxide layer may also contribute to the enhanced dissolution [118,120–123,141,169,170].

The aim of this work is to interpret the passivation and dissolution kinetics of a pure binary Al-Zn phase (α -phase of Al-Zn) as a function of temperature, in terms of the specific behavior of the component pure metals, Zn and Al. The Al-Zn phase is chosen for this work as a model case of a high Al content Zn coating but is also of interest from Zn-rich Al alloys such as the 6000 series. The scientific strategy is to compare the reactivity of the Zn-Al alloy with that of the pure metals so as to isolate and measure independently the role of each element of the alloy. Further, to identify the different reactions (dissolution, oxide formation and passivation, and the cathodic reaction), the polarization curves of the materials were investigated using atomic emission spectroelectrochemistry (AESEC) giving a direct measurement of elemental dissolution rates of the alloy components as a function of potential. The temperature dependence of the specific elementary phenomena may thus be determined.

7.2. Experimental

Materials

Zn metal (99.9 %) and Al metal (99.8 %) from *Goodfellow* and an α -phase of Al (Zn-68 wt.% Al, will be denoted as $\text{Al}_{5.2}\text{Zn}$ based on its molar composition) were used in the present work. The latter was produced and characterized by *Department of Metals and Corrosion Engineering, University of Chemistry and Technology, Prague*. The sample thicknesses were 0.06 cm for pure Zn and Al and 0.5 cm for $\text{Al}_{5.2}\text{Zn}$. The sample surface was prepared as stated in other chapters of this Ph.D. thesis.

All electrolytes were prepared from analytical grade reagents and deionized water of 18.2 M Ω cm obtained via a MilliporeTM system. A recirculating temperature controlled water bath and a hollow copper block were used to maintain a constant temperature of the solution and specimen. A temperature calibration has been previously published using a spot welded thermocouple on a 0.7 mm steel electrode [171]. It was found that the real temperature was approximately 3 °C below the temperature of the bath at 55 °C. This difference was not corrected in this work.

The AESEC technique

AESEC was used for analyzing the elemental dissolution kinetics of the specimens. In this work, the time resolved concentration of Zn was determined from the emission intensity of the plasma monitored at 213.86 nm wavelength on the polychromator and Al at 167.08 nm on the monochromator using standard inductively coupled plasma atomic emission spectrometry (ICP-AES) calibration techniques.

A Gamry Reference 600TM potentiostat was used to control and measure the electrochemical potential (E) and current density (j_c). A number of different electrochemical experiments were performed including measurements of the spontaneous dissolution at the open circuit potential (dissolution profile), linear sweep voltammetry (LSV) using a scan rate of 0.5 mV s⁻¹. Specific experimental descriptions will be given in the text.

Data analysis

The elemental dissolution rate, v_M , was converted to an equivalent elemental current density j_M as;

$$j_M = zF v_M \quad [7.1]$$

where z is the valence of the dissolving ions and F is Faraday constant. Both soluble (j_Σ) and insoluble (j_{ins}) component can contribute to anodic dissolution, $j_a = j_\Sigma + j_{ins}$. The total current may be written as:

$$j_e^* = j_\Sigma + j_{ins} + j_c \quad [7.2]$$

By a mass balance equation, j_Δ can be determined as:

$$j_\Delta = j_e^* - j_\Sigma = j_{ins} + j_c \quad [7.3]$$

If $j_\Delta > 0$, the formation of unsolved species is predicted. If $j_\Delta < 0$, cathodic corrosion rate (j_c) can be calculated.

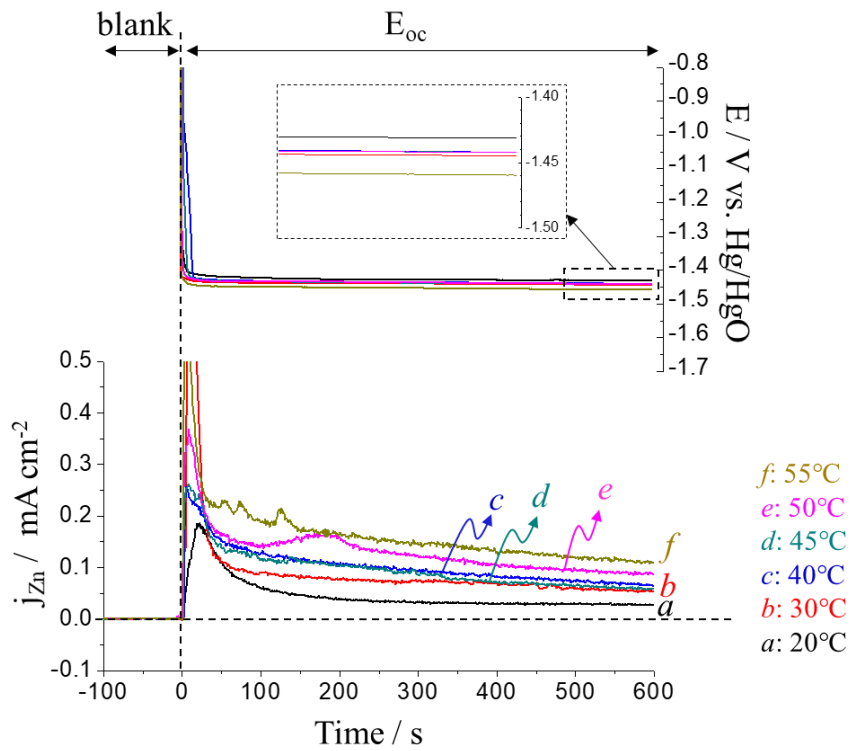
7.3. Results

The cleaning process is almost exclusively performed by simply exposing the material to the alkaline bath either in immersion or with a spray. To partially simulate the immersion process, the specimens were exposed to the alkaline electrolyte at open circuit to monitor the spontaneous elemental dissolution rates as a function of time (dissolution profile). The results are then interpreted using elemental polarization curves obtained under the same conditions of electrolyte and temperature.

7.3.1. Spontaneous dissolution

Spontaneous elemental dissolution rates (j_M) of Zn and Al metal are shown as a function of time in **Fig. 7.2**. In both cases, the steady state dissolution rates (j_{Zn}^s and j_{Al}^s) for nominally pure Zn and Al, **Fig. 7.2A and 7.2B**, increased with temperature with only a minor variation of the open circuit potential, E_{oc} . The average spontaneous elemental dissolution (j_M^s) and the E_{oc} values are provided in **Table 7.1**.

A



B

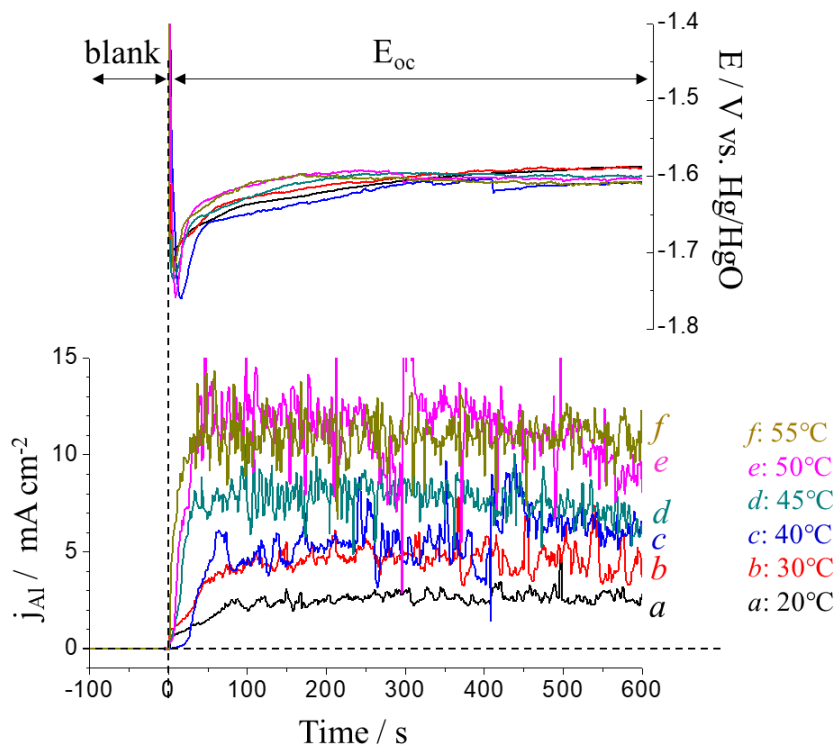


Fig. 7.2. Spontaneous dissolution rates (j_M) and open circuit potentials (E_{oc}) for **A**: pure Zn and **B**: pure Al in 0.1 M NaOH, Ar deaerated electrolyte at each temperature.

VII. Temperature dependence of Al, Zn and α -phase Zn-68Al

The spontaneous dissolution of $\text{Al}_{5.2}\text{Zn}$ phase (**Fig. 7.3**) showed a selective Al dissolution as previously reported for Zn-Al alloy coatings and pure phases [92,93,143]. Al dissolution rate, j_{Al} increased with temperature as observed for pure Al, and obtained significantly higher values at the higher temperature as compared to that of pure Al. Zn dissolution, j_{Zn} , was however below the detection limit except for $T = 50^\circ\text{C}$ and 55°C . For $T > 30^\circ\text{C}$, sharp j_{Zn} peaks were observed probably due to the release of Zn in the form of Zn containing particles in a non-faradaic process associated with the high etching rate. Such particle release has been previously documented for a number of different systems [67,121,172]. By mass balance, a Zn(0) enriched surface layer must form as a consequence of Al selective dissolution.

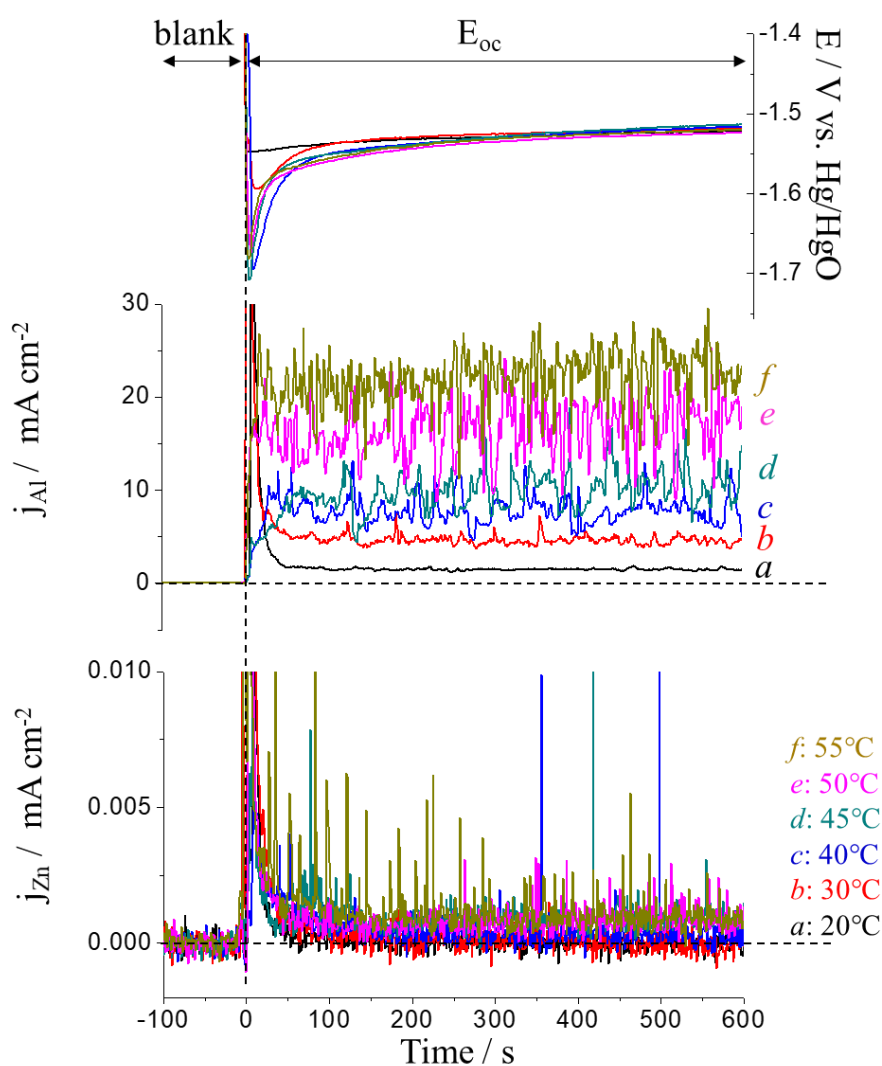


Fig. 7.3. Spontaneous dissolution rates (j_{M}) and open circuit potentials (E_{oc}) for $\text{Al}_{5.2}\text{Zn}$ phase in 0.1 M NaOH, Ar deaerated electrolyte at each temperature.

VII. Temperature dependence of Al, Zn and α -phase Zn-68Al

Aluminum dissolution occurs via the direct reaction with water to form hydrogen gas and dissolved Al(OH)_4^- :



The hydrogen evolution reaction (HER) may be observed visually in this system by the appearance of bubbles in the electrolyte flowing out of the cell. The HER is also apparent in the Al dissolution profiles of **Figs. 7.2B and 7.3** as perturbations in the j_{Al} signals induced by the bubbles in the nebulization system of the ICP. The standard deviation of the perturbations, $\sigma_{j_{\text{Al}}}$, for both Al metal and $\text{Al}_{5,2}\text{Zn}$ is proportional to j_{Al} . Thus, the amplitude of $\sigma_{j_{\text{Al}}}$ reflects the intensity of the cathodic reaction. In some cases, a slow decrease in the dissolution rate is observed followed by a rapid increase which correlates with an abrupt drop in E_{oc} . This is a result of the formation of H_2 bubbles which progressively block the surface and then are detached.

Table. 7.1. The average spontaneous elemental dissolution rates (j_{M}^{s}) and the open circuit potential (E_{oc}) of pure Zn, Al and $\text{Al}_{5,2}\text{Zn}$ phase at each temperature in 0.1 M NaOH, Ar deaerated electrolyte. All potential values presented in the current work are referenced to a Hg/HgO (0.1 M NaOH) electrode.

	Pure Al		Pure Zn		$\text{Al}_{5,2}\text{Zn}$		
	j_{Al}^{s}	E_{oc}	j_{Zn}^{s}	E_{oc}	j_{Al}^{s}	j_{Zn}^{s}	E_{oc}
T / °C	/mA cm ⁻²	/V	/μA cm ⁻²	/V	/mA cm ⁻²	/μA cm ⁻²	/V
20	2.6±0.3	-1.60	28±1	-1.43	1.5±0.1	-	-1.53
30	4.7±0.4	-1.61	39±1	-1.44	4.6±0.5	-	-1.52
40	6.3±0.5	-1.61	63±3	-1.44	7.9±1.4	-	-1.52
45	7.0±0.7	-1.60	55±2	-1.44	10.4±2.0	-	-1.52
50	8.8±0.9	-1.61	82±2	-1.44	17.2±2.5	0.9±0.4	-1.53
55	11.0±0.9	-1.61	116±4	-1.46	22.8±2.6	0.10±0.6	-1.53

7.3.2. AESEC Polarization Curves

The overall dissolution process may be decomposed into elementary reactions by consideration of the elemental polarization curves. AESEC linear sweep voltammetry (AESEC-

LSV) profiles are given in **Figs. 7.4 - 7.7** for pure Al, Zn and $\text{Al}_{5,2}\text{Zn}$ obtained at $T=20\text{ }^\circ\text{C}$, $30\text{ }^\circ\text{C}$, $45\text{ }^\circ\text{C}$ and $55\text{ }^\circ\text{C}$. The results at $T=40\text{ }^\circ\text{C}$ and $50\text{ }^\circ\text{C}$ were also measured but are not shown here. The curves were corrected for the uncompensated electrolyte resistance, R_Ω , by $E = E_{\text{measured}} - iR_\Omega$ with $R_\Omega=109\ \Omega$, determined by electrochemical impedance spectroscopy (EIS).

Pure Al

AESEC-LSV results of pure Al at each temperature are shown in **Fig. 7.4**. The Al dissolution rate, j_{Al} , was essentially constant, independent of potential, while j_e^* varied in the conventional manner. For $T \geq 30\text{ }^\circ\text{C}$ (**Fig. 7.4B - 7.4D**), the j_{Al} trend shows a regular decrease followed by a jump which is due to the formation of hydrogen bubbles as previously described. It is clear that at $T=20\text{ }^\circ\text{C}$ (**Fig. 7.4A**) the j_{Al} is completely independent of the electrochemical oxidation (j_e^*) for $E < -0.8\text{ V}$. For $E > -0.8\text{ V}$, the dissolution approaches a faradaic response with $z=3$, and increases slightly with potential (b_a approximately 1 V decade^{-1}).

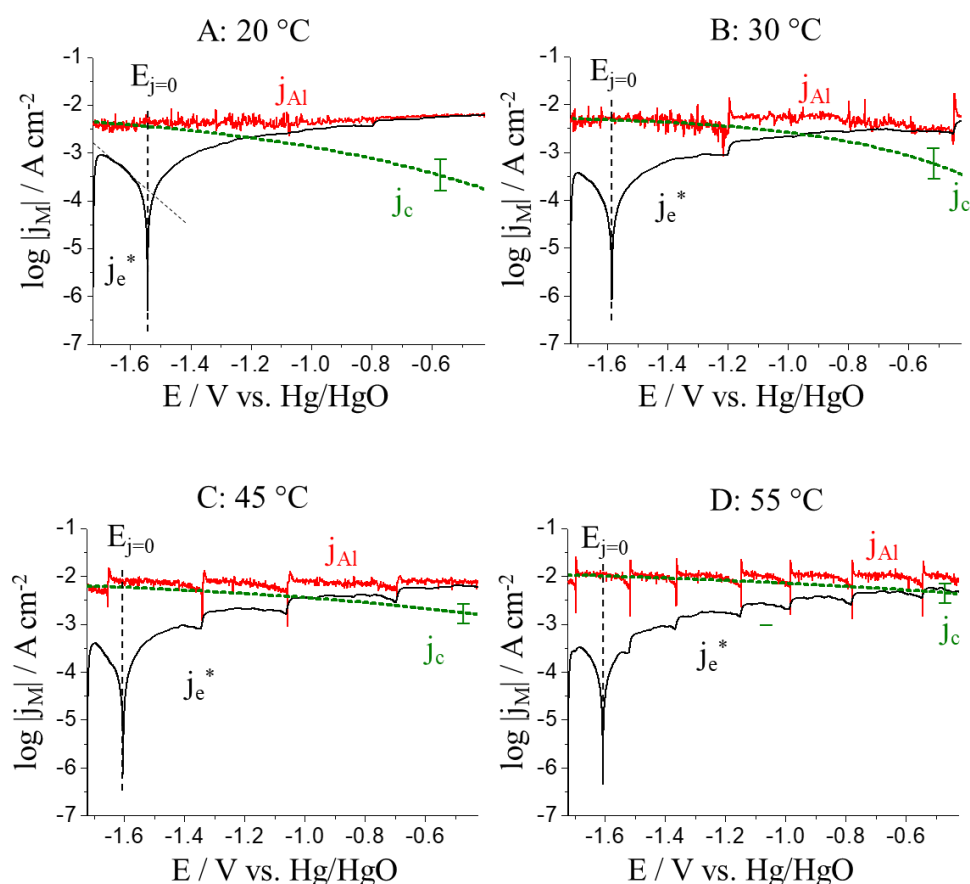


Fig. 7.4. AESEC-LSV of Al metal in 0.1 M NaOH, Ar deaerated electrolyte at **A:** $T=20\text{ }^\circ\text{C}$, **B:** $30\text{ }^\circ\text{C}$, **C:** $45\text{ }^\circ\text{C}$ and **D:** $55\text{ }^\circ\text{C}$ with 0.5 mV s^{-1} scan rate. j_c calculated by **Eq. 7.3** is shown in dashed line.

This potential dependence was not detectable at higher temperature due to perturbations on j_e^* and j_{Al} . Note that the real dissolution rate is an order of magnitude larger than what might be predicted from the polarization curve using an Evans diagram approach as shown in **Fig. 7.4A**. The elementary steps in Al dissolution in alkaline media can be written as **Reactions 7.5 - 7.7**:



The independence of j_{Al} and j_e^* demonstrates that the dissolution of Al oxide/hydroxide layer (**Reaction 7.6**) is the rate determining step (RDS) in accordance with previous studies [118,119,141]. Unfortunately, $Al(OH)_3$ formation (**Reaction 7.5**) was not measurable in these experiments by mass / charge balance as it is negligible as compared to the high dissolution rate. Nevertheless, the properties of the film most likely determine the reaction rate by controlling the access of H_2O to Al metal [118,120–123,141,169,170]. The cathodic current resulting from the HER may be determined simply as $j_c = j_{\Delta}$, shown as a dashed line with error bars determined by its noise signal in **Fig. 7.4**. Indeed, the decrease of j_{Δ} (HER) with increasing potential may be attributed to the increase in the $Al(OH)_3$ film thickness by **Reaction 7.5** [119,142,173]. The decrease in HER at $T=20$ °C, is also clearly indicated by a decrease in $\sigma_{j_{Al}}$ for $E > -1.1$ V.

Pure Zn

The AESEC-LSV of pure Zn (**Fig. 7.5**) may be divided into four potential domains as previously observed for galvanized steel and Zn-5Al alloy coatings [92,93]. These potential domains are indicated in **Fig. 7.5A**: (I) The cathodic domain where j_{Zn} was under the detection limit ($E < E_c^{Zn}$ where E_c^{Zn} is the onset potential of Zn dissolution); (II) the Tafel domain where j_{Zn} increased exponentially with potential; (III) the peak maximum domain where j_{Zn} obtained a maximum value over a fairly wide potential range and frequently showing two anodic peaks; and (IV) the passive domain where both j_e^* and j_{Zn} decreased to obtain a steady state, nearly independent of potential.

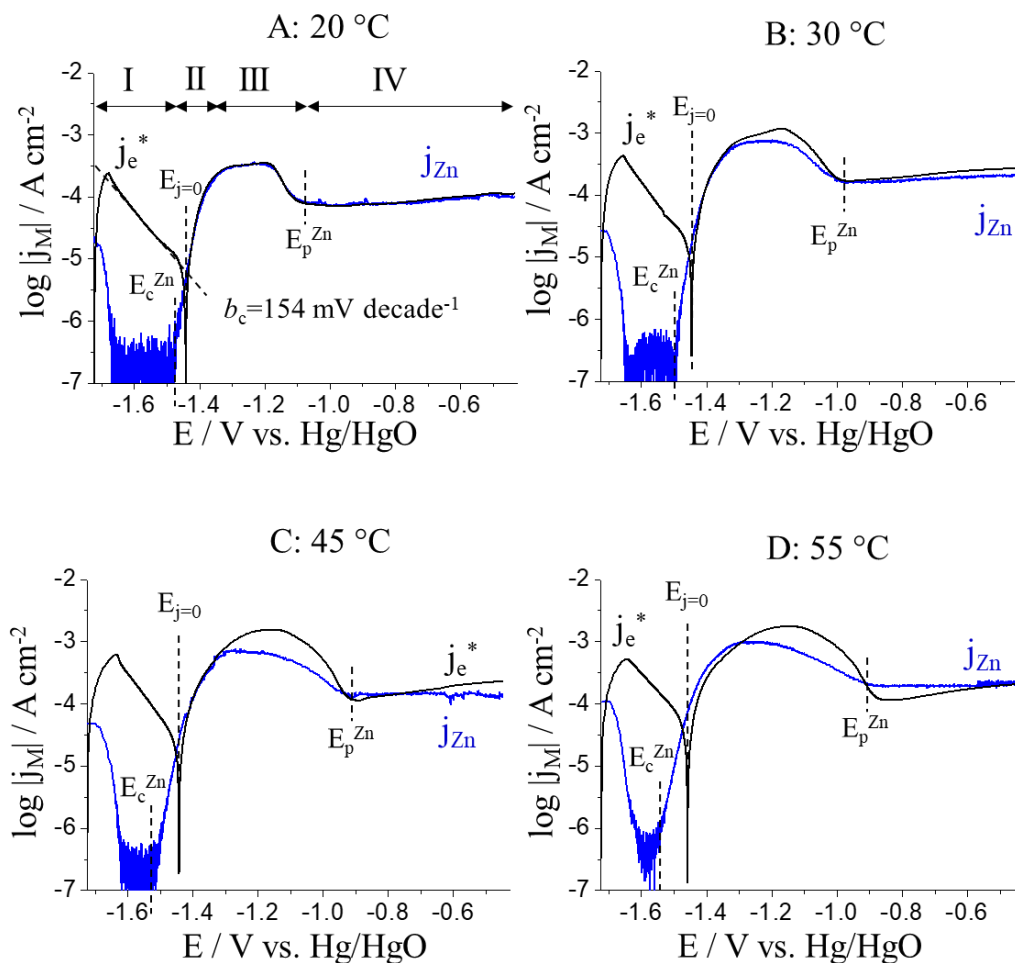
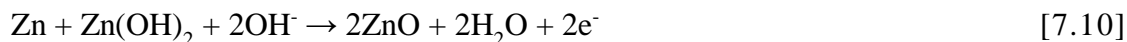


Fig. 7.5. AESEC-LSV of Zn metal in 0.1 M NaOH, Ar deaerated electrolyte at **A:** $T=20\text{ }^{\circ}\text{C}$, **B:** $30\text{ }^{\circ}\text{C}$, **C:** $45\text{ }^{\circ}\text{C}$ and **D:** $55\text{ }^{\circ}\text{C}$ with 0.5 mV s^{-1} scan rate. The curves were corrected taking into consideration of iR_{Ω} drop.

Consistent with previous studies, the anodic polarization curves may be interpreted in terms of four elementary reactions as follows. Although the precise nature of solid species formed during these experiments has not been clarified, these reactions will be used to interpret the polarization results:



The formation of ZnO (**Reaction 7.10**) leads to the passivation of the Zn [153], and would thus correspond to the “type III” oxide of reference [92]. Note that in this mechanism, ZnO formation may be considered to be in competition with Zn(OH)_2 dissolution (**Reaction 7.9**). Intermediates

such as ZnOH (or ZnOH_{ads}) are often proposed for Zn dissolution in alkaline media [92,95,174]. These species were not taken into consideration here because their formation was not readily measurable via a mass / charge balance on the experimental time scale used in the present work.

In the cathodic domain (I, $E < E_c^{Zn}$), it may be safely assumed that the HER made the only contribution to j_e^* because the oxidation and dissolution of Zn were negligible. The decreasing j_{Zn} for $E < -1.6$ V was due to residual Zn in the flow cell following the preceding open circuit dissolution and should be considered an artefact. Therefore, the cathodic current density (j_c) can be obtained in this domain by **Eq. 7.3**, $j_c = j_\Delta$. The effective cathodic Tafel slope ($b_c = 154 \pm 16$ mV decade⁻¹) was determined by j_e^* , also marked in **Fig. 7.5A**. The partial polarization curve for the HER is given in **Fig. 7.6A**. The magnitude of j_c increased by a factor of 2 between $T = 20$ °C, 30 °C, and 40°C but for $T > 40$ °C, the variation was not systematic.

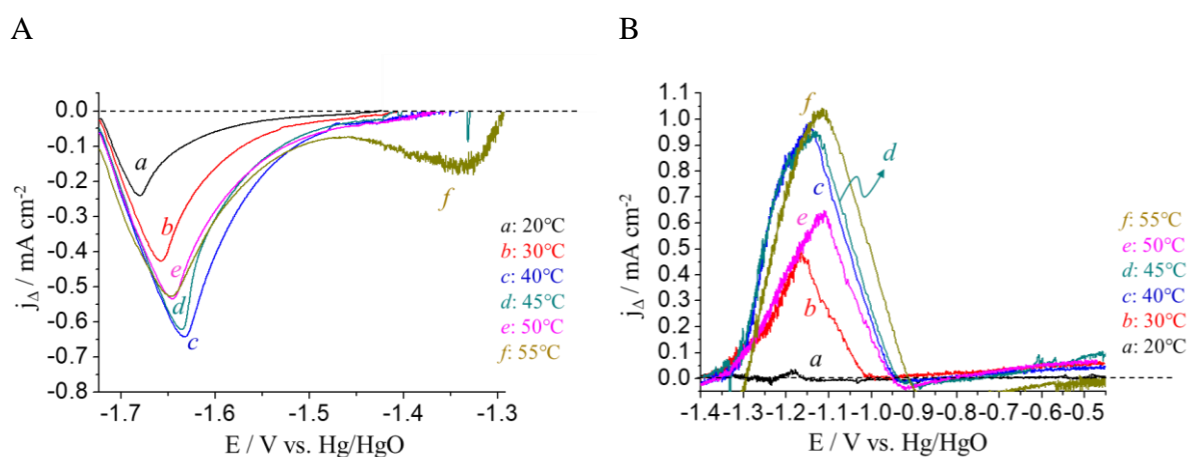


Fig. 7.6. Estimated non-faradaic dissolution, $j_\Delta = j_e^* - j_{Zn}$. **A:** cathodic current ($j_\Delta = j_c$) for $E < -1.3$ V **B:** insoluble species formation current ($j_\Delta = j_{ins}$) for $E > -1.40$ V and of Zn metal in the in 0.1 M NaOH, Ar deaerated electrolyte at each temperature.

In the Tafel domain (II), the onset of j_{Zn} occurs below the $j=0$ potential, $E_{j=0}$, suggesting that Zn oxidation (**Reaction 7.8**) leads immediately to Zn dissolution (**Reaction 7.9**) on the time scale of these experiments. Therefore, **Reaction 7.8** may be considered the rate determining step. This is hardly surprising in the highly alkaline conditions of these experiments. This is confirmed by the excellent faradaic response between j_{Zn} and j_e throughout the Tafel domain, and throughout the entire LSV curve for $T = 20$ °C. Note that, unlike the case for Al metal, a mixed potential analysis at $E_{j=0}$ does reasonably predict the dissolution rate.

In the peak maximum domain (III), the formation of a passivating oxide film occurred. This was clear visible in the LSV curves for $T \geq 30$ °C as indicated by $j_e^* > j_{Zn}$ ($j_{\Delta} > 0$). The cathodic current, j_c makes a negligible contribution to j_e^* in this domain, as indicated by the extrapolation of the Tafel line, for $E - E_{j=0} > 50$ mV. Therefore, j_e^* may be considered as the total Zn oxidation rate (**Reactions 7.8** and **7.10**). The formation of this oxide leads directly to the passivation of Zn and so it is reasonable to assume that this corresponds to ZnO formation, via **Reaction 7.10**. The formation of ZnO is therefore given by j_{Δ} . The partial polarization curves for ZnO formation (**Fig. 7.6B**) showed a fairly symmetrical peak, the maximum of which increased with temperature except for $T=50$ °C. This result is coherent with the thermodynamic prediction in **Fig. 7.1**.

The total amount Zn in the oxide film, Q_{ZnO} , may be quantified by integration of j_{Δ} peak as:

$$Q_{ZnO} = \int_{t_1}^{t_2} j_{\Delta} dt / z \quad [7.12]$$

where z is the number of electrons exchanged in the oxidation of Zn ($=2$), t_1 and t_2 are time at $E_{j=0}$ and E_p^{Zn} respectively. E_p^{Zn} is the onset potential for passive Zn dissolution. Q_{ZnO} increased markedly with temperature, 20 °C $\leq T \leq 40$ °C, as provided in **Table 7.2**.

Table 7.2. Quantified ZnO (Q_{ZnO}) for t_1 (t at $E_{j=0}$) $< t < t_2$ (t at E_p^{Zn}) of the AESEC-LSV of Zn metal in 0.1 M NaOH, Ar deaerated electrolyte at each temperature.

Q_{ZnO} / $\mu\text{mol cm}^{-2}$	20 °C	30 °C	40 °C	45 °C	50 °C	55 °C
$\int_{t_1}^{t_2} j_{\Delta} dt / z$	0.03	0.41	1.3	1.5	1.6	1.7

In the passive domain, (IV, $E > E_p^{Zn}$), the oxidation of Zn is controlled by the presence of a passive oxide film, via **Reactions 7.10** and **7.11**. Under all circumstances, j_{Zn} was independent of potential indicating that **Reaction 7.11** controls the dissolution step. We may consider j_{Zn} as the rate of ZnO dissolution via **Reaction 7.11**. Unlike the situation for Al metal, the cathodic reaction makes a negligible contribution to j_e^* such that j_e^* is a measure of the rate of ZnO formation, **Reaction 7.10**. At $T=20$ °C, ZnO formation and ZnO dissolution were in a

VII. Temperature dependence of Al, Zn and α -phase Zn-68Al

steady state, $j_{Zn} = j_e^*$. At higher temperatures, however, j_e^* did not follow j_{Zn} in systematic way. In the early part of domain IV, $j_{Zn} > j_e^*$. This is consistent with the passivation of Zn by an excess of ZnO, formed during domain III via **Reaction 7.10**. As the excess ZnO dissolution continued, j_e^* increased with the decreasing ZnO film thickness and increasing potential. At this point, Zn oxidation would occur at the Zn/ZnO interface via a conventional passive film formation mechanism, differing from the ZnO formation in domain III. In some cases, $j_e^* > j_{Zn}$ by the end of the potential sweep indicating the growth of the passive film.

Table 7.3 gives E_c^{Zn} , $E_{j=0}$, E_p^{Zn} (from **Fig. 5**), E_{oc} (from **Fig. 7.2A**) and Tafel slopes determined from j_{Zn} . Tafel slopes measured herein were in a good agreement with those measured with the same technique at the same electrolyte condition for galvanized steel, Zn-5Al alloy coating and $Al_{5.2}Zn$ phase (30~44 mV decade⁻¹) at room temperature [92,93,143]. The Tafel slope increased with temperature, indicating an increase in oxide/hydroxide film growth [142].

Table 7.3. Potential values after iR compensation obtained from AESEC-LSV of pure Zn in 0.1 M NaOH, Ar deaerated electrolyte at each temperature.

V vs. Hg/HgO		20 °C	30 °C	40 °C	45 °C	50 °C	55 °C
OCP	E_{oc}	-1.53	-1.52 V	-1.52 V	-1.52 V	-1.53 V	-1.53 V
LSV	$E_{j=0}$	-1.44	-1.45 V	-1.44 V	-1.44 V	-1.44 V	-1.46 V
	E_c^{Zn}	-1.47	-1.50 V	-1.52 V	-1.52 V	-1.52 V	-1.56 V
	E_p^{Zn}	-1.08	-0.97 V	-0.91 V	-0.90 V	-0.85 V	-0.87 V
Tafel $j_{Zn}/mV \text{ decade}^{-1}$		34	32	43	40	39	47

$Al_{5.2}Zn$

Fig. 7.7 gives j_M vs. E curves of $Al_{5.2}Zn$ at T=20 °C, 30 °C and 45 °C, at pH=12.80 with Ar deaeration. Because of the intense Al dissolution rate and high j_e^* , the iR_Ω correction considerably altered the curves so that the maximum anodic potential seemed to decrease with increasing temperature. For $T \geq 50$ °C, it was difficult to measure the exact elemental dissolution rate as a function of potential, especially at more positive potentials, with $j_e^* > 5$ mA cm⁻² and they are not shown herein.

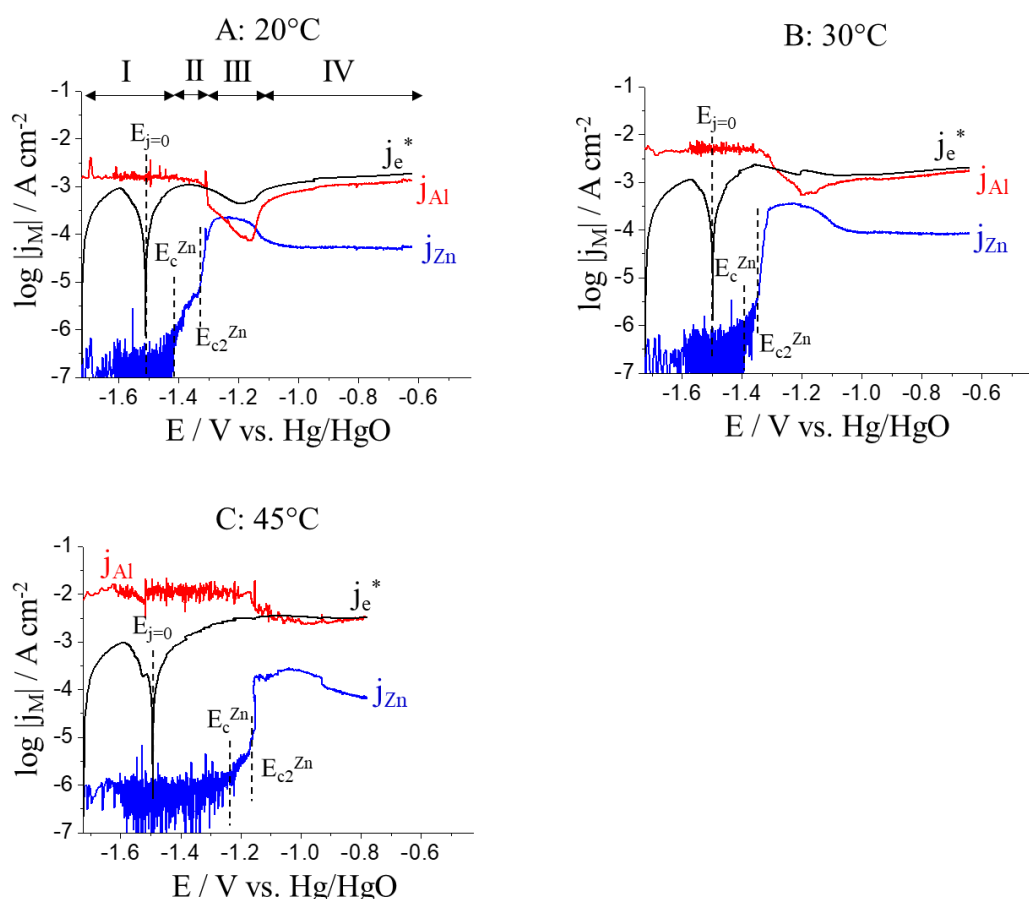


Fig. 7.7. AESEC-LSV of $\text{Al}_{5.2}\text{Zn}$ in 0.1 M NaOH, Ar deaerated electrolyte at **A:** $T=20^\circ\text{C}$, **B:** 30°C and **C:** 45°C with 0.5 mV s^{-1} scan rate. The curves were corrected taking into consideration of iR_Ω drop.

The overall form of the Zn dissolution was qualitatively the same as for pure Zn, except that the potential was shifted to more positive values perhaps due to iR_Ω correction. It is not possible to estimate the partial reactions of oxide formation because the total current involves both Al dissolution and the HER. The elementary Al dissolution profiles were similar to those obtained for pure Al for $E < E_c^{\text{Zn}}$. However, j_{Al} decreased by more than an order of magnitude in domain II and III. In the passive domain (IV) it rose again to obtain a new steady state value. This suggests a mechanism of ion transfer across an oxide film. The cathodic reaction was reduced to near zero as indicated by the faradaic dissolution, $j_e^* \approx j_{\text{Al}} + j_{\text{Zn}}$ and by the decrease of $\sigma_{j_{\text{Al}}}$.

It is convenient to define the more positive onset potential where j_{Zn} abruptly increased, E_{c2}^{Zn} . Zn dissolution was below the detection limit for $E < E_c^{\text{Zn}}$, and then increased without inhibiting Al dissolution. However, for $E > E_{c2}^{\text{Zn}}$, Al dissolution decreased as Zn dissolution

VII. Temperature dependence of Al, Zn and α -phase Zn-68Al

rose to its maximum value. The inhibitive effect of Zn on Al dissolution was attributed to dissolution of the Zn(0) enriched layer formed during the preceding potential sweep [175]. Both E_c^{Zn} and E_{c2}^{Zn} shifted to more positive values with increasing temperature. This may be correlated with the enhanced selective Al dissolution. The potential values are summarized in **Table 7.4**.

Table 7.4. Potential values after iR_Ω compensation obtained from AESEC-LSV of $Al_{5.2}Zn$ phase in 0.1 M NaOH, Ar deaerated electrolyte at each temperature.

vs. Hg/HgO		20 °C	30 °C	40 °C	45 °C	50 °C	55 °C
OCP	E_{oc}	-1.53 V	-1.51 V	-1.51 V	-1.51 V	-1.52 V	-1.51 V
LSV	$E_{i=0}$	-1.51 V	-1.50 V	-1.49 V	-1.49 V	-1.50 V	-1.49 V
	E_c^{Zn}	-1.42 V	-1.39 V	-1.32 V	-1.23 V	-1.41 V	-1.41 V
	E_{c2}^{Zn}	1.35 V	-1.34 V	-1.23 V	-1.17 V	-1.35 V	-1.20 V

7.4. Kinetic Analysis and discussion

The temperature dependence of the corrosion process may be evaluated quantitatively via the Arrhenius equation

$$\ln j_M = \ln A + (-E_a/RT) \quad [7.13]$$

where E_a is the activation energy, A is the pre-exponential factor, R is the universal gas constant and T is the absolute temperature in Kelvin. In this section, the activation energy will be referred to as E_a (M/M') where M is the dissolving element measured as j_M , and M' is the material (Al, Zn, or $Al_{5.2}Zn$).

7.4.1 Al dissolution

Fig. 7.8 shows Arrhenius plots, for Al dissolution, $\ln(j_{\text{Al}}^s)$ vs. $1/T$, for pure Al and the $\text{Al}_{5.2}\text{Zn}$ phase. The E_a values are provided in **Table 7.5**. For spontaneous dissolution of pure Al, $E_a(\text{Al}/\text{Al}) = 31 \text{ kJ mol}^{-1}$, which is significantly lower than that of $\text{Al}_{5.2}\text{Zn}$, $E_a(\text{Al}/\text{Al}_{5.2}\text{Zn}) = 60 \text{ kJ mol}^{-1}$. For comparison, $E_a = 57 \text{ kJ mol}^{-1}$ was previously reported [142] for pure Al in alkaline solution using a rotating cylinder electrode. This system had a much higher anodic dissolution rate due to the forced convection. For Al, it is impossible to separate the different reactions via a mass-charge balance as all three reactions are coupled together via the properties of the interfacial $\text{Al}(\text{OH})_3$ film. The Al dissolution rate of $\text{Al}_{5.2}\text{Zn}$ by LSV was relatively independent of potential for $E < E_c^{\text{Zn}}$ (near -1.4 V) as revealed by the similar $E_a(\text{Al}/\text{Al}_{5.2}\text{Zn})$ value to that at E_{oc} as given in **Table 7.5**.

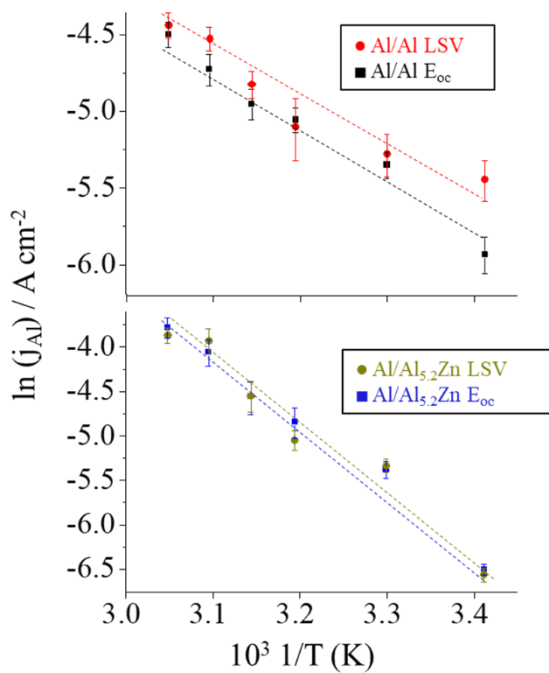


Fig. 7.8. Arrhenius plot for $E_a(\text{Al}/\text{Al})$ and $E_a(\text{Al}/\text{Al}_{5.2}\text{Zn})$ for spontaneous dissolution and AESEC-LSV experiments.

Table 7.5. $E_a(\text{Al}/\text{Al})$ and $E_a(\text{Al}/\text{Al}_{5.2}\text{Zn})$ obtained from **Fig. 7.8**.

	At E_{oc}	At $E = -1.4 \text{ V}$
$E_a(\text{Al}/\text{Al}) / \text{kJ mol}^{-1}$	31	24
	At E_{oc}	At Tafel (II)
$E_a(\text{Al}/\text{Al}_{5.2}\text{Zn}) / \text{kJ mol}^{-1}$	60	61

The apparent E_a reflects the kinetics of oxide film dissolution which is the rate limiting step. It is not clear why E_a (Al/Al_{5.2}Zn) > E_a (Al/ Al) however, it could be attributed to the fact that selective Al dissolution leads to the formation of an interfacial region enriched in metallic Zn. The rate at T= 20 °C is lower for Al_{5.2}Zn than for pure Al but becomes larger at higher temperatures. A possible interpretation of this result is that the Zn destabilizes the passive film on Al_{5.2}Zn, thereby enhancing the corrosion rate at higher temperature.

At high potential, for the Al/Al_{5.2}Zn, the transfer of cations through the oxide film, presumably ZnO, is the rate determining step for Al dissolution. Unfortunately, at higher temperatures this potential domain was not accessible in the LSV experiments described here, due to the extremely large currents and the resulting large iR_Ω correction. The remaining data gave a non-linear Arrhenius plot which is not surprising as the rate depends on several processes including the migration of the Al cations across the film, the thickness of the film, and its formation and dissolution rate.

7.4.2 Zn dissolution

As discussed previously, different elementary phenomena dominate Zn dissolution in the different potential domains of the LSV results. Open circuit dissolution of pure Zn (**Fig. 7.2A**) occurs around -1.45 V, in the Tafel region (domain II) of the LSV curves (**Fig. 7.5**). The rate determining reaction in this domain is considered to be the oxidation of Zn to form Zn(OH)₂, **Reaction 7.8**. Arrhenius plots for j_{Zn} at open circuit and in the Tafel domain of the LSV curves are shown in **Fig. 7.9** and the E_a values are given in **Table 7.6**. At open circuit, E_a (Zn/Zn) = 30 kJ mol⁻¹, while E_a (Zn/Al_{5.2}Zn) was undetectable as j_{Zn} was rose only slightly with temperature and was below the detection limit for T < 50°C (**Fig. 7.3**). This compares with a value of 38 kJ mol⁻¹ and 17 kJ mol⁻¹ in Tafel domain from LSV for Zn and Al_{5.2}Zn, respectively. The difference of the E_a values for Zn and Al_{5.2}Zn suggests that Zn oxidation and dissolution were affected by the presence of Al. This may in part be attributed to the presence of a surface layer enriched in metallic Zn formed by selective Al dissolution.

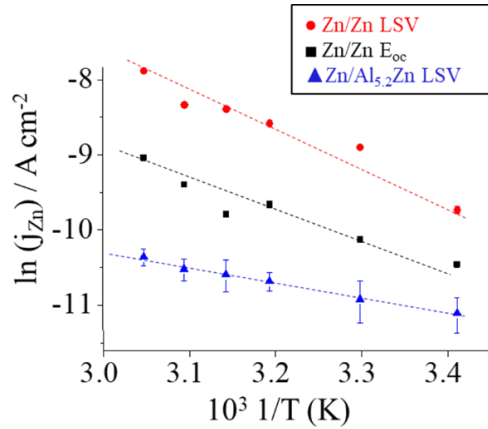


Fig. 7.9. Arrhenius plot for E_a (Zn/Zn) and E_a (Zn/Al_{5.2}Zn) for spontaneous dissolution and AESEC-LSV experiments.

Table 7.6. E_a (Zn/Zn) and E_a (Zn/Al_{5.2}Zn) obtained from **Fig. 7.9**.

$E_a/\text{kJ mol}^{-1}$	At E_{oc} (pure Zn)	At Tafel (II)	
		Pure Zn	Al _{5.2} Zn
	30	38	17

For the peak maximum (III), **Reactions 7.9** and **7.10** predominate, and for pure Zn, the two reactions may be decoupled by a mass-charge balance as by j_{Zn} and j_{Δ} (representing Q_{ZnO}), respectively. The Arrhenius plots are shown in **Fig. 7.10** and the E_a values are given in **Table 7.7**. The E_a (Zn/Zn) = 21 kJ mol⁻¹ and E_a (Zn/Al_{5.2}Zn) \approx 9 kJ mol⁻¹. The E_a for oxide formation (**Reaction 7.10**) was calculated from the maximum of the j_{Δ} vs. E curves, **Fig. 7.6B**, giving E_a (Q_{ZnO}/Zn) = 40 kJ mol⁻¹. No similar calculations were possible for Al_{5.2}Zn due to the intense cathodic activity associated with Al dissolution.

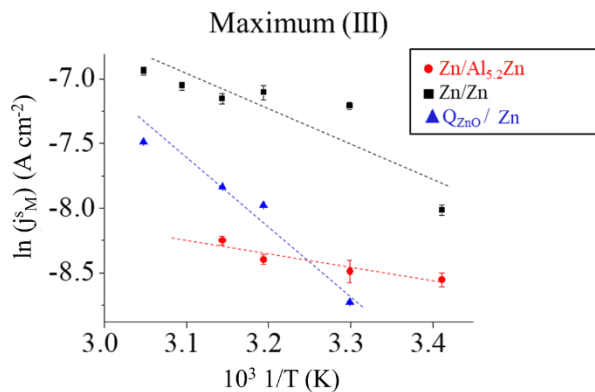


Fig. 7.10. Arrhenius plot for E_a (Zn/Zn), E_a (Q_{ZnO}/Zn) and E_a (Zn/Al_{5.2}Zn) at the peak maximum domain (III) of each AESEC-LSV curve.

Table 7.7. E_a (Zn/Zn), E_a (Q_{ZnO}/Zn) and E_a (Zn/ $Al_{5.2}Zn$) obtained from **Fig. 7.10**.

	At maximum (III)		
	Zn/Zn	Zn/ $Al_{5.2}Zn$	Q_{ZnO}/Zn
$E_a/kJ\ mol^{-1}$	21	9	40

The high activation energy for oxide formation is an interesting result in terms of the pretreatment process. The effect of increasing temperature is to enhance Al dissolution and favor Zn oxide formation over Zn dissolution. For a Zn-Al alloy coating, the net result would be to replace the native Al oxide film with a ZnO film. This is significant as the native Al oxide-hydroxide film is known to inhibit the nucleation and growth of many conversion coatings on galvanized steel [136,176,177]. In the passive domain (IV) of pure Zn, ZnO dissolution (j_{Zn}) and film formation (j_e^*) occur simultaneously but are decoupled from one another. The Arrhenius plot is shown in **Fig. 7.11**, however, no clear activation energy may be measured. Both j_{Zn} and j_e^* increase by more than an order of magnitude between 20 °C and 30 °C but do not increase significantly with further temperature increase.

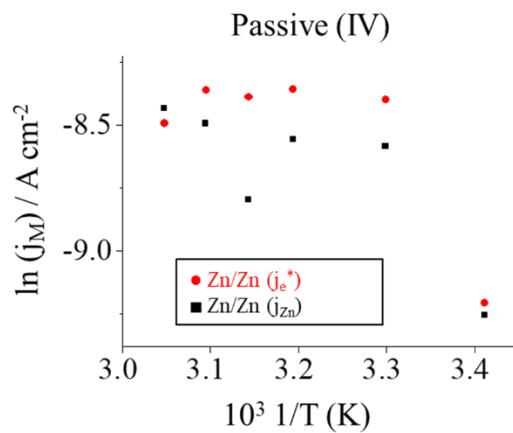
**Fig. 7.11.** Arrhenius plot for E_a (Zn/Zn) from j_e^* and j_{Zn} at the passive domain (IV).

Fig. 7.12 gives a summary of the elementary reactions during the dissolution of Zn and Al in alkaline media with their respective activation energies measured in this work.

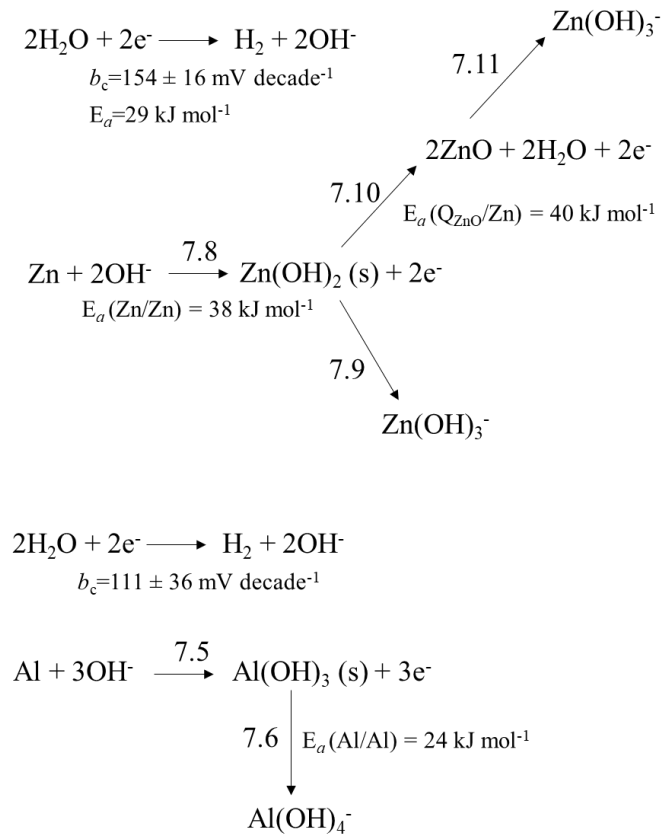


Fig. 7.12. Summary of elementary reactions during the pure Zn and Al dissolution in alkaline media.

7.5. Conclusions

The elementary reactions of dissolution, oxide formation, and passivation have been measured independently with AESEC during the exposure of Al, Zn and the pure α -phase $\text{Al}_{5.2}\text{Zn}$ to 0.1 M NaOH, Ar deaerated electrolyte. The idea was to identify and quantify the rates of the principal elementary reactions occurring during alkaline pretreatment of Al, Zn and Zn-Al alloys.

1) Al dissolution increased markedly with temperature for both pure Al and α -phase $\text{Al}_{5.2}\text{Zn}$ and was limited by the dissolution rate of the Al(OH)_3 film (**Reaction 7.6**).

2) At the open circuit, the $\text{Al}_{5.2}\text{Zn}$ phase reacted similarly to pure Al, undergoing selective Al dissolution to form a Zn(0) enriched layer. The presence of Zn in the Al alloy raised the OCP to just below the onset of Zn dissolution. Zn dissolution from the $\text{Al}_{5.2}\text{Zn}$ phase at open circuit was minimal and only observed at higher temperature.

VII. Temperature dependence of Al, Zn and α -phase Zn-68Al

- 3) The rate and activation energy of Al dissolution increased for $\text{Al}_{5.2}\text{Zn}$ with respect to pure Al for $T \geq 30$ °C. This was attributed to the presence of Zn destabilizing the passive film.
- 4) The kinetics of Zn dissolution was not strongly affected by alloying with Al perhaps because Al selective dissolution leads to the formation of a Zn(O) enriched film.
- 5) In the Tafel domain (II) for Zn dissolution, the rate determining reaction is the oxidation of Zn forming $\text{Zn}(\text{OH})_2$ (**Reaction 7.8**) as evidenced by nearly faradaic dissolution in this potential domain.
- 6) Zn exhibited a passive domain for higher potentials for both pure Zn and $\text{Al}_{5.2}\text{Zn}$. The dissolution rate was limited by charge transfer across the ZnO passive film in this domain.
- 7) At higher temperatures, Al dissolution and the formation of ZnO were favored. This is consistent with the practice of alkaline cleaning of Zn-Al alloy coatings on steel in which the goal is to eliminate native Al oxides and eventually replace them with a reproducible ZnO surface.
- 8) Kinetic parameters (activation energies and Tafel constants) for several of the elementary processes activation energies were measured and discussed.

Chapter VIII. Electrochemical database of Zn-Al-Mg system from neutral to alkaline media.

«Moi je souriais, mais à l'intérieur j'avais envie de crever. Des fois je sens que la vie, c'est pas ça, c'est pas ça du tout, croyez-en ma vieille expérience.»

La vie devant soi (1975),
Romain Gary (Emile Ajar)

8. Electrochemical database of Zn-Al-Mg system from neutral to alkaline media.

8.1. Introduction

The objective of this chapter is to characterize the stability of the various phases and technical samples over a range of pH values and alloy compositions. The previous chapters have however been focused on the reactivity of individual phases characterized in specific environments. There are a number of trends that are visible only by looking at all the alloys and all the pH values at the same time. In this chapter, the ensemble of AESEC-LSV curves are presented, the associated electrochemical parameters are tabulated, and the various trends are pointed out and discussed.

An AESEC-LSV curve and an open circuit dissolution profile were obtained for each pure metal, pure phase alloy and technical (commercial) alloy coatings. The electrochemical database presented herein consists of these polarization curves and tables that include E_{oc} (open circuit potential), E_c^{Zn} (onset potential of Zn dissolution), $E_c^{Zn/Zn-OH}$ (onset potential of cathodic Zn dissolution), E_c (onset potential of bulk material) and $E_{j=0}$ (potential where $j=0$), and elemental dissolution rates (j_M).

8.2. Experimental

Materials

The technical Zn-Al-Mg alloys used in this work were in the form of galvanized steel coatings with Zn-1.6 wt.% Al-1.6 wt.% Mg (MagiZincTM, denoted as Zn-1.6Al-1.6Mg) and Zn-2.5 wt.% Al-1.5 wt.% Mg (CorrenderTM, denoted as Zn-2.5Al-1.5Mg). These were produced by Tata steel and Voestalpine, respectively. Nominally pure η -phase of Zn (Zn-0.7 wt.% Al, denoted as Zn-0.7Al), β and α -phase of Al-Zn (Zn-22 wt.% Al (Zn-22Al) and Zn-68 wt.% Al (Zn-68Al) respectively, and the $MgZn_2$ (Zn-16 wt.% Mg) intermetallic compound were synthesized by *Department of Metals and Corrosion Engineering, University of Chemistry and Technology, Prague*. The pure metals of Zn (99.998 %), Al (99.99 %) and Mg (99.9 %) obtained from *Goodfellow* were also measured as a reference.

All samples were prepared in the same way to have a comparable surface state, reduce the effect of pre-existed surface oxide species, and have reproducible experimental results. Samples were degreased by ethanol, ground by emery paper then stored during 24 h in a humidity chamber with 50 % relative humidity (RH).

Electrolytes

As the elemental dissolution varies with pH, it was of interest to choose the electrolyte pH values so as to have a range of solubility for the more stable corrosion products. The total saturation concentrations, $C_M(\text{sat})$, of the different ions are shown as a function of pH in **Fig. 8.1** as calculated using the Hydra MedusaTM software and its default database. In this work, pH=8.4, 10.1 and 12.80 were chosen because these values reflect different extremes of insoluble corrosion products. For example, at pH=8.4, Mg is expected to dissolve easily and Al corrosion products are expected to be relatively insoluble. At pH=12.80, Al is highly soluble while Mg products are insoluble.

All electrolytes were prepared from analytical grade materials and deionized water of 18.2 M Ω cm obtained via a MilliporeTM system. For pH=8.4 and 10.1, a low concentration 30 mM NaCl solution was prepared to minimize the effect of chloride containing corrosion products. pH=12.80 solution was prepared with 0.1 M NaOH without chloride. The final pH was adjusted by NaOH. The electrolyte was not buffered to avoid complications due to the anion of the buffer and to more accurately represent field conditions and eliminate the need for the addition of an anion that is not representative of the corrosion conditions of interest. The electrolyte was either deaerated by bubbling Ar for 20–30 minutes prior to the experiment and maintained by flowing Ar above the electrolyte during the experiment, or saturated with O₂ using the same procedure with pure O₂ (Air Liquide, SA, 100% O₂ compressed gas). The objective of deaeration is to minimize the cathodic reaction which complicates the decomposition of the polarization curve as it cannot be measured independently with the experimental set-up used here.

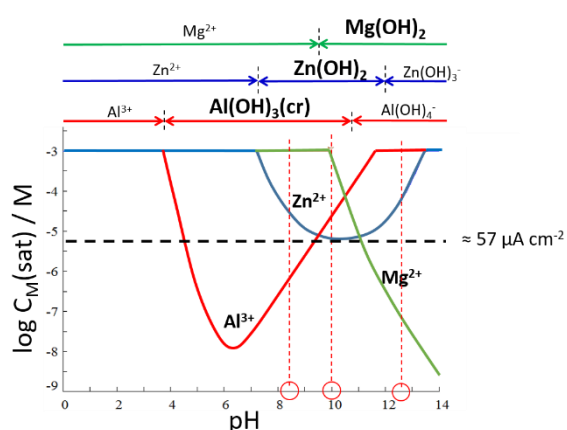


Fig. 8.1. $C_M(\text{sat})$ of Zn^{2+} , Al^{3+} and Mg^{2+} in pure water calculated by Hydra MedusaTM software using the default database. The arrows above the curve, indicate the predominant species in each pH range. The precipitated solid phase is indicated in bold. The three pH values investigated here are indicated with dashed vertical lines. They were chosen by the differing solubility of the various corrosion products.

A Gamry Reference 600TM potentiostat was used to control and measure the electrochemical potential and current. Elemental dissolution rates were measured at open circuit as a function

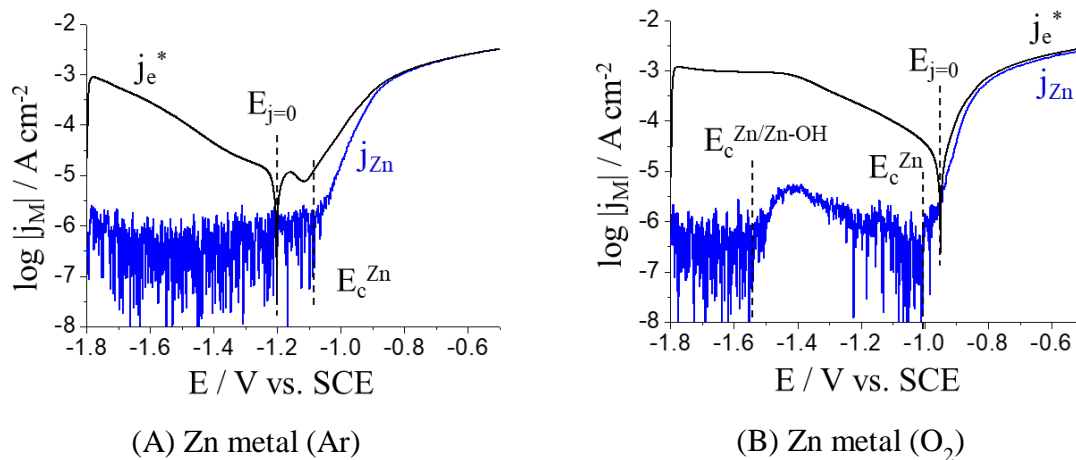
of time by the AESEC technique. After turning on the flow cell, the dissolution rates of Zn, Al and Mg were measured for approximately 10 minutes until stabilized. The AESEC linear sweep voltammetry, AESEC-LSV, was performed to characterize the dissolution rate vs. applied potential characteristic curve using a linear potential of 0.5 mV s^{-1} scan rate from cathodic (-1.80 V vs. SCE) to anodic potential (-0.50 V vs. SCE). At the $E_{j=0}$, where the transition from cathodic to anodic current is observed, the elemental dissolution rates was calculated and compared to those obtained during spontaneous open circuit dissolution.

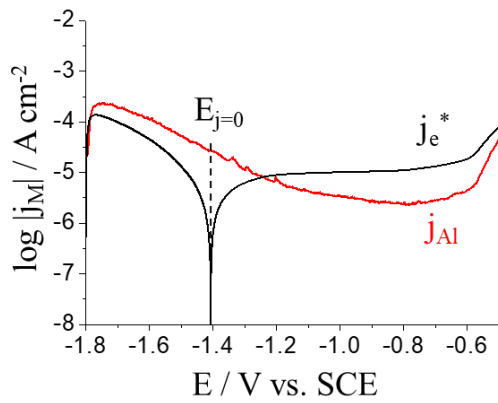
8.3. Results

8.3.1. AESEC-LSV at pH=10.1

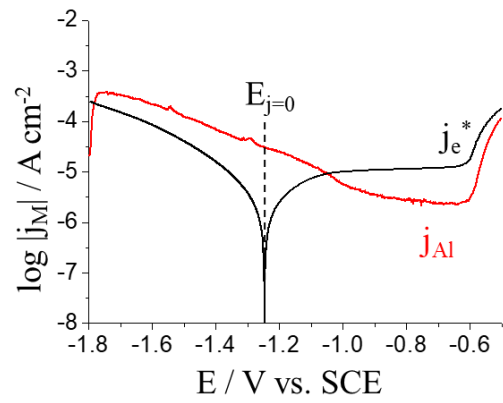
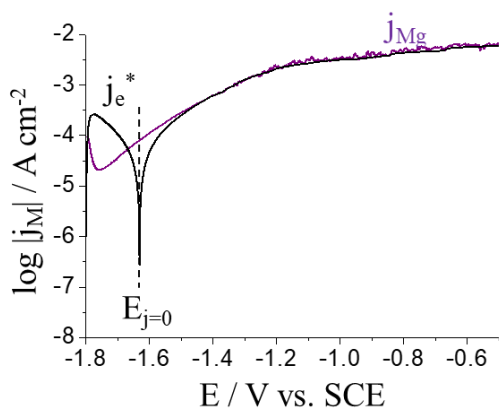
All specimens investigated in this Ph.D. work were electrochemically tested at pH=10.1, 30 mM NaCl either deaerated by Ar or saturated with O_2 electrolyte. The pH=10.1 was chosen as an intermediate pH where all three elements showed some solubility. Such pH values may easily be reached during the corrosion of galvanized steel for example on the cut edge where the cathodic and anodic reactions are in close proximity [7,84–86]. The results for MgZn₂ and Zn-68Al were previously discussed in detail in **Chapters IV** and **V**.

Typical results of the elemental AESEC-LSV curves are shown in **Fig. 8.2**. The potential values measured in this work are summarized in **Table 8.1**. The average j_M at the spontaneous dissolution condition, j_M^s , are summarized in **Table 8.2**. Tafel slopes determined from j_{Zn} are also given and compared to each other. All the potential values presented in this work are referenced to a SCE electrode unless otherwise stated.

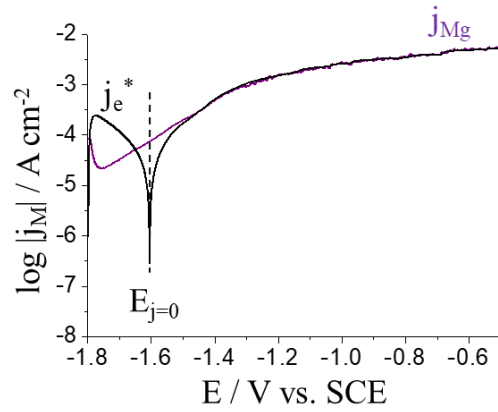
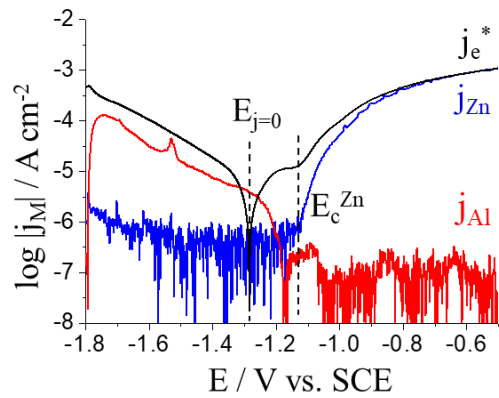




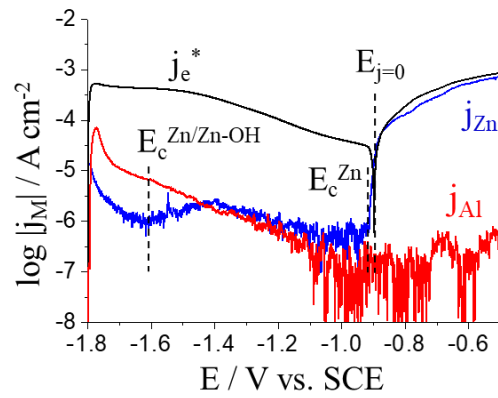
(C) Al metal (Ar)

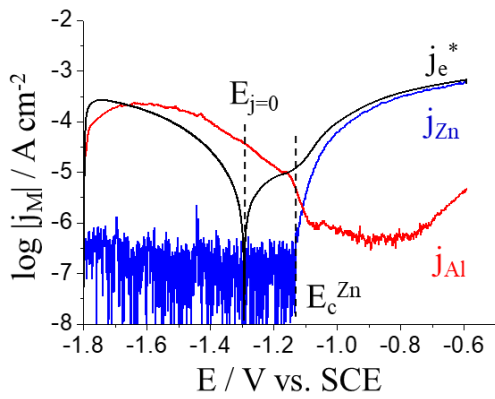
(D) Al metal (O₂)

(E) Mg metal (Ar)

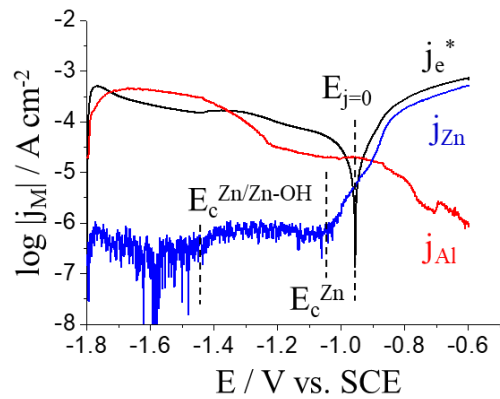
(F) Mg metal (O₂)

(G) Zn-0.7Al (Ar)

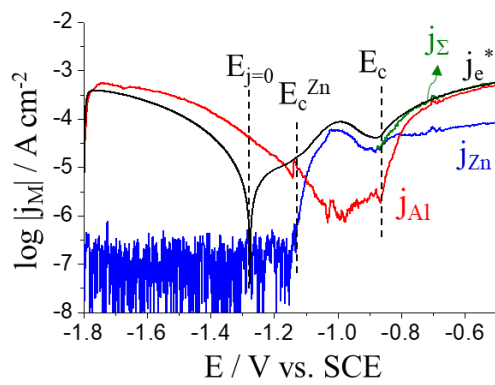
(H) Zn-0.7Al (O₂)



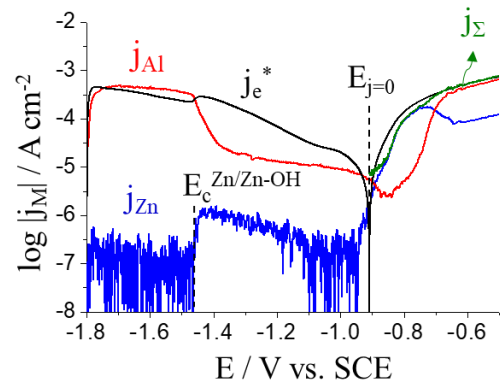
(I) Zn-22Al (Ar)



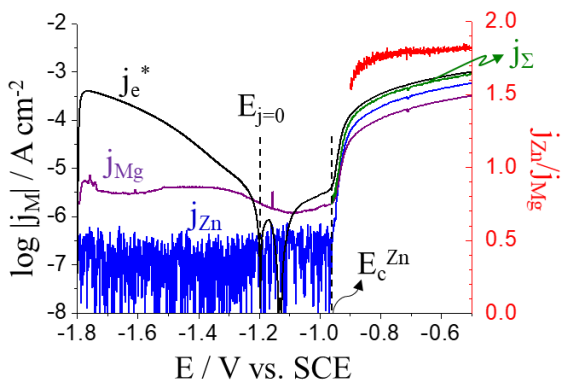
(J) Zn-22Al (O₂)



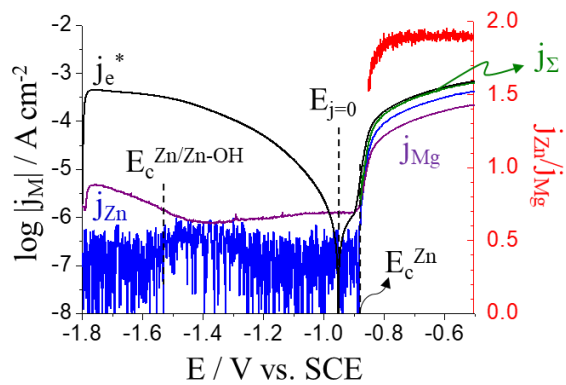
(K) Zn-68Al (Ar)



(L) Zn-68Al (O₂)



(M) MgZn₂ (Ar)



(N) MgZn₂ (O₂)

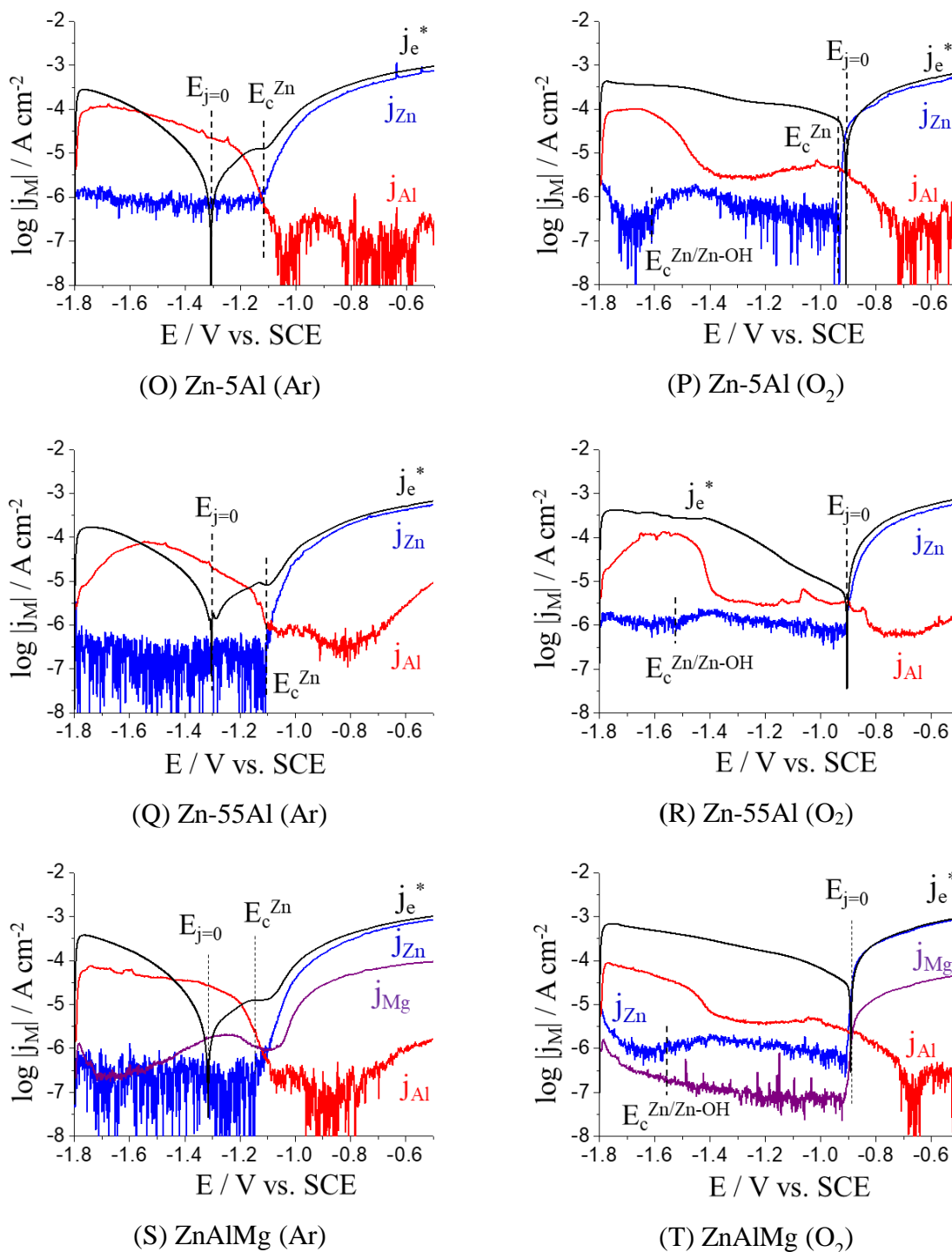


Fig. 8.2. AESEC-LSV curves at pH=10.1, 30 mM NaCl at T=25 °C.

COMMENTS:

1) The stoichiometry of the reactions indicates whether or not oxide forms. For pure Zn and Mg metals, at high anodic polarizations, $\eta \approx 1$ demonstrating that dissolution was faradaic with no significant oxide formation. This is an important result in that it confirms the accuracy of the method. Therefore, when $j_M < j_e^*$ ($\eta < 1$) we can assume that the difference is due to the

formation of insoluble oxidation products. For Al dissolution, however, significant insoluble oxide formation is indicated as $j_{\text{Al}}/j_e^* = 0.23$ at -0.60 V in Ar deaerated electrolyte.

2) Saturation with O_2 greatly enhanced the cathodic dissolution of pure Zn. A j_{Zn} peak was observed at $E = -1.40$ V masked by significantly increased cathodic current. On the other hand, the dissolution rate of pure Mg was not measurably affected by O_2 saturation. For pure Al, the cathodic current increased with O_2 saturation, however the stoichiometry of dissolution ($v_e^*/v_{\text{Al}} = -3j_e^*/j_{\text{Al}}$) was nearly unchanged indicating that Al dissolution was driven by the cathodic current, as discussed in **Chapter V**.

3) For Zn-0.7Al, significant selective Al dissolution in the cathodic potential domain was observed even though it contains only 0.7 wt.% Al both with Ar deaeration and O_2 saturation. The selective dissolution of Al should lead to the formation of a significant quantity of enriched Zn(0), and given the low % Al. It is surprising that this enriched Zn(0) layer, does not inhibit further Al dissolution. Interestingly, with O_2 saturation, j_{Al} in the cathodic potential branch was reduced with respect to that in Ar deaerated electrolyte.

4) For Zn-68Al, significant selective Al dissolution was monitored in the cathodic potential domain. Zn dissolution showed two onset potentials, at $E_c^{\text{Zn}} = -1.14$ V and $E_c = -0.88$ V. The former was due to the dissolution of a Zn(0) enriched layer formed by Al selective dissolution as demonstrated in **Chapter V**. The presence of the Zn(0) enriched layer was confirmed by chronoamperometry (CA) and chronoamperometric step experiments. The onset of Zn dissolution in the cathodic potential domain in O_2 saturated electrolyte was correlated with a decrease in the Al dissolution rate. This is referred to as the apparent inhibitive effect of Zn on Al dissolution.

5) For MgZn_2 , the onset of Mg and Zn dissolution occur simultaneously and at a potential that was shifted in the positive direction with respect to pure Zn. This probably reflects the fact that it is an intermetallic compound MgZn_2 and the bonding of the elements further stabilizes the material. Also, it can be attributed to a metallic Zn enriched layer (Zn(0)) formation during cathodic polarization.

6) In general, Zn dissolution for the alloy coating was nearly identical to pure Zn metal and the Zn-0.7Al synthetic phase. This is hardly surprising since the alloy coating is approximately 96 % Zn. Mg dissolution differed radically between the nominally pure Mg and the MgZn_2 phase/ZnAlMg alloy coating. This demonstrates that the dissolution rate of Mg was

highly affected by the presence of Zn, no doubt due to the formation of the MgZn_2 intermetallic. We attributed the reduced Mg dissolution rate from MgZn_2 and Zn-Al-Mg alloy coating in the cathodic polarization domain to the formation of Mg depleted Zn enriched layer, Zn(0), as described in the **Chapter IV**.

7) For ZnAlMg alloy coating in Ar deaerated electrolyte, the onset of Zn and Mg dissolution was occurred at precisely the same potential, $E_c = -1.11$ V. In the cathodic potential branch in O_2 saturated electrolyte, no Mg dissolution was detected for ZnAlMg alloy coating.

8) The apparent inhibitive (or restraining) effect of Zn dissolution on Al dissolution was observed for all specimen investigated in this work. This effect was enhanced in O_2 saturated electrolyte, even in the cathodic potential domain. It was attributed to the oxidation and dissolution of the Zn(0) enriched layer, discussed in the **Chapter VI**.

9) In **Table 8.1**, the Tafel slopes for Zn dissolution are presented, of about 55 mV decade⁻¹, nearly identical for all specimen containing η -phase of Zn (Zn-0.7Al, ZnAlMg, Zn-5Al and Zn-55Al).

10) In **Table 8.1**, E_c^{Zn} of Zn metal, Zn-Al and Zn-Al-Mg system showed similar values around -1.13 V (Ar) and -0.93 V (O_2). It demonstrates that the Zn(0) enriched layer, formed by Al selective dissolution during the cathodic potential polarization, has an onset potential, regardless of Al composition and microstructure. For MgZn_2 , the Zn dissolution rate rose at a more positive potential than others, both with Ar deaeration and O_2 saturation. This can be attributed to the Zn(0) enriched layer formed by Mg selective dissolution which delayed Zn dissolution.

Table 8.1. Potential values of each specimen used in this work at pH=10.1, 30 mM NaCl in Ar deaerated and O_2 saturated electrolyte at T=25 °C. Note that the Tafel slopes are measured at the E_c^{Zn} and are valid only over a very narrow potential range.

E/V _{sce}	Zn metal		Al metal		Mg metal		Zn-0.7Al		Zn-22Al		Zn-68Al	
	Ar	O ₂	Ar	O ₂	Ar	O ₂	Ar	O ₂	Ar	O ₂	Ar	O ₂
E_{oc}/V	-0.98	-0.95	-1.44	-1.29	-1.65	-1.63	-0.96	-0.93	-1.30	-1.01	-1.31	-1.11
$E_{j=0}/V$	-1.21	-0.96	-1.41	-1.25	-1.64	-1.62	-1.27	-0.90	-1.29	-0.96	-1.28	-0.91
E_c^{Zn}/V	-1.10	-0.96	-	-	-	-	-1.12	-0.91	-1.13	-1.06	-1.14	-0.94
Tafel j_{Zn} /mV decade ⁻¹	71	45	-	-	-	-	54	14	39	105	27	49
E_c/V											-0.88	-0.88

VIII. Electrochemical database of Zn-Al-Mg

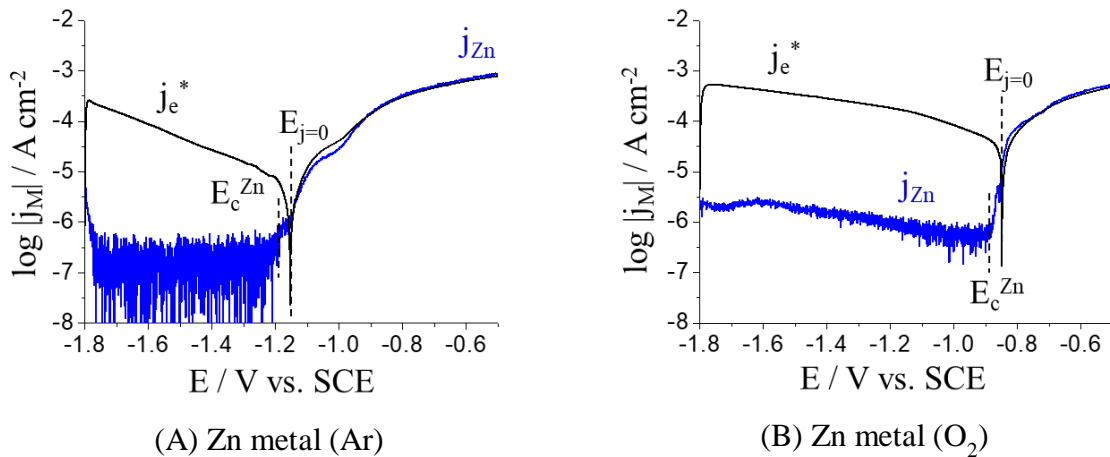
E/V _{sce}	MgZn ₂		Zn-5Al		Zn-55Al		ZnAlMg	
	Ar	O ₂	Ar	O ₂	Ar	O ₂	Ar	O ₂
E _{oc} /V	-1.06	-0.98	-1.12	-0.93	-1.22	-1.10	-1.07	-0.95
E _{j=0} /V	-1.21	-0.96	-1.31	-0.91	-1.30	-0.90	-1.31	-0.89
E _c ^{Zn} /V	-0.96	-0.88	-1.12	-0.93	-1.10	-0.91	-1.14	-0.90
Tafel j _{Zn} /mV decade ⁻¹	20	20	59	7	54	31	55	12
E _c /V	-0.96	-0.88						

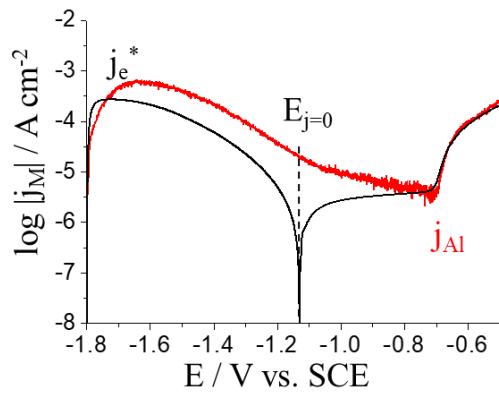
Table 8.2. The average elemental dissolution rate of each specimen at pH=10.1, 30 mM NaCl in Ar deaerated and O₂ saturated electrolytes at T=25 °C.

	j _{Zn} ^s / μA cm ⁻²		j _{Al} ^s / μA cm ⁻²		j _{Mg} ^s / μA cm ⁻²	
	Ar	O ₂	Ar	O ₂	Ar	O ₂
Zn metal	0.7±0.6	17±1	-	-	-	-
Al metal	-	-	20.7±0.2	19.9±0.2	-	-
Mg metal	-	-	-	-	93±1	82±1
Zn-0.7Al	1.3±0.6	11.1±1.5	0	0.3±0.2	-	-
Zn-22Al	0.35±0.2	0.29±0.15	12.6±2.9	20.0±0.7	-	-
Zn-68Al	0	0	36.9±0.8	27.5±0.7	-	-
MgZn ₂	0.1±0.2	0±0.2	-	-	2.2±0.1	1.70±0.04
Zn-5Al	1.0±0.5	2.2±0.5	3.8±0.3	1.5±0.4	-	-
Zn-55Al	0.3±0.4	0.9±0.4	2.0±0.3	4.2±0.3	-	-
ZnAlMg	0.3±0.4	6.0±1.3	1.9±0.2	5.9±0.6	0.29±0.07	0.84±0.06

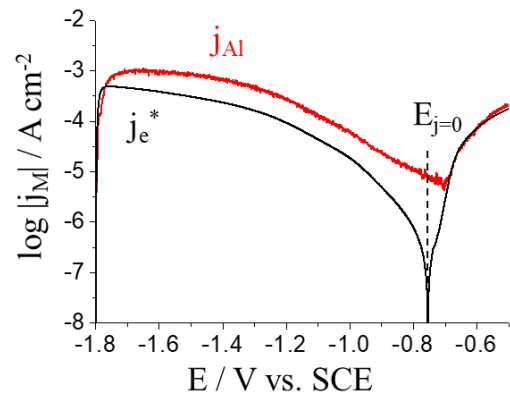
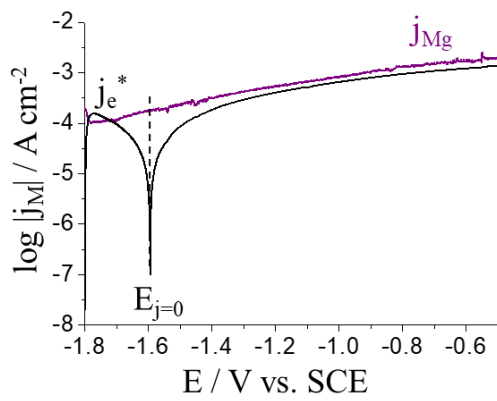
8.3.2. AESEC-LSV at pH=8.4

The database of polarization curves at pH=8.4, 30 mM NaCl Ar deaerated electrolyte are present in **Fig. 8.3**. **Table 8.3** summarizes the potential information measured from the polarization experiment. **Table 8.4** provides j_M^s values of each specimen in the open circuit condition.

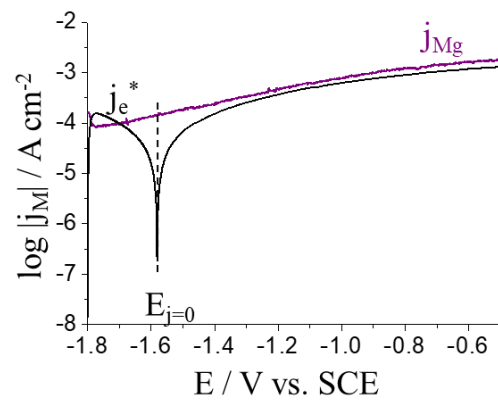
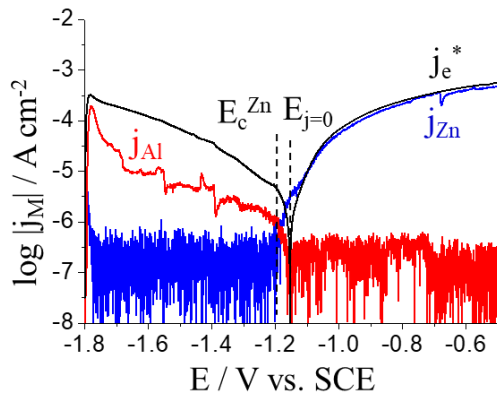




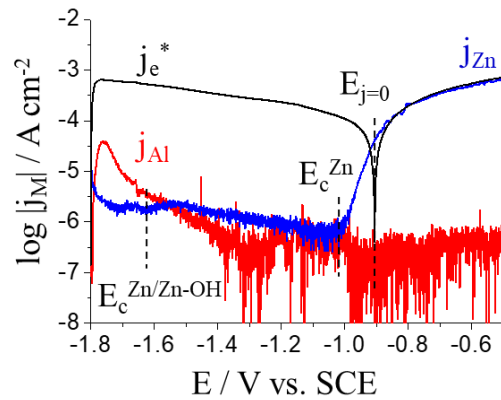
(C) Al metal (Ar)

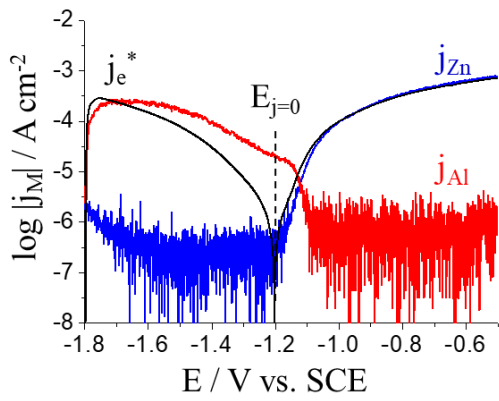
(D) Al metal (O₂)

(E) Mg metal (Ar)

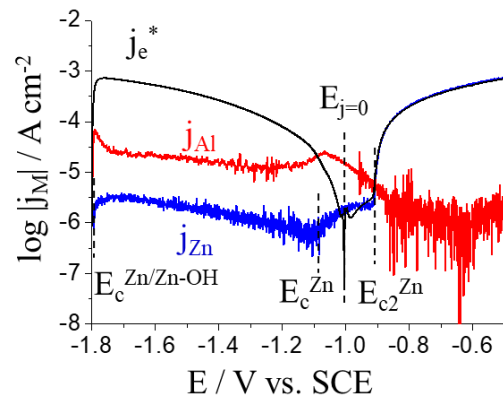
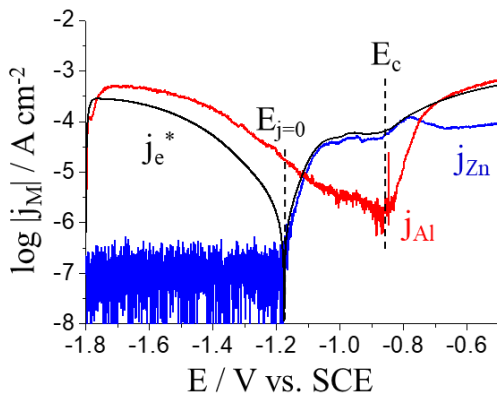
(F) Mg Metal (O₂)

(G) Zn-0.7Al (Ar)

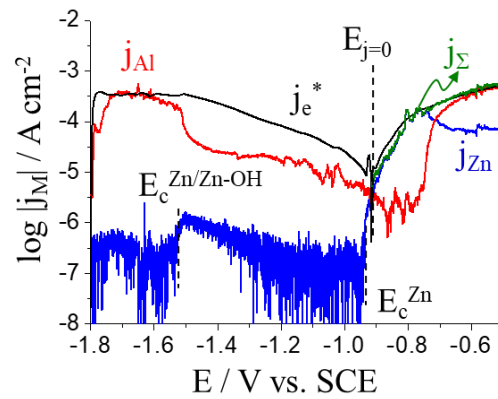
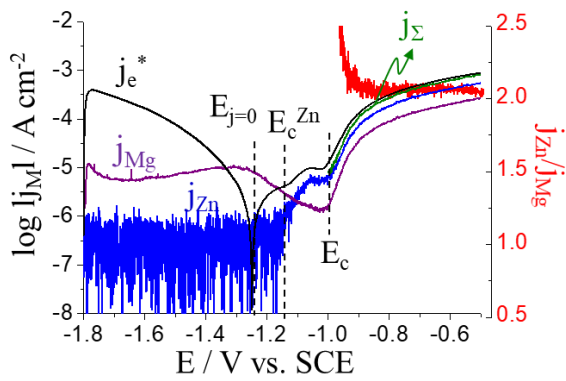
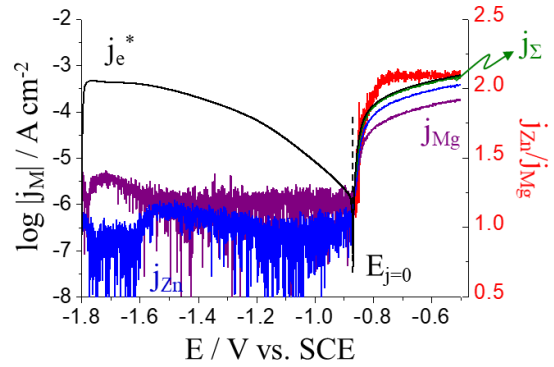
(H) Zn-0.7Al (O₂)

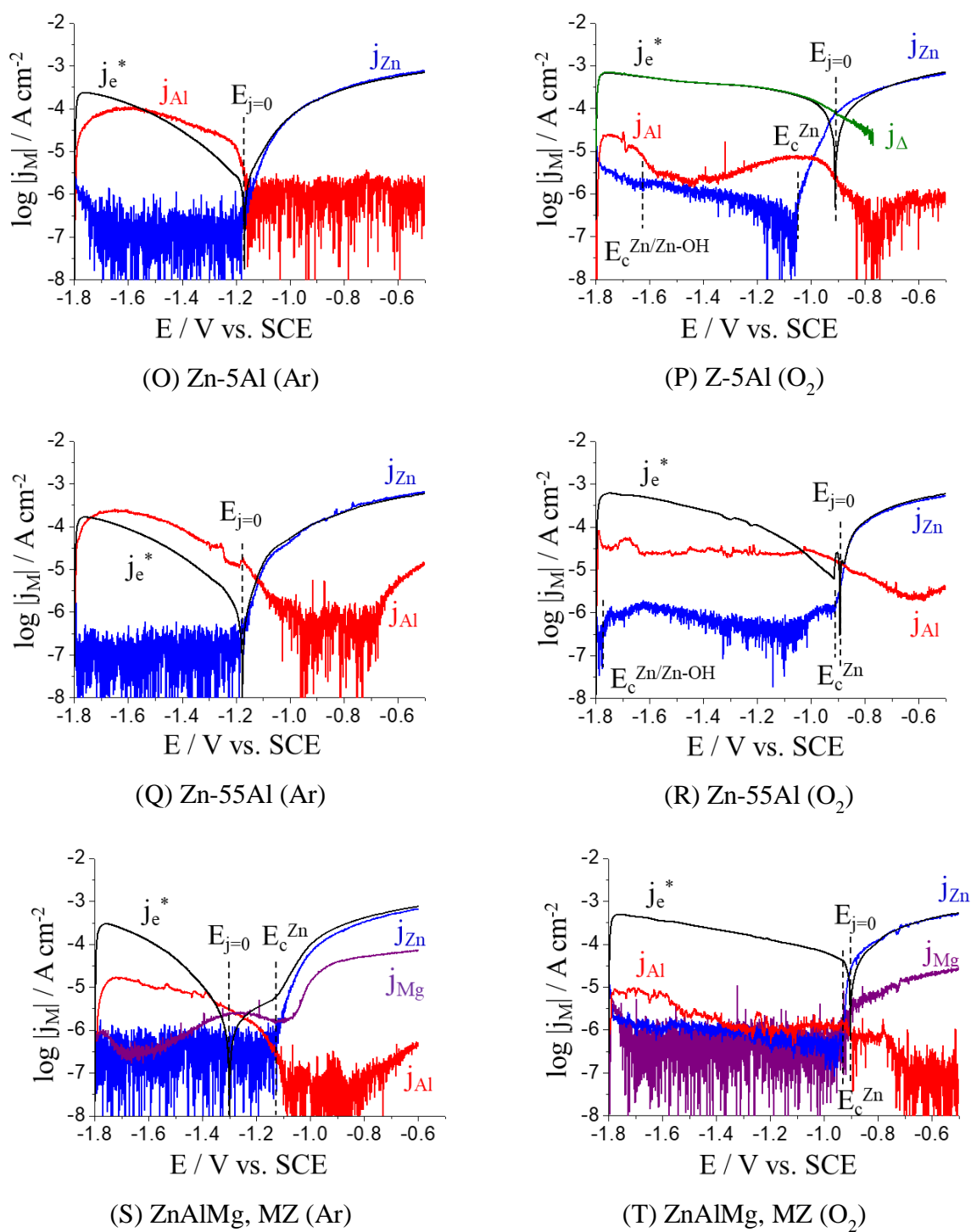


(I) Zn-22Al (Ar)

(J) Zn-22Al (O₂)

(K) Zn-68Al (Ar)

(L) Zn-68Al (O₂)(M) MgZn₂ (Ar)(N) MgZn₂ (O₂)



VIII. Electrochemical database of Zn-Al-Mg

Table 8.3. Potential values obtained from the polarization curves at pH=8.4, 30 mM NaCl Ar deaerated electrolyte at T=25 °C. Note that the Tafel slopes are measured at the E_c^{Zn} and are valid only over a very narrow potential range.

E/V _{sce}	Zn metal		Al metal		Mg metal		Zn-0.7Al		Zn-22Al	
	Ar	O ₂	Ar	O ₂	Ar	O ₂	Ar	O ₂	Ar	O ₂
E_{oc}/V	-1.00	-0.93	-1.20	-0.71	-1.61	-1.60	-1.11	-0.94	-1.10	-1.05
$E_{j=0}/V$	-1.15	-0.85	-1.13	-0.75	-1.59	-1.58	-1.16	-0.90	-1.20	-1.00
E_c^{Zn}/V	-1.21	-0.90	-	-	-	-	-1.20	-1.01	-1.12	-1.08
Tafel j_{Zn} mV decade ⁻¹	75	28	-	-	-	-	64/95	51	48	13
E_c/V										

E/V _{sce}	Zn-68Al		MgZn ₂		Zn-5Al		Zn-55Al		ZnAlMg	
	Ar	O ₂	Ar	O ₂	Ar	O ₂	Ar	O ₂	Ar	O ₂
E_{oc}/V	-1.10	-0.99	-1.09	-0.99	-0.99	-0.93	-1.12	-0.98	-1.13	-0.95
$E_{j=0}/V$	-1.17	-0.91	-1.25	-0.87	-1.17	-0.91	-1.17	-0.89	-1.30	-0.90
E_c^{Zn}/V	1.17	-0.94	-1.15	-0.87	-1.18	-1.05	-1.17	-0.91	-1.13	-0.93
Tafel j_{Zn} mV decade ⁻¹	47	82	104/79	21	57	55	52	35	55	11
E_c/V	-0.87		-1.00	-0.87						

Table 8.4. The average elemental dissolution rate of each specimen at pH=8.4, 30 mM NaCl in Ar deaerated electrolyte at T=25 °C.

	$j_{Zn}^s/\mu A cm^{-2}$		$j_{Al}^s/\mu A cm^{-2}$		$j_{Mg}^s/\mu A cm^{-2}$	
	Ar	O ₂	Ar	O ₂	Ar	O ₂
Zn metal	3.8±0.5	2.1±0.2	-	-	-	-
Al metal	-	-	2.3±0.1	5.0±0.8	-	-
Mg metal	-	-	-	-	194±6	165±5
Zn-0.7Al	5.4±0.3	8.2±1.0	0	0	-	-
Zn-22Al	2.3±0.3	1.5±0.3	3.2±0.8	7.5±0.7	-	-
Zn-68Al	0.1±0.1	0	4.7±0.6	2.9±0.3	-	-
MgZn ₂	0.6±0.4	0.3±0.2	-	-	1.7±0.1	4.3±0.6
Zn-5Al	2.5±0.3	10±1	0	0	-	-
Zn-55Al	0.5±0.2	0.6±0.2	2.7±0.5	1.1±0.2	-	-
ZnAlMg	0.5±0.4	12±1	0.5±0.1	3.0±0.3	0.7±0.1	1.7±0.7

COMMENTS:

1) Zn metal: The overall dissolution profiles in Ar deaerated and O₂ saturated electrolytes showed similar features to those obtained in pH=10.1 electrolyte. However, at pH=8.4, $E_c^{Zn} < E_{j=0}$ whereas $E_c^{Zn} > E_{j=0}$ at pH=10.1 indicating that oxide/hydroxide formation was more intense in the latter case consistent with the solubility calculations presented earlier.

In O₂ saturated electrolyte, Zn dissolution in the cathodic potential was observed as was the case for the pH=10.1 electrolyte.

2) Al metal: Al dissolution showed a similar result to that obtained at pH=10.1. The cathodic current increased in O₂ saturated electrolyte, however the dissolution stoichiometry was relatively constant, $v_e^*/v_{Al} = 1.09 \pm 0.07$ (Ar) and 0.7 ± 0.04 (O₂), and similar to that obtained at pH=10.1. This demonstrates the prevalence of the cathodic Al dissolution mechanism.

3) Mg metal: Mg dissolution was not affected by the presence of O₂ at pH=8.4. Interestingly, $j_{Mg} > j_e^*$ throughout potential sweep which may indicate an apparent ‘negative difference effect’ [77,87–90,178,179] where the cathodic rate increases with increasing anodic potential.

4) Zn-0.7Al: The Al dissolution in the cathodic potential domain was reduced by an order of magnitude in the presence of O₂, as previously observed at pH=10.1. This can be attributed to Zn(0) and ZnO complex formation in O₂ saturated electrolyte, the dissolution of which shows an inhibiting effect on Al dissolution in the cathodic potential domain. No $j_e^* - j_{Zn}$ peak was found.

5) Zn-68Al: The results were nearly identical to those obtained at pH=10.1 in form and the critical potential, $E_c = -0.87$ V.

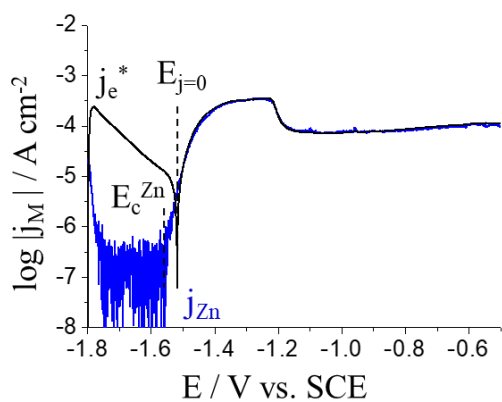
6) Zn-Al and Zn-Al-Mg alloy coating showed no significant difference as compared to those at pH=10.1. One thing needs to be remarked is, in Ar deaeration, Mg dissolution was observed showing two maximum peaks at -1.75 V and -1.35 V for Mg containing system. However, with O₂ saturation, Mg dissolution showed a peak only at -1.75 V then was nearly under the detection limit throughout cathodic potential sweep.

8.3.3. AESEC-LSV at pH=12.80

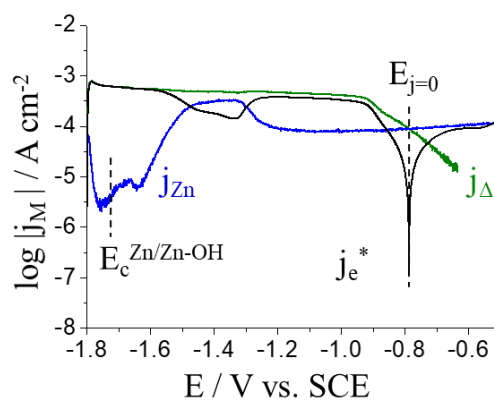
The polarization curves in highly alkaline solution at pH=12.80 for each specimen are shown in **Fig. 8.4**. This pH value may represent the upper end of the pH range that galvanized steel would be exposed to during atmospheric corrosion. Galvanized steel is also exposed to such alkaline conditions during surface degreasing and when used to reinforce cement. The electrode herein was referenced to Hg/HgO in 0.1 M NaOH, however the potential values were converted into V vs. SCE ($\Delta E = -0.076$ V with respect to Hg/HgO in 0.1 M NaOH) to facilitate

VIII. Electrochemical database of Zn-Al-Mg

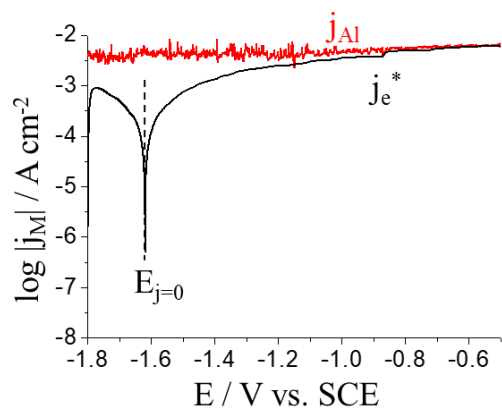
comparison with other results performed with SCE electrode. All potential values are given in **Table 8.5** and j_M^s values are provided in **Table 8.6**.



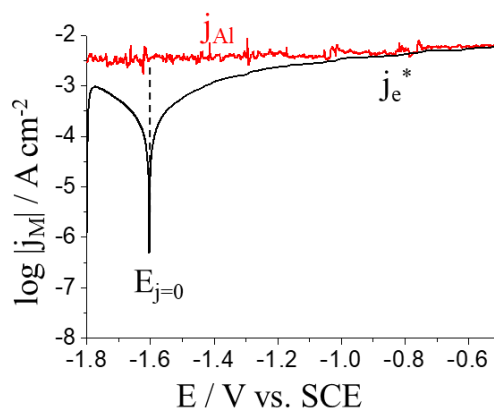
(A) Zn metal (Ar)



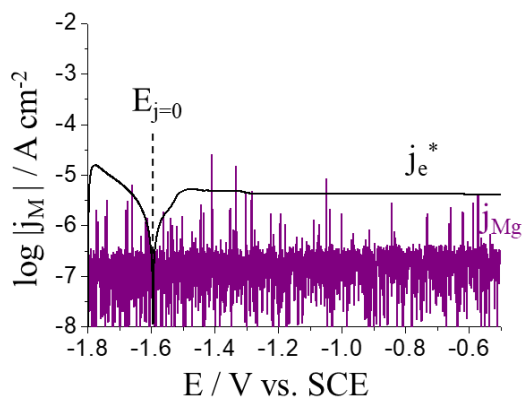
(B) Zn metal (O₂)



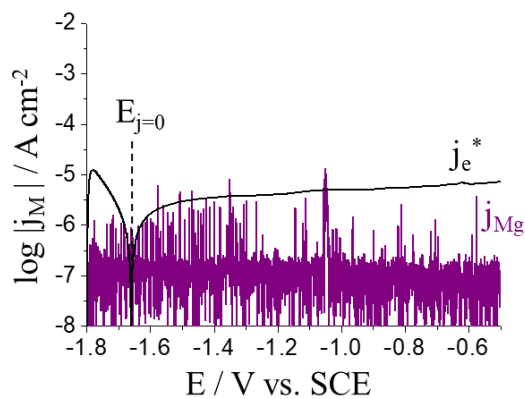
(C) Al metal (Ar)



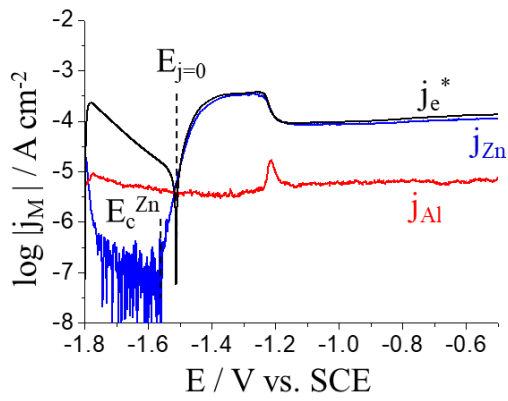
(D) Al metal (O₂)



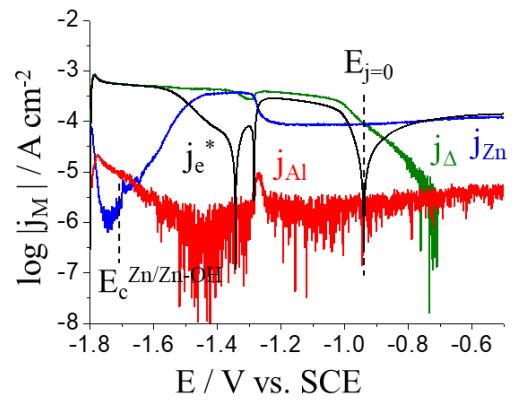
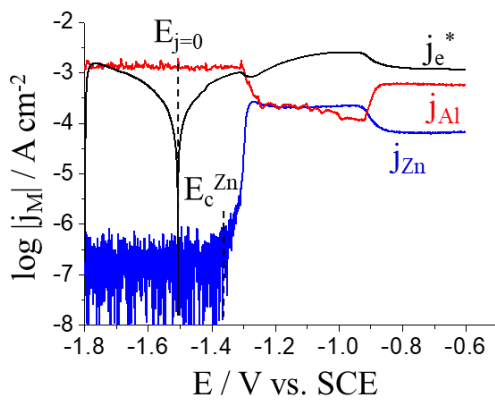
(E) Mg metal (Ar)



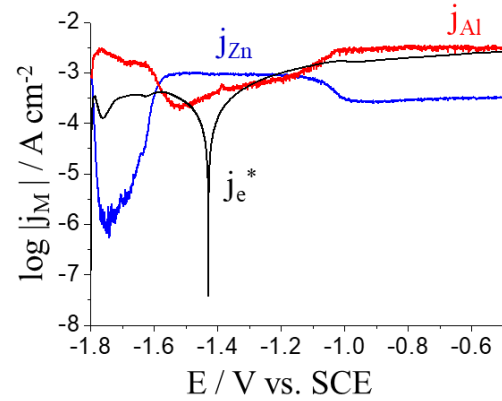
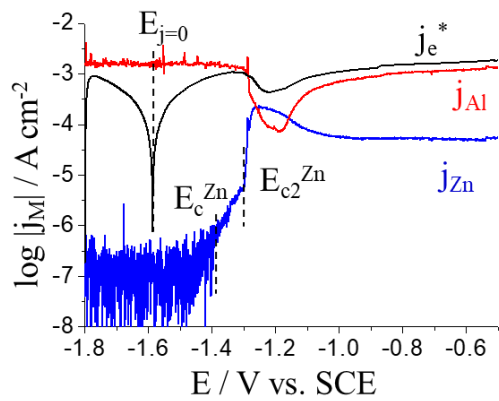
(F) Mg metal (O₂)



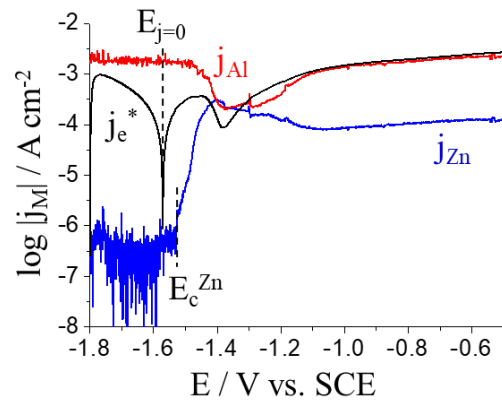
(G) Zn-0.7Al (Ar)

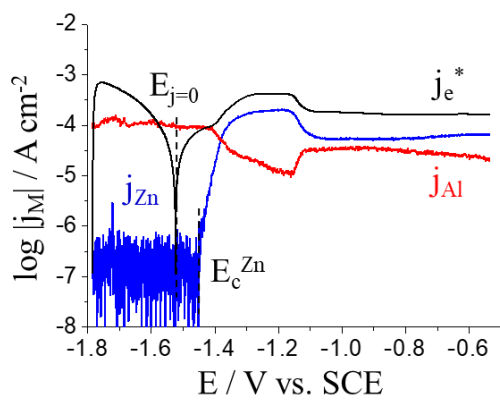
(H) Zn-0.7Al (O₂)

(I) Zn-22Al (Ar)

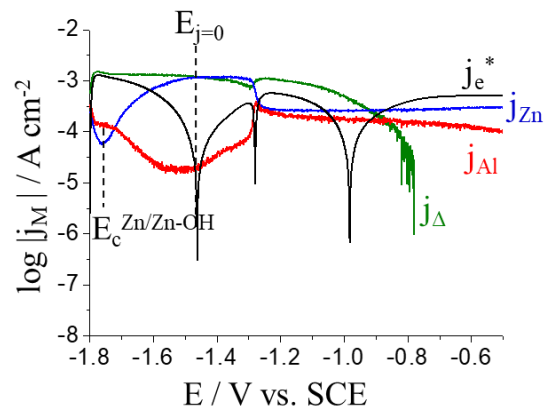
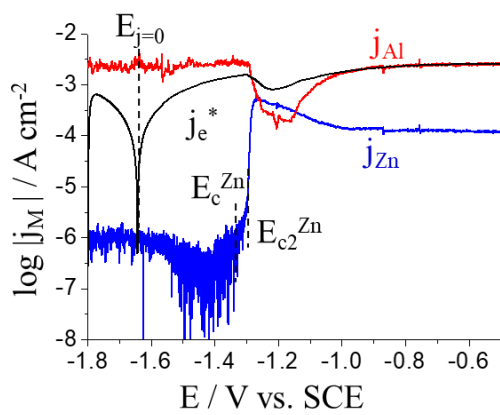
(J) Zn-22Al (O₂)

(K) Zn-68Al (Ar)

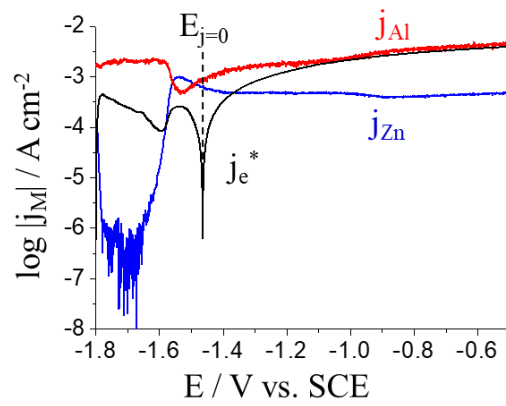
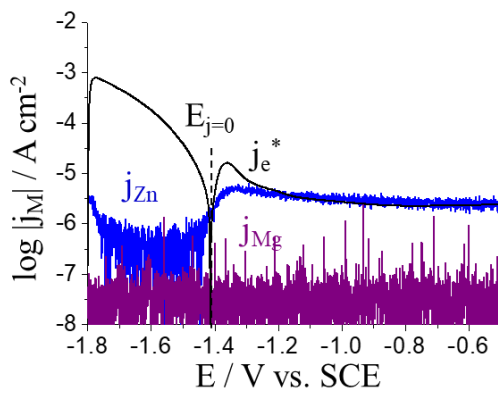
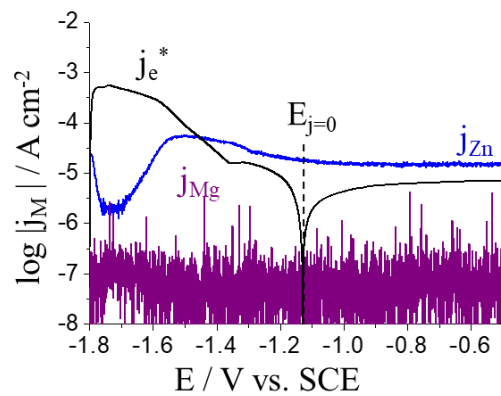
(L) Zn-68Al (O₂)

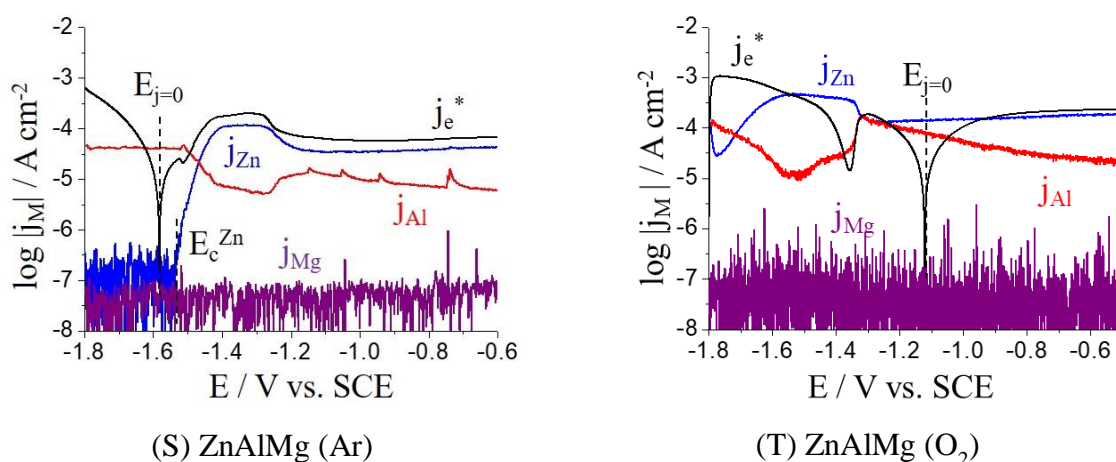


(M) Zn-5Al (Ar)

(N) Zn-5Al (O₂)

(O) Zn-55Al (Ar)

(P) Zn-55Al (O₂)(Q) MgZn₂ (Ar)(R) MgZn₂ (O₂)



(S) ZnAlMg (Ar) (T) ZnAlMg (O₂)
Fig. 8.4. AESEC-LSV curves at pH=12.80, 0.1 M NaOH at T=25 °C.

Table 8.5. Potential values obtained from the polarization curves at pH=12.80, 0.1 M NaOH. Note that the Tafel slopes are measured at the E_c^{Zn} and are valid only over a very narrow potential range.

E/V _{sce}	Zn metal		Al metal		Mg metal		Zn-0.7Al		Zn-22Al	
	Ar	O ₂	Ar	O ₂	Ar	O ₂	Ar	O ₂	Ar	O ₂
E _{oc} /V	-1.51	-0.92	-1.62	-1.61	-1.65	-1.68	-1.51	-1.01	-1.53	-1.49
E _{j=0} /V	-1.52	-0.79	-1.62	-1.61	-1.59	-1.66	-1.51	-0.94	-1.51	-1.43
E _c ^{Zn} /V	-1.45	-1.73	-	-	-	-	-1.56	-1.71	-1.36	-1.72
E _{c2} ^{Zn} /V	-	-	-	-	-	-	-	-	-1.31	-1.63
Tafel j _{Zn} mV decade ⁻¹	36	76	-	-	-	-	33	109	47/9	45/25
E/V _{sce}	Zn-68Al		MgZn ₂		Zn-5Al		Zn-55Al		ZnAlMg	
	Ar	O ₂	Ar	O ₂	Ar	O ₂	Ar	O ₂	Ar	O ₂
E _{oc} /V	-1.60	1.59	-1.41	-1.24	-1.58	-1.15	-1.66	-1.56	-1.59	-1.22
E _{j=0} /V	-1.59	-1.57	-1.41	-1.13	-1.52	-0.98	-1.64	-1.47	-1.58	-1.12
E _c ^{Zn} /V	-1.39	-1.53	-1.45	-1.70	-1.45	-1.76	-1.33	-1.65	-	-1.77
E _{c2} ^{Zn} /V	-1.30	-1.49	-	-	-	-	-1.30	-1.60	-1.53	-
Tafel j _{Zn} mV decade ⁻¹	102/10	24	96	104	31	92	30/6	44	34	111

Table 8.6. The average elemental dissolution rate of each specimen at pH=12.80, 0.1 M NaOH in Ar deaerated and O₂ saturated electrolytes at T=25 °C.

	$j_{Zn}^s / \mu A cm^{-2}$		$j_{Al}^s / mA cm^{-2}$		$j_{Mg}^s / \mu A cm^{-2}$	
	Ar	O ₂	Ar	O ₂	Ar	O ₂
Zn metal	22±1	64±2	-	-	-	-
Al metal	-	-	4.0±0.9	3.7±0.5	-	-
Mg metal	-	-	-	-	0.1±0.2	0.054±0.42
Zn-0.7Al	20±1	77±2	0.007±0.001	0.006±0.001	-	-
Zn-22Al	0	721±22	1.4±0.1	0.77±0.06	-	-
Zn-68Al	0.1±0.2	0.4±0.2	1.6±0.2	1.8±0.1	-	-
MgZn ₂	3.2±0.4	25±1	-	-	0.05±0.1	0.1±0.2
Z-5Al	0	232±5	0.086±0.006	0.33±0.02	-	-
Zn-55Al	0.2±0.4	1±1	2.0±0.3	2.0±0.1	-	-
ZnAlMg	0.01±0.3	121±3	0.048±0.003	0.15±0.02	0	0.06±0.1

COMMENTS:

1) Zn dissolution in both Ar purge and O₂ saturation showed identical j_{Zn} vs. E profiles. However, considerably increased cathodic current was measured with O₂ saturation in a wide range of potential for pure Zn, Zn-0.7Al, Zn-22Al, Zn-5Al, MgZn₂ and ZnAlMg. This indicates that O₂ is the major oxidizing agent for Zn dissolution. The Al dissolution rate for pure Al was not measurably affected by saturation O₂, although it should be noted that the dissolution rate by HER is so large that diffusion limited O₂ reduction could hardly be measured. Elemental dissolution of pure Zn and Al at pH=12.80 is described in **Chapter VI** and its temperature dependent reactivity is discussed in **Chapter VII**.

2) The η -phase of Zn (Zn-0.7Al) showed a similar polarization behavior as Zn metal. Al dissolution in the cathodic potential domain was clearly reduced in the presence of O₂, and this correlated with the Zn dissolution rate increase in this potential range. Curiously, a j_{Al} peak was observed in both electrolytes when Zn dissolution entered the passivation domain near -1.1 V.

3) Al dissolution was evidently restrained for $E > E_c^{Zn}$ for Zn-68Al. The dissolution of Zn-68Al and the apparent inhibitive effect of Zn dissolution on Al dissolution are presented in **Chapter VI**.

5) ZnAlMg alloy showed nearly the same elemental dissolution profile as Zn-5Al alloy.

6) Mg dissolution was not observed for either the MgZn₂ intermetallic or ZnAlMg alloy due to the low solubility of Mg²⁺ at this pH.

8.4. Data analysis with sample composition

8.4.1. Spontaneous dissolution analysis as a function of pH

The steady state rates of elemental dissolution rates (j_M^s) for the pure metals and the Zn-Al-Mg alloy coating at each pH values are shown in **Figs. 8.5** and **8.6**, respectively. The dominant element in solution varies from one case to another in good qualitative agreement with the equilibrium solubility predicted in **Fig. 8.1**. For pure metals (**Fig. 8.5**), O_2 had no significant effect on Al and Mg dissolution, however, at pH=10.1 and 12.80, j_{Zn} increased considerably in O_2 saturated electrolyte.

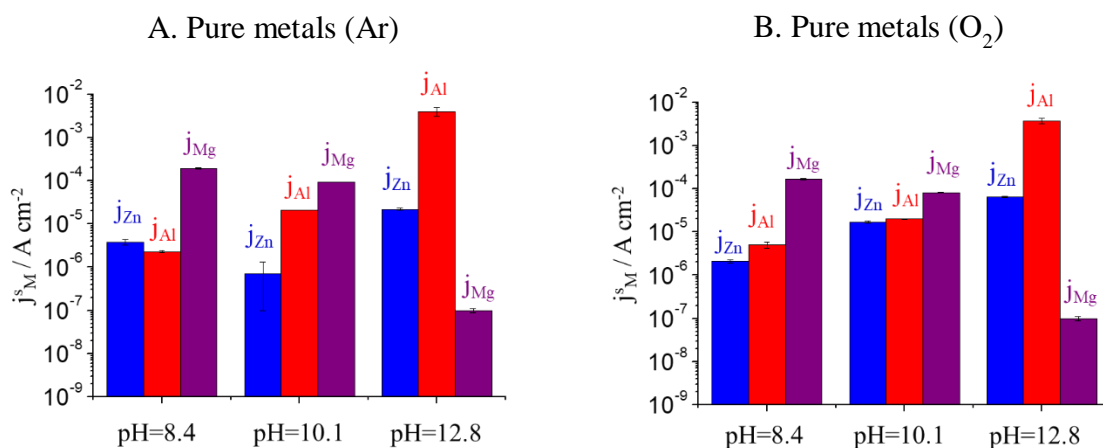


Fig. 8.5. j_M^s for pure metals at each pH in **A**: Ar deaerated and **B**: O_2 saturated electrolytes.

The overall trend of j_M^s for Zn-Al-Mg alloy (**Fig. 8.6**) was in good accordance with that of pure metals (**Fig. 8.5**), with some exceptions. Note that j_M^s for the Zn-1.6Al-1.6Mg alloy presented in **Fig. 8.6** was normalized based on its composition. At pH=8.4, Mg selectively dissolved to Zn for the alloy, similar to more pronounced j_{Mg}^s than other metals as shown in **Fig. 8.5**. j_{Al} for alloy both in Ar deaerated and O_2 saturated electrolytes was increased an order of magnitude as compared to those for Al metals at pH=8.4. At pH=10.1, $j_{Mg}^s > j_{Al}^s > j_{Zn}^s$ for the pure metals (**Fig. 8.5**) whereas Al dissolution was more pronounced than Mg for the alloys (**Fig. 8.6**). It can be understood as Mg dissolution was restrained due to the Zn(0) enriched layer for the alloys, as described in **Chapter IV**. j_{Al} for the alloys was not reduced, as this Zn(0) layer showed no inhibitive effect on Al dissolution at these pH level, demonstrated in **Chapter V**. At pH=12.80, Zn dissolution was significantly reduced for the alloy in Ar deaeration (**Fig. 8.6A**) as compared to that for pure metal (**Fig. 8.5A**) because of the selective Al dissolution.

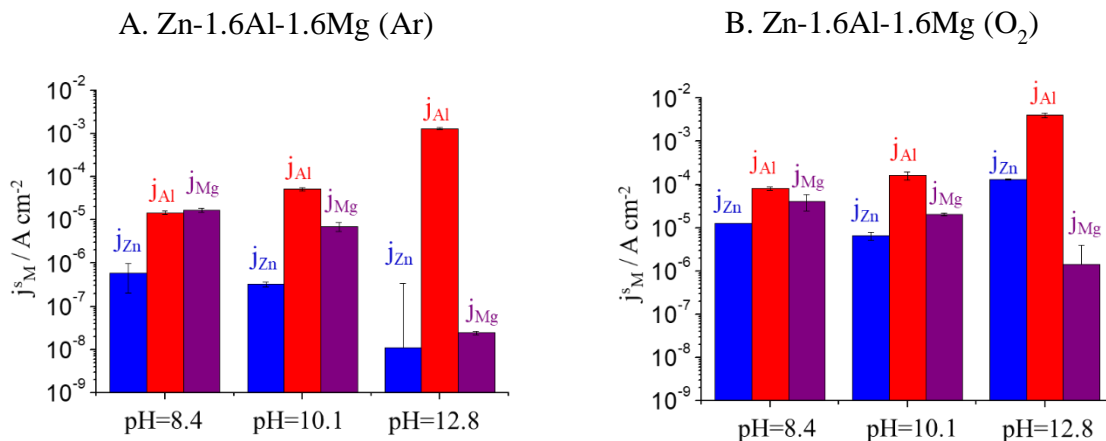


Fig. 8.6. j_M^s for the Zn-Al-Mg alloy coating at each pH in **A**: Ar deaerated and **B**: O₂ saturated electrolytes. j_M^s values were normalized based on its composition.

The E_{oc} values of each sample are shown in **Fig. 8.7** with increasing % Zn. At pH=8.4, with the exception of Zn-5Al, the addition of even a small quantity of Al to the alloy (Zn-0.7Al and Zn-Al-Mg) led to a significant decrease in E_{oc} close to the level of pure Al. All Al containing species showed analogous $E_{oc} \approx -1.1$ V at pH=8.4. The observation of E_{oc} (Zn-5Al) $\approx E_{oc}$ (Zn metal) may be attributed to the selective Zn dissolution from Zn-rich dendrite phase of Zn-5Al.

At pH=10.1, however, the E_{oc} distinctively shifted to more negative potential values with increasing % Al with exception of Zn-22Al. The E_{oc} of Zn-68Al at pH=10.1 was more negative than that of MgZn₂ and Zn-0.7Al indicating that the Zn-68Al phase, a component of the Zn-Al-Mg alloy, may selectively dissolve when in contact with the other phases in the moderately alkaline solution. It also reflects the fact that Al dissolution is more pronounced than other elements in the alloy coating (**Fig. 8.6**) at pH=10.1. E_{oc} of Zn-22Al at pH=10.1 was nearly the same level as that of Zn-68Al, which can be explained by the selective dissolution of the Al-rich phase present in Zn-22Al. The more positive E_{oc} for MgZn₂ was due to Mg(OH)₂ formation.

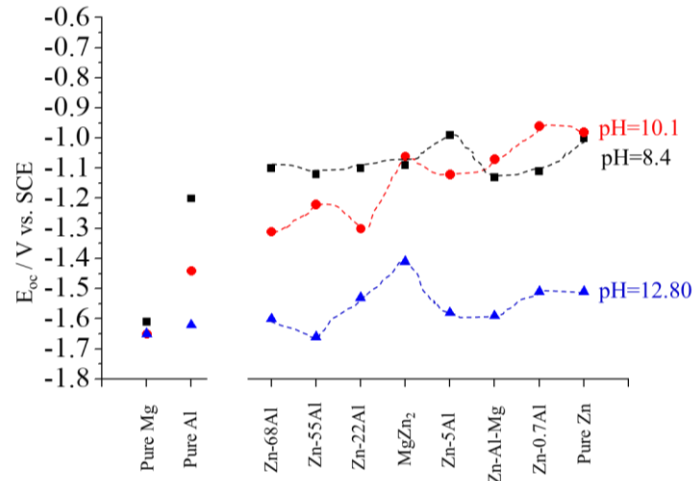


Fig. 8.7. E_{oc} for all specimen with increasing % Zn in Ar deaerated electrolyte.

Saturation with O_2 led to more positive E_{oc} of Zn-rich species, such as pure Zn, Zn-0.7Al, MgZn₂ and Zn-5Al as shown in **Fig. 8.8**. The E_{oc} became more positive with increasing % Zn at pH=10.1 and pH=12.80. At pH=8.4, this trend is less clear than other pH values, however, the E_{oc} was the reasonably the same as at pH=10.1 for % Zn t MgZn₂. Further, the E_{oc} of pure Al at pH=8.4 was +300 mV more positive than for any other specimen indicative of passivation.

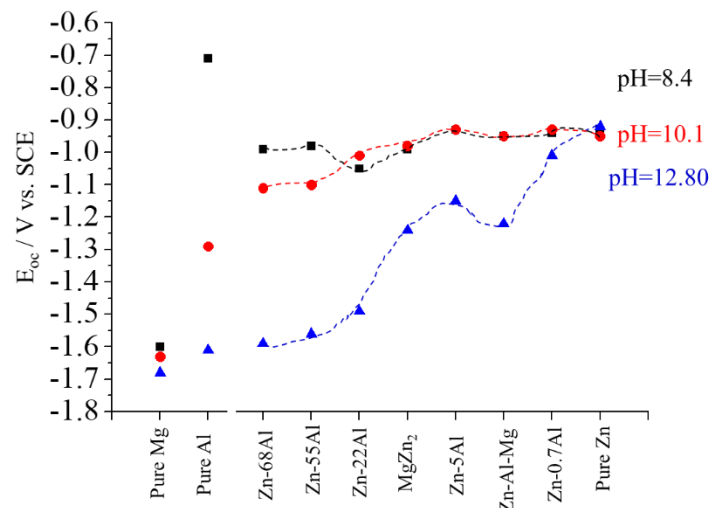


Fig. 8.8. E_{oc} for all specimen with increasing % Zn in O_2 saturated electrolyte.

In **Fig. 8.9~8.11**, j_M^s of Zn, Al and Mg for all specimen investigated in three pH solutions are given. In general, j_{Zn}^s was not proportional to % Zn (**Fig. 8.9**), probably due to the selective Al/Mg dissolution. j_{Zn}^s significantly increased in O_2 saturated electrolyte for all samples. j_{Al}^s was higher with increasing % Al (**Fig. 8.10**), for pH=10.1 and 12.80. j_{Al}^s increased with pH for all cases. O_2 had no significant effect on j_{Al} .

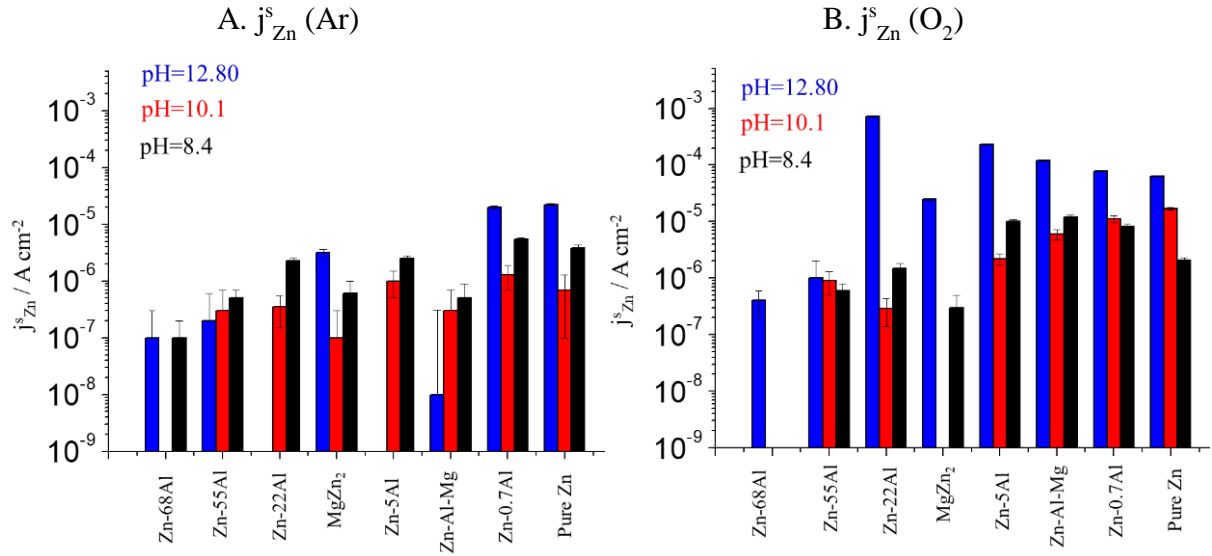


Fig. 8.9. A: j_{Zn}^s (Ar), B: j_{Zn}^s (O_2) of all specimen as a function of % Zn.

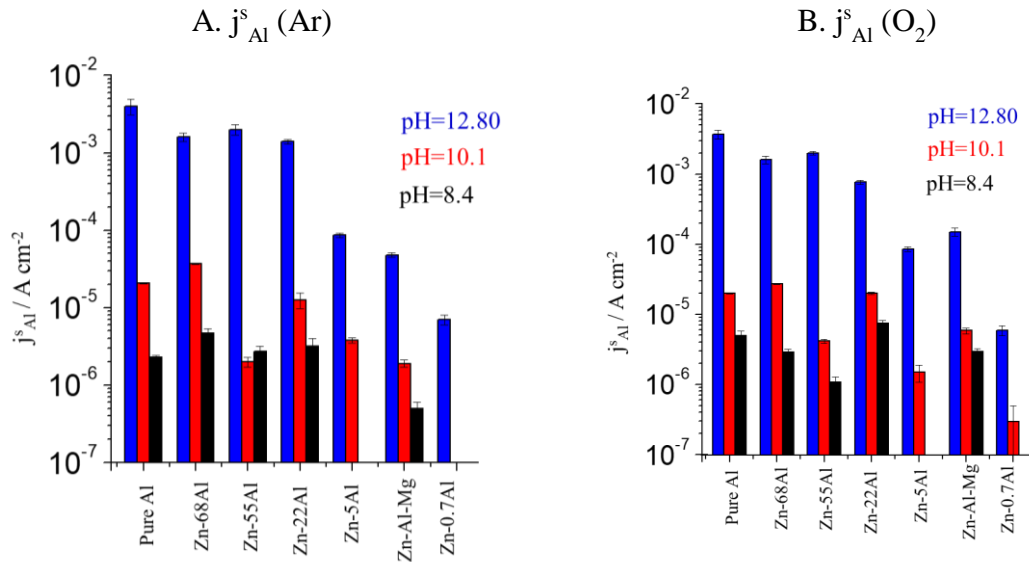


Fig. 8.10. A: j_{Al}^s (Ar), B: j_{Al}^s (O_2) of all specimen as a function of % Zn.

Mg dissolution rate showed a clearly tendency with % Mg for mildly and slightly alkaline pH as shown in **Fig. 8.11**. However, it was nearly unmeasurable at pH=12.80.

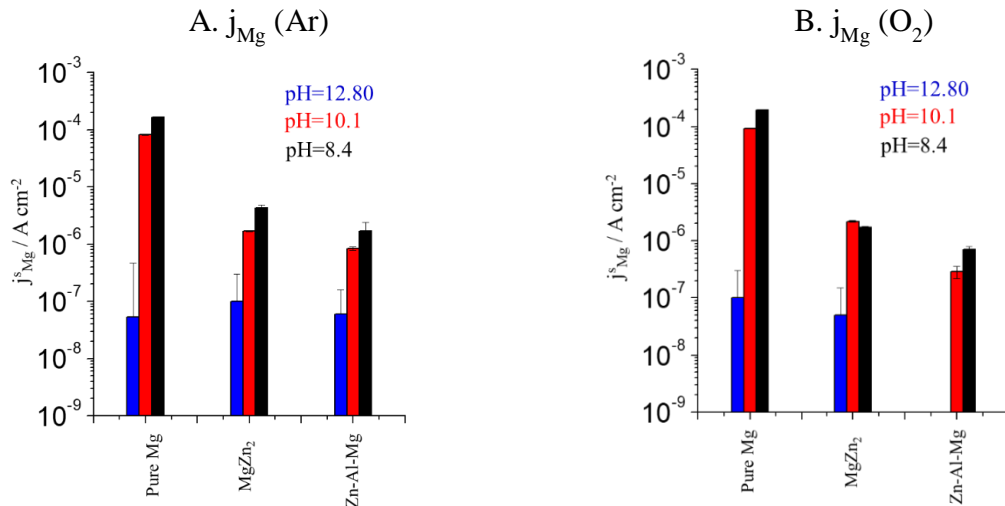


Fig. 8.11. A: j_{Mg}^{s} (Ar), B: j_{Mg}^{s} (O_2) of all specimen as a function of % Zn.

Mg forms a stable $\text{Mg}(\text{OH})_2$ film in alkaline solution which has been suggested to enhance corrosion resistance [25,29,170]. This film would be more fragile in O_2 saturated electrolyte as evidenced by highly perturbed j_{Mg} signal at $\text{pH}=12.80$, shown in **Fig. 8.12**. The nature of the peaks are indicative of the detachment of solid Mg or $\text{Mg}(\text{OH})_2$ which is subsequently carried to the plasma.

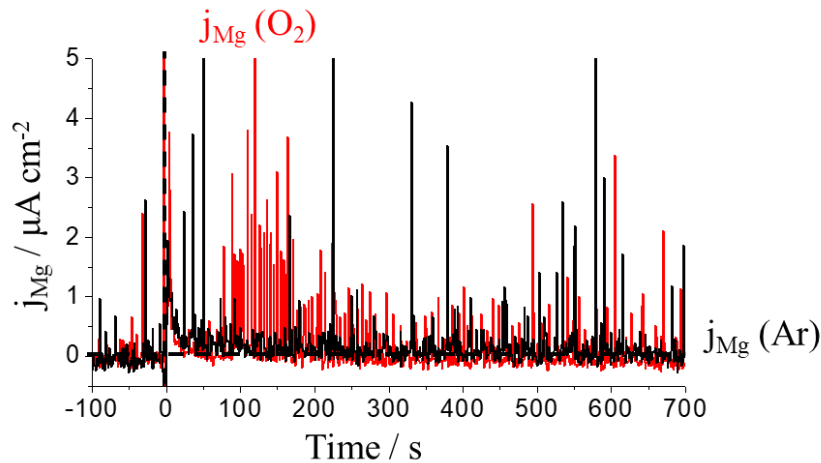


Fig. 8.12. Spontaneous dissolution of Mg metal in Ar deaerated and O_2 saturated electrolyte at $\text{pH}=12.80$.

8.4.2. Kinetic analysis

Fig. 8.13 shows the spontaneous steady state dissolution rates obtained as a function of the values extracted from the elemental polarization curves as previously described. It is clear that there is a reasonably good linear relationship between the two, which is at least a partial confirmation that the mixed potential theory may be applied to this system.

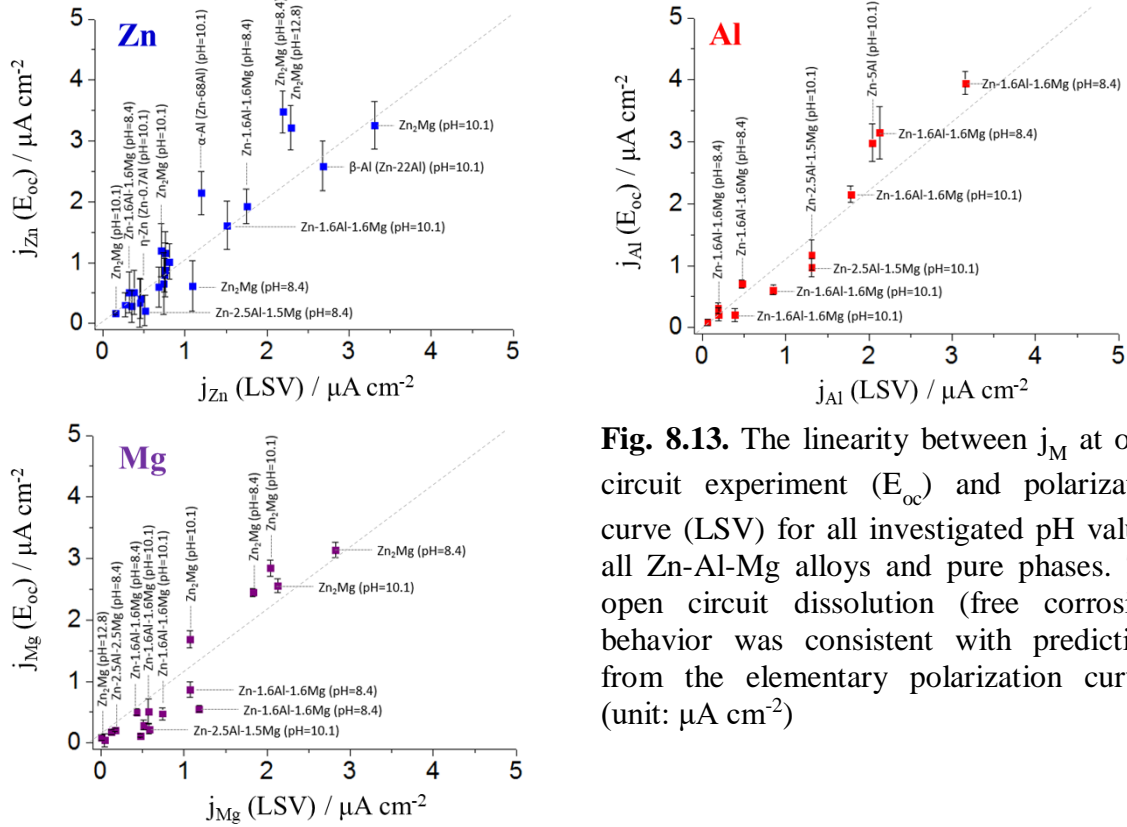


Fig. 8.13. The linearity between j_M at open circuit experiment (E_{oc}) and polarization curve (LSV) for all investigated pH values, all Zn-Al-Mg alloys and pure phases. The open circuit dissolution (free corrosion) behavior was consistent with predictions from the elementary polarization curves. (unit: $\mu A cm^{-2}$)

8.4.3. The effect of pH on Al dissolution mechanism

Fig. 8.14 compares the Zn-68Al AESEC-LSV with those of pure Zn and pure Al. At pH=8.4 for Zn-68Al, Al dissolution was not measurably altered from that of pure Al. Zn dissolution, however, was restrained in the Al transpassive potential domain. It can be concluded that Zn dissolution in this case occurred across an Al passive film which also dissolved. Elemental dissolution trend of the Zn-68Al was altered when pH increases indicating that the interaction between two elements was more significant at higher pH.

Cathodic Al dissolution was nearly the same between pH=8.4 and 10.1, showing potential dependent dissolution. The stoichiometry of cathodic Al dissolution (v_e^*/v_{Al}) for Zn-68Al and pure Al is summarized in **Table 8.7** showing reasonably identical values. However, Cathodic Al dissolution mechanism was totally altered in pH=12.80 as evidenced by nearly potential independent Al dissolution.

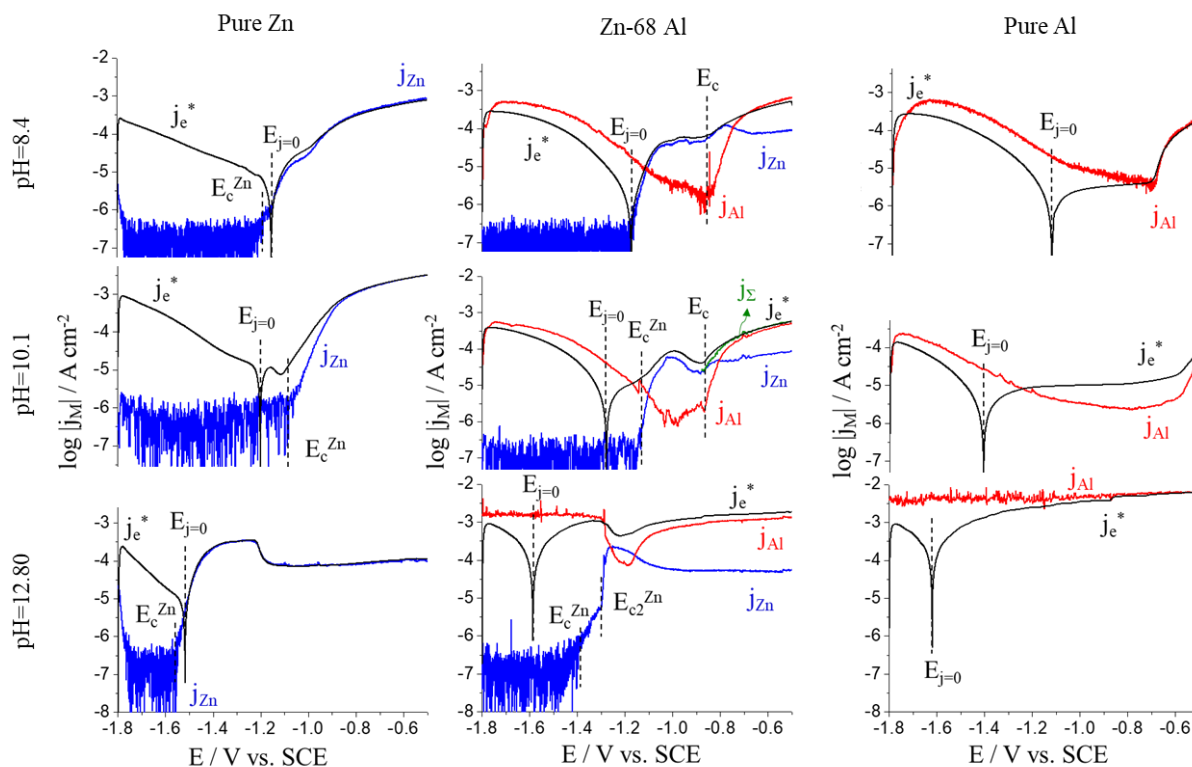


Fig. 8.14. AESEC-LSV of pure Zn, Zn-68Al and pure Al in three different pH solutions.

Table 8.7. Cathodic Al dissolution stoichiometry analysis of Al metal and Zn-68Al.

v_e^*/v_{Al}	Al metal	Zn-68Al
	Ar deaerated electrolyte	
pH=8.4	1.0±0.1	1.0±0.4
pH=10.1	1.2±0.3	1.6±0.4

8.5. Conclusions

1) An electrochemical database has been established in this work at three different pH values, with Ar deaeration and saturation O_2 , with 10 specimens of variably alloy composition of the Zn-Al-Mg system including pure metals and pure phases.

2) Dealloying of the pure phases was analogous at near neutral and slightly alkaline pH values. During the dealloying process, Zn(0) enriched layer was formed by a selective dissolution mechanism of either Al (Al-Zn phase) or Mg ($MgZn_2$). The Zn(0) phase inhibits Mg dissolution in the latter example, but does not hinder Al dissolution in the former.

VIII. Electrochemical database of Zn-Al-Mg

3) Cathodic Al dissolution was observed at near neutral and slightly alkaline pH, even for a very low content sample (Zn-0.7Al). This is an important result for the corrosion in that it can be a reservoir of Al^{3+} may form a surface protective layered double hydroxides (LDHs) for all Zn-Al system.

4) Inhibitive effect of Zn dissolution on Al dissolution was monitored for all specimens at all pH values investigated in this work. This can be an important factor to explain the selective leaching of Zn after the field exposure test of Zn-Al (or Zn-Al-Mg) system.

5) Database of the polarization curves and spontaneous elemental dissolution for pure metal and phases can be used as an input data to predict the corrosion of the multi-phase alloy system.

Chapter IX:

Characterization of the artificially formed corrosion product by Raman spectroscopy

«On se fait toujours des idées exagérées de ce qu'on ne connaît pas.»

L'étranger (1942)

Albert Camus

9. Characterization of the artificially formed corrosion product by Raman spectroscopy

9.1. Introduction.

In the previous chapters, the corrosion and elemental dissolution behavior of the pure phases were measured to separate the effect of individual phase from the complex alloy coatings. In this chapter, the corrosion products formed on the samples were compared with those precipitated in solution (titration) and also with those predicted by thermodynamics. This will allow us to measure possible corrosion products of the Zn-Al-Mg system determined from solution chemistry, distinguished from the reactions on the sample surface. The question, can we use the thermodynamic models directly or do we need to account for precipitation kinetics? In order to answer this question, we have performed titration experiments with solutions containing Zn^{2+} , Mg^{2+} , Al^{3+} , $\text{Zn}^{2+}/\text{Mg}^{2+}$, $\text{Zn}^{2+}/\text{Al}^{3+}$, $\text{Mg}^{2+}/\text{Al}^{3+}$ and $\text{Zn}^{2+}/\text{Mg}^{2+}/\text{Al}^{3+}$ forming precipitation species at different pH. A thermodynamic based software was used to simulate the titration and the precipitations. The artificially formed precipitations were filtered and dried, then characterized by *ex-situ* Raman spectroscopy. The corrosion products formed after the electrochemical measurements from the previous chapters were also compared with those results. A schematic image describing the objective of this work is given in **Fig. 9.1**.

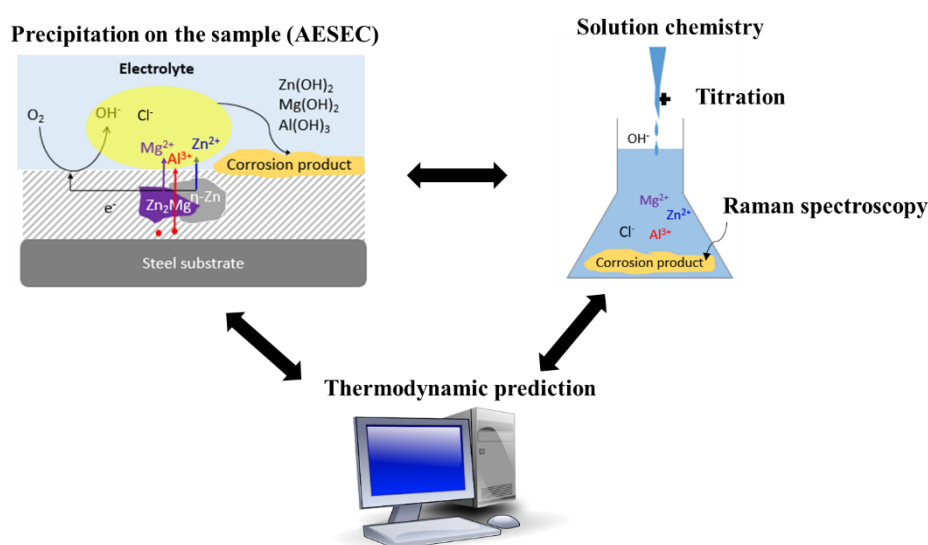


Fig. 9.1. Schematic description of the comparison and correlation between experiments.

9.2. Experimental

Titration experiment

Titration experiments were conducted with Metrohm Titrando™ titrator using 1.0 M NaOH solution deaerated by N_2 gas. The pH values were monitored with a combined 3M KCl glass electrode (Metrohm™), calibrated with standard buffer solutions. The dosing rate of

IX. Comparison of the corrosion products

titration was controlled as $20 \mu\text{L min}^{-1}$ by and TiamoTM software and modified when it is needed. The solutions were prepared with analytical grade of ZnCl_2 (99.999%, VWR), MgCl_2 (99%, VWR) and AlCl_3 (99.999%, Sigma-Aldrich) with deionized water (MilliporeTM, $18 \Omega \text{ cm}$). The series composition of the elements in the solutions is summarized in **Table 9.1**. The initial volume was 50 mL. The temperature of the solutions was controlled to be stable at $T=25 \text{ }^\circ\text{C}$.

Characterization of the precipitated species

The precipitated species collected during the titration experiment were characterized by Renishaw In ViaTM Raman microscope equipped with a ReinshawTM CDD camera detector. An Ar ion laser was used with an excitation line at 532 nm focused through a $20 \times 0.75 \text{ NA}$ objective. The acquisition and evaluation of Raman spectra was performed by WireTM software.

Simulation of the titration/precipitation based on the thermodynamic database

All titrations and the precipitation of each elemental composition were compared with the simulations based on the thermodynamic database using PhreeqcTM software (version 2.0) using database of thermochemie_phreeqc_v9', concrete_3T_v07, phreeqc_thermoddemv1.10 and PSINA DAV.

Table 9.1. Elemental composition and experimental conditions of the titration experiments.

	ZnCl_2	MgCl_2	AlCl_3	Characterization of the precipitations
(a) Zn^{2+}	0.01 M	-	-	Raman
(b) Mg^{2+}	-	0.01 M	-	Raman (not shown)
(c) Al^{3+}	-	-	0.01 M	No precipitation
(d) $\text{Zn}^{2+}+\text{Mg}^{2+}$	0.01 M	0.01 M	-	Raman
(f) $\text{Zn}^{2+}+\text{Al}^{3+}$	0.01 M	-	0.01 M	No precipitation
(g) $\text{Al}^{3+}+\text{Mg}^{2+}$	-	0.01 M	0.01 M	Raman
(h) $\text{Zn}^{2+}+\text{Mg}^{2+}+\text{Al}^{3+}$	0.01 M	0.01 M	0.01 M	Raman
0.03 M NaCl was added in all solutions				

9.3. Results

9.3.1. Comparison between titration experiments and the thermodynamic simulation

In **Fig. 9.2**, the titration results of each solution and thermodynamic simulation are displayed.

Zn^{2+} : **Fig. 9.2(a)** shows the titration result of Zn^{2+} , simulated titration curve and the predicted precipitation species. The precipitation of simonkolleite was identified by both results in that

the ratio of added moles of OH^- and cations, $n^{\text{OH}^-}/n^{\text{M}^{z+}}=1.6$ corresponding to the chemical formula of simonkolleite ($\text{Zn}_5(\text{OH})_8\text{Cl}_2\cdot\text{H}_2\text{O}$). Simonkolleite formation was favored for $\text{pH} < 10$ by the thermodynamic database (precipitation in M in the second y-axis). According to the equilibrium calculations, ZnO formation is favored for $\text{pH} > 8$ while simonkolleite dissolves in this pH range.

Mg^{2+} : **Fig. 9.2(b)** shows the titration result of Mg^{2+} , simulated titration curve and the predicted precipitation species. It clearly shows the precipitation of $\text{Mg}(\text{OH})_2$ at $n^{\text{OH}^-}/n^{\text{M}^{z+}}=2$.

Al^{3+} : The titration results of Al^{3+} are shown in **Fig. 9.2(c)**. Two equivalence points (EP) were observed by titration at $n^{\text{OH}^-}/n^{\text{M}^{z+}}=2.7$ and 3.2, although the simulation showed only one EP at $n=3$ which is coherent to the formation of $\text{Al}(\text{OH})_3$. No visible solid precipitated species could be obtained.

$\text{Zn}^{2+} + \text{Mg}^{2+}$: **Fig. 9.2(d)** shows the titration of the mixture of Zn^{2+} and Mg^{2+} . Precipitation of simonkolleite at $n^{\text{OH}^-}/n^{\text{M}^{z+}}=1.6$ was predicted as could be seen for only Zn^{2+} case in **Fig. 9.2(a)**. The further addition of OH^- to the mixture would result in the transformation of simonkolleite to ZnO according to the thermodynamic predictions although this was not apparent from the titration curve. $\text{Mg}(\text{OH})_2$ was precipitated for $n^{\text{OH}^-}/n^{\text{M}^{z+}} > 2$, as only Mg^{2+} case in **Fig. 9.2(b)**. It can be concluded that Zn^{2+} and Mg^{2+} were not forming a complex but precipitated individually without affecting each other.

$\text{Zn}^{2+} + \text{Al}^{3+}$: **Fig. 9.2(e)** also shows no interference between each element in that it showed almost the same precipitation as the individual elements (**Fig. 9.2(a)** and **9.2(c)**). It is, however, a different result from the corrosion product of coating samples. For example, Zn/Al LDH species were found after the outdoor exposure and laboratory experiments [6,19,26–28,31].

$\text{Al}^{3+}+\text{Mg}^{2+}$: **Fig. 9.2(f)** shows the titration result of Al^{3+} and Mg^{2+} mixture. In the lower pH range of the titration curve, $\text{Al}(\text{OH})_3$ precipitation occurred until $n^{\text{OH}^-}/n^{\text{M}^{z+}}=3$, as expected from the stoichiometry of $\text{Al}(\text{OH})_3$. Hydrotalcite ($\text{Mg}_6\text{Al}_2(\text{CO}_3)(\text{OH})_{16}\cdot 4\text{H}_2\text{O}$) formation was predicted for $n^{\text{OH}^-}/n^{\text{M}^{z+}} > 3$ from approximately $\text{pH}=6$ of the simulation, indicating the LDHs of

IX. Comparison of the corrosion products

Mg^{2+} and Al^{3+} formation. No indication of $\text{Mg}(\text{OH})_2$ precipitation was observed. The stoichiometry of hydrotalcite can be verified as $\Delta n^{\text{OH}^-}/n^{\text{M}^{2+}}=2$ consistent with the titration result.

$\text{Zn}^{2+}+\text{Al}^{3+} + \text{Mg}^{2+}$: **Fig. 9.2(g)** shows the combination of Zn^{2+} , Al^{3+} and Mg^{2+} . As $\text{Al}^{3+}+\text{Mg}^{2+}$ case, no $\text{Mg}(\text{OH})_2$ was predicted by the simulation. However, the titration result shows one EP at $n^{\text{OH}^-}/n^{\text{M}^{2+}}=5.7$ indicating that another product, most probably the hydrotalcite of Mg-Al.

IX. Comparison of the corrosion products

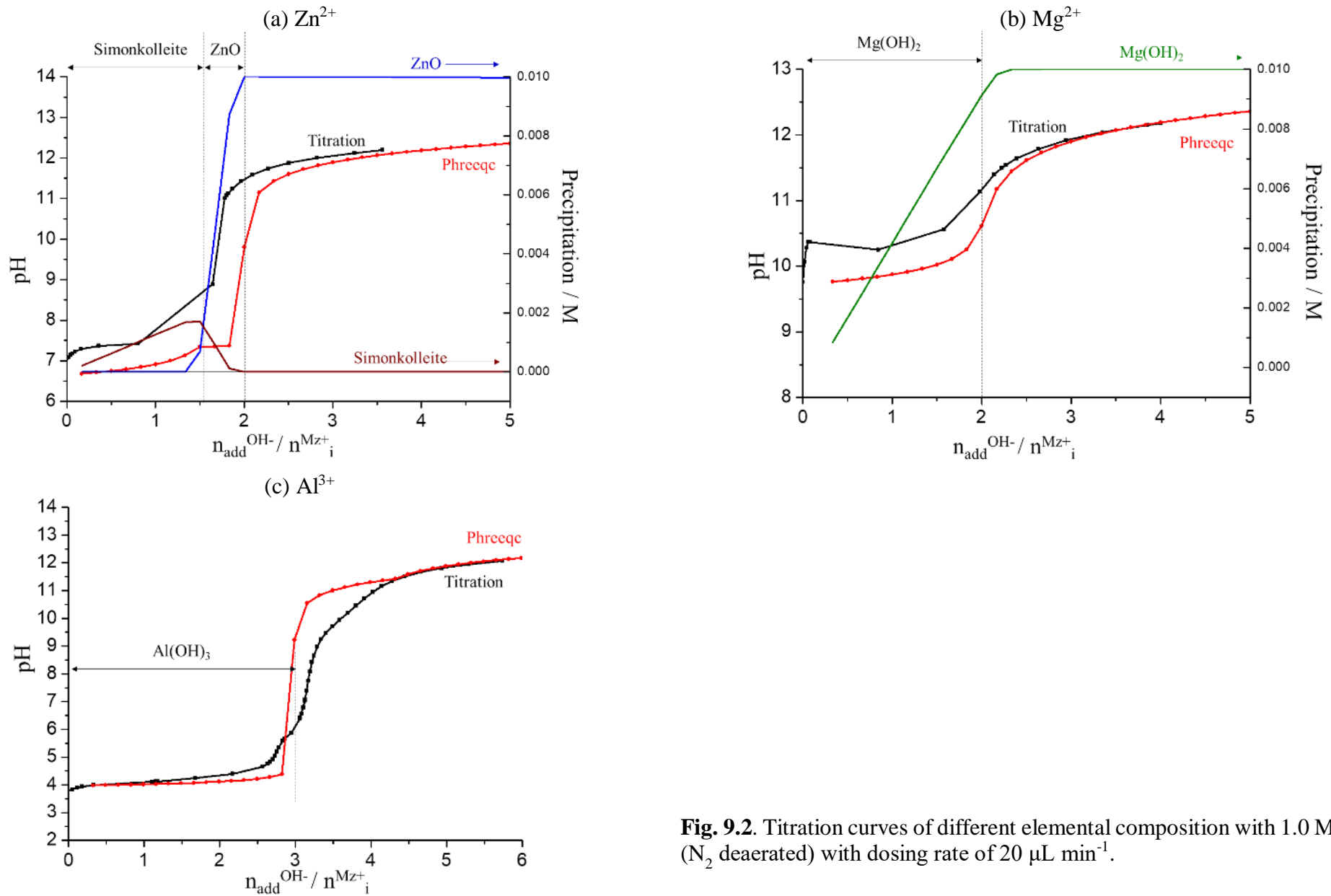
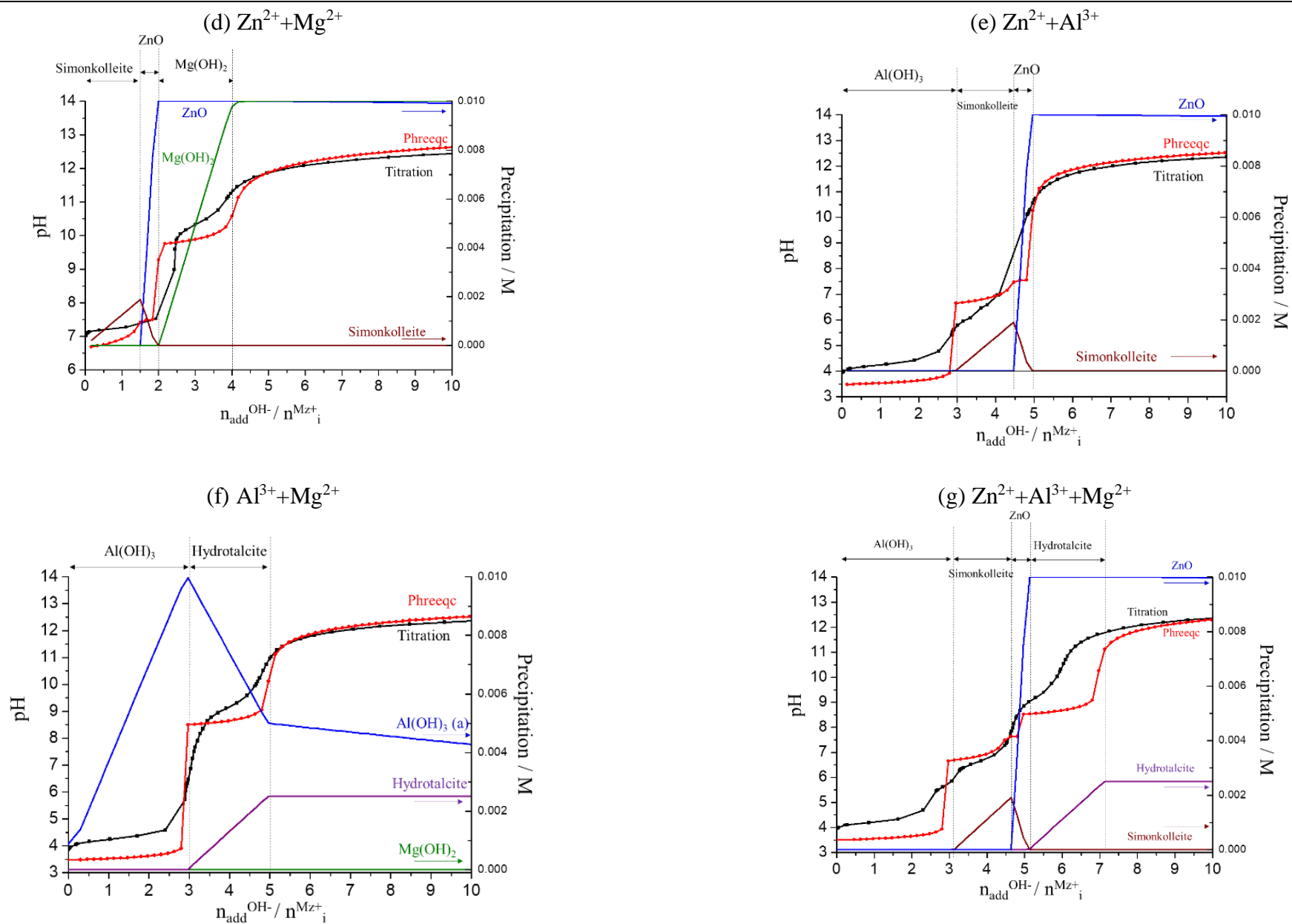


Fig. 9.2. Titration curves of different elemental composition with 1.0 M NaOH (N_2 deaerated) with dosing rate of $20 \mu\text{L min}^{-1}$.

IX. Comparison of the corrosion products



9.3.2. Characterization of artificially formed precipitations by titration experiments

The precipitated species were filtered during the titration experiments in different pH values, then dried by flowing N_2 . These species were characterized by Raman spectroscopy afterward.

Individual Zn^{2+} , Al^{3+} and Mg^{2+}

During individual titration of Zn^{2+} and Mg^{2+} , visible precipitated species could be obtained whereas for Al^{3+} , no clear solid species could be filtered. Raman spectra of Mg precipitated species showed broad peaks near 3610 cm^{-1} , well agreed to indicate $Mg(OH)_2$ precipitation [180], not displayed in here.

Fig. 9.3 and **Table 9.2** show the Raman shift of $0.5\text{ mmol } Zn^{2+}$ by the titration experiment in the previous section. It shows that the different precipitated species formed at each pH. For example, at $pH=7.4$, broad peaks near 3500 cm^{-1} and a clear peak at 1065 cm^{-1} indicate simonkolleite precipitation [80,124]. This is coherent to the simulation of Zn^{2+} titration (**Fig. 9.2(a)**) where simonkolleite formed for $pH < 8.0$. Simonkolleite might be transformed to $ZnO/Zn(OH)_2$ for $pH > 8.0$ identified by Raman spectroscopy at 410 cm^{-1} and near 3200 cm^{-1} .

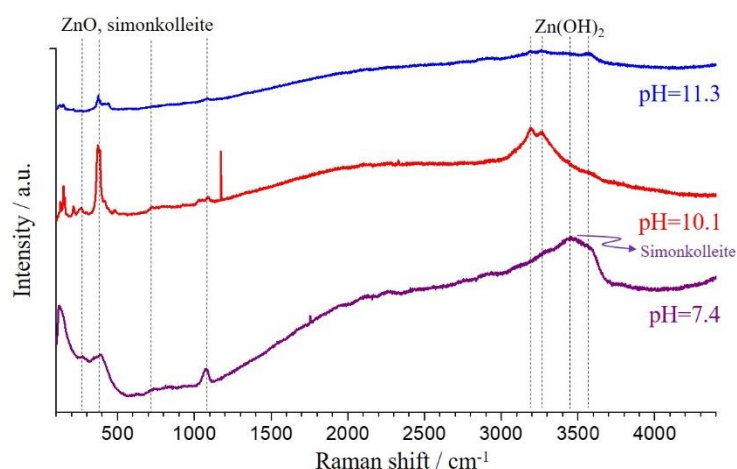
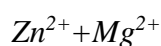


Fig. 9.3. Raman spectra from the titration experiment of $0.5\text{ mmol } Zn^{2+}$ (**Fig. 9.2(a)**). The precipitated species at three different pH were measured.

Table 9.2. Raman shift found from the titration of $0.5\text{ mmol } Zn^{2+}$ at $pH=7.4$, 10.1 and 11.3 .

	$pH=7.4$	$pH=10.1$	$pH=11.3$
Raman shift $/\text{cm}^{-1}$		147, 156, 210, 256	148
	370, 389	370, 380, 410, 438	370, 380, 415, 436
		722	
	1070	1030, 1084	1080, 1333
	3459, 3580	3193, 3267	2910, 3075, 3187, 3267, 3566
Precipitation	ZnO, simonkolleite [80,124]	HZ, ϵ - $Zn(OH)_2$ [124]	HZ, $Zn(OH)_2$ [80,124]



In **Fig. 9.4** for $\text{Zn}^{2+} + \text{Mg}^{2+}$ mixture at pH=13, Raman shifts identified at 489 cm^{-1} and 3276 cm^{-1} can be attributed to the precipitation of $\epsilon\text{-Zn(OH)}_2$ [124]. Simonkolleite could be precipitated as indicated by Raman shift at 550 cm^{-1} and broad peak near 3459 cm^{-1} [80,124]. Raman shift at 3616 cm^{-1} indicates that Mg(OH)_2 precipitation. The characterization of the precipitated species was reasonably coherent to those simulated by phreeqcTM software shown in **Fig. 9.2(d)**.

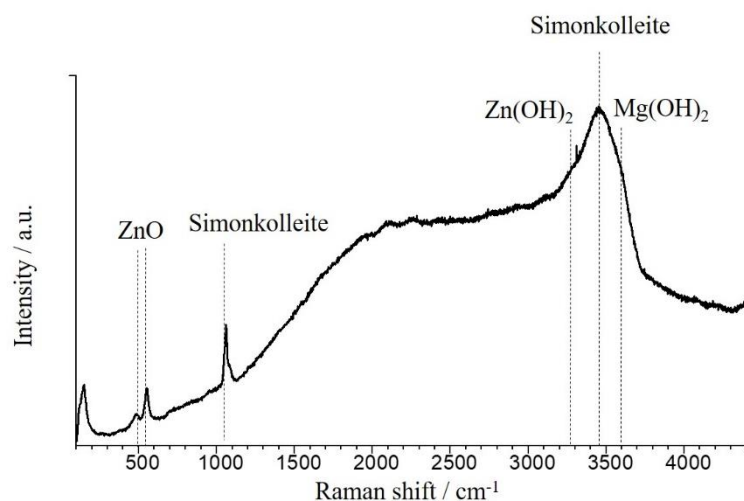


Fig. 9.4. Raman spectra of 0.5 mmol $\text{Zn}^{2+} + \text{Mg}^{2+}$ with 30 mM NaCl at pH=13.

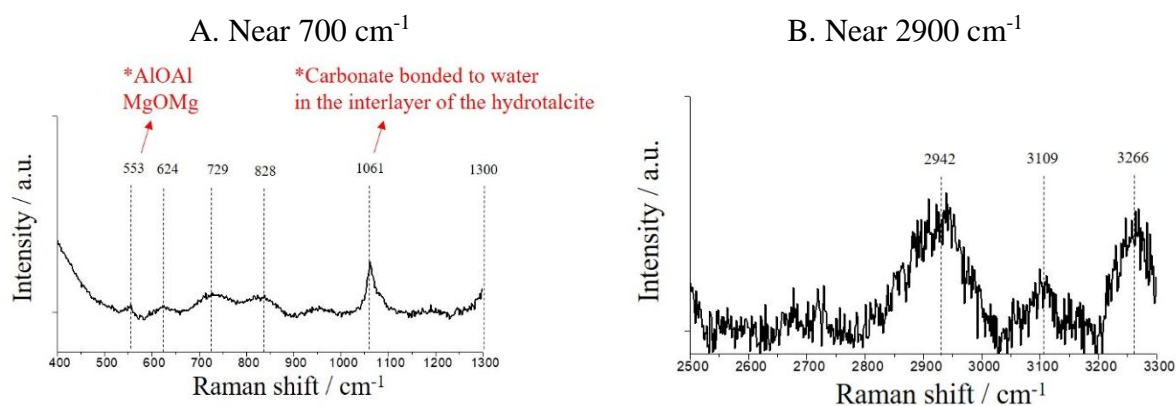
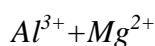


Fig. 9.5. Raman spectra of 0.5 mmol $\text{Al}^{3+} + \text{Mg}^{2+}$ with 30 mM NaCl at pH=12.5.

In **Fig. 9.5**, the baseline of the spectra was subtracted by Renishaw Wire 4.2TM software as the spectra of the precipitated species of 0.5 mmol Al^{3+} and Mg^{2+} showed highly noise peaks. The Raman shift at 553 cm^{-1} can be considered to the Al-O-Al and Al-O-Mg linkage in hydroxalcite [181–184]. A clear peak at 1061 cm^{-1} can be attributed to the hydroxalcite containing carbonate anion. The Raman spectroscopy of the OH stretching vibrations from the hydroxalcite can be observed at $2900\text{--}3300 \text{ cm}^{-1}$ [182]. Precipitation of the hydroxalcite was also

identified by the thermodynamic simulation at higher pH, consistent with the reference in [185]. Interestingly, $\text{Mg}(\text{OH})_2$ was not observed both by Raman spectroscopy and thermodynamic simulation. Therefore, it can be concluded that in the presence of both Al^{3+} and Mg^{2+} , the formation of LDHs is favored to $\text{Mg}(\text{OH})_2$ precipitation. This means that the Mg-Al hydrotalcite can be formed in the solution. Xu et al. [185] investigated the modification and dissolution behavior of Mg-Al hydrotalcite particles. It was found that for $4.2 < \text{pH} \leq 9.4$ in $(\text{NH}_4)_2\text{SO}_4$ solution, the $\text{Mg}(\text{OH})_2$ sheets were partially dissolved then Mg-Al hydrotalcite species formed inward along the edges of the $\text{Mg}(\text{OH})_2$ film, in accordance with the present work.

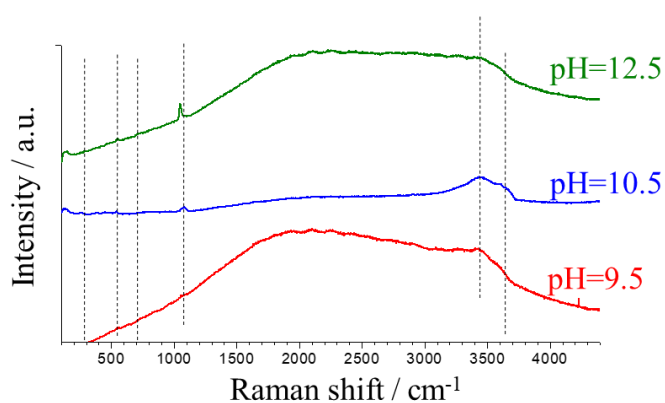
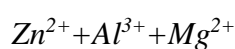


Fig. 9.6. Raman spectra of 0.5 mmol $\text{Zn}^{2+} + \text{Al}^{3+} + \text{Mg}^{2+}$ at pH=9.5, 10.5 and 12.5.

Fig. 9.6 shows the Raman shift of 0.5 mmol $\text{Zn}^{2+} + \text{Al}^{3+} + \text{Mg}^{2+}$ at pH=9.5, 10.5 and 12.5. Not shown here is at pH=7.4 which showed highly noise Raman shift and only showed the peaks corresponding to simonkolleite. No $\text{Mg}(\text{OH})_2$ was observed as in the $\text{Al}^{3+} + \text{Mg}^{2+}$ case. The formation of Mg-Al hydrotalcite was again identified. The precipitated species were characterized by Raman spectroscopy summarized in **Table 9.3**.

Table 9.3. Raman shift found from the titration of 0.5 mmol $\text{Zn}^{2+} + \text{Al}^{3+} + \text{Mg}^{2+}$ at pH=9.5, 10.5 and 12.5.

	pH=9.5	pH=10.5	pH=12.5
Raman shift / cm^{-1}	153	153, 255, 382, 456	153
	554	554	554, 718
	1048	1048, 1084	1048
	3262, 3427, 3610	3271, 3447, 3606	3451, 3603
Precipitation	$\text{Zn}(\text{OH})_2$ [124], HZ [182], $\text{Mg}(\text{OH})_2$ [180]	Simonkolleite, ZnO, $\text{Zn}(\text{OH})_2$ [124], HZ [182], $\text{Mg}(\text{OH})_2$ [180]	$\text{Zn}(\text{OH})_2$ [124], HZ, Mg-Al LDHs [182]

9.3.3. Comparison with the electrochemically formed corrosion products

The Raman spectra of the precipitate species were compared with that of the Zn-1.6Al-1.6Mg/Zn-2.5Al-1.5Mg alloy coatings (denoted as ZAM in this chapter) after the electrochemical measurement as shown in **Figs. 9.7** and **9.8**. A chronoamperometric (CA) experiment was conducted, applying a constant potential near the E_{oc} for 1000 s in pH=10.1, 30 mM NaCl (**Fig. 9.7**) and pH=12.80, 0.1 M NaOH (**Fig. 9.8**), Ar deaerated electrolytes.

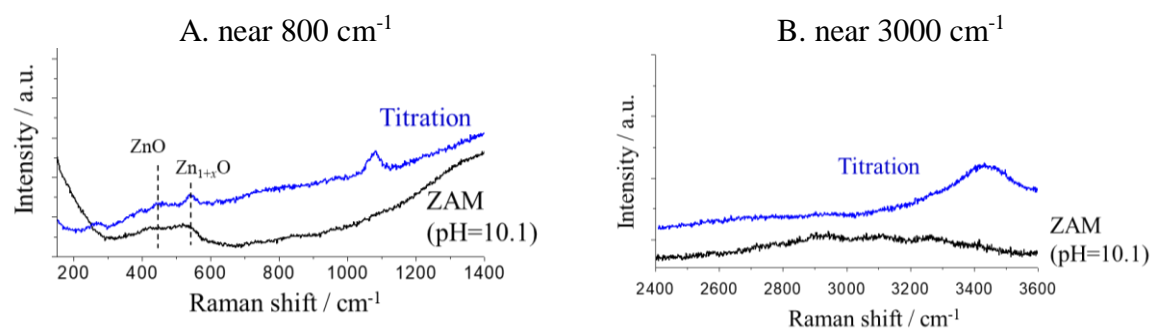


Fig. 9.7. Raman spectra comparison between the electrochemical measurement in pH=10.1, 30 mM NaCl, Ar deaerated electrolyte (CA experiment near E_{oc}) and precipitated species from the titration experiment.

At pH=10.1 near 800 cm⁻¹ (**Fig. 9.7A**), a clear ZnO and Zn_{1+x}O formation are indicated both from titration and electrochemical measurement. A peak at 1080 cm⁻¹ found in titration was not observed for the electrochemical measurement. Simonkolleite precipitation was observed for the titration experiment near 3450 cm⁻¹ (**Fig. 9.7B**), also correlated with the peak near 1060 cm⁻¹. Zn(OH)₂ formation was identified from the electrochemical measurement near 3100 cm⁻¹.

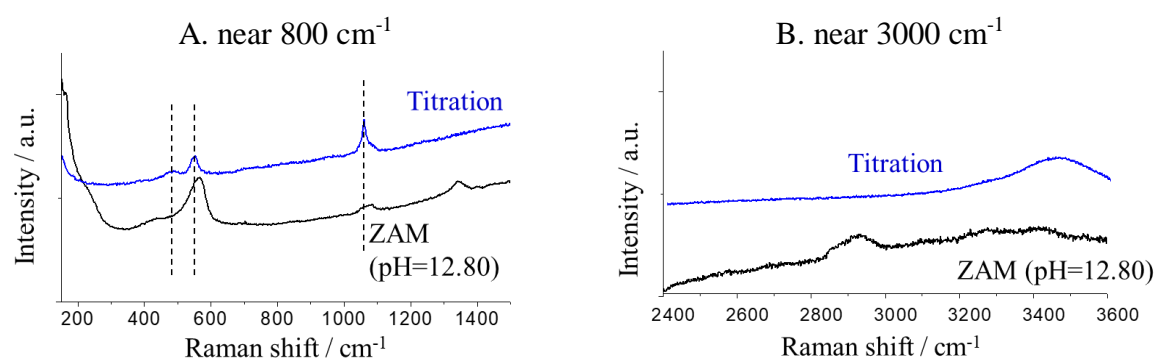


Fig. 9.8. Raman spectra comparison between the electrochemical measurement in pH=12.80, 0.1 M NaOH, Ar deaerated electrolyte (CA experiment near E_{oc}) and precipitated species from the titration experiment.

At pH=12.80, near 800 cm⁻¹ (**Fig. 9.8A**), ZnO and Zn_{1+x}O formation were monitored in both experiments, with relatively higher peak intensities than at pH=10.1. The peak at 1080 cm⁻¹

¹ was observed for both cases indicating hydrocarbonate (HZ) and/or Mg-Al hydrotalcite species formation. Mg-Al hydrotalcite formation was coherent with titration and thermodynamic predictions. No Mg(OH)₂ formation was monitored also in accordance with the thermodynamic prediction. As there was no carbonate ion in the electrolyte composition, the HZ and hydrotalcite species would be formed on the ZAM surface after the experiment.

The corrosion products identified by Raman spectra during the electrochemical tests (marked as *) are summarized in **Table 9.4**. Identified phases of Zn-Al pure phases were coherent with the field exposure and the laboratory tests. Interestingly, Mg-Al LDHs species were found after the CA and LSV experiment at pH=12.80 coherent with previous observations from the titration and thermodynamic simulations.

Table 9.4. Identified phases on the Zn-Al/Zn-Al-Mg surface after the electrochemical test conducted in this work (marked as *) and field exposure/laboratory test in the literatures.

	Materials	Test types	Identified phases
Zn-Al	*Zn-22Al, Zn-68Al (pure phases)	CA and LSV in pH=10.1, 12.80	Simonkolleite (pH=10.1), ZnO, Zn _{1+x} O, Zn(OH) ₂ , HZ
	Zn-5Al [107]	5 years marine field and laboratory exposure	Simonkolleite, ZnO, LDHs, Al ₂ O ₃
	Zn-5Al [19]	Air / low CO ₂ conditions	Simonkolleite, ZnO, HZ, LDHs
Zn-Al-Mg	*Zn2.5Al1.5Mg, Zn1.6Al1.6Mg	CA and LSV in pH=12.80	Simonkolleite, ZnO, Zn _{1+x} O, Zn(OH) ₂ , HZ, Mg-Al LDHs
	Zn2Al2Mg [27]	15 h of humid air exposure	Mg-Al LDHs Zn-Al LDHs
	Zn3Al3Mg [30]	Cyclic corrosion test	Simonkolleite, ZnO, LDHs, HZ

9.4. Discussion and conclusions

The artificially formed precipitated species by titration reasonably correspond to those predicted by a thermodynamic simulation.

1) In the presence of Mg²⁺ and Al³⁺, Mg-Al hydrotalcite (LDHs of Mg/Al) was formed rather than Mg(OH)₂ precipitation. The preferential formation of the Mg-Al hydrotalcite to Mg(OH)₂ at higher pH is in accordance with the reference [185]. This observation is in accordance with the laboratory corrosion test in the presence of Cl⁻ for the Zn-Al-Mg alloy coating in that the Mg/Al LDHs were observed in the initial corrosion while no Mg(OH)₂ was monitored [6,27].

IX. Comparison of the corrosion products

2) However, no LDHs of Zn/Al was identified by titration and simulation while this was found in most of the literature of Zn-Al/Zn-Al-Mg coating alloys in the field exposure and laboratory tests [6,19,26–28,31].

3) ZnO, Zn(OH)₂ and simonkolleite formation was observed for titration, thermodynamic prediction and electrochemical test of the Zn-Al pure phases and the Zn-Al-Mg alloy coating.

4) As the identified phases were reasonably identical to the thermodynamic prediction, precipitations in the solution and electrochemical test, the methodology presented herein can be used to model real corrosion situation.

Conclusions

X. Summary and perspectives

«Ce qu'il faut c'est écrire une seule phrase vraie. Ecris la phrase la plus vraie que tu connais.»

Paris est une fête (1964),

Ernest Hemingway

10. Summary and perspectives of this Ph.D. project.

The objective of this Ph.D. project was to investigate the electrochemistry of the pure phase components of the Zn-Al-Mg coating alloys as an input data for the prediction of corrosion behavior of the technical coatings. To this end, a database of elemental polarization curves was established as a function of pH by using atomic emission spectroelectrochemistry (AESEC). The dealloying mechanisms of the binary pure phase alloys were investigated and compared with that of alloy coatings. Elemental dissolution mechanisms of the pure phases were suggested taking into accounts the elemental interactions and corrosion products under given conditions. The most stable species precipitated in the solution were compared with the corrosion products on the alloy and thermodynamic simulations.

10.1. Specific dealloying mechanisms of the binary phase were investigated.

Dealloying of the MgZn_2 intermetallic and α -phase of Al-Zn (Zn-68Al) were investigated at pH=10.1, presented in Chapter IV and Chapter V. These two phases represent the extremes of Mg and Al content in the Zn-Al-Mg alloy coating, respectively. In the cathodic polarization, the Zn(0) enriched layer was formed in both cases by selective dissolution of Mg and Al respectively. However, the influence of this layer on cathodic dealloying differed: for MgZn_2 , Mg selective dissolution was restrained by the dealloyed layer, whereas for Zn-68Al, Al selective dissolution was not affected by this layer. Given that the onset potential of the Zn(0) enriched layer, E_c^{Zn} , was reasonably the same for all Zn containing system in pH=8.4 and 10.1, it can be concluded that this layer may determine the corrosion potential of the Zn-Al-Mg system. Both MgZn_2 and Zn-68Al showed a simultaneous dissolution potential, E_c . MgZn_2 showed a typical 'Type II' dissolution behavior as referenced by Pickering's convention stated in Chapter II. For Zn-68Al, even though it showed an E_c , this classification cannot be applied because Al already dissolved for $E < E_c$ by cathodic dealloying. The Zn(0) enriched layer formation was verified and quantified by the chronoamperometric step experiment shown in **Fig. 10.1**.

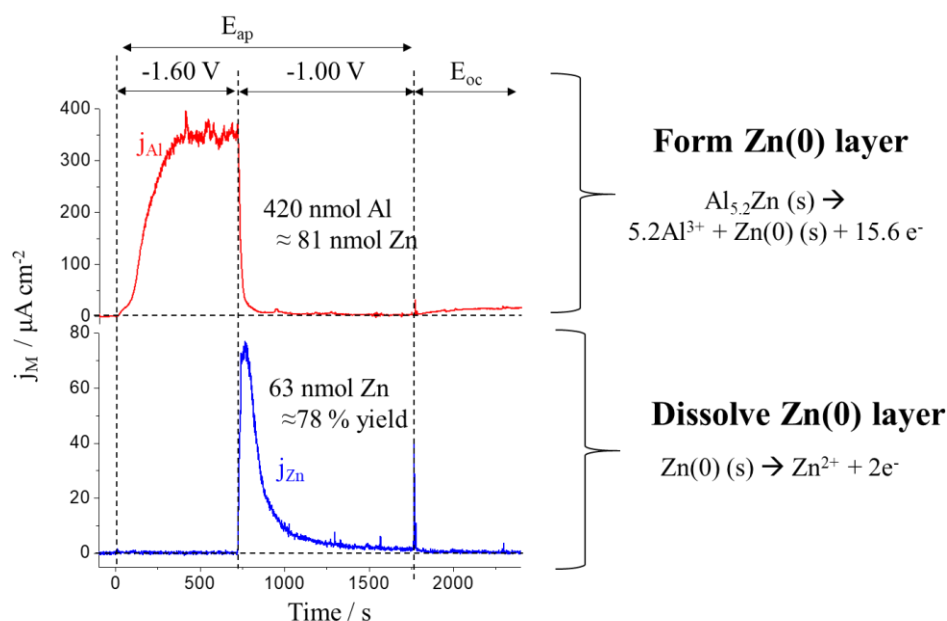


Fig. 10.1. Quantification of the Zn(0) enriched layer for Zn-68Al in pH=10.1 electrolyte by the chronoamperometric step experiment.

10.2. Interaction between Zn and Al dissolution was examined in different electrochemical conditions.

For all Zn-Al systems investigated in this Ph.D. project, it was observed that the onset of active Zn dissolution coincided with a reduction in the Al dissolution rate, suggesting an inhibitive effect of Zn dissolution on Al dissolution. This phenomenon was observed in two domains in the LSV experiment; 1) when Zn dissolution was activated for $E_c^{Zn} < E < E_c$; 2) when the potential was released then the specimen underwent a spontaneous dissolution. The former case was attributed to $Zn(OH)_2$ formation on the porous Zn(0) enriched layer formed by cathodic dealloying of Al during cathodic potential domain, blocked the Al dissolution. The latter case was understood as, a passive ZnO formed during the anodic potential domain was not completely dissolved even when the potential released. Al dissolution was limited by the ZnO layer then occurred across this film as evidenced by reduced perturbation signal. When this film dissolved, Al dissolution returned to the open circuit dissolution behavior. A schematic diagram describing the interactive Al-Zn dissolution mechanism as a function of potential is given in **Fig. 10.2**.

X. Summary and perspectives

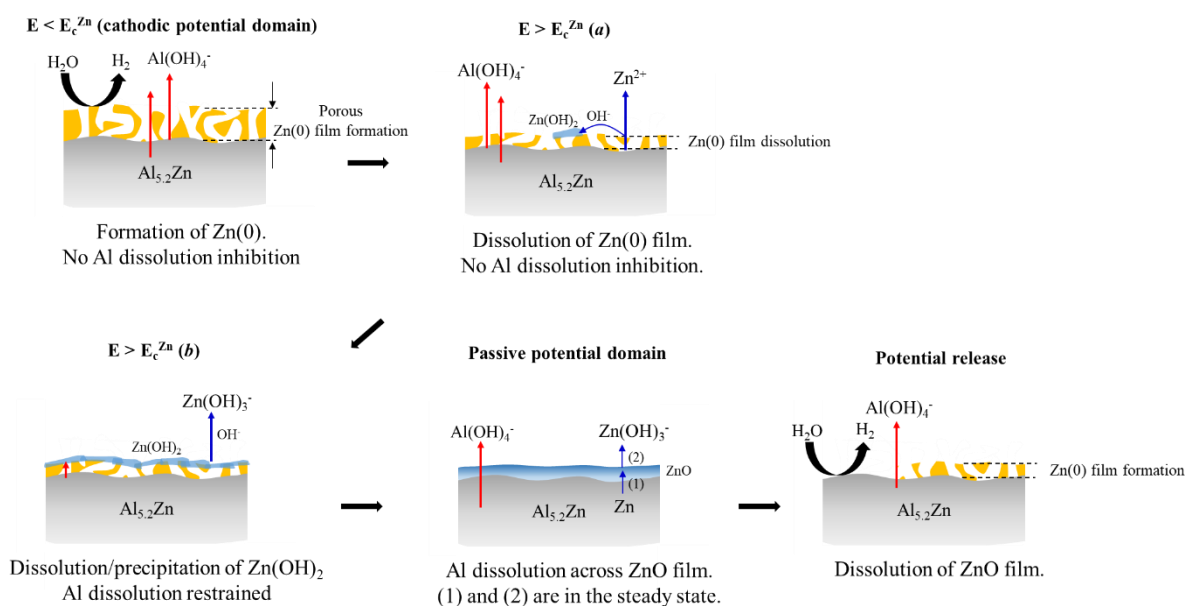


Fig. 10.2. Schematic diagram of the dissolution of Al-Zn phase in alkaline solution.

10.3. Elemental dissolution mechanisms of Zn, Al and Al-Zn phase in the alkaline media were analyzed as a function of temperature.

Al dissolution increased with temperature for pure Al and Zn-68Al phase at pH=12.80 as described in **Chapter VII**. It was observed that Al dissolution in alkaline media was limited by the dissolution rate of the Al(OH)_3 film, evidenced by potential independent Al dissolution. Other Al containing Zn-Al specimen investigated in this work also showed a potential independent dissolution behavior for $E < E_c^{\text{Zn}}$ at pH=12.80. For $\text{Al}_{5.2}\text{Zn}$ phase, Zn may play a role to destabilize the passive film as evidenced by higher activation energy than that of pure Al. ZnO formation was favored at higher temperatures, which is significant for the alkali cleaning of the Zn-Al alloy coatings because the alkali cleaning is normally conducted at high temperature.

10.4. An electrochemical database of the Zn-Al-Mg system has been established in a wide range of electrolyte condition.

An extensive electrochemical database of the Zn-Al-Mg system was established in **Chapter VIII**. The stability of the pure phases and coating alloys was characterized in a range of pH and alloy compositions. **Fig. 10.3** shows the AESEC-LSV curves as a function of % Al and the solution pH for the Zn-Al system. Interactions between elemental dissolutions vary with both chemical composition and the solution pH. Al dissolution mechanism was changed from

pH=8.4 and 10.1 to pH=12.80 in that it showed a nearly potential independent dissolution in the cathodic potential domain at pH=12.80. Zn dissolution was not significantly altered by alloying with Al, however, was reduced in the transpassive Al dissolution potential domain at pH=8.4 and 10.1 for Zn-68Al. The electrochemical database of various composition of alloys and pure phases in a range of pH obtained in this chapter can be used to predict the corrosion behavior of the alloy coatings.

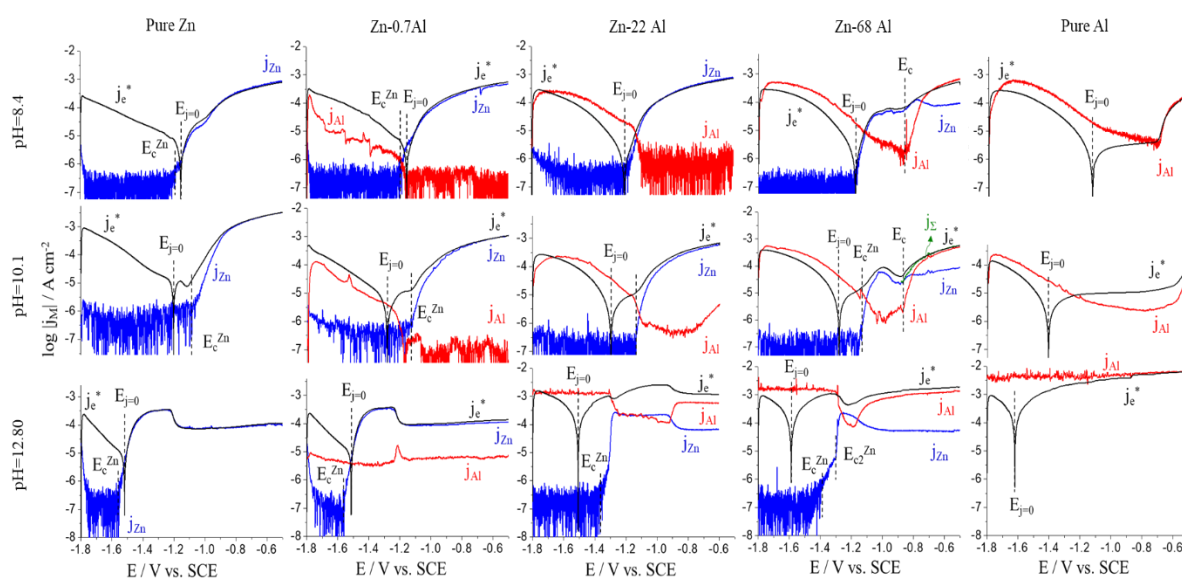


Fig. 10.3. AESEC-LSV of Zn-Al phases with increasing % Al, in three pH values investigated in this work. LSV curves are obtained from **Chapter VIII**.

10.5. The stable corrosion products were correlated by different methodologies.

The most stable corrosion products formed by electrochemical measurements, precipitated species in the solution during titration experiment and the thermodynamic database were reasonably coherent with each other (**Chapter IX**). Most of the precipitated species formed in the solution corresponded reasonably well to those predicted by thermodynamic database. It was in a good agreement with the corrosion products of the alloy, characterized after the electrochemical measurements. Therefore, it can be concluded that the thermodynamic database can be used to predict and eventually model the real corrosion situation.

10.6. A new approach of using AESEC technique was suggested.

The AESEC technique has an indisputable advantage of measuring the elementary reactions and electrochemical response in real time. Chronoamperometric step experiment revealed, for the first time, the formation/dissolution mechanism of the Zn(0) enriched layer in

a quantitative level. The terminology ‘cathodic dealloying’, first introduced in this work, was thereby verified by this technique.

The corrosion study can be expanded for more complex alloy coatings and pure phases with the methodology developed in this Ph.D. study. It was revealed that the experimental methods used in this Ph.D. project were useful to investigate the dealloying and elemental interactions for the multi-phase system. This can be applied to other complicated alloy systems.

Hydrogen evolution reaction (HER) was qualitatively analyzed by the perturbed Al dissolution signal, $\sigma_{j_{Al}}$ for the first time. A linear relationship between j_{Al} and $\sigma_{j_{Al}}$ was observed all Al containing specimen investigated in this work. Further methodological development will be needed to investigate the dynamics of bubble transfer to the plasma by the nebulization system. High data acquisition rate will allow us to detect the particles having rapid transient.

A deeper understanding about the elemental dissolution mechanism can be obtained by the coupling AESEC technique with the electrochemical impedance spectroscopy (EIS) which allows to investigate the ionic transfer across an oxide film on the surface. The AC-AESEC technique (**Appendix 1**) verified the interaction of Mg and Zn in the cathodic potential domain of the polarization curve by the formation of the Zn(0) enriched layer. It was demonstrated that the Mg dissolution oscillation caused by the AC potential was restrained by the Zn(0) enriched layer.

Different surface preparation methods were compared with each other for the Zn-Al alloy coating (**Appendix 4**). The initial elemental dissolution transient of each methods was also compared by means of the AESEC technique. The AESEC results were also correlated with the SEM-EDS analysis investigating the surface morphology, homogeneity and composition after each surface preparation methods. The humidity chamber method, which showed a less surface oxide formation and better reproducible surface condition, can be used for the Zn-based coating alloys in the laboratory tests.

Appendix

Appendix

A1. Alternative current-atomic emission spectroelectrochemistry (AC-AESEC).**A1.1. Introduction**

In this chapter, elemental dissolution oscillation was monitored by applying alternative-current (AC) perturbations (AC-AESEC) with low frequency. The goal of this work is to distinguish the metal oxidation results in whether direct formation of metal cations or passing across an intermediate film. The origin of the phase shift of elemental dissolution rate was investigated for Zn-Al, Zn-Al-Mg alloys and Zn-Al pure phases. A phase shift between Zn and Al dissolution rate was observed for all Zn-Al containing system except for the Al-rich Al-Zn phase (Zn-68 wt.% Al, Al_{5,2}Zn). For the Zn-Al-Mg alloy coating, Al and Mg dissolution phase was varied depending on the potential.

Coupling AESEC technique with electrochemical impedance spectroscopy (EIS) was proposed in reference [78]. In this work, a fixed low frequency (0.0046 Hz) potential perturbation near open circuit potential was tested.

A1.2. Experimental*Materials*

The Zn-5Al and Zn-2.5Al-1.5Mg (denoted in this work as Zn-Al-Mg) alloy coatings were tested supplied by *ArcelorMittal*, France and *Voestalpine*, Austria, respectively. Pure phases of Zn-0.7Al, Zn-22Al and Zn-68Al were also analyzed. The samples were prepared as the same method as in other chapters, stored in the humidity chamber after physical abrasion. The experiments were performed in a slightly alkaline and alkaline electrolytes, pH=10.1 (30 mM NaCl) and pH=12.80 (0.1 M NaOH), respectively. The electrolytes were prepared in deionized water via a Millipore™ system (18 MΩ cm) with analytical grade of materials.

Alternative current-atomic emission spectroelectrochemistry (AC-AESEC) technique

A low frequency alternative current (AC) perturbations was applied to the specimen of interest coupled with atomic emission spectroelectrochemistry (AESEC). After the background measurement, at t=0 s, whether a constant potential was applied or the spontaneous dissolution was measured until the elemental dissolution reaches a steady state. A potentiostatic pulse at a

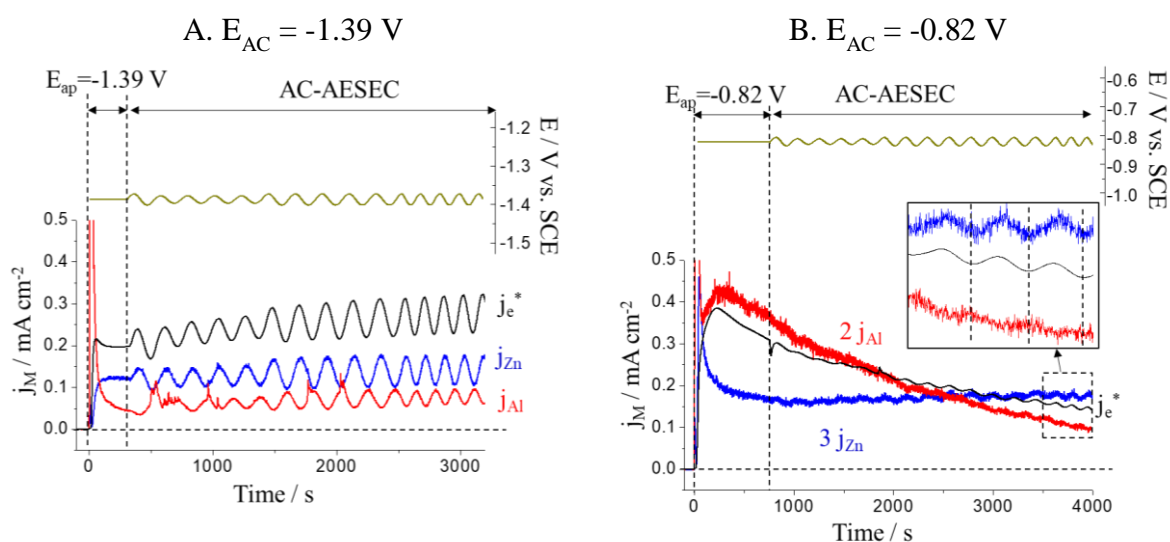
fixed frequency (0.0046 Hz) with ± 10 mV root mean square (rms) at the potential of interest was applied which will be denoted in this work as E_{AC} . The electrical current, j_e , and potential (E) were measured by a Gamry Reference 600TM potentiostat. Note that in this work the electrical current density was convoluted j_e^* taking into account the residence time distribution of the flow cell, which enables a direct comparison with elemental dissolution rates (j_M) in the same time sequence. All potential values presented herein is referenced by a saturated calomel electrode (SCE).

A1.3. Results and discussions

A1.3.1. At pH=12.80

Zn-Al and Zn-Al-Mg alloy coatings

A pH=12.80, 0.1 M NaOH solution was chosen in order to avoid the complication may be caused by chloride ions in the electrolyte. The Zn-5Al alloy was tested at two potentials: 1) $E_c^{Zn} < E < E_p^{Zn}$ where Al dissolution was inhibited; 2) $E > E_p^{Zn}$ where both Zn and Al showed a passive dissolution behavior, as shown in **Fig. A1.1**. Note that E_p^{Zn} is the potential where Zn dissolved with a passivation of ZnO film. It was clearly seen that in both potentials, j_{Zn} was in phase with E_{AC} and j_e^* while j_{Al} was 180° phase shifted.



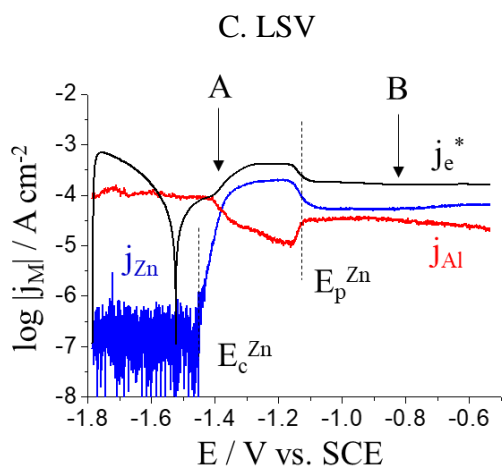


Fig. A1.1. AC-AESEC test for Zn-5Al in pH=12.80, 0.1 M NaOH, Ar deaerated electrolyte. **A:** $E_{AC} = -1.39$ V and **B:** $E_{AC} = -0.82$ V. **C:** the LSV curve taken from Chapter VIII.

The phase shift between j_{Zn} and j_{Al} was also seen for the Zn-Al-Mg alloy in the same electrolyte condition as shown in Fig. A1.2.

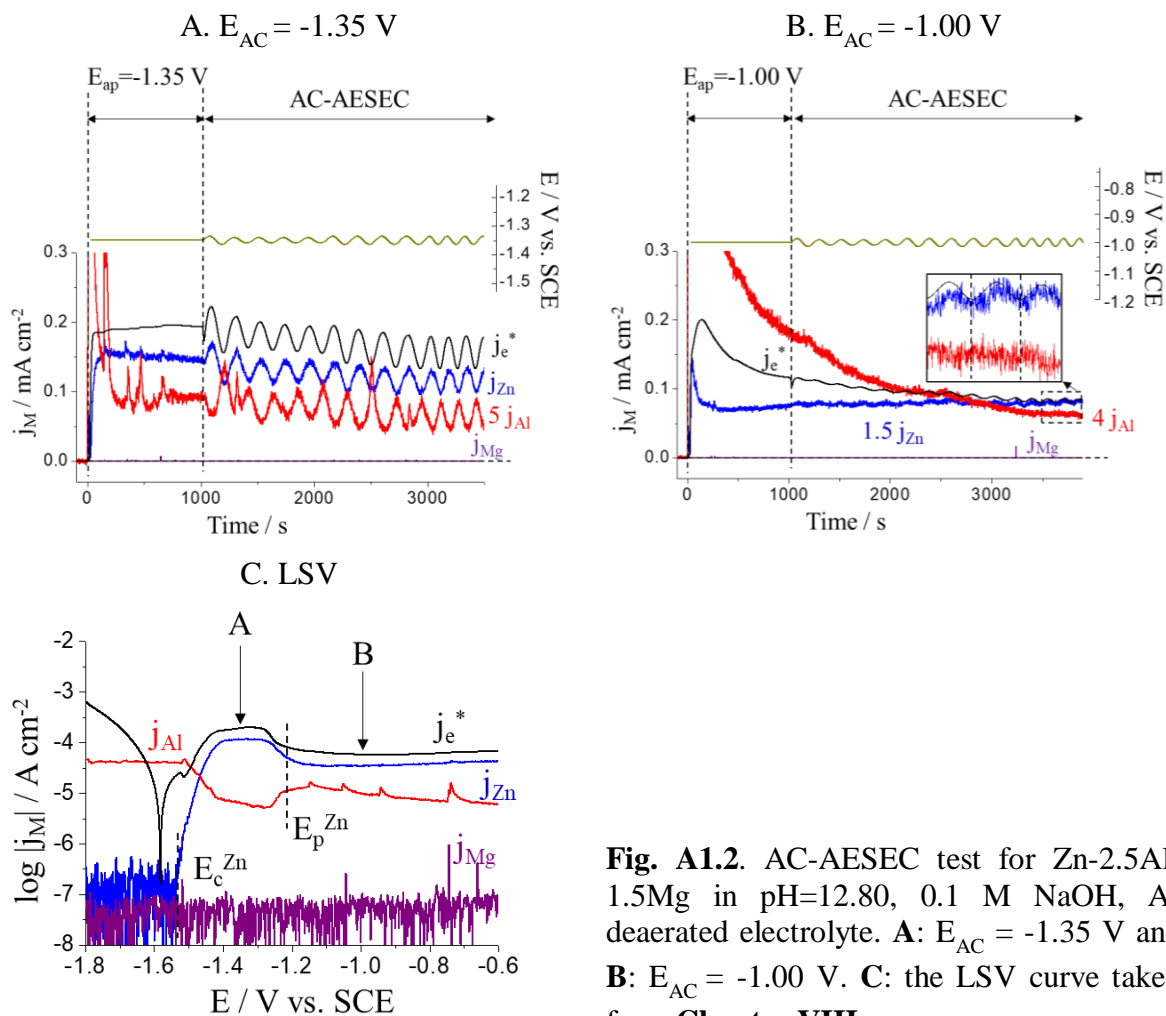
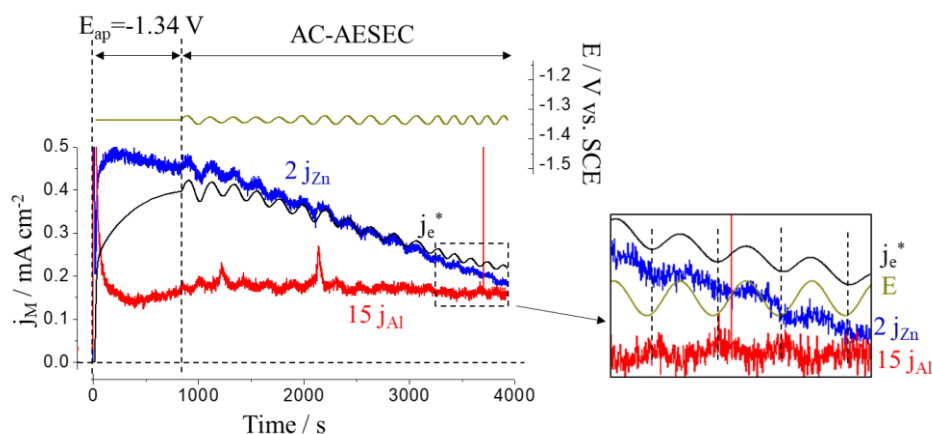


Fig. A1.2. AC-AESEC test for Zn-2.5Al-1.5Mg in pH=12.80, 0.1 M NaOH, Ar deaerated electrolyte. **A:** $E_{AC} = -1.35$ V and **B:** $E_{AC} = -1.00$ V. **C:** the LSV curve taken from Chapter VIII.

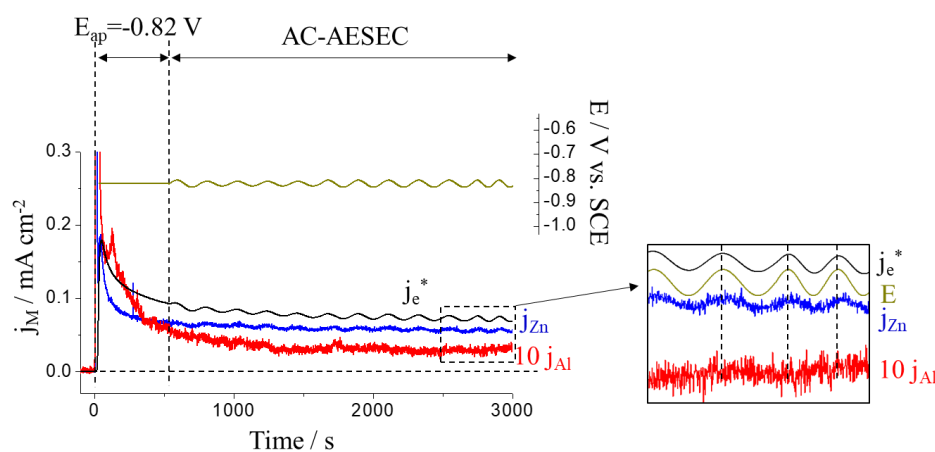
Zn-Al pure phases

The Zn-Al pure phases were also tested in 0.1 M NaOH, Ar deaerated solution. For Zn-0.7Al, a homogeneous η -phase of Zn, showed also j_{Zn} and j_{Al} phase shift as shown in **Fig. A1.3**.

A. $E_{\text{AC}} = -1.34 \text{ V}$



B. $E_{\text{AC}} = -0.82 \text{ V}$



C. LSV

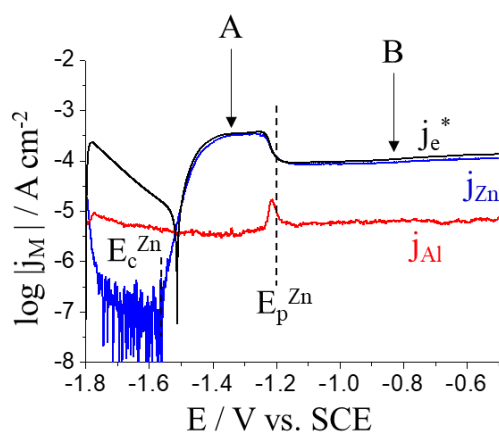
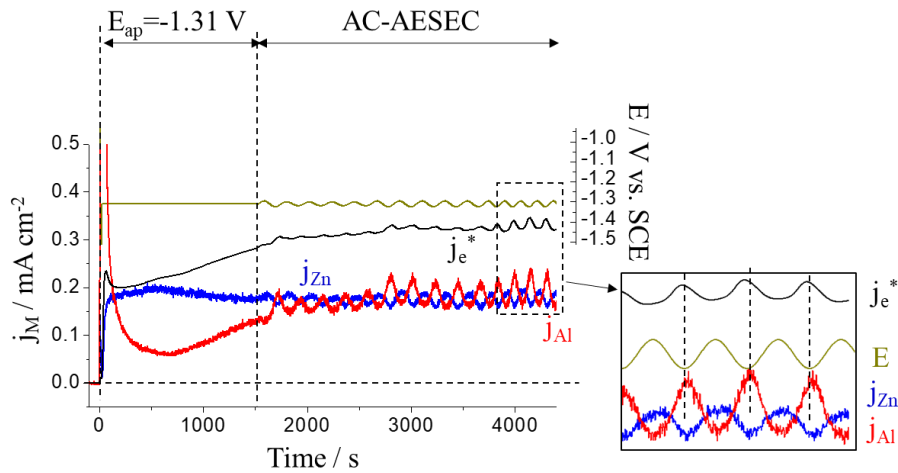


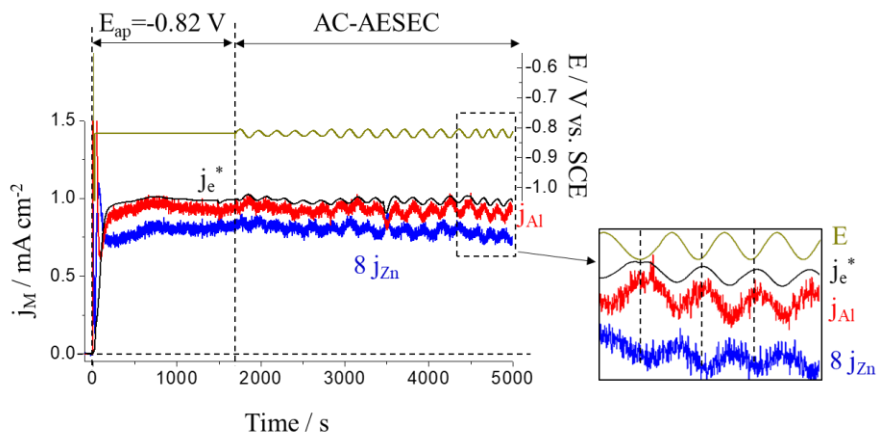
Fig. A1.3. AC-AESEC test for Zn-0.7Al in pH=12.80, 0.1 M NaOH, Ar deaerated electrolyte. **A:** $E_{\text{AC}} = -1.34 \text{ V}$ and **B:** $E_{\text{AC}} = -0.82 \text{ V}$. **C:** the LSV curve taken from **Chapter VIII**.

Zn-22Al also showed 180 ° phase shift as shown in **Fig. A1.4**. j_e^* was also 180 ° shifted to j_{Al} because Al dissolution was predominant to j_{Zn} . One possible explanation of the 180 ° phase shifted j_{Al} was the ‘cathodic Al dissolution’ coupled with water reduction. This hypothesis can be ruled out because this shift was monitored even in anodic dissolution conditions for Zn-5Al, Zn-Al-Mg and Zn-22Al.

A. $E_{AC} = -1.31$ V



B. $E_{AC} = -0.82$ V



C. LSV

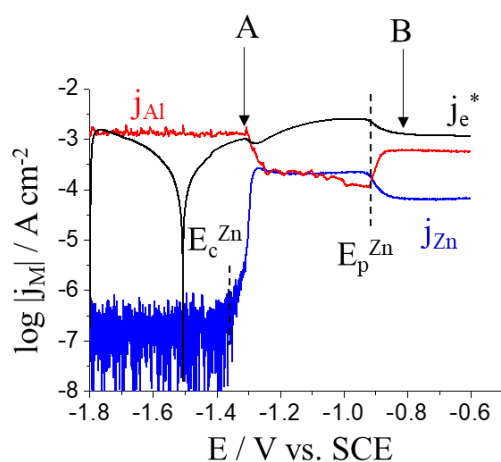
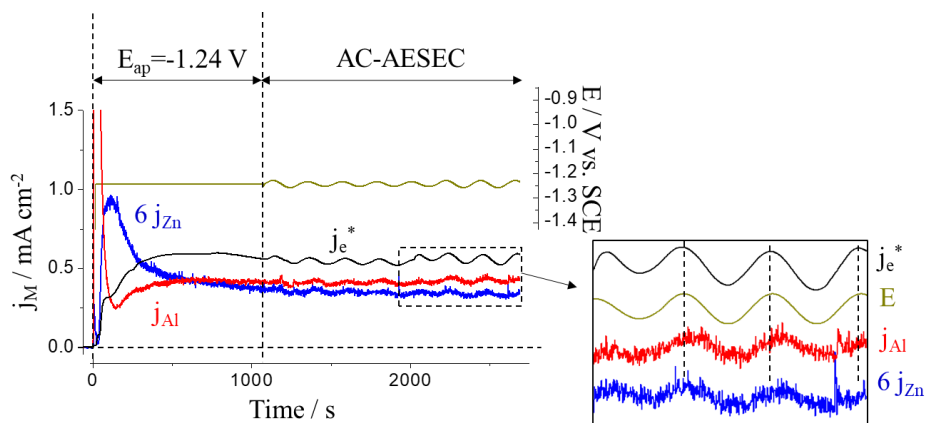
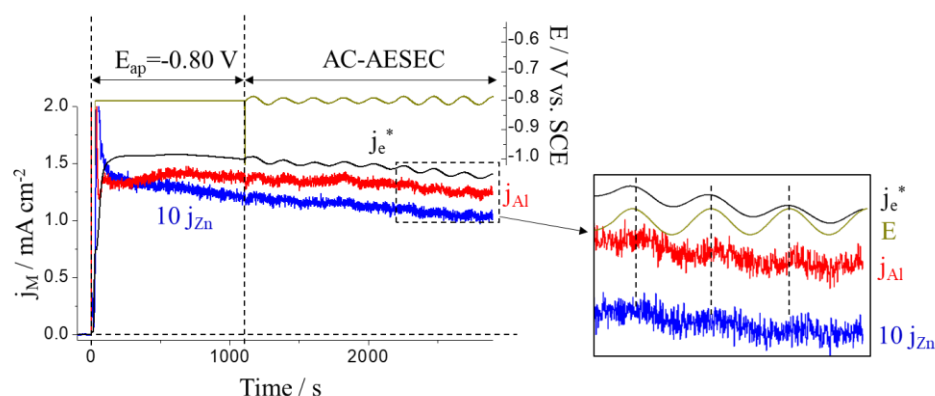


Fig. A1.4. AC-AESEC test for Zn-22Al in pH=12.80, 0.1 M NaOH, Ar deaerated electrolyte. **A:** $E_{AC} = -1.31$ V and **B:** $E_{AC} = -0.82$ V. **C:** the LSV curve taken from Chapter VIII.

Surprisingly, Zn-68Al showed no phase shift between two elements in that all elemental dissolution was in phase as depicted in **Fig. A1.5**. Another hypothesis, potential dependent phase shift can be ruled out because at $E = -1.24$ V from LSV (**Fig. A1.5C**), Al dissolution was decreasing and Zn dissolution was increasing with potential, whereas j_{Zn} and j_{Al} were in phase in the AC-AESEC experiment at this potential (**Figs. A1.5A and A15.B**).

A. $E_{AC} = -1.24$ VB. $E_{AC} = -0.80$ V

C. LSV

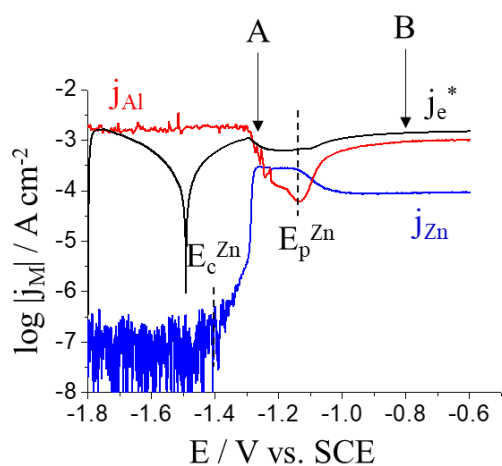
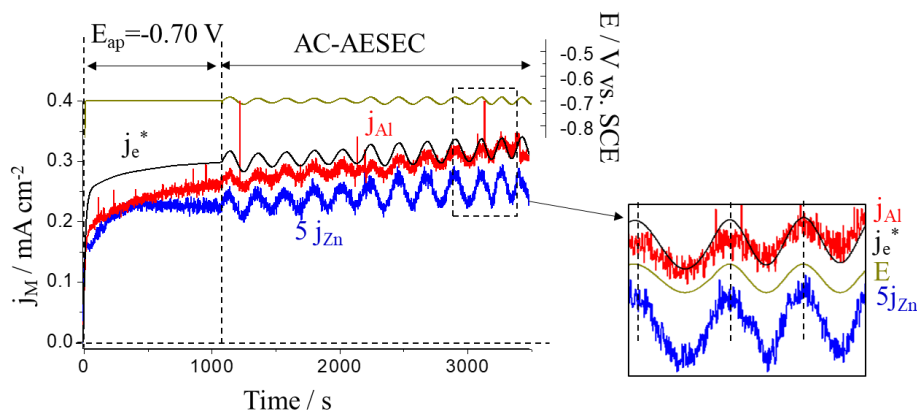


Fig. A1.5. AC-AESEC test for Zn-68Al in pH=12.80, 0.1 M NaOH, Ar deaerated electrolyte. A: $E_{AC} = -1.24$ V and B: $E_{AC} = -0.80$ V. C is the LSV taken from **Chapter VIII**.

A1.3.2. At pH=10.1

Zn-68Al

As only Zn-68Al showed in phase elemental dissolution at pH=12.80, it was also tested in a pH=10.1, chloride containing solution. An anodic potential was chosen for the E_{AC} experiment, shown in **Fig. A1.6**. j_{Al} and j_{Zn} were in phase with the AC, as seen at pH=12.80.

A. $E_{AC} = -0.70$ V

B. LSV

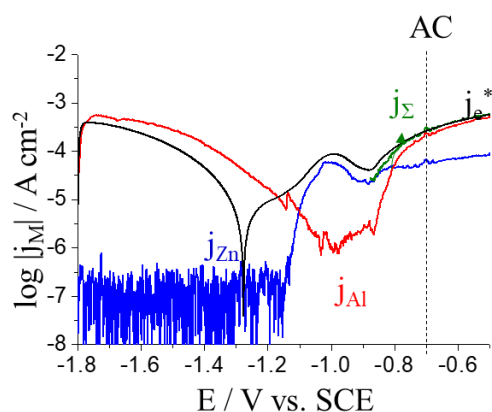
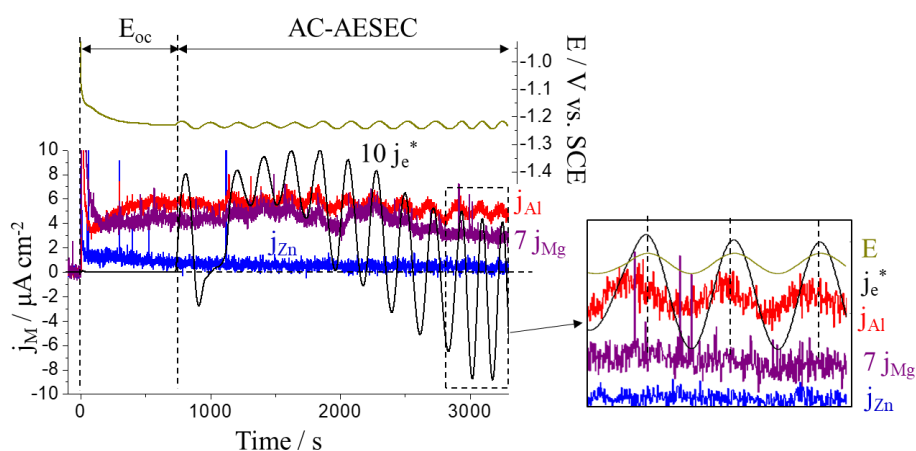
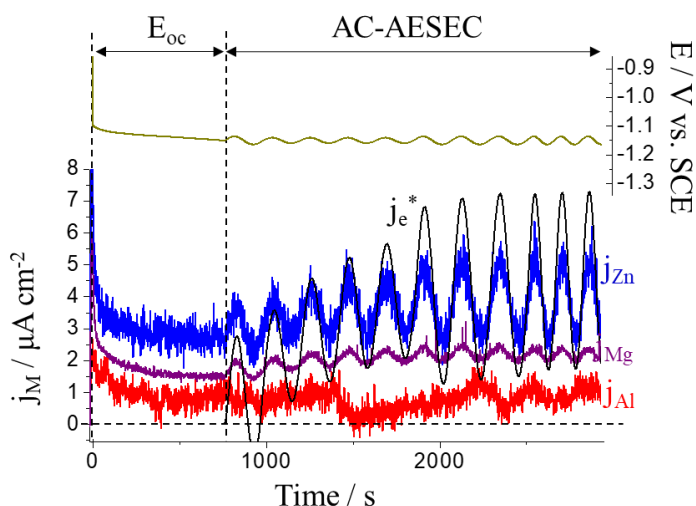


Fig. A1.6. A: AC-AESEEC test for Zn-68Al in pH=12.80, 0.1 M NaOH, Ar deaerated electrolyte. **B:** the LSV curve taken from Chapter VIII.

Zn-Al-Mg alloy coating at E_{oc}

The oscillation of each element in the alloy coating is more complicated in pH=10.1, 30 mM NaCl solution. Cl⁻ in the electrolyte may complicate the surface by forming a complex corrosion film. Two AC-AESEEC test are shown in **Fig. A1.7** at open circuit conditions. The different E_{oc} value may be due to different surface status after the humidity chamber storage. Firstly, at $E_{AC} = E_{oc} = -1.23$ V, both j_{Al} and j_{Mg} were in phase with AC perturbation whereas j_{Zn} was slightly above the detection limit without showing oscillation. At $E_{AC} = E_{oc} = -1.15$ V, however, j_{Zn} and j_{Mg} were in phase with AC while j_{Al} showed no oscillation. These results are coherent with that of the LSV curve in that j_{Zn} was under detection limit at A ($E = -1.23$ V in **Fig. A1.7C**) and j_{Al} dissolution inhibited at B ($E = -1.15$ V in **Fig. A1.7C**).

A. E_{AC} at $E_{oc} = -1.23$ V

B. E_{AC} at $E_{oc} = -1.15$ V

C. LSV

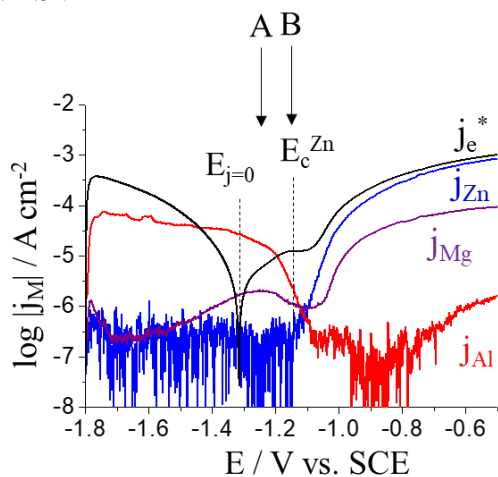


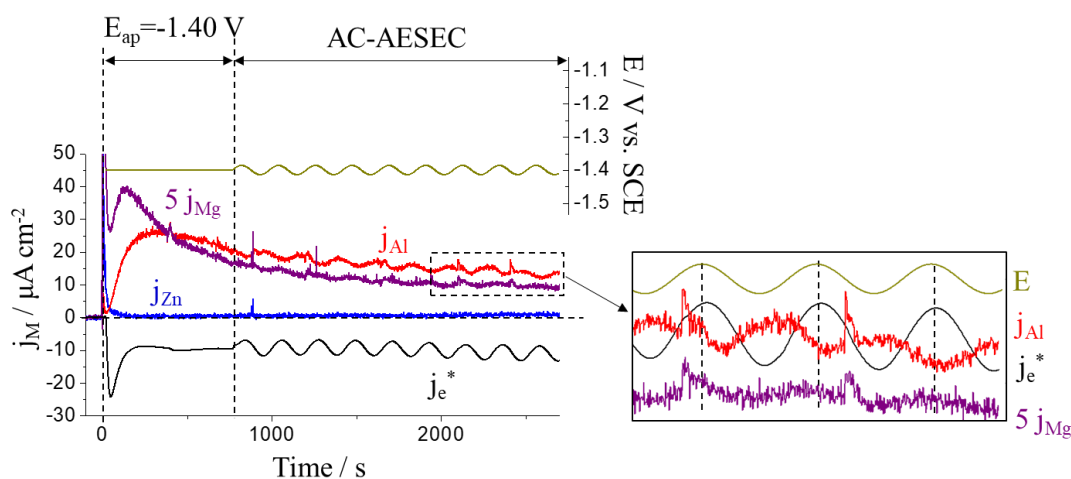
Fig. A1. 7. AC-AESECC for Zn-1.6Al-1.6Mg in pH=10.1, 30 mM NaCl, Ar deaerated electrolyte in two different open circuit potentials. **A:** E_{AC} at $E_{oc} = -1.23$ V and **B:** E_{AC} at $E_{oc} = -1.15$ V. **C:** the LSV curve taken from **Chapter VIII**.

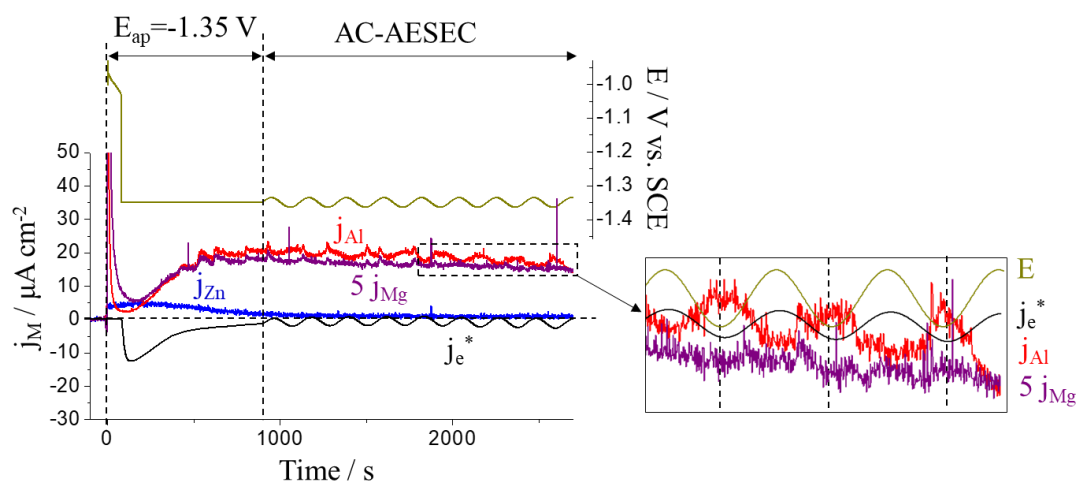
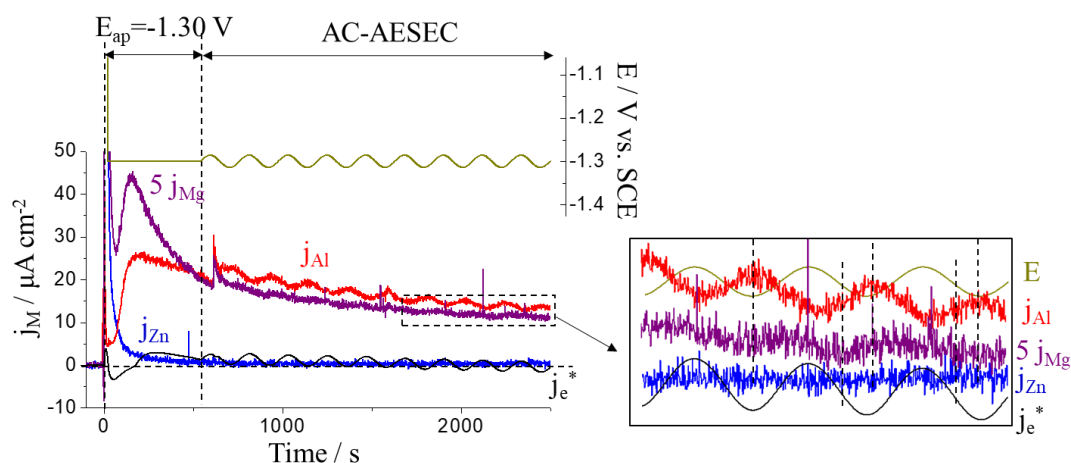
Zn-Al-Mg alloy coating at $E \leq E_{j=0}$

Three potentials for $E \leq E_{j=0}$ were chosen for the AC-AESECC test as shown in **Fig. A1.8**. The elemental dissolution in the E_{ap} period differed from each potential. For $E_{ap} = -1.40$ V and $E_{ap} = -1.30$ V (**Figs. A1.8A** and **A1.8C**), j_{Mg} showed a peak at $t \approx 150$ s then decreased whereas j_{Al} obtained a maximum value. For $E_{ap} = -1.35$ V (**Fig. A1.8B**), Zn dissolution was observed where both j_{Mg} and j_{Al} decreased to a minimum value. As Zn dissolution decreased, j_{Mg} and j_{Al} increased to obtain a steady state. It may indicate that at $E = -1.35$ V, Zn dissolved from $Zn(OH)_2$, possibly formed at this potential, inhibiting Al and Mg dissolution. At $E = -1.30$ V, inhibition of Al and Mg dissolution was not pronounced as $Zn(OH)_2$ readily dissolved.

It is clearly seen that at these E_{AC} , j_{Al} was 180° phase shifted to j_e^* and E , j_{Zn} was essentially under the detection limit, not surprising in the cathodic potential domain. The signal oscillation of j_{Mg} was not clear, however, it was most likely in phase with j_e^* and E opposite to j_{Al} . The unclear oscillation of j_{Mg} as compared to at $E_{oc} = -1.15$ V (**Fig. A1.7B**) can be understood as Mg dissolution at these cathodic potential pulses may occur across the Zn(0) enriched film (**Chapter IV**). The phase shift between j_{Al} and j_{Mg} can be attributed to the potential effect in that j_{Al} was decreasing and j_{Mg} was increasing at this potential range of the LSV curve **Fig. A1.8D**.

A. $E_{AC} = -1.40$ V



B. $E_{AC} = -1.35$ VC. $E_{AC} = -1.30$ V

D

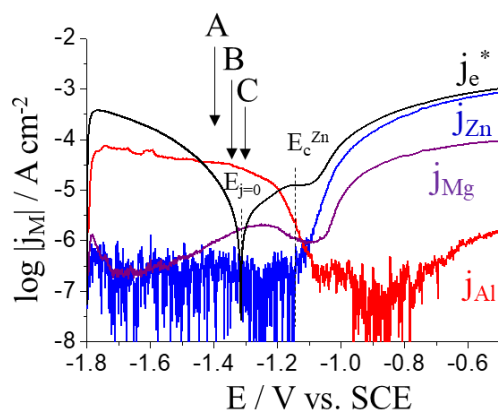


Fig. A1.8. **A:** $E_{AC} = -1.40$ V, **B:** $E_{AC} = -1.35$ V and **C:** $E_{AC} = -1.30$ V at pH=10.1, 30 mM NaCl, Ar deaerated electrolyte. **D:** the LSV curve taken from the **Chapter VIII**.

As the oscillation of the j_{Mg} signal was not clear except for **Fig. A1.7B**, Mg metal at pH=10.1 was also measured in the open circuit dissolution as shown in **Fig. A1.9**. The objective

of measuring pure Mg is to verify whether this ambiguity came from other elements or Mg itself. In this case, an evident j_{Mg} signal oscillation was observed in phase with the AC. Two possible mechanism can be proposed:

1) When Zn dissolved in the alloy, Mg dissolved simultaneously indicating that it was MgZn_2 dissolution as evidenced by in phase j_{Zn} and j_{Mg} in **Fig. A1.7B**.

2) When Zn was not dissolved, whether for the spontaneous condition or in the LSV, Al selectively dissolved forming a $\text{Zn}(0)$ enriched layer. As Mg dissolution occurred across this layer, the oscillation of j_{Mg} was not clear or shifted.

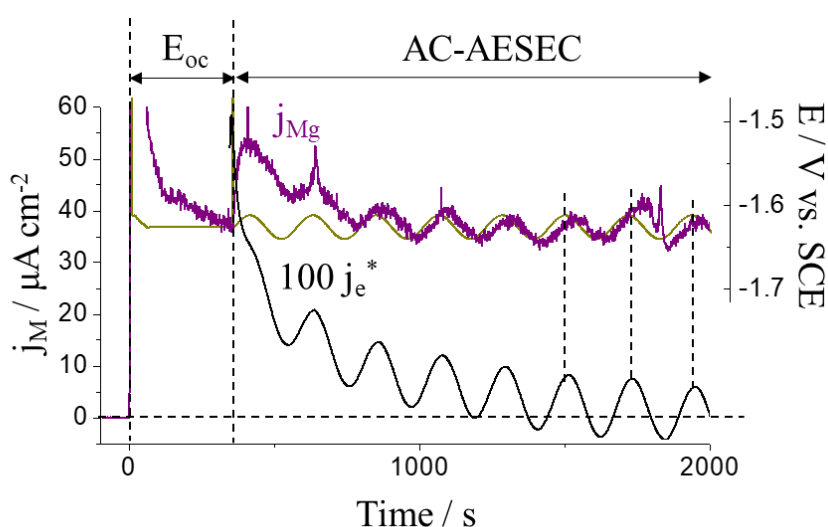


Fig. A1.9. E_{AC} at $E_{\text{oc}} = -1.63$ V of Mg metal at pH=10.1, 30 mM NaCl, Ar deaerated electrolyte.

Mg dissolution across the $\text{Zn}(0)$ film can be further justified by the AC-AESEEC experiment of MgZn_2 phase. At $E_{\text{AC}} = E_{\text{oc}} = -1.16$ V and $E_{\text{AC}} = -1.40$ V are shown in **Fig. A1.10A** and **A1.10B**, respectively. In both cases, no j_{Mg} oscillation was monitored. j_{Zn} was under the detection limit indicating that in these potential domain, $\text{Zn}(0)$ enriched layer formed (**Chapter IV**).

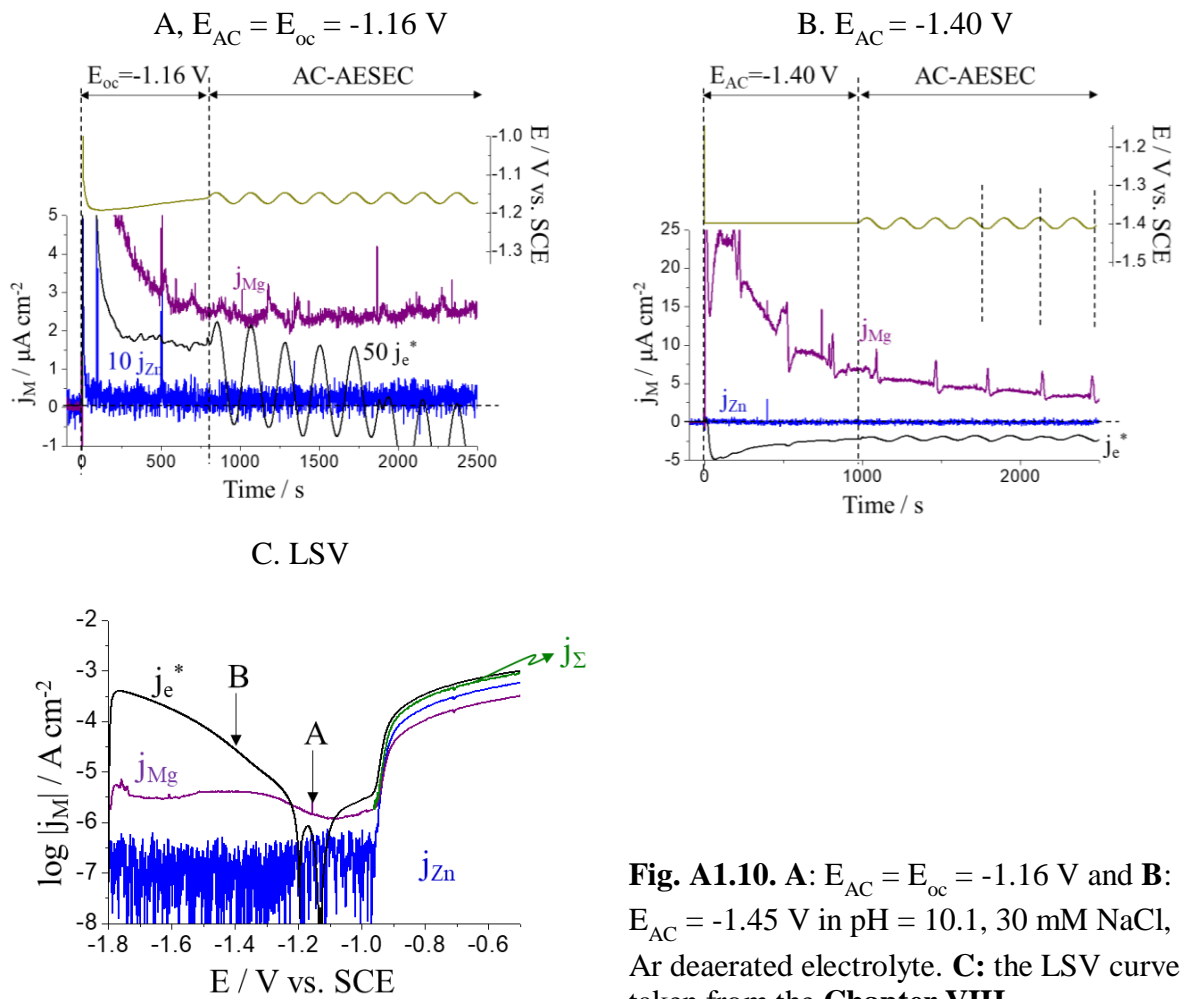
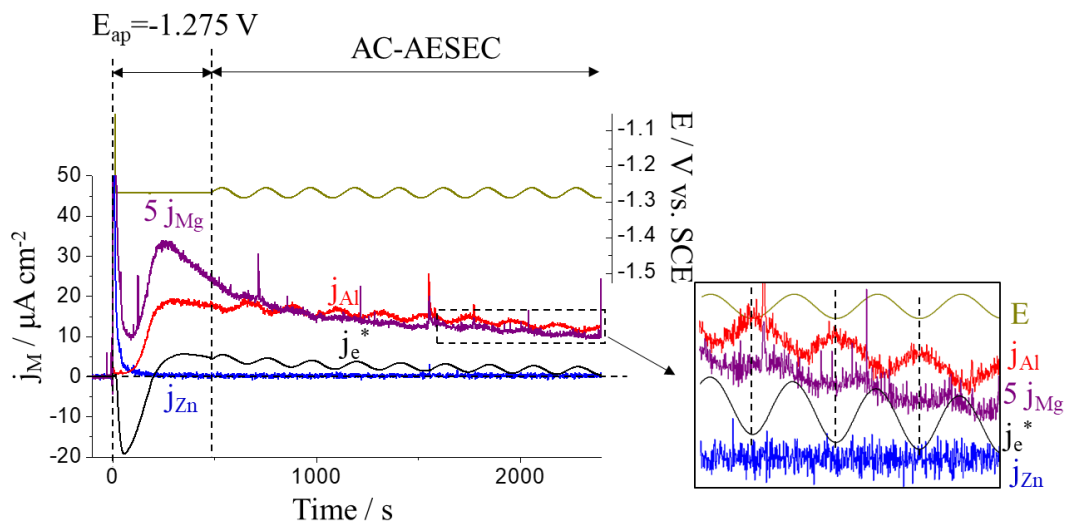


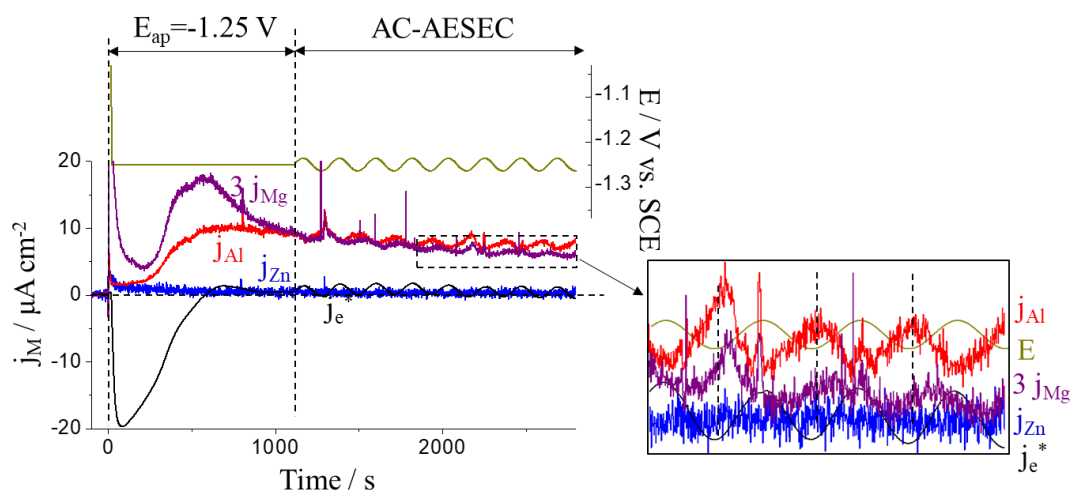
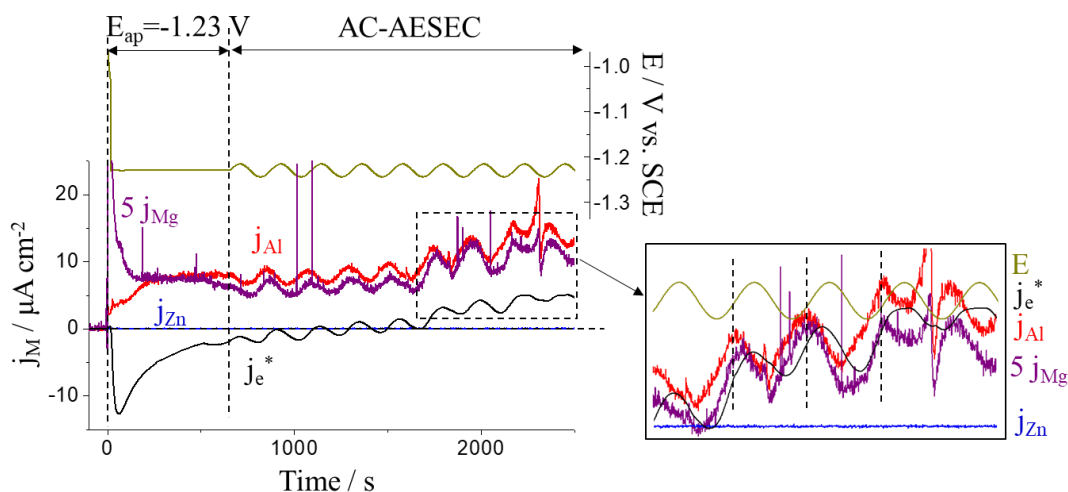
Fig. A1.10. **A:** $E_{AC} = E_{oc} = -1.16$ V and **B:** $E_{AC} = -1.45$ V in pH = 10.1, 30 mM NaCl, Ar deaerated electrolyte. **C:** the LSV curve taken from the **Chapter VIII**.

Zn-Al-Mg alloy coating at $E > E_{j=0}$

AC-AESEEC for the Zn-Al-Mg alloy for $E_{j=0} < E < E_c^{Zn}$ is shown in **Fig. A1.11**.

A. $E_{AC} = -1.275$ V



B. $E_{AC} = -1.25$ VC. $E_{AC} = -1.23$ V

D

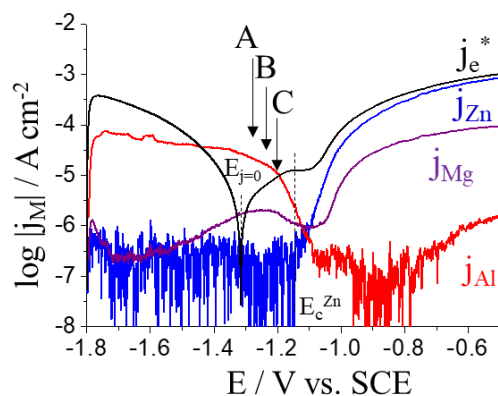


Fig. A1.11. A: $E_{AC} = -1.275$ V, B: $E_{AC} = -1.25$ V and C: $E_{AC} = -1.23$ V at pH=10.1, 30 mM NaCl, Ar deaerated electrolyte. D: the LSV curve taken from the **Chapter VIII**.

At $E_{AC} = -1.275$ V (**Fig. A1.11A**), j_{Al} and j_{Mg} were out of phase as in **Fig. A1.8** for $E \leq E_{j=0}$. However, at more positive potentials (**Figs. A1.11B and A1.11C**), j_{Al} and j_{Mg} were becoming in phase even though j_{Mg} seems to be delayed as compared to j_{Al} signal. This phase shift change

also can be attribute to the Zn(0) enriched layer. For $E_{j=0} < E < E_c^{Zn}$, the Al selective dissolution was less pronounced as compared to that for $E \leq E_{j=0}$, which may mean that the Mg dissolution occurred directly from the alloy, not through the Zn(0) film. Further, this potential domain is sufficiently anodic to make Zn dissolve then form $Zn(OH)_2$ on the surface, not forming the Zn(0) enriched layer.

A1.4. Conclusions and perspectives

- 1) For Zn-5Al and Zn-2.5Al-1.5Mg alloy coatings, j_{Zn} and j_{Al} were out of phase to each other at pH=12.80, 0.1M NaOH without Cl⁻. Pure phases of Zn-Al, however, showed different phase shift. For the Zn-0.7Al and Zn-22Al phases, j_{Zn} and j_{Al} were phase shifted as the alloy coatings. For the Zn-68Al phase, j_{Zn} and j_{Al} were in phase both at Zn active and passive potential domains.
- 2) ‘Cathodic Al dissolution’ driven phase shift can be ruled out because the phase shift between j_{Zn} and j_{Al} was monitored at anodic potential domain for Zn-5Al, Zn-Al-Mg alloys and Zn-22Al phase.
- 3) Potential driven phase shift can also be ruled out by the AC-AESEC results of Zn-68Al in that j_{Zn} and j_{Al} were in phase in the potential domain where j_{Zn} increased and j_{Al} decreased.
- 4) For the Zn-Al-Mg alloy coating, at pH=10.1, j_{Mg} oscillation would be interrupted by the Zn(0) enriched layer limiting Mg dissolution across this film. For $E > E_{j=0}$, j_{Mg} oscillation was observed as the Zn(0) formation was less pronounced.
- 5) The results presented in this chapter introduce an approach of coupling the AESEC and EIS technique. The experimental conditions, such as the exposure time of the electrolyte before the AC potential perturbation, should be carefully chosen because it may change the elemental interaction by forming a passive layer.

A2. Comparison between ICP-AES and ICP-MS

The ICP can be coupled with mass spectroscopy (MS) because the ICP has sufficient energy to generate singly charged ions from the elements. It is different from AES which obtains analytical information from the emitted radiation of atoms/ions. For MS, ions are introduced into a quadrupole mass spectrometer and differentiated in accordance with the mass to charge ratio (m/z) of the element either qualitatively or quantitatively detected. It shows high sensitivity and superior detection limits in ppt level as compared to the AES in ppb level. However, the mass spectra are complicated by mass interference from molecular ions which form in the cooler regions of the plasma (recombination). This leads to significant matrix effects. It is well adapted for use with very dilute solutions, for example $[Cl] < 100$ mM.

The work with ICP-MS was performed in Max-Planck-Institut für Eisenforschung GmbH, Düsseldorf, Germany in August 2017. In order to compare the performance of two techniques, the same experimental condition was used for both measurements. The working electrode was chosen as $MgZn_2$ intermetallic phase (produced by University of Prague) and MagiZincTM alloy coating (Zn-1.6 wt.% Al-1.6 wt.% Mg, Tata steel) with pH=10.1, 30 mM NaCl electrolyte in the presence of O_2 . The experimental details are summarized in **Table A2.1**. ICP-MS has 160 times less flow rate and 130 times less surface area than the ICP-AES system used in this work. The detection limit in this work is defined as 3 times of standard deviation of concentration signal divided by the sensitivity factor, $3C_{\sigma}/\kappa_{\lambda}$, in background measurement where the working electrode was not in contact with the electrolyte. The detection limit of ICP-MS for Zn showed remarkably lower value than that of ICP-AES, more than 100 times less, while those of Al and Mg showed also the detection limits more than 5 times less.

Table A2.1. Comparison of experimental condition and detection limits of elemental dissolution between ICP-MS and ICP-AES.

Exp. Conditions		ICP-MS (MPIE)			ICP-AES (ENSCP)		
Flow rate / $\mu\text{L min}^{-1}$		180			2941		
Surface area / cm^{-2}		0.00785			1		
Electrolyte (30 mM NaCl)		pH=10.1, in the presence of oxygen					
Sample	Exp.	Detection limit (ppb)			Detection limit (ppb)		
		Zn	Al	Mg	Zn	Al	Mg
$MgZn_2$ Zn-1.6Al-1.6Mg	Open circuit, LSV	0.07	0.20	0.07	8.8	1.2	0.4

The system at MPIE uses a capillary electrochemical flow cell as depicted in **Fig. A2.1**. The surface exposed approximately 1 mm diameter which allows for some spatial resolution but is not sufficient to isolate specific regions of the Zn-Al-Mg microstructure.

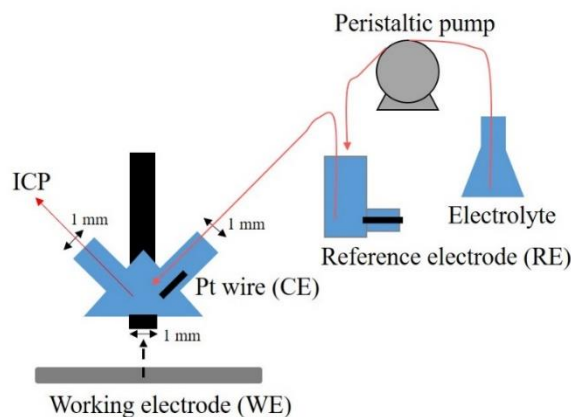


Fig. A2.1. Schematic description of ICP-MS capillary system.

A2.1. Open circuit dissolution

The open circuit dissolution of the Zn-1.6Al-1.6Mg alloy coating is shown in **Fig. A2.2** both for ICP-MS and ICP-AES. The elemental dissolutions of Al, Mg and Zn are expressed in concentration as a function of time. At $t < 0$, the electrode was not in contact with electrolyte, measuring background signals. In MS, the potential signal of initial stage during approximately 30 s could not be measured when the sample was approaching to the capillary. This signal loss cannot be avoided in the current system as this process should be done manually. Nevertheless, the open circuit values were the same at $E_{oc} = -0.98$ V. It is clear that the detection limit of Zn was markedly lower in MS as compared to that in AES.

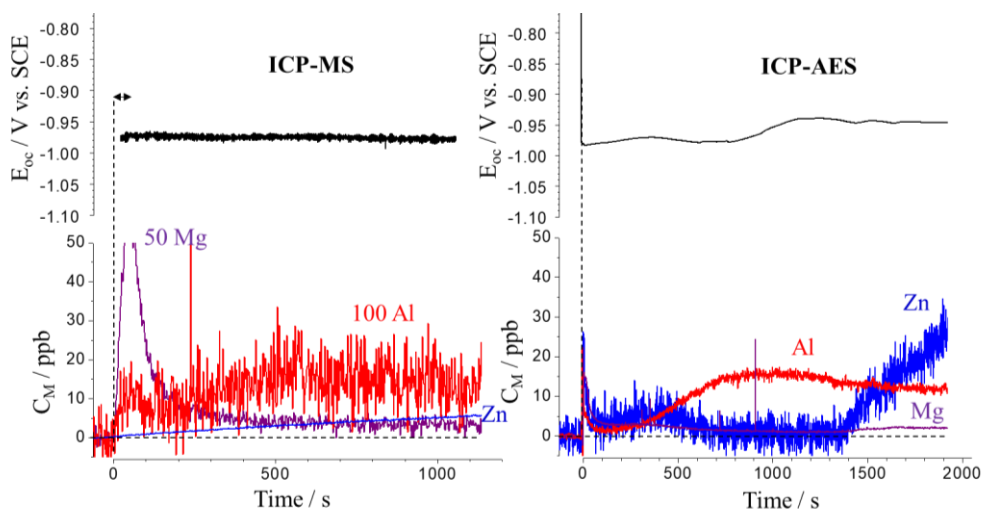


Fig. A2.2. Spontaneous elemental dissolution of Al, Mg and Zn of Zn-1.6Al-1.6Mg alloy coating in pH=10.1, 30 mM NaCl electrolyte measured by ICP-MS and ICP-AES.

A2.2. Elemental linear sweep voltammetry experiments

AESEC-linear sweep voltammetry (AESEC-LSV) experiment of MgZn_2 intermetallic phase was conducted in the same electrolyte condition as in **Fig. A2.3**. The potential was swept from -1.80 V in the anodic direction with 0.5 mV s^{-1} scan rate. The elemental dissolution signals of Mg and Zn are expressed in current density to facilitate the comparison with j_e^* .

Current ICP-MS setup showed a problem of the electronics in that the first potentiodynamic signal switched from the open circuit condition, was increased to an upper limit value probably due to the mode change of the system. Therefore, the initial part of the polarization curve, marked as 'a' in **Fig. A2.3**, data obtained in this potential range cannot be a real one. Furthermore, the unexpected increase in elemental current densities would have an effect on the rest of the potential sweep due to the decaying signals. That would be the reason why j_{Zn} in MS is almost two orders magnitude higher than that in AES. When the potential increased above -0.86 V and -0.88 V respectively, at the onset potential of MgZn_2 , the j_{Mg} and j_{Zn} signals increased considerably caused by simultaneous dissolution. In MS, because of the systematical problem, the intensity signal above 2,000,000 / a.u. cannot be measured marked as region 'b'. Therefore, it was not possible to continue measuring above a certain potential value. Nevertheless, the comparison between these two techniques showed a meaningful result in that the onset potential of simultaneous Mg and Zn dissolution were nearly the same.

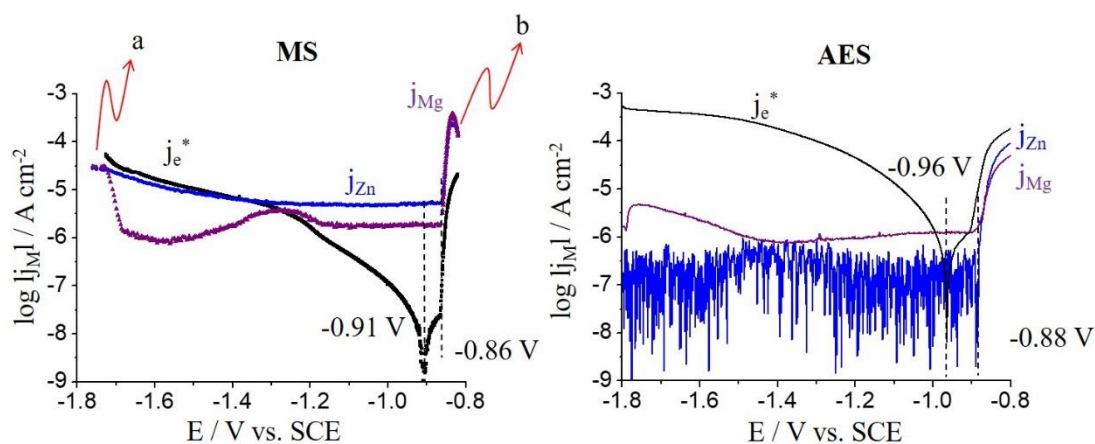


Fig. A2.4. AESEC-LSV results of the MgZn_2 intermetallic pure phase in $\text{pH}=10.1$, 30 mM NaCl electrolyte with the scan rate of 0.5 mV s^{-1} measured by ICP-MS and ICP-AES.

A2.3. Residence time distribution

Residence time dissolution experiment of ICP-MS was conducted in order to compare it with ICP-AES. Since the flow rate and the reaction surface value are lower than ICP-AES, diluted 0.1 mM HCl was used applying reduced galvanostatic pulse, 0.1 mA, during 1 s. **Fig A2.4** shows the residence time dissolution of Cu in log-time scale. Two things are remarkably different from ICP-AES. Firstly, the signal did not fit the log-normal distribution trend as well as in ICP-AES, in that the experimental Cu signals (I_{Cu}) and curve fitting by software ($I_{\text{Cu}}^{\text{fit}}$) were not superimposed perfectly. Secondly, the time needed to reach a peak maximum, $\tau = 38.9 \pm 1.2$ s, was markedly longer than ICP-AES (11 s) probably indicating that the migration time of element in ICP-MS takes longer time than ICP-AES.

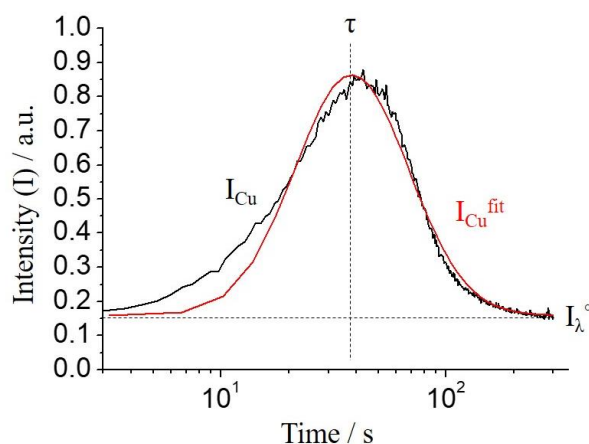


Fig. A2.4. Log-normal distribution of experiment of Cu dissolution (I_{Cu}) and numerical curve fitting by OriginTM software ($I_{\text{Cu}}^{\text{fit}}$) as a function of time measured by ICP-MS. τ is the time when the Cu signal reaches the maximum value. I_{λ}° is background Cu signal.

A3. Bi-electrode analysis

A3.1 Introduction

It was shown in this Ph.D. dissertation in **Chapter VII** that all Zn-Al system showed an inhibitive effect of Zn dissolution on Al dissolution. These results are consistent with previous studies [13,93,186]. It was commonly observed that for the AESEC-LSV experiments in **Chapter VIII**, when Zn dissolution was activated at E_c^{Zn} , Al dissolution rate decreased to reach its minimum level. This effect was attributed to Zn corrosion products formed during the Zn active potential domain inhibited the Al dissolution [187,188]. It was concluded that Zn^{2+} may precipitate on the entire surface, physically blocking the active Al sites. It was also suggested that once the Zn-rich phase is oxidized to form Zn^{2+} , these ions consume OH^- in the electrolyte making the local pH near Al lower, resulting in a decrease in Al solubility. Further, Al_2O_3 passive film could be formed on the Al-rich phase caused by the lowered interfacial pH. To elucidate the interaction of different elements, a bi-electrode made of Zn and Al metals was constructed in the dissertation of Vu [186]. He observed that Zn dissolution from the Zn/Al bi-electrode was not altered from pure Zn while Al dissolution was systematically inhibited at the Zn active domain.

In this chapter, the same bi-electrode was tested in different electrolyte conditions; at pH=8.4, 10.1 and 12.80. Further, three bi-electrode configurations were examined; I) Al to Zn, II) Zn to Al and III) Zn/Al in parallel, in order to distinguish which ion affected to the elemental dissolution inhibition.

A3.2. Experimental

A schematic image of bi-electrode design is given in **Fig. A3.1**. 99.99 % Zn and 99.99 % Al rods were provided by *Goodfellow*. Zn and Al rods were positioned in an epoxy resin with 1 mm distance. Each metal rods were welded by Cu wires enabling electrical contact with or without coupling to each other.

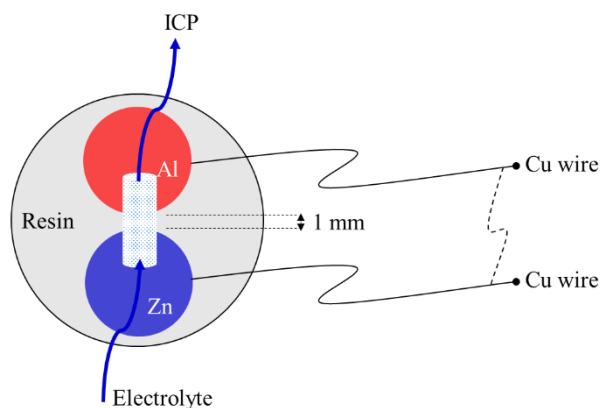


Fig. A3.1. Schematic image of bi-electrode of Zn and Al metals.

In this work, three configurations of the bi-electrode were tested; I) Al to Zn, II) Zn to Al and III) Zn/Al in parallel as depicted in **Fig. A3.2**. The objective of changing configuration is to differentiate the effect of one cation to the other. Three different pH electrolyte conditions chosen so as to facilitate comparison with pure metals, other pure phases and alloy coatings used in this Ph.D. project; pH=8.4 (30 mM NaCl), pH=10.1 (30 mM NaCl) and pH=12.80 (0.1 M NaOH). All experiments were performed in Ar deaerated electrolyte.

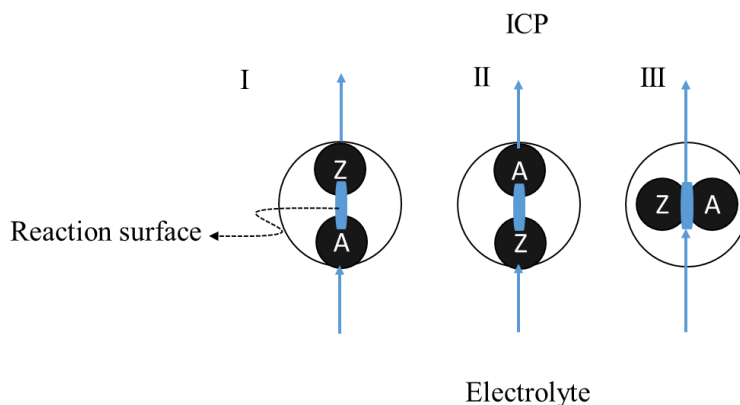


Fig. A3.2. Three configuration of the bi-electrode; I) Al to Zn, II) Zn to Al and III) Zn/Al in parallel.

A3.3. Results and discussions

pH=8.4

Spontaneous dissolution of the bi-electrode in a pH=8.4, 30 mM NaCl, Ar deaerated electrolyte is shown in **Fig. A3.3**. In the configuration I, j_{Al} was under the detection limit whereas for the II and III, discernable Al dissolution was measured. In the **Chapter VIII**, spontaneous Al dissolution was measured at $j_{Al}^s = 2.3 \pm 0.1 \mu A cm^{-2}$ in the same electrolyte condition. Therefore, it can be concluded that Al dissolution in the configuration I would be

restrained by Zn dissolution. It is interesting to note that the $E_{oc} \approx -1.00$ V, reasonably the same as Zn metal (E_{oc} Zn metal: -1.00 V, E_{oc} Al metal: -1.20 V, from **Chapter VIII**).

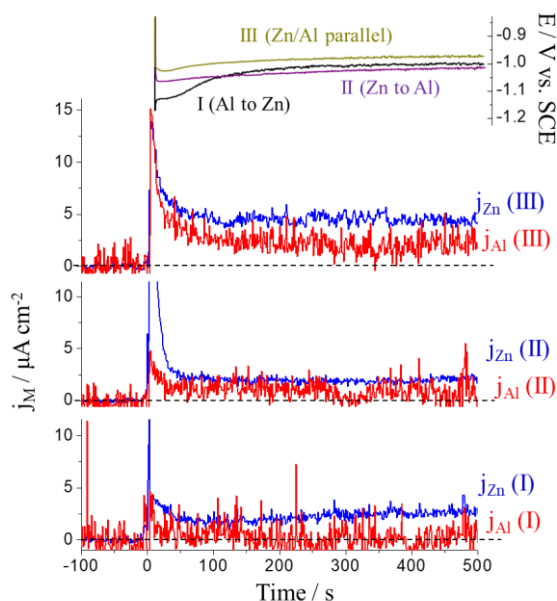
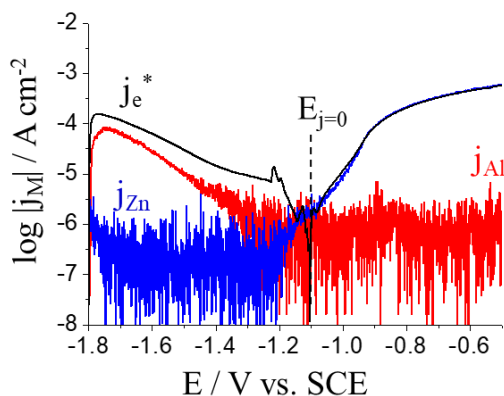


Fig. A3.3. Spontaneous dissolution of the bi-electrode of Zn and Al metal; I) Al to Zn, II) Zn to Al and III) Zn/Al in parallel configurations in pH=8.4, 30 mM NaCl, Ar deaerated electrolyte.

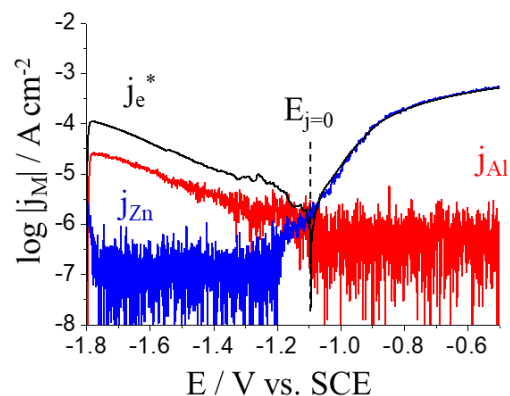
AESEC-LSV of the bi-electrode in a pH=8.4, 30 mM NaCl, Ar deaerated electrolyte is shown in **Fig. A3.4**. In all three cases, j_{Zn} vs. E was analogous to that for pure metal (**Chapter VIII**). Al dissolution, however, seemed to be altered especially in the anodic potential domain as compared to that of pure metal. For pure Al (**Chapter VIII**), a transpassive Al dissolution was observed for $E > -0.7$ V whereas in the bi-electrodes, j_{Al} was under the detection limit for $E > E_{j=0}$. It may be due to the inhibited Al dissolution by the dissolved Zn cations, regardless of the sample configuration, probably caused by the hydrodynamic effect of the electrolyte [75] mixing up cations between top and bottom sides of the reaction surface. Cathodic Al dissolution for all three cases was exponentially proportional to cathodic current density, indicating Al dissolved in the cathodic domain as;



I. Al to Zn



II. Zn to Al



III. Zn/Al in parallel

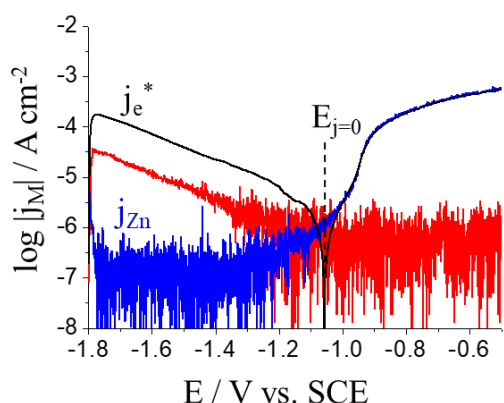


Fig. A3.4. AESEC-LSV of the bi-electrode of Zn and Al metal; I) Al to Zn, II) Zn to Al and III) Zn/Al in parallel configurations in pH=8.4, 30 mM NaCl, Ar deaerated electrolyte.

pH=10.1

Spontaneous dissolution of the bi-electrode in a pH=10.1, 30 mM NaCl, Ar deaerated electrolyte is shown in **Fig. A3. 5**. Two configurations showed totally different results. As $j_{Al}^s = 20.7 \pm 0.2 \mu\text{A cm}^{-2}$ and $j_{Zn}^s = 0.7 \pm 0.6 \mu\text{A cm}^{-2}$ for pure metals (**Chapter VIII**), it is clear that Al and Zn dissolution were not altered by the bi-electrode for the configuration I. However, increased j_{Zn} may be correlated to a reduction in j_{Al} for the configuration II. Unlike at pH = 8.4, the E_{oc} was varied depending on the electrode configuration. In both cases, E_{oc} was measured between those of pure metals, $E_{oc} = -0.98 \text{ V}$ (Zn metal) and -1.44 V (Al metal). For the I, E_{oc} was closer to that of Zn metal whereas for the II, E_{oc} was more close to that of Al metal. This may indicate that metal positioned at the upper side of the bi-electrode would react more efficiently with the electrolyte than the electrode at the bottom, again because of the hydrodynamics of the electrolyte in the flow cell.

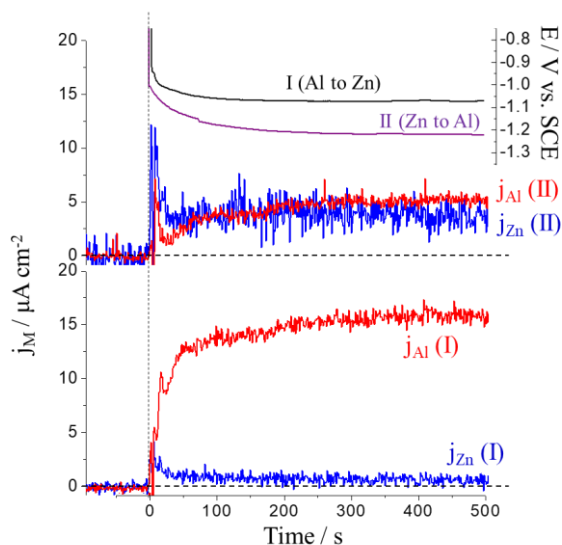


Fig. A3.5. Spontaneous dissolution of the bi-electrode of Zn and Al metal; I) Al to Zn and II) Zn to Al configurations in pH=10.1, 30 mM NaCl, Ar deaerated electrolyte.

AESEC-LSV of the bi-electrode in a pH=10.1, 30 mM NaCl, Ar deaerated electrolyte is shown in **Fig. A3.6**. A clear inhibitive effect of Zn dissolution to Al was observed for the I above the onset potential of Zn dissolution (E_c^{Zn}) whereas for the II, Al dissolution decreased with potential without showing a clear inhibition. For both cases, again, transpassive Al dissolution was not observed. Given the fact that the inhibitive effect of Zn to Al dissolution was different from spontaneous dissolution and the LSV, this inhibitive effect may be affected by the potential driven Zn-O/-OH formation/dissolution. It should be noted that for the I, the Al dissolution was nearly potential independent in the cathodic potential domain, $j_{Al} \approx 31.6 \mu A cm^{-2}$, different from at pH=8.4. It may mean that the cathodic reaction (water reduction) on the Zn surface supplied continuous OH^- in the vicinity of Al surface, making local pH more alkaline than pH=10.1, resulting in potential independent Al dissolution.

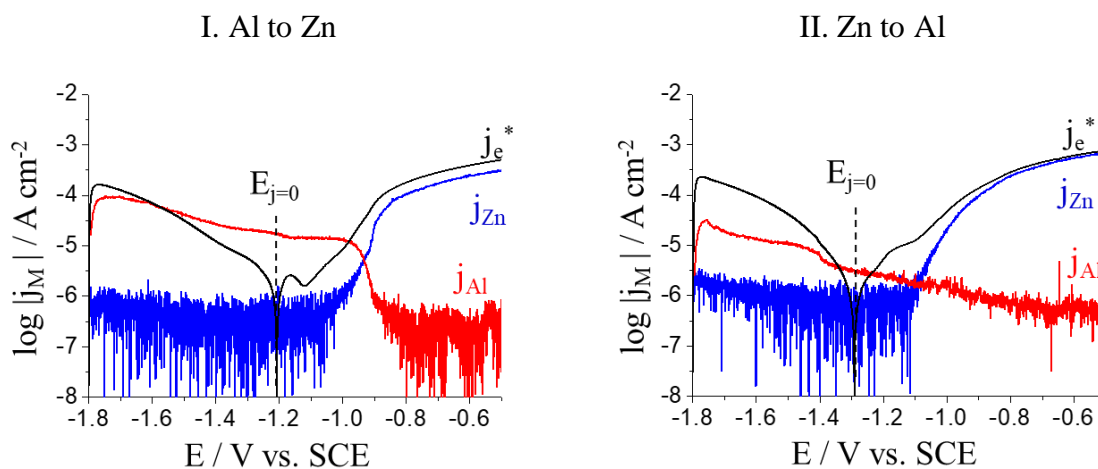


Fig. A3.6. AESEC-LSV of the bi-electrode of Zn and Al metal; I) Al to Zn and II) Zn to Al configurations in pH=10.1, 30 mM NaCl, Ar deaerated electrolyte.

$pH=12.80$

Spontaneous dissolution of the bi-electrode in a $pH=12.8$, 0.1 M NaOH , Ar deaerated electrolyte is shown in **Fig. A3.7**. For the I, perturbation signal of Al dissolution, $\sigma_{j_{Al}}$ was not observed whereas for the II, $\sigma_{j_{Al}}$ was clearly monitored. This indicates that for the II, Al dissolved coupled with water reduction forming H_2 bubbles whereas for the I, Al dissolution might occur across the Zn-O/-OH film could be formed on the Al surface.

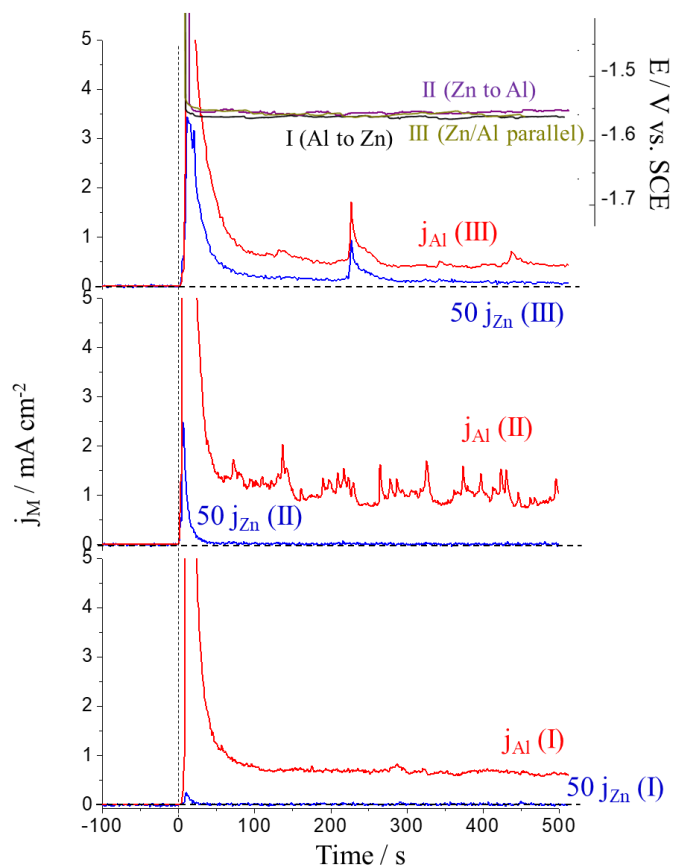


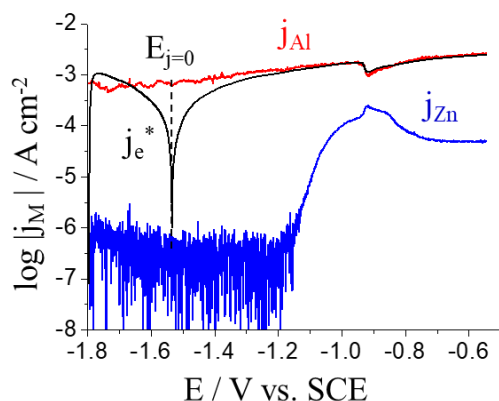
Fig. A3.7. Spontaneous dissolution of the bi-electrode of Zn and Al metal; I) Al to Zn and II) Zn to Al configurations in $pH=12.8$, 0.1 M NaOH , Ar deaerated electrolyte.

AESEC-LSV of the bi-electrode in a $pH=12.8$, 0.1 M NaOH , Ar deaerated electrolyte is shown in **Fig. A3.8**. For the I, it is clearly seen that at the j_{Zn} maximum, $E \approx -0.90\text{ V}$, an increase of j_{Zn} was correlated to a drop in j_{Al} , as observed for the alloys and pure phases in the previous chapters. For the II and III, however, this inhibitive effect was not observed. This may be understood as a relatively large amount of ZnO was detached from the Zn surface at $E \approx -0.90\text{ V}$, dissolved as;

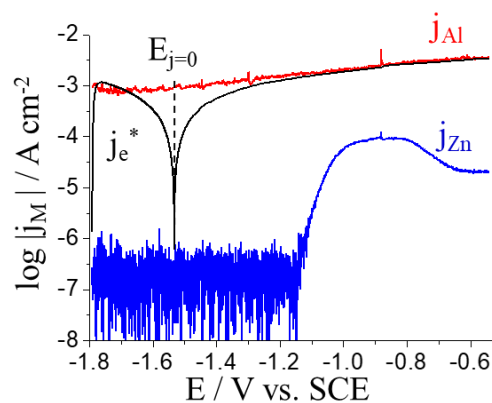


may lead lower local pH.

I. Al to Zn



II. Zn to Al



III. Zn/Al in parallel

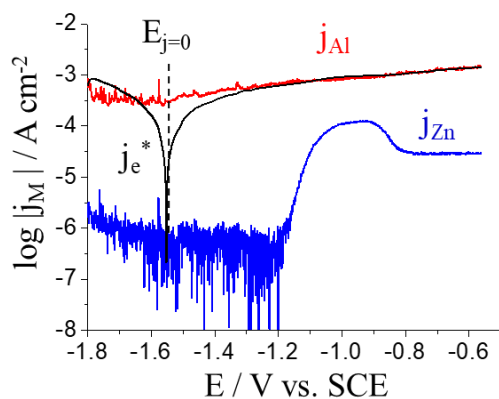


Fig. A3.8. AESEC-LSV of the bi-electrode of Zn and Al metal; I) Al to Zn, II) Zn to Al and III) Zn/Al in parallel configurations in pH=12.80, 0.1 M NaOH, Ar deaerated electrolyte.

A3.3. Conclusions and perspectives

1) Al dissolution rate at pH=8.4 in the cathodic potential domain was proportional to the cathodic current density. This may indicate that Zn had no inhibitive effect in the cathodic domain in the slightly neutral electrolyte.

2) At pH=10.1, in the spontaneous dissolution, Al dissolution inhibition was observed for the configuration II (Zn to Al) while not for the configuration I (Al to Zn). Opposite result was obtained for the LSV experiment in that Al dissolution rate was significantly reduced at E_c^{Zn} where Zn dissolution initiated for the I. For the II, it was not clear to see the inhibitive effect for the LSV experiment. Surface pH might play a role because a potential independent Al dissolution was observed for $E < E_c^{Zn}$ for the I, probably due to H_2O reduction on the Zn surface.

3) For the II at pH=12.80, a clear H_2 bubble formation was found for the spontaneous dissolution as evidenced by increased $\sigma_{j_{Al}}$.

4) The cell design has an inevitable limitation in that the exact reaction surface is not easy to define precisely. A new design of the bi-electrode will be constructed controlling the reaction surface. Also, the effect of hydrodynamics in the flow cell will be verified by decoupling Al and Zn. Other combinations of the elements, such as Mg-Zn bi-electrode can be designed to compare them with the electrochemical response of Mg-Zn pure phases.

A4. Comparison of surface preparation methods for Zn-5Al commercial alloy coatings.

Abstract

In this chapter, conventional surface preparation methods for Zn based alloy coatings were compared from acid to alkaline pH for laboratory level corrosion studies. The stability, reproducibility and predictability of Zn-5 wt.% Al alloy coating (GalfanTM) were investigated by the atomic emission spectroelectrochemistry (AESEC) technique in chloride containing electrolyte. A series of surface preparation methods such as alkaline/acid etching, physical abrasion, Nital and emery paper/humidity chamber storage were tested. Coating composition was changed when the surface was chemically treated and showed unpredictable elemental dissolution behavior. Physical grinding also changed the coating composition showing unstable spontaneous dissolution. Nital made the surface passive resulting in accumulation of Zn/Al corrosion species on the sample surface. Stored in the humidity showed reproducible elemental dissolution behavior as compared to other surface preparation methods. This work can give a general idea of how to prepare Zn-Al and other Zn based alloy coatings for the laboratory experiments.

Keywords: surface preparation, alloy, Zn, Al

A4.1. Introduction

Zn based coating alloys have been widely used for the protection of a steel substrate from corrosion. Zn oxide/hydroxide species can play an important role in that under certain circumstances, they can create a physical barrier preventing further Zn corrosion. On the Zn coating, various type of oxides, hydroxides and carbonates can be formed not only when it contacts with aqueous solution but also in atmospheric condition [18,19,22,33,80,82,109,124,166,167]. Efforts have been made to understand the properties of these surface species such as ZnO, Zn(OH)₂, hydrozincite (HZ) and simonkolleite (Zn₅(OH)₈(Cl₂)·H₂O). Simonkolleite and hydrozincite have significantly different properties from each other and from ZnO/Zn(OH)₂ in terms of isoelectric point and wettability [138]. Therefore, different compositions of surface oxide may have great influence on the surface electrochemical properties.

The effect of surface preparation of Zn and Al-Zn coating alloys was investigated by different authors. Azmat et al. [138] tried to find the suitable pre-treatment method for Zn coating surface by using droplet profiles and SEM. They concluded that Zn surfaces pre-treated with diamond particles of size 9, 6, 3 and 1 μm showed the most stable, hydrophobic and contamination free Zn surfaces covered by thin natural ZnO. Gentile et al. [189] investigated the influences of pre-treatment on the composition of Al-Zn alloys by scanning transmission electron microscopies (STEM), glow discharge-optical emission spectroscopy (GD-OES) and ion beam analysis. It was concluded that by alkaline etching, Zn species were enriched on the surface depending on the alloy composition and topography. **Table A4.1** summarizes different surface preparation method conducted for Zn or Zn based alloys.

For the Zn-Al commercial alloys, various types of surface preparation methods have been suggested. Depending on applications of the final product, surface preparation method of electropolishing, physical abrasion, alkaline and acid etching can be applied. However, comparison of surface preparation methods in different electrolyte conditions has not been thoroughly studied. Further, it has never been standardized because it is not easy to quantify the effect of surface preparation. Therefore, it is of interest to find a proper surface preparation method to maintain homogenous, reproducible, predictable and stable surface condition for the Zn-based alloy coatings. To this end, atomic emission spectroelectrochemistry (AESEC) technique is used to analyze the spontaneous elemental dissolution behavior of Al and Zn in

Appendix 4. Comparison of surface preparation of Zn-Al alloy coating

different surface preparation methods. Simultaneously, open circuit potential (E_{oc}) was recorded to show stability of the surface. The intensity of initial transient and time needed to obtain a steady state were monitored.

Table A4.1. List of different surface preparation methods for Zn-based alloy coatings.

	References	Sample	
Alkaline etching	Berger et al. [137]	HDG	Ultrasonic bath in acetone and methanol during 2 min. Ytex 4324 (2% aqueous KOH with surfactant, pH=12.8) under agitation. Rinsed by water and dried with N ₂ gas.
	Fink et al. [136]	HDG	Ultrasonic bath in tetrahydrofuran (THF), iso-propanol and ethanol consecutively during 10 min each. Immersion in 30 g/L Ridoline 1570, 3 g/L Ridosol (Henkel KGaA) heating to 55 °C during 30 s. Rinsed by water and dried with N ₂ gas.
	Xi et al. [190]	HDG	Brushing in warm aqueous alkali solution. Rinsed with H ₂ O, immersed in supersonic ethanol bath.
Physical abrasion	Azmat et al. [138]	99.96 % Zn	Mechanical wet grinding with Si-C paper (P800, 1000, 2400 and 4000)
	Nelson et al. [191]	HDG	Sanding, sand-blasting, and wire-brushing
	Zhang et al. [107]	Zn-5Al	Ultrasonic bath with ethanol and dried by cold N ₂ in a desiccator during overnight. Ground by 0.25 μm diamond paste.
Humidity	Stouilil et al. [33]	ZnAl, ZnAlMg	Degreased with acetone, ground with P1200, 2500 emery paper. Pre-exposed in air at 50 % RH (20 °C) for 24h.
Nital	Sullivan et al. [21]	ZnAlMg	Physical abrasion with 1 μm emery cloth and diamond slurry. Etching with 1% Nital.
Acid etching	Zhang et al. [192]	Pure Zn sheet	Polished with 1 μm diamond grains. Ultrasonic bath in acetone and ethanol during 2 min. Dipped in 0.25 nitric acid for 10 s.
	Azevedo et al. [35]	HDG, ZnAlMg	1 M HCl wash directly to the sample during 5 s.

A4.2. Experimental

Surface preparation methods

Spontaneous elemental dissolution of commercial Zn-5Al alloy (Galfan™) supplied by *ArcelorMittal* was measured by the AESEC. A commercial Zn-Al-Mg alloy of Zn-1.6Al-1.6Mg (MagiZinc™) coating supplied by *Tata steel* was also tested. Prior to measurement, each sample was degreased by ethanol then dried by N₂ gas. Three pH values were chosen, pH = 2.0, 6.0 and 12.8 representing acid, neutral and alkaline media. 100 mM NaCl solution was added to solution for pH = 2.0 and 6.0 adjusting pH by analytical grade of NaOH, HCl and deionized water via Milipore™ system (18.2 MΩ cm). Electrolyte was deaerated by Ar gas around 10–15 minutes before and during all the experiment in order to separate the effect of CO₂ and O₂ in ambient air that could change interfacial condition and pH.

Commonly used surface preparation methods for industrial alloys are summarized in **Table A4.2** and detailed procedure is described as follows:

- (a) As received: In order to compare it with other methods as a reference (non-prepared).
- (b) Alkaline etching: Immersing in 0.1 M NaOH solution during 5 minutes at room temperature (25°C).
- (c) Physical abrasion: Grinding with ethanol using Si-C emery paper (P2400 and P4000).
- (d) Acid etching: Immersing in 1 M HCl solution for 5 seconds at room temperature.
- (e) 1 wt.% Nital: Dipped in 1 wt.% Nital (ethanol and nitric acid) for 1 minute.
- (f) Humidity chamber: Firstly ground by emery paper as (C) then stored in a humidity chamber maintained 50 % relative humidity (RH) saturated with Mg (NO₃)₂·H₂O for around 24 hours.

Table A4.2. List of surface preparation methods.

Methods	Name	Description
(a)	Non prepared	As received surface.
(b)	Alkaline etching	Dipped in 0.1M NaOH for 5 minutes.
(c)	Physical abrasion	Emery paper (Si-C) grinding, P2400/P400.
(d)	Acid etching	Dipped in 1M HCl for 5 seconds.
(e)	1 wt.% Nital	Dipped in 1 wt.% Nital for 1 minute.
(f)	Humidity chamber	Stored in a humidity chamber (50 % relative humidity) for 20-24 hours after being ground by emery paper.

AESEC technique

The elemental dissolution rate was calculated by the emission intensity of Zn and Al in the plasma monitored at 213.86 and 167.08 nm respectively. The AESEC technique was used to measure electrochemical response of Zn and Al at the open circuit condition which reflects the free corrosion behavior of the system. The open circuit potential (E_{oc}) and the elemental dissolution rates were measured for approximately 20 minutes.

Surface characterization

Surface characterization was performed after each surface preparation method by scanning electron microscopy coupled with energy dispersive X-ray (SEM-EDX) spectroscopy, using a Gemini 1530 microscope with field emission gun (FEG) source at 15 keV, Si(Li) detector for EDX and QUANTAX software (Bruker AXS).

A4.3. Results

A4.3.1. At pH=12.80

Fig. A4.1 shows the E_{oc} trend of Zn-5Al for each surface preparation method as a function of time in 100 mM NaOH at pH=12.80, Ar deaerated electrolyte. For **Fig. A4.1(b)**, (c) and (d), the E_{oc} obtained a steady state value hundreds of seconds after the electrolyte exposure. Nitral treatment showed a passivating effect as the E_{oc} value increased throughout the open circuit exposure shown in **Fig. A4.1(e)** corresponding to previously observed passivating effect due to nitric acid for Zn-based alloy coatings and the stainless steel [43,104]. The E_{oc} for humidity chamber (**Fig. A4.1(f)**) decreased to its steady state value during the first 100 s similar to that of **Fig. A4.1(a)**. This may indicate that the surface after emery paper grinding would stabilize during storage in the humidity chamber. Further, **Fig. A4.1(f)** shows the lowest E_{oc} value among others demonstrating that the pre-existed oxide film would be successfully removed and did not form during storage.

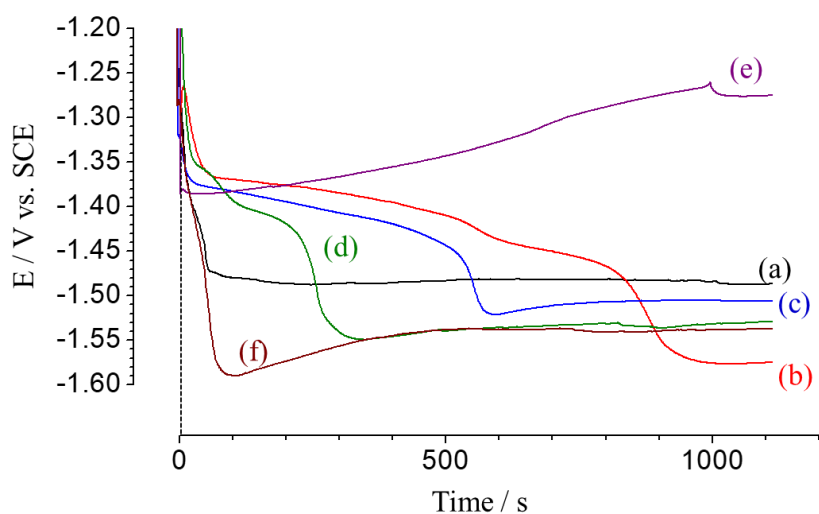
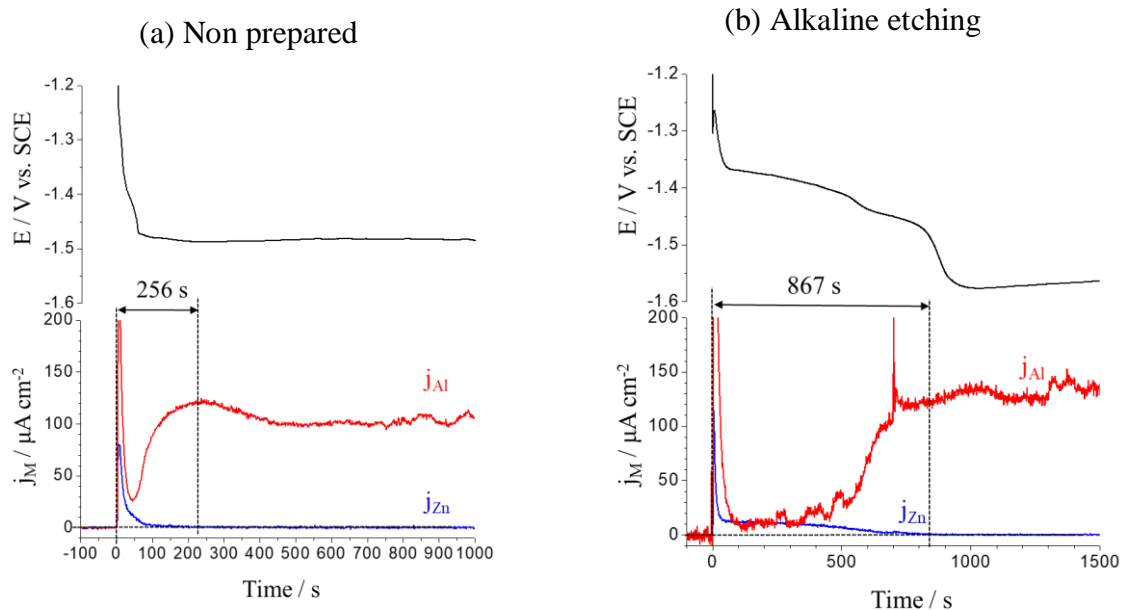


Fig. A4.1. Open circuit potential (E_{oc}) values of each surface preparation method at pH=12.80, 0.1 M NaOH, Ar deaerated solution. (a) non-prepared, (b) alkaline etching, (c) physical abrasion, (d) acid etching, (e) 1 wt.% Nital, (f) humidity chamber.

Figs. A4.2(a)~(f) show Zn/Al elemental dissolution transient of Zn-5Al for each surface preparation method.



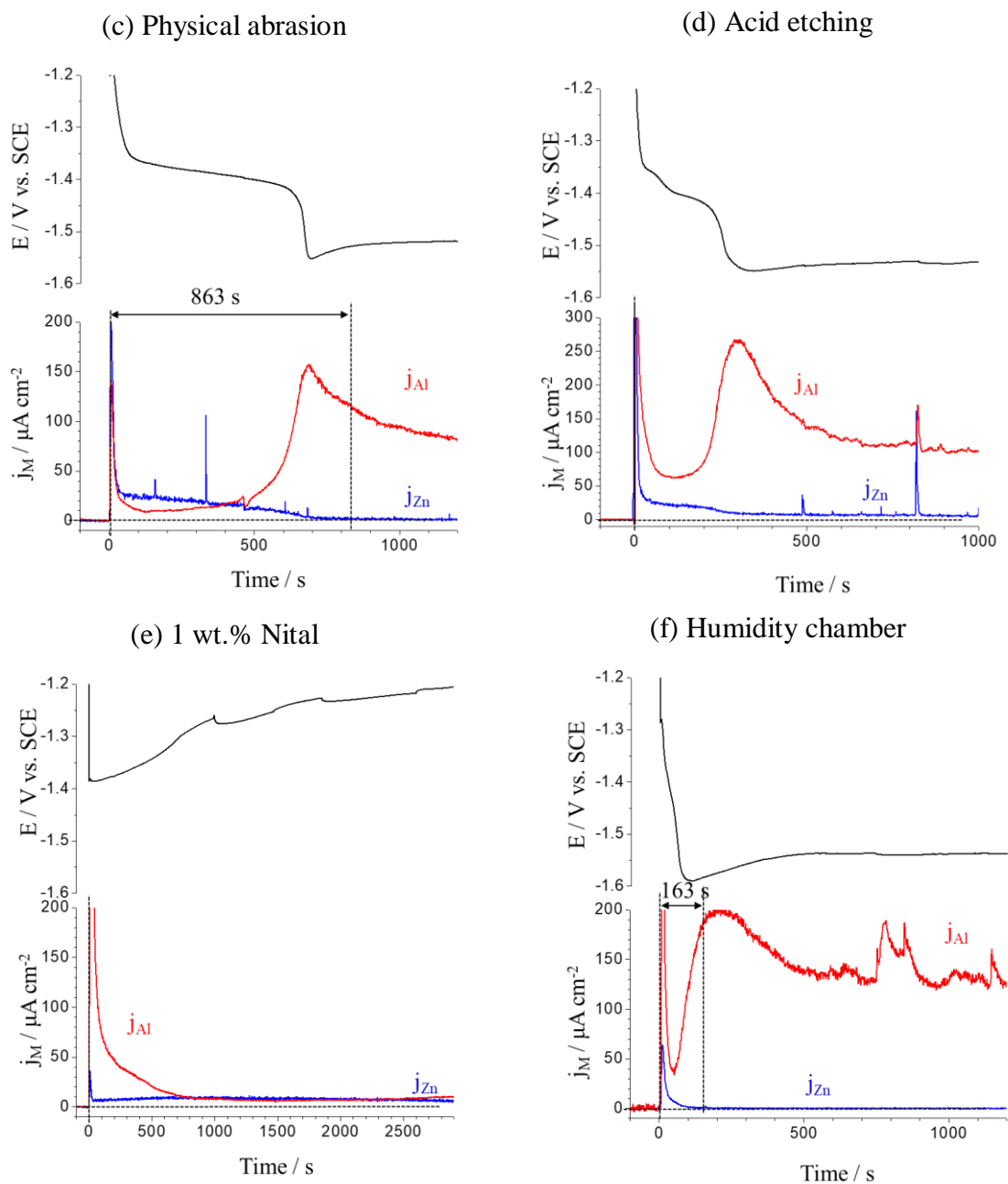


Fig. A4.2. Elemental dissolution rate (j_M) at open circuit condition of each surface preparation method.

For **Figs. A4.2(b), (c)** and **(d)**, an initial j_{Zn} peak was observed corresponding to the E_{oc} decrease at the same time period which may be due to dissolution of pre-existing Zn corrosion products. Assuming a homogenous ZnO layer formation during the surface preparation, integration of Zn dissolution peak gives 5.4, 10.6 and 7.0 nm of ZnO for **Figs. A4.2(b), (c)** and **(d)** (M_{ZnO} : 81.408 g mol⁻¹, ρ_{ZnO} : 5.61 g cm⁻³). For acid etching (**Fig. A4.2(d)**), j_{Zn} did not decrease to the detection limit even when j_{Al} had obtained a steady state value showing a

passivating effect of Zn. The passivating effect was more significant for Nital (**Fig. A4.2(e)**) as evidenced by continuously increased j_{Zn} and a relatively higher E_{oc} value than for the other preparation methods. Humidity chamber preparation (**Fig. A4.2(f)**) shows relatively shorter initial Zn dissolution time as could be seen in (a). The same assumption of a homogenous Zn oxide layer gives only 1.0 nm of ZnO in the case of (a) and (f) which was significantly thinner than other surface preparation methods.

Surface characterizations

SEM-EDS analysis results are given in **Fig. A4.3** to characterize surface after each surface preparation method. Non-prepared case (**Fig. A4.3(a)**), shows η -phase of Zn dendrites and lamella structure of Zn rich β -phase of Al as reported in elsewhere [193]. For alkaline etching, **Fig. A4.3(b)**, Al composition in β -phase of Al decreased to 1.2 wt.%. For physical abrasion, **Fig. A4.3(c)** and acid etching, **Fig. A4.3(d)**, Zn composition in η -phase of Zn decreased to 90 wt.%. However, Zn composition was increased in β -phase of Al probably due to ZnO formation in β -phase of Al. 1 wt.% Nital (**Fig. A4.3(e)** and **Fig. A4.4**) shows a distinctive surface morphology. The surface showed higher porosity with significantly increased Al composition up to 23 wt.% measured by EDS technique. Combined with the elemental dissolution result from **Fig. A4.2**, it is reasonable to conclude that Nital removed a large amount of Zn. Therefore, when the surface was exposed to the electrolyte, Zn could easily form a passive layer. Further, not only the chemical composition but also the surface morphology was significantly altered in that the lamella structure was no longer visible. The humidity chamber preparation (**Fig. A4.3(f)**) showed an interesting result in that the surface seemed to appear a homogeneous layer rather than having the multi-phase microstructure of the non-prepared material. EDS showed a range of 1~5 wt.% Al for all over the surface indicating that the surface microstructure was altered by the surface preparation to give a uniform composition of Zn and Al. For physical abrasion (**Fig. A4.3(c)**), the composition showed relatively larger variation as compared to that of humidity chamber (**Fig. A4.3(f)**).

Appendix 4. Comparison of surface preparation of Zn-Al alloy coating

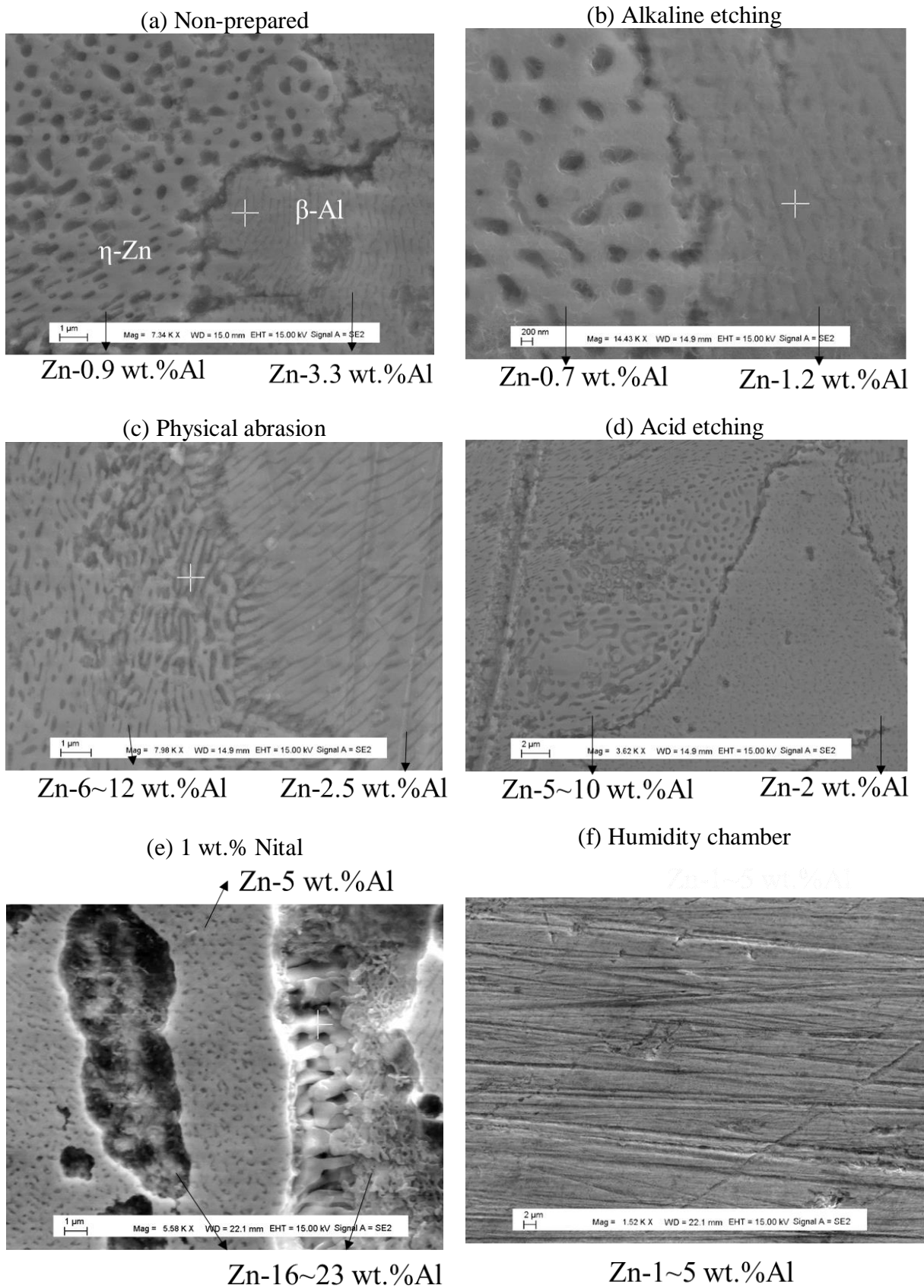


Fig. A4.3. Scanning electron microscopy (SEM) coupled with energy dispersive spectroscopy (EDS) technique images after each surface preparation method.

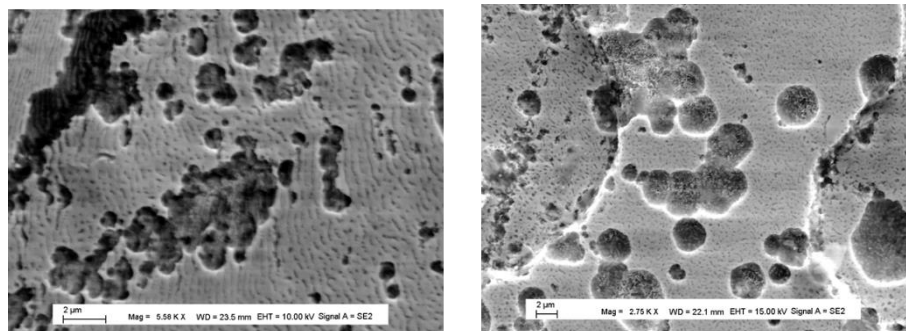


Fig. A4.4. Higher magnification for 1 wt.% Nital surface preparation.

A4.3.2. At pH=2.0 and pH=6.0

The alkaline etching and humidity chamber preparation methods were tested in acidic media, pH=2.0, 100 mM NaCl solution shown in **Fig. A4.5**. In all three cases, the E_{oc} values were approximately +400 mV higher with respect to those in pH=12.80 electrolyte consistent with previous study on the effect of pH for open circuit dissolution of the Zn-5Al alloy coating [194]. The variation of E_{oc} depending on different surface preparation method was less significant in acidic media in that all three E_{oc} obtained instantaneously a steady state at -1.07 V vs. SCE.

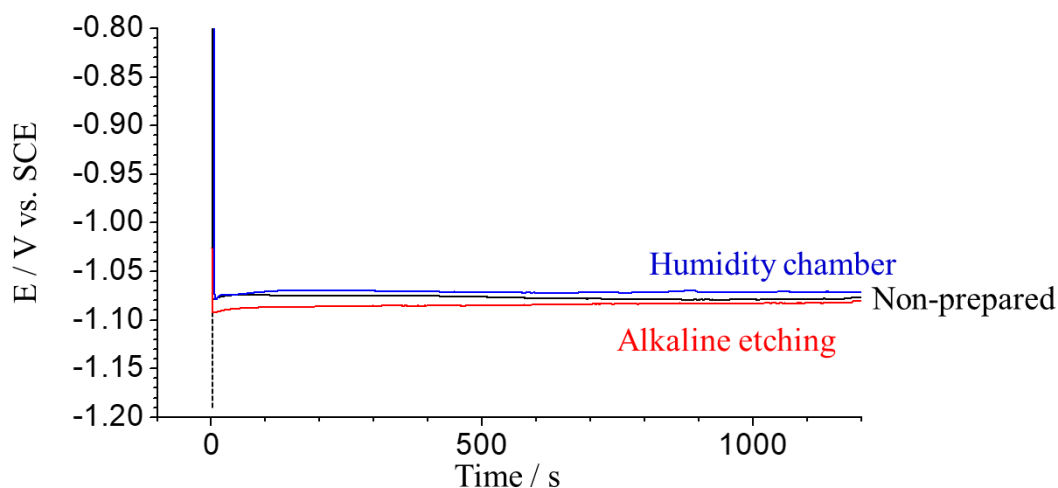


Fig. A4.5. E_{oc} transients of each surface preparation method in pH=2.0, 100 mM NaCl, Ar deaerated electrolyte.

The difference among each surface preparation methods was more significant in nominally neutral pH=6.0 electrolyte, than in pH=2.0 electrolyte as depicted in **Fig. A4.6**. For the humidity chamber, it was measured that approximately 70 mV lower E_{oc} with respect to that in non-prepared, indicating less surface film. Acid etching showed initially a highly negative E_{oc} value

at -1.27 V vs. SCE then increased rapidly to -1.03 V vs. SCE, probably due to passivating Zn film.

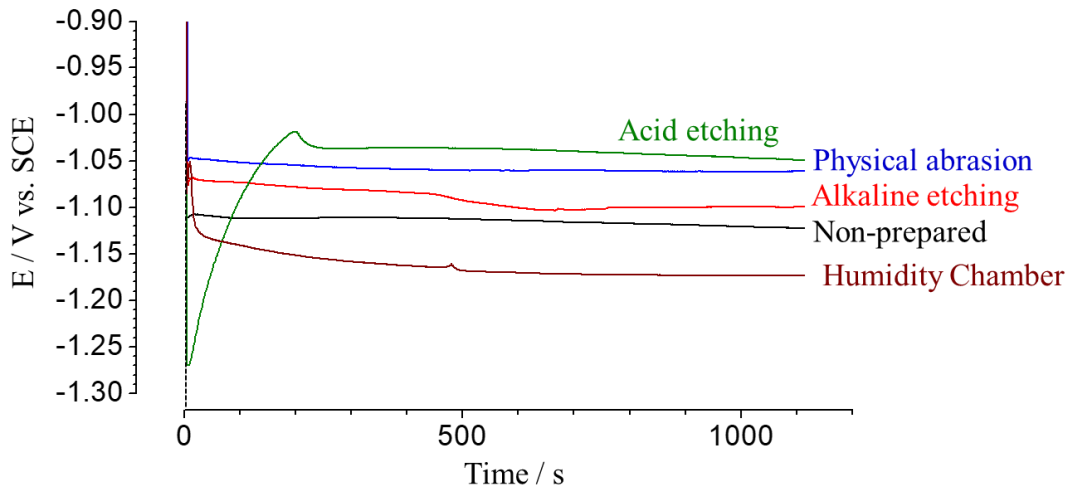


Fig. A4.6. E_{oc} values of each surface preparation method in pH=6.0 electrolyte.

A4.3.3. Effect of exposure time in the humidity chamber

Surface preparation can have a large effect on the spontaneous elemental dissolution of Zn-Al-Mg alloy coating which has more complicated microstructure than the Zn-5Al alloy coating. To this end, the time exposure in the humidity chamber of the Zn-1.6Al-1.6Mg commercial alloy coating was investigated at pH=10.1, 30 mM NaCl Ar deaerated electrolyte. The E_{oc} values are displayed as a function of time in **Fig. A4.7**.

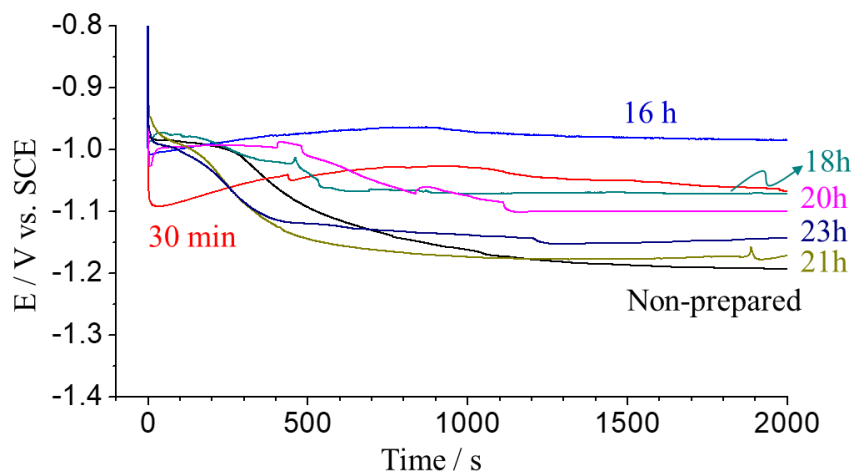


Fig. A4.7. Comparison of E_{oc} trend in pH=10.1, 30 mM NaCl Ar deaerated electrolyte as a function of exposure time in the humidity chamber from 30 minutes to 23 hours.

Appendix 4. Comparison of surface preparation of Zn-Al alloy coating

It can be clearly seen that a 30 min and a 16 h exposure showed relatively higher E_{oc} values increasing with time. It may indicate that until 16 h, a surface film can be easily formed when the sample surface was in contact with electrolyte. Above 18 h of exposure, all the E_{oc} values were relatively lower and close to the non-prepared case, as monitored for Zn-5Al case shown in **Fig. A4.3(f)**.

The j_M depending on exposure time in the humidity chamber is given in **Fig. A4.8**. The error bars were calculated from three different measurements. The non-prepared surface showed a high deviation in j_{Al} and j_{Mg} dissolution which justifies the necessity of surface preparation. Exposure time above 21h showed a reasonably reproducible value, very close to non-prepared case value of j_M .

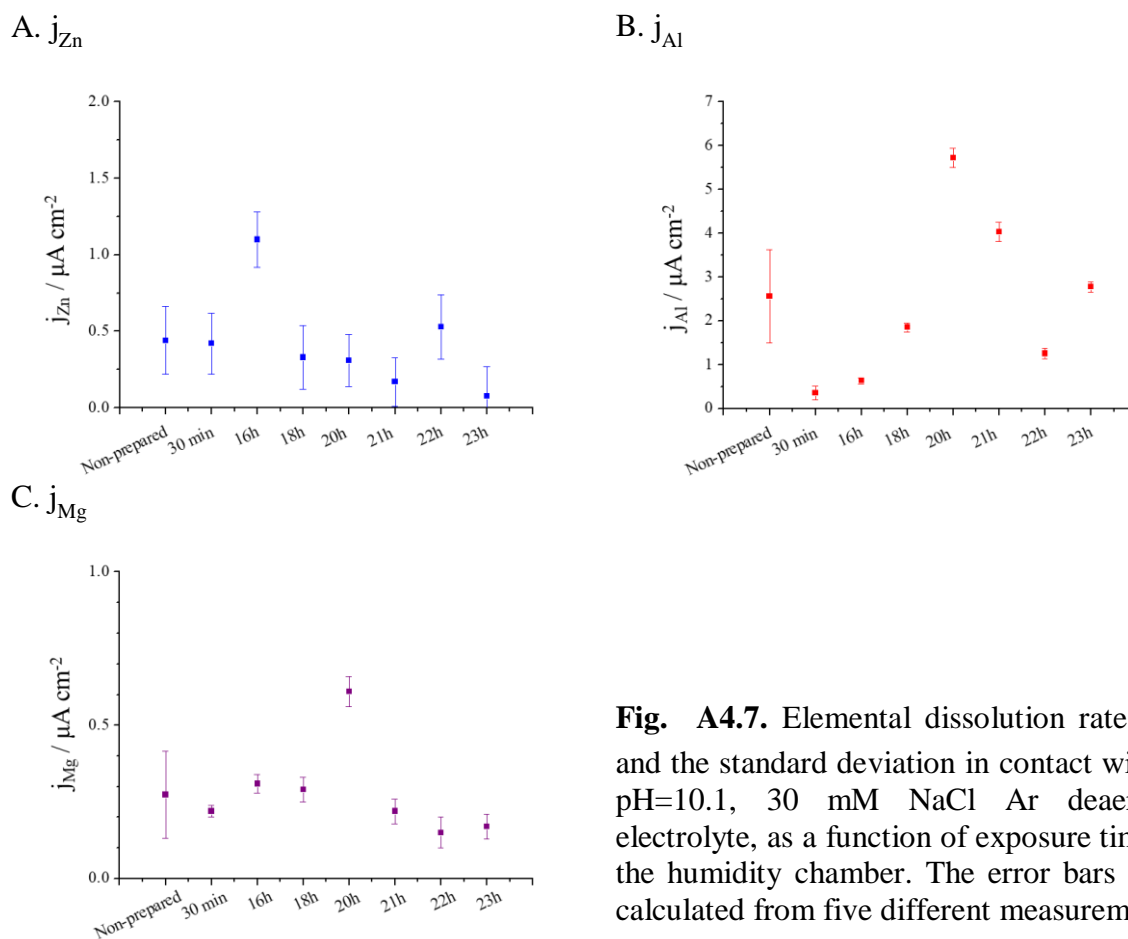


Fig. A4.7. Elemental dissolution rate (j_M) and the standard deviation in contact with at pH=10.1, 30 mM NaCl Ar deaerated electrolyte, as a function of exposure time in the humidity chamber. The error bars were calculated from five different measurements.

A4.4. Discussion

In the present work, it was proved that the humidity chamber surface preparation method showed the best reproducibility and stability for Zn-Al and Zn-Al-Mg commercial alloys in terms of both stable/low E_{oc} trend and less pre-existed oxide film in different pH values investigated here. The E_{oc} value varied with surface preparation method due to the surface condition such as pre-existed corrosion species. Chemical etching and physical abrasion could provide the same microstructure after surface preparation, however, the variation of chemical composition would be altered causing unpredictable elemental spontaneous dissolution. Nitric acid greatly modified surface morphology and chemical composition. Also, surface seemed to show a passivating effect of Zn as previously reported in nitric acid for Zn-based alloy coatings [195].

A4.5. Conclusion

- 1) Humidity chamber surface preparations can be considered as the most reproducible surface preparation method for Zn-Al and Zn-Al-Mg commercial alloy, probably for other alloy coatings.
- 2) The E_{oc} of humidity chamber showed the lowest value, indicating the least oxide film existed on the specimen surface.
- 3) By grinding emery paper, pre-existed surface oxide was removed and chemical composition of the outmost surface would be recovered in the humidity chamber.
- 4) Above 20 h of exposure in the humidity chamber showed the best reproducible j_M for the Zn-Al-Mg alloy coating.
- 5) The surface preparation method using the humidity chamber can be used for the laboratory test of Zn-based alloy coatings.

References

- [1] E. Steel, P. Facility, Growth Opportunities & Challenges : Coated Steel Market.
- [2] K. Wagner, S.R. Brankovic, N. Dimitrov, K. Sieradzki, Dealloying below the Critical Potential, *J. Electrochem. Soc.*, **144**(10) (1997) 3545–3555.
- [3] D.E.L. Europe, Déclaration du 9 mai 1950 prononcée par Robert Schuman, (2011).
- [4] R. Cited, K. Watanabe, P. Examiner, D. Jones, A.E. Miranda, (12) United States Patent, 1 (2001).
- [5] Galvanized Steel Sheet Forum, (2006).
- [6] S. Schuerz, M. Fleischanderl, G.H. Luckeneder, K. Preis, T. Haunschmied, G. Mori, A.C. Kneissl, Corrosion behaviour of Zn-Al-Mg coated steel sheet in sodium chloride-containing environment, *Corros. Sci.* **51** (2009) 2355–2363. doi:10.1016/j.corsci.2009.06.019.
- [7] J. Elvins, J.A. Spittle, J.H. Sullivan, D.A. Worsley, The effect of magnesium additions on the microstructure and cut edge corrosion resistance of zinc aluminium alloy galvanised steel, *Corros. Sci.* **50** (2008) 1650–1658. doi:10.1016/j.corsci.2008.02.005.
- [8] B. Li, A. Dong, G. Zhu, S. Chu, H. Qian, C. Hu, B. Sun, J. Wang, Investigation of the corrosion behaviors of continuously hot-dip galvanizing Zn – Mg coating, *Surf. Coatings Technol.* **206** (2012) 3989–3999. doi:10.1016/j.surfcoat.2012.03.079.
- [9] T. Prosek, A. Nazarov, F. Goodwin, J. Šerák, D. Thierry, Improving corrosion stability of Zn[sbnd]Al[sbnd]Mg by alloying for protection of car bodies, *Surf. Coatings Technol.* **306** (2016) 439–447. doi:10.1016/j.surfcoat.2016.03.062.
- [10] S. Mehraban, J. Malone, N. Lavery, J. Sullivan, D. Penny, S. G. R. Brwon, Increased Corrosion Resistance of Zinc Magnesium Aluminum Galvanised Coating through Germanium Additions, *E.C.S. Transactions*, T.E. Society, **75** (2017) 1–15.
- [11] S. Li, B. Gao, G. Tu, L. Hu, S. Sun, G. Zhu, S. Yin, Effects of magnesium on the microstructure and corrosion resistance of Zn–55Al–1.6Si coating, *Constr. Build. Mater.* **71** (2014) 124–131. doi:10.1016/j.conbuildmat.2014.08.023.
- [12] N. Shimoda, K. Ueda, and Y. Kubo, Corrosion Resistance of Several Zn-Al-Mg Alloy Coated Steels, *Nippon steel & sumitomo metal technical report*, **108** (2015) 14–17.
- [13] T. Prosek, J. Hagström, D. Persson, N. Fuertes, F. Lindberg, O. Chocholaty, C. Taxén, J. Serak, D. Thierry, Effect of the microstructure of Zn-Al and Zn-Al-Mg model alloys on corrosion stability, *Corros. Sci.* **110** (2015) 71–81. doi:10.1016/j.corsci.2016.04.022.
- [14] C. Yao, H. Lv, T. Zhu, W. Zheng, X. Yuan, W. Gao, Effect of Mg content on microstructure and corrosion behavior of hot dipped Zn–Al–Mg coatings, *J. Alloys Compd.* **670** (2016) 239–248. doi:10.1016/j.jallcom.2016.02.026.
- [15] C. B. Boss and K. J. Fredeen, Concepts, Instrumentation and Techniques in Inductively Coupled Plasma Optical Emission Spectrometry, *Perkin Elmer Inc.*, 3rd edition, (2004).

- [16] K. Asheley, Solution Infrared spectroelectrochemistry; A review, *Talanta*, **38**(11), 1209-1218 (1991).
- [17] J. Elvins, J.A. Spittle, D.A. Worsley, Microstructural changes in zinc aluminium alloy galvanising as a function of processing parameters and their influence on corrosion, *Corros. Sci.* **47** (2005) 2740–2759. doi:10.1016/j.corsci.2004.11.011.
- [18] J. Duchoslav, M. Arndt, R. Steinberger, T. Keppert, G. Luckeneder, K.H. Stellnberger, J. Hagler, C.K. Riener, G. Angeli, D. Stifter, Nanoscopic view on the initial stages of corrosion of hot dip galvanized Zn-Mg-Al coatings, *Corros. Sci.* **83** (2014) 327–334. doi:10.1016/j.corsci.2014.02.027.
- [19] N. Lebozec, Atmospheric Corrosion of Zinc-Aluminum Alloyed Coated Steel in Depleted Carbon Dioxide Environments, *J. Electrochem. Soc.* **165** (2018). doi:10.1149/2.0721807jes.
- [20] J. Sullivan, N. Cooze, C. Gallagher, T. Lewis, In situ monitoring of corrosion mechanisms and phosphate inhibitor surface deposition during corrosion of zinc – magnesium – aluminium (ZMA) alloys using novel time-lapse microscopy, *Faraday Discuss.* **180** (2015) 361–379. doi:10.1039/C4FD00251B.
- [21] J. Sullivan, S. Mehraban, J. Elvins, In situ monitoring of the microstructural corrosion mechanisms of zinc-magnesium-aluminium alloys using time lapse microscopy, *Corros. Sci.* **53** (2011) 2208–2215. doi:10.1016/j.corsci.2011.02.043.
- [22] N.C. Hosking, P.H. Shipway, C.D. Rudd, Corrosion resistance of zinc–magnesium coated steel, *Corros. Sci.* **49** (2007) 3669–3695. doi:10.1016/j.corsci.2007.03.032.
- [23] T. Prosek, A. Nazarov, U. Bexell, D. Thierry, J. Serak, Corrosion mechanism of model zinc-magnesium alloys in atmospheric conditions, *Corros. Sci.* **50** (2008) 2216–2231. doi:10.1016/j.corsci.2008.06.008.
- [24] M. Salgueiro Azevedo, C. Allély, K. Ogle, P. Volovitch, Corrosion mechanisms of Zn(Mg,Al) coated steel: 2. The effect of Mg and Al alloying on the formation and properties of corrosion products in different electrolytes, *Corros. Sci.* **90** (2015) 482–490. doi:10.1016/j.corsci.2014.07.042.
- [25] M. Salgueiro Azevedo, C. Allély, K. Ogle, P. Volovitch, Electrochemical properties of corrosion products formed on Zn-Mg, Zn-Al and Zn-Al-Mg coatings in model atmospheric conditions, *Corros. Sci.* **52** (2015) 2372–2378. doi:10.1016/j.electacta.2010.09.058.
- [26] S. Schürz, G.H. Luckeneder, M. Fleischanderl, P. Mack, H. Gsaller, A.C. Kneissl, G. Mori, Chemistry of corrosion products on Zn-Al-Mg alloy coated steel, *Corros. Sci.* **52** (2010) 3271–3279. doi:10.1016/j.corsci.2010.05.044.
- [27] D. Persson, D. Thierry, N. LeBozec, T. Prosek, In situ infrared reflection spectroscopy studies of the initial atmospheric corrosion of Zn-Al-Mg coated steel, *Corros. Sci.* **72** (2013) 54–63. doi:10.1016/j.corsci.2013.03.005.
- [28] J. Duchoslav, R. Steinberger, M. Arndt, T. Keppert, G. Luckeneder, K.H. Stellnberger, J. Hagler, G. Angeli, C.K. Riener, D. Stifter, Evolution of the surface chemistry of hot dip galvanized Zn-Mg-Al and Zn coatings on steel during short term exposure to sodium chloride containing environments, *Corros. Sci.* **91** (2015) 311–320.

doi:10.1016/j.corsci.2014.11.033.

- [29] P. Volovitch, C. Allely, K. Ogle, Understanding corrosion via corrosion product characterization: I . Case study of the role of Mg alloying in Zn–Mg coating on steel, *Corros. Sci.* **51** (2009) 1251–1262. doi:10.1016/j.corsci.2009.03.005.
- [30] P. Volovitch, T.N. Vu, C. Allély, A.A. Aal, K. Ogle, Understanding corrosion via corrosion product characterization: II . Role of alloying elements in improving the corrosion resistance of Zn–Al–Mg coatings on steel, *Corros. Sci.* **53** (2011) 2437–2445. doi:10.1016/j.corsci.2011.03.016.
- [31] K. Ueda, A. Takahashi, Y. Kubo, Investigation of corrosion resistance of pre-painted Zn-11 % Al-3 % Mg-0.2 % Si alloy coated steel sheet through outdoor exposure test in Okinawa, *La Metallurgia Italiana*, **2** (2012) 13–19.
- [32] N. Lebozec, D. Thierry, M. Rohwerder, D. Persson, G. Luckeneder, L. Luxem, Effect of carbon dioxide on the atmospheric corrosion of Zn–Mg–Al coated steel, *Corros. Sci.* **74** (2013) 379–386. doi:10.1016/j.corsci.2013.05.011.
- [33] J. Stoullil, T. Prosek, A. Nazarov, J. Oswald, P. Kriz, D. Thierry, Electrochemical properties of corrosion products formed on Zn-Mg, Zn-Al and Zn-Al-Mg coatings in model atmospheric conditions, *Mater. Corros.* **66** (2015) 777–782. doi:10.1002/maco.201408058.
- [34] M. Salgueiro Azevedo, C. Allély, K. Ogle, P. Volovitch, Corrosion mechanisms of Zn(Mg, Al) coated steel in accelerated tests and natural exposure: 1. The role of electrolyte composition in the nature of corrosion products and relative corrosion rate, *Corros. Sci.* **90** (2015) 472–481. doi:10.1016/j.corsci.2014.05.014.
- [35] M. Salgueiro Azevedo, C. Allély, K. Ogle, P. Volovitch, Corrosion mechanisms of Zn(Mg,Al) coated steel: The effect of HCO_3^- and NH_4^+ ions on the intrinsic reactivity of the coating, *Electrochim. Acta.* **153** (2015) 159–169. doi:10.1016/j.electacta.2014.09.140.
- [36] E. Diler, B. Rouvellou, S. Rioual, B. Lescop, G. Nguyen Vien, D. Thierry, Characterization of corrosion products of Zn and Zn-Mg-Al coated steel in a marine atmosphere, *Corros. Sci.* **87** (2014) 111–117. doi:10.1016/j.corsci.2014.06.017.
- [37] G. Luckeneder, M. Fleischanderl, T. Steck, K. Stellnberger, J. Faderl, S. Schuerz, G. Mori, Corrosion Mechanisms and Cosmetic Corrosion Aspects of Zinc-Aluminium-Magnesium and Zinc-Chromium Alloy Coated Steel Strip, *BHM*, **157** (2012) 121–125.
- [38] H.W. Pickering, Electrolytic Dissolution of Binary Alloys Containing a Noble Metal, *J. Electrochem. Soc.*, **114**(7) 698–706 (1968).
- [39] H.W. Pickering, Characteristic features of alloy polarization curves, *Corros. Sci.* **23** (1983). doi:10.1016/0010-938X(83)90092-6.
- [40] K.N. Han, M.C. Fuerstenau, Dissolution behavior of metals from binary alloys, *Int. J. Miner. Process.* **72** (2003) 355–364. doi:10.1016/S0301-7516(03)00110-8.
- [41] H. Lu, Y. Li, F. Wang, Dealloying behaviour of Cu–20Zr alloy in hydrochloric acid solution, *Corros. Sci.* **48** (2006) 2106–2119. doi:10.1016/j.corsci.2005.08.009.

- [42] K. Sieradzki, R.R. Corderman, K. Shukla, R.C. Newman, Computer simulations of corrosion : Selective dissolution of binary alloys, *Philosophical Magazine*, **59**(4), 713-746 (1989). doi:10.1080/01418618908209817.
- [43] J. Laurent, D. Landolt, Anodic dissolution of binary single phase alloy at subcritical potential, *Electrochim. Acta.* **36** (1991) 49–58.
- [44] K. Sieradzki, N. Dimitrov, D. Movrin, C. McCall, N. Vasiljevic, The Dealloying Critical Potential, *J. Electrochem. Soc.*, **149**(8), (2002) B370–B377. doi:10.1149/1.1492288.
- [45] N. Birbilis, R.G. Buchheit, Electrochemical Characteristics of Intermetallic Phases in Aluminum Alloys An Experimental Survey and Discussion, *J. Electrochem. Soc.*, **152**(4) (2005) B140–B151. doi:10.1149/1.1869984.
- [46] N. Birbilis, R.G. Buchheit, Investigation and Discussion of Characteristics for Intermetallic Phases Common to Aluminum Alloys as a Function of Solution pH, *J. Electrochem. Soc.*, **155**(3), (2008) C117-C126. doi:10.1149/1.2829897.
- [47] A. Pareek, S. Borodin, A. Bashir, G.N. Ankah, P. Keil, G.A. Eckstein, M. Rohwerder, M. Stratmann, Y. Gründer, F.U. Renner, Initiation and inhibition of dealloying of single crystalline Cu₃Au (111) surfaces., *J. Am. Chem. Soc.* **133** (2011) 18264–71. doi:10.1021/ja2054644.
- [48] M.K. Cavanaugh, J. Li, N. Birbilis, R.G. Buchheit, Electrochemical Characterization of Intermetallic Phases Common to Aluminum Alloys as a Function of Solution Temperature, *J. Electrochem. Soc.*, **161**(12) (2014) C535–C543. doi:10.1149/2.0361412jes.
- [49] K. Geng, K. Sieradzki, Dealloying at High Homologous Temperature : Morphology Diagrams, *J. Electrochem. Soc.*, **164**(6) (2017) C330–C337. doi:10.1149/2.0061707jes.
- [50] T. Ramgopal, P. Schmutz, G.S. Frankel, Electrochemical Behavior of Thin Film Analogs of Mg (Zn, Cu , Al)₂, *J. Electrochem. Soc.*, **148**(9) (2001) B348–B356. doi:10.1149/1.1386626.
- [51] P. Zhou, M.J. Hutchison, J.W. Erning, J.R. Scully, K. Ogle, An in situ kinetic study of brass dezincification and corrosion, *Electrochim. Acta.* **229** (2017) 141–154. doi:10.1016/j.electacta.2017.01.078.
- [52] R. Cerrato, A. Casal, M.P. Mateo, G. Nicolas, Dealloying evidence on corroded brass by laser-induced breakdown spectroscopy mapping and depth profiling measurements ☆, *Spectrochim. Acta Part B At. Spectrosc.* **130** (2017) 1–6. doi:10.1016/j.sab.2016.11.006.
- [53] H. Dafydd, D.A. Worsley, H.N. McMurray, The kinetics and mechanism of cathodic oxygen reduction on zinc and zinc – aluminium alloy galvanized coatings, *Corros. Sci.*, **47** (2005) 3006–3018. doi:10.1016/j.corsci.2005.05.036.
- [54] W. Melitz, J. Shen, A.C. Kummel, S. Lee, Kelvin probe force microscopy and its application, *Surf. Sci. Rep.* **66** (2011) 1–27. doi:10.1016/j.surfrep.2010.10.001.
- [55] Y. Baek, G.S. Frankel, Electrochemical Quartz Crystal Microbalance Study of Corrosion of Phases in AA2024, *J. Electrochem. Soc.*, **150**(1) (2003) B1-B9. doi:10.1149/1.1524172.

- [56] W. Kaim, J. Fiedler, Spectroelectrochemistry : the best of two worlds, *Chemical Society Reviews*, (2009) 3373–3382. doi:10.1039/b504286k.
- [57] F. Weinert, D.L. Feldheim, Infrared spectroscopy to probe the double layer, *Electrochim. Acta.*, **36** (1991).
- [58] C. Han, S. Hong, A Novel Electrochemical Method for Enhancing the Conductivity of Polyaniline Solid Matrices in Preformed Films, *Macromolecules*, (2001) 4937–4941.
- [59] S.P. Best, S.J. Borg, K.A. Vincent, Infrared Spectroelectrochemistry, *Royal Society of Chemistry* (2008).
- [60] H. Zhang, S. Park, Rotating Ring-Disk Electrode and Spectroelectrochemical Studies on the Oxidation of Iron in Alkaline Solutions, *J. Electrochem. Soc.*, **141**(3) (1994) 718–724.
- [61] M. Keddam, A. Hugot-Le-Goff, H. Takenouti, D. Thierry, M.C. Arevalo, The influence of a thin electrolyte layer on the corrosion process of zinc in chloride-containing solutions, *Corros. Sci.* **33** (1992) 1243–1252. doi:10.1016/0010-938X(92)90133-N.
- [62] B.P. Laskova, L. Kavan, M. Zukalova, K. Mocek, O. Frank, In situ Raman spectroelectrochemistry as a useful tool for detection of TiO₂ (anatase) impurities, *Monatsh. Chem.*, **147**, (2016) 951–959. doi:10.1007/s00706-016-1678-x.
- [63] R. Sfez, L. De-zhong, I. Turyan, D. Mandler, S. Yitzchaik, Polyaniline Monolayer Self-Assembled on Hydroxyl-Terminated Surfaces, *Langmuir*, **17**, (2001) 2556–2559. doi:10.1021/la001343d.
- [64] P. Hudhomme, E. Levillain, L. Perrin, Y. Sahin, C. Wartelle, Electrochemistry coupled to fluorescence spectroscopy: a new versatile approach, *Electrochemistry Communications*, **6** (2004) 325–330. doi:10.1016/j.elecom.2004.01.010.
- [65] K. Ogle, and S. Weber, Anodic Dissolution of 304 Stainless Steel Using Atomic, *J. Electrochem. Soc.*, **147**(5) (2000) 1770-1780. doi:10.1149/1.1393433.
- [66] B. Laurent, N. Gruet, B. Gwinner, F. Miserque, M. Tabarant, K. Ogle, A Direct Measurement of the Activation Potential of Stainless Steels in Nitric Acid, *J. Electrochem. Soc.*, **164**(9) (2017)C481-C487. doi:10.1149/2.0081709jes.
- [67] O. Gharbi, N. Birbilis, K. Ogle, In-Situ Monitoring of Alloy Dissolution and Residual Film Formation during the Pretreatment of Al-Alloy AA2024-T3, *J. Electrochem. Soc.*, **163**(5) (2016) 240–251. doi:10.1149/2.1121605jes.
- [68] L. Léon, J. D. Mozo, Designing spectroelectrochemical cells : A review, *Trends in Analytical Chemistry*, **102** (2018) 147-169. doi:10.1016/j.trac.2018.02.002.
- [69] T.J. Manning, W.R. Grow, Inductively Coupled Plasma - Atomic Emission Spectrometry, *Springer-Verlag New York Inc.*, **2**(1) (1997) 1–2.
- [70] H. Haraguchi, Inductively coupled plasmas in analytical atomic spectrometry: Excitation mechanisms and analytical feasibilities, *Pure & Appl. Chem.*, **60**(5) (1988). 685-696 doi:10.1351/pac198860050685.
- [71] K. Ogle, C. Paristech, Research paper, (2012).

- [72] W. Paper, Sensitivity , Background , Noise , and Calibration in Atomic Spectroscopy : Effects on Accuracy and Detection Limits, *Perkin Elmer Inc.*, 1–11.
- [73] X. Hou, B.T. Jones, Inductively Coupled Plasma / Optical Emission Spectrometry, *Encyclopedia of Analytical Chemistry*, (2000) 9468–9485.
- [74] K. Ogle, J. Baeyens, J. Swiatowska, P. Volovitch, Atomic emission spectroelectrochemistry applied to dealloying phenomena: I. The formation and dissolution of residual copper films on stainless steel, *Electrochim. Acta.* **54** (2009) 5163–5170. doi:10.1016/j.electacta.2009.01.037.
- [75] V. Shkirskiy, P. Maciel, J. Deconinck, K. Ogle, On the time resolution of the atomic emission spectroelectrochemistry method, *J. Electrochem. Soc.* **163** (2016) 1–8. doi:10.1149/2.0991602jes.
- [76] R.A. Cottis, Interpretation of Electrochemical Noise Data, *Corrosion*, **57**(3) (2001) 265–285.
- [77] S. Lebouil, A. Duboin, F. Monti, P. Tabeling, P. Volovitch, K. Ogle, A novel approach to on-line measurement of gas evolution kinetics: Application to the negative difference effect of Mg in chloride solution, *Electrochim. Acta.* **124** (2014) 176–182. doi:10.1016/j.electacta.2013.07.131.
- [78] V. Shkirskiy, K. Ogle, A novel coupling of electrochemical impedance spectroscopy with atomic emission spectroelectrochemistry: Application to the open circuit dissolution of zinc, *Electrochim. Acta.* **168** (2015) 167–172. doi:10.1016/j.electacta.2015.03.171.
- [79] B. K. Agarwal, Introduction to Energy Dispersive X-ray Spectrometry (EDS), 2nd edition, *Springer-Verlag, Berlin* (1991) 1–12.
- [80] M.C. Bernard, A.H. Goff, D. Massinon, N. Phillips, Underpaint corrosion of zinc-coated steel sheet studied by in situ Raman spectroscopy, *Corros. Sci.*, **35** (1993).
- [81] P. Delichere, A.H. Goff, S. Joiret, Study of Thin Corrosion Films by in situ Raman Spectroscopy Combined with Direct Observation of Nuclear Reactions, *Surf. & Int. Anal.* **12** (1988) 419–423.
- [82] J. Rodriguez, L. Chenoy, A. Roobroeck, S. Godet, M. Olivier, Effect of the electrolyte pH on the corrosion mechanisms of Zn-Mg coated steel, *Eval. Corros. Sci.*, **108** (2016) 47–59. doi:10.1016/j.corsci.2016.02.041.
- [83] W. Liu, Q. Li, M. Li, Corrosion behaviour of hot-dip Al–Zn–Si and Al–Zn–Si–3Mg coatings in NaCl solution, *Eval. Corros. Sci.*, **121** (2017) 72–83. doi:10.1016/j.corsci.2017.03.013.
- [84] K. Ogle, S. Morel, D. Jacquet, Observation of Self-Healing Functions on the Cut Edge of Galvanized Steel Using SVET and pH Microscopy, *J. Electrochem. Soc.*, **153**(1) (2006) B1–B5. doi:10.1149/1.2126577.
- [85] K. Ogle, V. Baudu, L. Garrigues, X. Philippe, Localized Electrochemical Methods Applied to Cut Edge Corrosion, *J. Electrochem. Soc.*, **147**(10) (2000) 3654–3660.
- [86] R. Krieg, M. Rohwerder, S. Evers, B. Schuhmacher, J. Schauer-pass, Cathodic self-

- healing at cut-edges : The effect of Zn^{2+} and Mg^{2+} ions, *Corros. Sci.* **65** (2012) 119–127. doi:10.1016/j.corsci.2012.08.008.
- [87] R. Tunold, H. Holtan, M.B.H. Berge, A. Lasson, R. Steen-Hansen, The corrosion of magnesium in aqueous solution containing chloride ions, *Corros. Sci.* **17** (1977) 353–365. doi:10.1016/0010-938X(77)90059-2.
- [88] S. Lebouil, O. Gharbi, P. Volovitch, K. Ogle, Mg dissolution in phosphate and chloride electrolytes: Insight into the mechanism of the negative difference effect, *Corrosion.* **71** (2015) 234–241. doi:10.5006/1459.
- [89] U.R. Evans, Inhibition, passivity and resistance: A review of acceptable mechanisms, *Electrochim. Acta.* **16** (1971) 1825–1840. doi:10.1016/0013-4686(71)85141-1.
- [90] J.L. Robinson, P.F. King, Electrochemical Behavior of the Magnesium Anode, *J. Electrochem. Soc.* **108** (1961) 36. doi:10.1149/1.2428007.
- [91] G. Baril, G. Galicia, C. Deslouis, N. Pébère, V. Vivier, G. Baril, G. Galicia, C. Deslouis, N. Pébère, B. Tribollet, An Impedance Investigation of the Mechanism of Pure Magnesium Corrosion in Sodium Sulfate Solutions, *HAL*, Id : hal-00806016, (2013).
- [92] M. Mokaddem, P. Volovitch, K. Ogle, The anodic dissolution of zinc and zinc alloys in alkaline solution. I. Oxide formation on electrogalvanized steel, *Electrochim. Acta.* **55** (2010) 7867–7875. doi:10.1016/j.electacta.2010.02.020.
- [93] T.N. Vu, M. Mokaddem, P. Volovitch, K. Ogle, The anodic dissolution of zinc and zinc alloys in alkaline solution. II. Al and Zn partial dissolution from 5% Al-Zn coatings, *Electrochim. Acta.* **74** (2012) 130–138. doi:10.1016/j.electacta.2012.04.037.
- [94] V. Shkirskiy, P. Keil, H. Hintze-Bruening, F. Leroux, P. Volovitch, K. Ogle, Observation of l-cysteine enhanced zinc dissolution during cathodic polarization and its consequences for corrosion rate measurements, *Electrochim. Acta.* **184** (2015) 203–213. doi:10.1016/j.electacta.2015.09.009.
- [95] J. O'M. Bockris, Z. Nagy, and A. Damjanovic, On the Deposition and Dissolution of Zinc in Alkaline Solutions, *J. Electrochem. Soc.*, **119**(3) 285-295 (1972).
- [96] P. Mao, B. Yu, Z. Liu, F. Wang, Y. Ju, Mechanical properties and electronic structures of $MgCu_2$, Mg_2Ca and $MgZn_2$ Laves phases by first principles calculations, *Trans. Nonferrous Met. Soc. China*, **24** (2014) 2920–2929. doi:10.1016/S1003-6326(14)63427-0.
- [97] X. Li, H. Ma, Z. Dai, Y. Qian, L. Hu, Y. Xie, First-principles study of coherent interfaces of Laves-phase $MgZn_2$ and stability of thin $MgZn_2$ layers in Mg-Zn alloys, *J. Alloys Compd.* **696** (2017) 109–117. doi:10.1016/j.jallcom.2016.11.217.
- [98] B.G. Ateya, H.W. Pickering, The effects of potential and kinetic parameters on the formation of passivating noble metal rich surface layers during the selective dissolution of binary alloys, *Corros. Sci.* **38** (1996) 1245–1267. doi:10.1016/0010-938X(96)00015-7.
- [99] Y. Guan, K.N. Han, An Electrochemical Study on the Dissolution of Gold and Copper from Gold / Copper Alloys, *Met. & Mat. Trans. B*, **25B** (1994) 817-827.

- [100] X. Su, J. Zhou, J. Wang, C. Wu, Y. Liu, H. Tu, H. Peng, Thermodynamic analysis and experimental study on the oxidation of the Zn-Al-Mg coating baths, *Appl. Surf. Sci.* **396** (2017) 154–160. doi:10.1016/j.apsusc.2016.11.043.
- [101] T. Lostak, A. Maljusch, B. Klink, S. Krebs, M. Kimpel, J. Flock, S. Schulz, W. Schuhmann, Zr-based conversion layer on Zn-Al-Mg alloy coated steel sheets: Insights into the formation mechanism, *Electrochim. Acta.* **137** (2014) 65–74. doi:10.1016/j.electacta.2014.05.163.
- [102] C. Commenda, J. Pühringer, Microstructural characterization and quantification of Zn – Al–Mg surface coatings, *Mater. Charact.* **61** (2010) 943–951. doi:10.1016/j.matchar.2010.06.008.
- [103] M. Dutta, A. Kumar, S. Brat, Morphology and properties of hot dip Zn – Mg and Zn – Mg – Al alloy coatings on steel sheet, *Surf. Coat. Technol.* **205** (2010) 2578–2584. doi:10.1016/j.surfcoat.2010.10.006.
- [104] L. Jiang, P. Volovitch, M. Wolpers, K. Ogle, Activation and inhibition of Zn – Al and Zn–Al–Mg coatings on steel by nitrate in phosphoric acid solution, *Corros. Sci.*, **60** (2012) 256–264.
- [105] N. Lebozec, D. Thierry, L. Luxem, G. Luckeneder, G. Marchiaro, and M Rohwerder, Corrosion performance of Zn–Mg–Al coated steel in accelerated corrosion tests used in the automotive industry and field exposure, *Mat. and Corros.* **64** (2013). doi:10.1002/maco.201206959.
- [106] Y. Meng, G. Jiang, TEM study on the microstructure of the Zn-Al-Mg alloy, *Mater. Charact.* **129** (2017) 336–343. doi:10.1016/j.matchar.2017.05.011.
- [107] X. Zhang, C. Leygraf, I. Odnevall Wallinder, Atmospheric corrosion of Galfan coatings on steel in chloride-rich environments, *Corros. Sci.* **73** (2013) 62–71. doi:10.1016/j.corsci.2013.03.025.
- [108] A.P. Yadav, H. Katayama, K. Noda, H. Masuda, A. Nishikata, T. Tsuru, Effect of Al on the galvanic ability of Zn-Al coating under thin layer of electrolyte, *Electrochim. Acta.* **52** (2007) 2411–2422. doi:10.1016/j.electacta.2006.08.050.
- [109] P. Qiu, C. Leygraf, I. Odnevall Wallinder, Evolution of corrosion products and metal release from Galvalume coatings on steel during short and long-term atmospheric exposures, *Mater. Chem. Phys.* **133** (2012) 419–428. doi:10.1016/j.matchemphys.2012.01.054.
- [110] A.R. Moreira, Z. Panossian, P.L. Camargo, M.F. Moreira, I.C. Da Silva, J.E. Ribeiro De Carvalho, Zn/55Al coating microstructure and corrosion mechanism, *Corros. Sci.* **48** (2006) 564–576. doi:10.1016/j.corsci.2005.02.012.
- [111] T.A. Lowe, G.G. Wallace, A.K. Neufeld, Insights into the cut edge corrosion of 55% Al-Zn metal coating on steel from simultaneous electrochemical polarization and localised pH sensing experiments, *Corros. Sci.* **55** (2012) 180–186. doi:10.1016/j.corsci.2011.10.015.
- [112] R. Mathew, P.R. Stoddart, D. Nolan, Y. Durandet, Microstructural refinement of aluminium-zinc-silicon coated steels, *Surf. Coat. Technol.* **306** (2016) 490–496. doi:10.1016/j.surfcoat.2016.01.024.

- [113] X. Zhang, T.N. Vu, P. Volovitch, C. Leygraf, K. Ogle, I.O. Wallinder, The initial release of zinc and aluminum from non-treated Galvalume and the formation of corrosion products in chloride containing media, *Appl. Surf. Sci.* **258** (2012) 4351–4359. doi:10.1016/j.apsusc.2011.12.112.
- [114] J. Han, K. Ogle, Dealloying of MgZn₂ Intermetallic in Slightly Alkaline Chloride, *J. Electrochem. Soc.*, **164**(14) (2017) C952–C961. doi:10.1149/2.0341714jes.
- [115] E. De Bruycker, Z. Zermout, B.C. De Cooman, Zn-Al-Mg Coatings : Thermodynamic Analysis and Microstructure Related Properties, *Mat. Sci. Forum*, **543** (2007) 1276–1281. doi:10.4028/www.scientific.net/MSF.539-543.1276.
- [116] Y. H. Zhu, General Rule of Phase Decomposition in Zn-Al Based Alloys (II) — On Effects of External Stresses on Phase Transformation, *Mat. Trans.*, **45**(11) (2004) 3083–3097.
- [117] J. Dorantes-rosales, V.M. Lo, A.A.T. Castillo, N. Cayetano-castro, M.L. Saucedo-mun, Phase Decomposition in Zn-22 mass % Al and Zn-22 mass % Al-2 mass % Cu Alloys at Room Temperature, *Mat. Trans.*, **48**(10) (2007) 2791–2794. doi:10.2320/matertrans.MRP2007058.
- [118] S.-I. Pyun, S.-M. Moon, Corrosion mechanism of pure aluminium in aqueous alkaline solution, *J. Solid State Electrochem.* **4** (2000) 267–272. doi:10.1007/s100080050203.
- [119] J. Zhang, M. Klasky, B.C. Letellier, The aluminum chemistry and corrosion in alkaline solutions, *J. Nucl. Mater.* **384** (2009) 175–189. doi:10.1016/j.jnucmat.2008.11.009.
- [120] K. Ogle, M. Serdechnova, M. Mokaddem, P. Volovitch, The cathodic dissolution of Al, Al₂Cu, and Al alloys, *Electrochim. Acta.* **56** (2011) 1711–1718. doi:10.1016/j.electacta.2010.09.058.
- [121] M. Serdechnova, P. Volovitch, K. Ogle, Atomic emission spectroelectrochemistry study of the degradation mechanism of model high-temperature paint containing sacrificial aluminum particles, *Surf. Coat. Technol.* **206** (2012) 2133–2139. doi:10.1016/j.surfcoat.2011.09.044.
- [122] M. Serdechnova, P. Volovitch, F. Brisset, K. Ogle, On the cathodic dissolution of Al and Al alloys, *Electrochim. Acta.* **124** (2014) 9–16. doi:10.1016/j.electacta.2013.09.145.
- [123] T.T.M. Tran, B. Tribollet, E.M.M. Sutter, New insights into the cathodic dissolution of aluminium using electrochemical methods, *Electrochim. Acta.* **216** (2016) 58–67. doi:10.1016/j.electacta.2016.09.011.
- [124] N.S. Azmat, K.D. Ralston, B.C. Muddle, I.S. Cole, Corrosion of Zn under acidified marine droplets, *Corros. Sci.* **53** (2011) 1604–1615. doi:10.1016/j.corosci.2011.01.044.
- [125] L. P. Devillers, and P. Niessen, The mechanism of intergranular corrosion of dilute zinc-aluminum alloys in hot water, *Corros. Sci.*, **16** (1976) 243-252.
- [126] R. Ghiaasiaan, B. Shalchi, S. Shankar, Quantitative metallography of precipitating and secondary phases after strengthening treatment of net shaped casting of Al-Zn-Mg-Cu (7000) alloys, *Mater. Sci. Eng. A.* **698** (2017) 206–217. doi:10.1016/j.msea.2017.05.047.
- [127] N. Pasupulety, H. Driss, Y. Abobakor, A. Ahmed, M.A. Daous, L. Petrov, General

- Studies on Au / Cu – Zn – Al catalyst for methanol synthesis from CO₂, *Applied Catal. A, Gen.* **504** (2015) 308–318. doi:10.1016/j.apcata.2015.01.036.
- [128] X. M. Li, M. J. Starink, The effect of compositional variations on the characteristics of coarse intermetallic particles in overaged 7xxx Al alloys, *Mater. Sci. Tech.* **17** (2001) 1324-1328. *Mater. Sci. Techn.*, 2001, **17**, 1324-28, 17 (2001).
- [129] E. Salamci, R.F. Cochrane, Investigation of secondary phase particles in spray deposited 7000 series aluminium alloys, *Mater. Sci. Tech.* **18** (2002) 1445-1452. doi:10.1179/026708302225007727.
- [130] C. Wu, K. Ma, D. Zhang, J. Wu, S. Xiong, G. Luo, Precipitation phenomena in Al- Zn-Mg alloy matrix composites reinforced with B 4 C particles, *Sci. Rep.* (2017) 1–11. doi:10.1038/s41598-017-10291-4.
- [131] S. Wang, G.S. Frankel, J. Jiang, J. Chen, Mechanism of Localized Breakdown of 7000 Series Aluminum Alloys, *J. Electrochem. Soc.*, **160**(10) (2013) C493-C502. doi:10.1149/2.080310jes.
- [132] B. Vuillemin, R. Oltra, K. Ogle, C. Allely, Investigation of self-healing mechanism on galvanized steels cut edges by coupling SVET and numerical modeling, *Electrochim. Acta.* **53** (2008) 5226–5234. doi:10.1016/j.electacta.2008.02.066.
- [133] F. Zhu, D. Persson, D. Thierry, Formation of Corrosion Products on Open and Confined Metal Surfaces Exposed to Periodic Wet / Dry Conditions — A Comparison Between Zinc and Electrogalvanized Steel, *Corrosion* (2001) 582–590.
- [134] O.T. De Rinco, Galvanic Anodes for Reinforced Concrete Structures: A Review, *Corrosion*, **74**(6) (2018) 715–723.
- [135] R. Brousseau, and B. Baldock, Laboratory Study of Sacrificial Anodes for Reinforced Concrete NRCC-43606, *Corrosion*, **54**(3) (1998) 241-245. doi:10.5006/1.3284849.
- [136] N. Fink, B. Wilson, G. Grundmeier, Formation of ultra-thin amorphous conversion films on zinc alloy coatings Part 1 . Composition and reactivity of native oxides on ZnAl (0.05%) coatings, *Electrochim. Acta.* **51** (2006) 2956–2963. doi:10.1016/j.electacta.2005.08.030.
- [137] R. Berger, U. Bexell, N. Stavlid, T.M. Grehk, The influence of alkali-degreasing on the chemical composition of hot-dip galvanized steel surfaces, *Surf. and Int. Anal.* **38** (2006) 1130–1138. doi:10.1002/sia.
- [138] N.S. Azmat, K.D. Ralston, I.S. Cole, Pre-treatment of Zn surfaces for droplet corrosion studies, *Surf. Coat. Technol.* **205** (2010) 928–935. doi:10.1016/j.surfcoat.2010.08.065.
- [139] C. Cachet, B. Saidani, R. Wiart, The Behavior of Zinc Electrode in Alkaline Electrolytes, I. A Kinetic Analysis of Cathodic Deposition, *J. Electrochem. Soc.*, **138**(3) (1991) 678–687.
- [140] C. Cachet, B. Sadani, R. Wiart, The Behavior of Zinc Electrode in Alkaline Electrolytes II. A Kinetic Analysis of Anodic Dissolution, *J. Electrochem. Soc.*, **139**(3) (1992) 644–654.
- [141] S. -M. Moon and S. -I. Pyun., The corrosion of pure aluminium during cathodic

- poalrization in aqueous solutions, *Corros. Sci.*, **39**(2) (1997) 399–408.
- [142] D. Chu., R. F. Savinell, Experimental data on aluminum in KOH electrolytes, *Electrochim. Acta.*, **36**(10) (1991) 1631–1638.
- [143] J. Han, K. Ogle, Cathodic Dealloying of α -Phase Al-Zn in Slightly Alkaline Chloride Electrolyte and its Consequence for Corrosion Resistance, *J. Electrochem. Soc.*, **165**(7) (2018) C334–C342. doi:10.1149/2.0581807jes.
- [144] T.N. Vu, P. Volovitch, K. Ogle, The effect of pH on the selective dissolution of Zn and Al from Zn-Al coatings on steel, *Corros. Sci.* **67** (2013) 42–49. doi:10.1016/j.corsci.2012.09.042.
- [145] T. Shinagawa, A.T. Garcia-esparza, K. Takanabe, Insight on Tafel slopes from a microkinetic analysis of aqueous electrocatalysis for energy conversion, *Nat. Publ. Gr.* (2015) 1–21. doi:10.1038/srep13801.
- [146] A.C.D. Angelo, Electrocatalysis of hydrogen evolution reaction on Pt electrode surface-modified by S^{-2} chemisorption, *Int. J. Hydro. Ener.* **32** (2007) 542–547. doi:10.1016/j.ijhydene.2006.06.052.
- [147] M. Popovic, B. Grgur, M. Vojnovic, On the kinetics of the hydrogen evolution reaction on nickel in alkaline solution Part I . The mechanism, *J. Electrochem. Soc.*, **512** (2001) 16–26.
- [148] V. I. Briss, A. Damjanovic, Oxygen Evolution at Platinum Electrodes in Alkaline Solutions, I. Dependence on Solution pH and Oxide Film Thickness, *J. Electrochem. Soc.*, **134**(1) (1987).
- [149] V.I. Birss, A. Damjanovic, and P. G. Hudson, Oxygen Evolution at Platinum Electrodes in Alkaline Solutions, II. Mechanism of the Reaction, *J. Electrochem. Soc.*, **133**(8) 1621–1625.
- [150] D. Gilory, B.E. Conway, Surface oxidation and reduction of platinum electrodes : Coverage, kinetic and hysteresis studies, *Canadian J. of Chem.* **46** (1968) 875-890.
- [151] T. C. Damen, S. P. S. Porto, and B. Tell, Raman effect in zinc oxide, *Phys. Review*, **142**(2) (1966) 570-574.
- [152] A.R. Moshaweh, G.T. Burstein, Evolution of unpredictable behaviour of a passivated stainless steel measured electrochemically, *Corros. Sci.*, **113** (2016) 126–132. doi:10.1016/j.corsci.2016.10.013.
- [153] F. Touri, A. Sahari, A. Zouaoui, F. Deflorian, Detection and Characterization of ZnO on a Passive Film of Pure Zinc, *Int. J. Electrochem. Sci.*, **12** (2017) 10813–10823. doi:10.20964/2017.11.20.
- [154] M. Liu, G.M. Cook, N.P. Yao, Passivation of Zinc Anodes in KOH Electrolytes, *J. Electrochem. Soc.*, **128**(8), 1663–1668 (1981).
- [155] R.D. Armstrong, Diagnostic criteria for distinguishing between the dissolution-precipitation and the solid state mechanisms of passivation, *Corros. Sci.*, **11** (1971) 693–697.

- [156] T.P. Dirkse, N.A. Hampso, The anodic behaviour of zinc in aqueous KOH solution II: Passivation experiments using linear sweep voltammetry, *Electrochim. Acta.*, **17** (1972) 387–394.
- [157] M.N. Hull, J.E. Ellison, J.E. Toni, The Anodic Behavior of Zinc Electrodes in Potassium Hydroxide Electrolytes, *J. Electrochem. Soc.*, **117**(2), (1970) 192-198.
- [158] L.M. Baugh, A. Higginson, Passivation of zinc in concentrated alkaline solution I: characteristics of active dissolution prior to passivation, *Electrochim. Acta.* **30**(9) (1985) 1163–1172.
- [159] L.M. Baugh, A. R. Baikie, Passivation of zinc in concentrated alkaline solution II Role of various experimental factors and the distinction between the solid state and dissolution-precipitation mechanisms, *Electrochim. Acta.* **30**(9) (1985) 1173–1183.
- [160] N.R. Short, S. Zhou, J.K. Dennis, Electrochemical studies on the corrosion of a range of zinc alloy coated steel in alkaline solutions, *Surf. and Coat. Tech.* **79** (1996) 218–224.
- [161] R.D.E.L. Bridger, R.D.E.L. Bridger, Pretreatment of Galvanized Surfaces Prior to Powder Coating, *Trans. Inst. Met. Fini.*, **61** (1982) 13-18. doi:10.1080/00202967.1983.11870629.
- [162] V.U. Brussel, J. Vereecken, Department of the Navy, (2004). doi:10.1149/1.1637355.
- [163] King. surface treatment and finishing of aluminium, 1st edition, p13-25 (1988).
- [164] M.J. Isaacson, F.R. Mclarnon, E.J. Cairns, Zinc Electrode Rest Potentials in Concentrated KOH-K₂Zn(OH)₄ Electrolytes, *J. Electrochem. Soc.*, **137**(8) (1990) 3–6.
- [165] R. B. Hoxeng, and C. F. Prutton, Electrochemical behavior of Zn and steel in aqueous media, *Corrosion* **5**(10) (1949) 330-338.
- [166] G.K. Glass, V. Ashworth, The corrosion behaviour of the zinc-mild steel galvanic cell in hot sodium carbonate solution, *Corros. Sci.* **25**(11) (1985) 971–983.
- [167] P.T. Gilbert, The Nature of Zinc Corrosion Products, *J. Electrochem. Soc.*, **99**(1), (1952) 16-21.
- [168] S. Thomas, I.S. Cole, M. Sridhar, N. Birbilis, Revisiting zinc passivation in alkaline solutions, *Electrochim. Acta.* **97** (2013) 192–201. doi:10.1016/j.electacta.2013.03.008.
- [169] M.R. Tabrizi, S.B. Lyon, G.E. Thompson, J.M. Ferguson, Long-term corrosion of aluminium alkaline media, *Corro. Sci.* **32**(7) (1991) 733–742.
- [170] M. Mokaddem, P. Volovitch, F. Rechou, R. Oltra, K. Ogle, The anodic and cathodic dissolution of Al and Al–Cu–Mg alloy, *Electrochim. Acta.* **55** (2010) 3779–3786. doi:10.1016/j.electacta.2010.01.079.
- [171] K. Ogle, A. Tomandl, M. Wolpers, M. Valette, technical steel research, European Commission, 2002.
- [172] R. Oltra, A. Zimmer, C. Sorriano, F. Rechou, C. Borkowski, O. Néel, Simulation of pH-controlled dissolution of aluminium based on a modified Scanning Electrochemical Microscope experiment to mimic localized trenching on aluminium alloys, *Electrochim. Acta.* **56** (2011) 7038–7044. doi:10.1016/j.electacta.2011.06.002.

- [173] D.M. Drazic, J. Popic, Hydrogen evolution on aluminium in chloride solutions, *J. Electrochem. Soc.*, **357** (1993) 105–116.
- [174] M. Bockelmann, L. Reining, U. Kunz, T. Turek, Electrochemical characterization and mathematical modeling of zinc passivation in alkaline solutions : A review, *Electrochim. Acta.* **237** (2017) 276–298. doi:10.1016/j.electacta.2017.03.143.
- [175] K. Ogle and J. Han, Aluminum Surface Science and Technology (ASST), 2018, Helsingor, Denmark..
- [176] B. Wilson, N. Fink, G. Grundmeier, Formation of ultra-thin amorphous conversion films on zinc alloy coatings Part 2 : Nucleation , growth and properties of inorganic–organic ultra-thin hybrid films, *Electrochim. Acta.* **51** (2006) 3066–3075. doi:10.1016/j.electacta.2005.08.041.
- [177] K. Ogle and R. G. Buchheit, Conversion coatings in corrosion and oxide films, eds. A. J. Bard, M. Stratmann, G. S. Frankel, *Encyclopedia of Electrochemistry*, vol. 4 (Weinheim, Germany: Wiley-VCH Verlag, 2003), 460-499.
- [178] E. Marina, S. Ramakrishnan, Z. Hussain, Synthesis of Biodegradable Mg-Zn Alloy by Mechanical Alloying : Effect of Milling Time, *Procedia Chem.* **19** (2016) 525–530. doi:10.1016/j.proche.2016.03.048.
- [179] S. Thomas, N. V Medhekar, G.S. Frankel, N. Birbilis, Corrosion mechanism and hydrogen evolution on Mg, *Curr. Opin. Solid State Mater. Sci.* **19** (2015) 85–94. doi:10.1016/j.cossms.2014.09.005.
- [180] P. Dawson, C.D. Hadfield, G.R. Wilkinson, The polarized infra-red and Raman spectra of Mg(OH)₂ and Ca(OH)₂, *J. Phys. Chem. Solids*, **34** (1973) 1217–1225.
- [181] R.L. Frost, M.L. Weier, J.T. Kloprogge, Raman spectroscopy of some natural hydrotalcites with sulphate and carbonate in the interlayer, *J. Raman Spec.* **34** (2003) 760–768. doi:10.1002/jrs.1050.
- [182] S.J. Palmer, R.L. Frost, G. Ayoko, T. Nguyen, Synthesis and Raman spectroscopic characterisation of hydrotalcite with CO₃²⁻ and (MoO₄)²⁻ anions in the interlayer, *J. Raman Spec.* **39** (2008) 395–401. doi:10.1002/jrs.
- [183] J. T. Kloprogge, D. Wharton, L. Hickey, and R. L. Frost, Infrared and Raman study of interlayer aions CO₃²⁻, NO₃⁻, SO₄²⁻ and ClO₄⁻ in Mg/Al-hydrotalcite, *American Mineralogist*, **87** (2002) 623–629.
- [184] Y. Chen. P. Schneider, B. J. Liu, S. Borodin, B. Ren, and A. Erbe, Electronic structure and morphology of dark oxides on zinc generated by electrochemical treatment, *Physi. Chem. Chem. Phys.*, **15** (2013) 9812-9822. doi:10.1039/c3cp44714f.
- [185] S. Xu, M. Liao, H. Zeng, X. Liu, J. Du, P. Ding, Surface modification and dissolution behavior of Mg – Al hydrotalcite particles, *J. Taiwan Inst. Chem. Eng.* **56** (2015) 174–180. doi:10.1016/j.jtice.2015.04.013.
- [186] T.N. Vu, Selective dissolution from Zn-Al alloy coatings on steel, thesis, HAL id: tel-00839479, 2013.
- [187] M. Mokaddem, P. Volovitch, K. Ogle, The anodic dissolution of zinc and zinc alloys in

- alkaline solution. I. Oxide formation on electrogalvanized steel, *Electrochim. Acta.* **55** (2010) 7867–7875. doi:10.1016/j.electacta.2010.02.020.
- [188] T.N. Vu, M. Mokaddem, P. Volovitch, K. Ogle, The anodic dissolution of zinc and zinc alloys in alkaline solution. II. Al and Zn partial dissolution from 5% Al-Zn coatings, *Electrochim. Acta.* **74** (2012) 130–138. doi:10.1016/j.electacta.2012.04.037.
- [189] M. Gentile, E. V. Koroleva, P. Skeldon, G.E. Thompson, P. Bailey, T.C.Q. Noakes, Influence of pre-treatment on the surface composition of Al-Zn alloys, *Corros. Sci.* **52** (2010) 688–694. doi:10.1016/j.corsci.2009.10.023.
- [190] Z.-G. Xi, Q.-F. Zhang, S.-M. Jiang, G.-Q. Yu, Effect of the process parameters on the microstructure and corrosion resistance of ZnMg alloy coatings prepared via a combined PVD and reaction-diffusion process, *Surf. Coatings Technol.* **306** (2016) 418–427. doi:10.1016/j.surfcoat.2016.05.017.
- [191] H.A. Nelson, W. W. Kittelberger, Preparation of Zinc and Zinc-Alloy Surfaces for Coating, *New Jersey Zinc Company*, Palmerlon, Pa, **25**(1) (1933) 27-32. doi:10.1021/ie50277a007.
- [192] X. Zhang, W.G. Sloof, A. Hovestad, E.P.M. Van Westing, H. Terryn, J.H.W. De Wit, Characterization of chromate conversion coatings on zinc using XPS and SKPFM, *Surf. & Coatings Technol.* **197** (2005) 168–176. doi:10.1016/j.surfcoat.2004.08.196.
- [193] X. Zhang, C. Leygraf, I. Odnevall Wallinder, Atmospheric corrosion of Galfan coatings on steel in chloride-rich environments, *Corros. Sci.* **73** (2013) 62–71. doi:10.1016/j.corsci.2013.03.025.
- [194] T.N. Vu, P. Volovitch, K. Ogle, The effect of pH on the selective dissolution of Zn and Al from Zn-Al coatings on steel, *Corros. Sci.* **67** (2013) 42–49. doi:10.1016/j.corsci.2012.09.042.
- [195] L. Jiang, P. Volovitch, M. Wolpers, K. Ogle, Activation and inhibition of Zn-Al and Zn-Al-Mg coatings on steel by nitrate in phosphoric acid solution, *Corros. Sci.* **60** (2012) 256–264. doi:10.1016/j.corsci.2012.03.028.

Curriculum Vitae – HAN Junsoo

Born in Seoul, South Korea, 6th May 1985
4 avenue de la cure d'air, 91400, Orsay, France
+33 7 82 86 91 00
juinhan85@gmail.com

Education

Sep. 2018 – present **IRCP** (Institut de Recherche de Chimie Paris), Paris, France
ENSCP (Ecole Nationale Supérieure de Chimie de Paris)
Post Doc.

- *Subject:* Kinetic analysis of the multi-element system by atomic emission spectroelectrochemistry (AESEC) coupled with electrochemical impedance spectroscopy.

Sep. 2015 – Aug. 2018 **IRCP** (Institut de Recherche de Chimie Paris), Paris, France
ENSCP (Ecole Nationale Supérieure de Chimie de Paris)
Ph. D. Physical Chemistry

- *Subject of the thesis:*
Electrochemistry and dealloying of Zn-Mg and Zn-Al phases; its significance for the corrosion of the Zn-Al-Mg alloy coatings.
- Advisor: Prof. Kevin Ogle
- Member of the European RFCS (research fund for coal and steel) project (2015-2019).

Sep. 2014 – Aug. 2015 **Ecole Polytechnique**, Palaiseau, France
Master of Science and Technology
Renewable Energy Science and technology (REST)
GPA: 17/20

- 'Blaise Pascal' scholarship student by French government (2014-2015).

Mar. 2005 – Feb. 2011 **Korea University**, Anam, Seoul, South Korea
(Military service 2005-2007) *Bachelor of Science in Chemistry*
GPA: 3.88/4.50

- Academic scholarship awarded 7 times (2007-2011) by Korea University.

Research Experiences

Aug. 2017

Max-Planck-Institut für Eisenforschung, Düsseldorf, Germany
Collaboration of the Microcorr project.

- Subject: Local electrochemistry of the Zn-Al-Mg alloy and MgZn₂ pure phases with inductively coupled plasma mass spectroscopy (ICP-MS) technique.
-

Mar. 2015 – Aug. 2015

IRCP (Institut de Recherche de Chimie Paris), Paris, France
ENSCP (Ecole Nationale Supérieure de Chimie de Paris)
Internship of Master 2

- Subject: Electrochemical analysis of the methylated Si electrode for Li-ion batteries by using electrochemical techniques and X-ray photoelectron spectroscopy (XPS).
 - Advisors: Prof. Michel Cassir (team I2E), Dr. Jolanta Swiatowska (team PCS).
-

Jun. 2011 – May. 2013

Samsung Corning Precision Materials, Cheonan, South Korea
Full time engineer

- Responsible engineer of the new generation display glass for the smartphone and OLED TV.
-

Jan. 2011 – Feb. 2011

Samsung Fine Chemical, Ulsan, South Korea
Internship

- Chemical analysis of the commercial product ‘MecelloseTM (methylated cellulose)’ for the application of construction materials.
-

Nov. 2008 – Feb. 2009

Gas Ion Chemistry Lab, Korea University, Seoul, South Korea
Undergraduate internship student

- Analysis of peptide sequence measured by FT-IR and mass spectroscopy using a home-made software.

Résumé

L'objectif de cette thèse est d'analyser l'électrochimie des phases pures, composants des alliages de revêtement Zn-Al-Mg. Les données électrochimiques ont été utilisées pour prédire le comportement à la corrosion des revêtements d'alliage multiphasé. A cette fin, une base de données de courbes de polarisation élémentaire a été établie en fonction du pH en utilisant la spectroélectrochimie d'émission atomique (AESEC). Le désalliage de la phase intermétallique $MgZn_2$ et de la phase α de Zn-Al (Zn-68Al) ont été étudiés à pH=10,1. Les extrêmes contiennent Mg et en Al dans le revêtement d'alliage Zn-Al-Mg, respectivement. Dans la polarisation cathodique, la couche enrichie en Zn (0) a été formée dans les deux cas par dissolution sélective de Mg et Al, respectivement. Cependant, l'influence de cette couche sur le désalliage cathodique différait: pour $MgZn_2$, la dissolution sélective de Mg était restreinte par la couche désaliée, alors que pour Zn-68Al, la dissolution sélective de l'Al n'était pas affectée par cette couche. Il a été observé que le début de la dissolution active de Zn coïncidait avec une réduction de la vitesse de dissolution de l'Al, suggérant un effet inhibitif de la dissolution de Zn sur la dissolution de l'Al. Il a aussi été observé que la dissolution de l'Al dans des milieux alcalins était limitée par la vitesse de dissolution du film de $Al(OH)_3$, mise en évidence par une dissolution de l'Al indépendante de potentiel. Les produits de corrosion les plus stables formés pendant des mesures électrochimiques, les solides précipités dans la solution pendant la titration et la simulation thermodynamique étaient raisonnablement cohérents entre eux. La plupart des espèces précipitées formées dans la solution correspondaient bien à celles prédites par la base de données thermodynamique. Il était en bon accord avec les produits de corrosion de l'alliage, caractérisés après les mesures électrochimiques. Par conséquent, on peut conclure que la base de données thermodynamique peut être utilisée pour prédire et éventuellement modéliser la situation de corrosion réelle.

Mots Clés :

Désalliage, électrochimie, corrosion de Zn-Al-Mg, revêtement Zn, technique AESEC, phase pure

Abstract

The objective of this Ph.D. project is to investigate the electrochemistry of the pure phases, components of the Zn-Al-Mg coating alloys. The electrochemical data was used as an input for the prediction of corrosion behavior of the multi-phase alloy coatings. To this end, a database of elemental polarization curves was established as a function of pH by using atomic emission spectroelectrochemistry (AESEC). Dealloying of the $MgZn_2$ intermetallic and α -phase of Al-Zn (Zn-68Al) were investigated at pH=10.1. The extremes of Mg and Al content in the Zn-Al-Mg alloy coating, respectively. In the cathodic polarization, the Zn(0) enriched layer was formed in both cases by selective dissolution of Mg and Al, respectively. However, the influence of this layer on cathodic dealloying differed: for $MgZn_2$, Mg selective dissolution was restrained by the dealloyed layer, whereas for Zn-68Al, Al selective dissolution was not affected by this layer. It was observed that the onset of active Zn dissolution coincided with a reduction in the Al dissolution rate, suggesting an inhibitive effect of Zn dissolution on Al dissolution. It was observed that Al dissolution in alkaline media was limited by the dissolution rate of the $Al(OH)_3$ film, evidenced by potential independent Al dissolution. The most stable corrosion products formed by electrochemical measurements, precipitated species in the solution during titration experiment and the thermodynamic simulation were reasonably coherent with each other. Most of the precipitated species formed in the solution corresponded reasonably well to those predicted by thermodynamic database. It was in a good agreement with the corrosion products of the alloy, characterized after the electrochemical measurements. Therefore, it can be concluded that the thermodynamic database can be used to predict and eventually model the real corrosion situation.

Keywords:

Dealloying, electrochemistry, corrosion of Zn-Al-Mg, Zn coating, AESEC technique, pure phase